IPP-Report

Max-Planck-Institut
für Plasmaphysik

Emanuele Poli

Magnetic Islands In Tokamak Plasmas

IPP 5/131
August, 2012

MAGNETIC ISLANDS IN TOKAMAK PLASMAS

Emanuele Poli

Kumulative Habilitationsschrift
zur Erlangung der Lehrbefugnis
für das Fachgebiet Theoretische Physik

Fakultät für Naturwissenschaften
der Universität Ulm

August 2011

Acknowledgements

I am indebted to Prof. J. Ankerhold for his guidance through the bureaucratic hurdles of the Habilitation procedure and to Profs. S. Günter, K. Lackner and H. Zohm for their encouragement and support. I wish also to thank Prof. F. Jenko for the fruitful collaboration in the teaching activity at the University of Ulm.

Many colleagues, at the Max-Planck-Institut für Plasmaphysik and abroad, have shared with me their time and interests in the past years, in the frame of a collaboration or just in front of a cup of tea (or something more tasty). From them I have learned, and I am still learning, a great deal. Such a friendly and stimulating environment is a fundamental contribution to making research a rewarding task.

Finally I want to express my thankfulness to those who have been on my side day by day: my friends for finding the time, sometimes fighting against kilometres and years, my family for warmth and protection and particularly my wife for accepting the complete package (including the physicist).

Note: In this thesis, I have highlited the references of which I am first author (in red) or co-author (in blue).

Contents

Chapter 1

Nuclear fusion and magnetic confinement

1.1 Nuclear fusion and plasma physics

The fusion of light nuclei into heavier nuclei is an extremely powerful energy source, the energy per elementary process being in the range of several MeV, whereas the energy released in chemical reactions, like combustion of fossil fuels, is about six orders of magnitude smaller. In the Sun, a reaction chain leads to the fusion of four hydrogen nuclei into a nucleus of ${}^4_2\mathrm{He}$, delivering an energy of 26.7 MeV. On Earth, a commercial exploitation of nuclear fusion for energy production in a power plant requires a higher reaction rate than for the proton-proton chains occurring in the Sun. For this reason, it is envisaged to employ the reaction

$$D + T \rightarrow\ {}^4_2\mathrm{He} + n + 17.6\ \mathrm{MeV}$$

in which deuterium and tritium combine to an α-particle and a neutron with an energy of 3.5 and 14.1 MeV respectively. Since the Coulomb barrier between the positively-charged deuterium and tritium ions opposes the fusion process, the reactants need a sufficient energy in order for the reaction to take place. The most promising approach to overcome this problem is to heat the deuterium-tritium mixture to a temperature[1] of the order of tens of keV. At these temperatures, deuterium and tritium are in the plasma state, where the gas is almost completely ionized. As charged particles react to electric and magnetic fields, a possibility to confine a burning plasma on Earth (in the Sun, the plasma is held together by gravitational attraction) is to employ a properly shaped magnetic field. The principles of magnetic confinement, and in particular of a tokamak reactor, are briefly described in the next section. The optimum temperature for the plasma of a fusion reactor is determined by the condition that in a burning plasma the heating through the α-particles generated in the fusion processes[2] exceeds the power lost through transport and radiation, $P_\alpha > P_{\mathrm{loss}}$ with $P_{\mathrm{loss}} = P_{\mathrm{transp}} + P_{\mathrm{rad}}$. The power density generated through fusion reactions is the product of the energy of the α particle released in a single reaction ($E_\alpha = 3.5$ MeV) times the number of reaction per unit volume and time $R_{DT} = n_D n_T \langle \sigma(u) u \rangle$, where u is the relative velocity of the colliding particles and σ is the

---

[1] The temperature is here always treated as an energy, i. e. multiplied by the Boltzmann constant $k_B = 0.86 \times 10^{-4}$ eV/K. An energy of 10 keV thus corresponds to a temperature of more than 100 million Kelvin.

[2] The neutrons do not interact with the plasma and hence do not heat it. In a reactor, their energy should be absorbed by the walls of the vessel enclosing the plasma and the resulting heat exploited for the generation of electricity.

cross section for the reaction under consideration. The power lost through radiation (mainly bremsstrahlung) is proportional to the density squared and to the square root of temperature, $P_{\text{loss}} = c_B n_e^2 \sqrt{T}$, where n_e is the electron density. A theoretical model giving a quantitative prediction of the energy losses due to transport is still missing, although much progress has been achieved in this field particularly in the past two decades. It is therefore customary to write $P_{\text{transp}} = 3n_e T/\tau_E$, introducing the energy confinement time τ_E which is determined empirically on the basis of the results of present experiments. The condition for a burning plasma becomes then

$$n_e \tau_E > \frac{3T}{\langle \sigma(u) u \rangle E_\alpha / 4 - c_B \sqrt{T}} \equiv f(T), \tag{1.1}$$

where the fact that the maximum fusion rate is obtained for $n_D = n_T = n_e/2$ has been employed. The function $f(T)$ on the right-hand side of this inequality, called the Lawson criterion [1], has a minimum in the region between 20 and 30 keV[3]. Exploiting the fact that $\langle \sigma u \rangle$ in the temperature range 10-20 keV is approximately a quadratic function of T and neglecting the radiation losses against the transport losses, the previous inequality can be cast in the form of a threshold condition for the so-called "fusion triple product", $n_e T \tau_E > 3 \times 10^{21}$ m^{-3} s keV, cf. Fig. 1a.

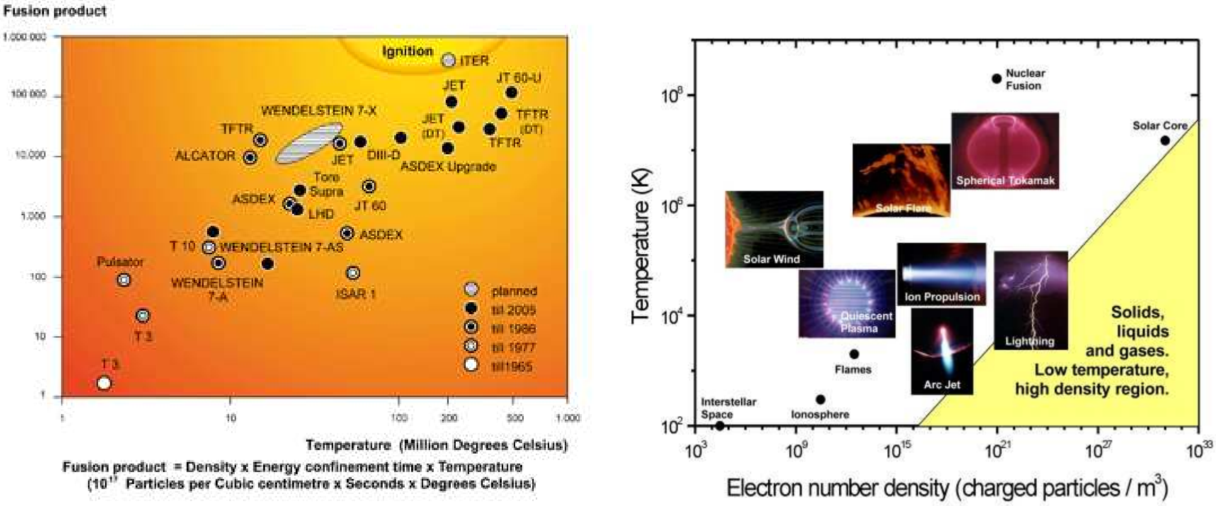

Fig. 1. *The fusion triple product as a function of temperature, including the results achieved on different fusion facilities (a) and the parameter range typical of classical plasmas (b).*

In present-day (not ignited) machines, the heat losses must be compensated by supplying energy from the outside, i. e. by means of external heating. Thus, a useful figure to characterize the performance of a fusion reactor is the ratio between the power produced by fusion reactions and the injected auxiliary power,

$$Q \equiv \frac{P_\alpha}{P_{\text{aux}}}, \tag{1.2}$$

which is called the fusion gain factor. An ignited plasma, in which no external heating is required, corresponds to the limit $Q \to \infty$. The main physics goal of the ITER machine [3], presently under construction, is to demonstrate that nuclear fusion can be exploited as an energy source by reaching a gain factor $Q = 10$.

The densities and temperatures resulting from the Lawson criterion determine not only the values envisaged for a fusion reactor but also define the theoretical framework needed for

---

[3] It has to be noted, however, that τ_E itself is a function of temperature. It turns out that the the optimum temperature for ignition is likely to be somewhat lower[2].

a proper description of a burning plasma. As a matter of fact, plasmas occurring both in laboratory and in nature are often classified with reference to these two quantities. An example is shown in Fig. 1b. Over a wide range of values, including those typical of nuclear fusion, ionized gases represent a non-relativistic, classical, weakly-coupled system. This means that (a) the mean kinetic energy of the electrons is much smaller than their rest energy[4], (b) the temperature of the plasma is much larger than its Fermi energy (or in other words, the average distance between particles is much larger than their de Broglie length) and (c) the potential energy associated to the Coulomb interaction is much smaller than the mean kinetic energy. Such plasmas are called ideal and their theoretical treatment is based on the equations of classical physics.

1.2 Magnetic confinement

The confinement of a hot plasma can be achieved by means of an appropriately shaped magnetic field. The reason is clearly that the plasma is composed by charged particles, that are accelerated by the Lorentz force[5] $m\dot{\mathbf{v}} = Ze\mathbf{v} \times \mathbf{B}/c$. This force acts only in the direction perpendicular to the magnetic field. If $\mathbf{B}$ is homogeneous, the motion of a charged particle due to the Lorentz force is the superposition of a free streaming with constant velocity in the direction parallel to the magnetic field and a circular motion in the plane perpendicular to it, characterized by the gyrofrequency (or cyclotron frequency) $\Omega = ZeB/mc$ and by the gyroradius (or Larmor radius) $\rho = v_\perp/\Omega$. A magnetic field thus offers a direct way to confine charged particles. To avoid end losses, one can imagine to bend the magnetic field lines to a ring (torus). This simple design, with a set of planar coils arranged in a ring generating a purely toroidal magnetic field (Fig. 2a), is unfortunately not sufficient to ensure confinement.

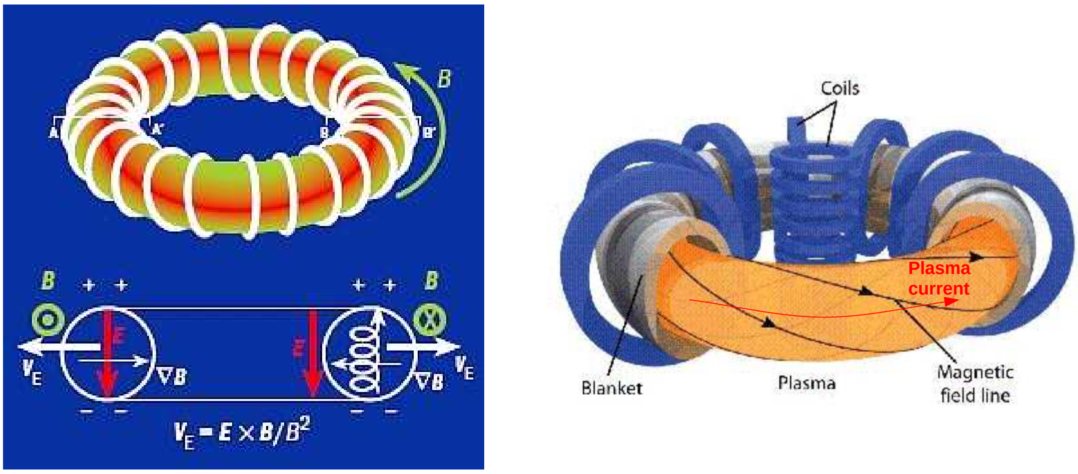

Fig. 2. *(a) Schematic diagram showing the magnetic field created by a system of coils arrayed in the toroidal direction and the resulting particle motion leading to the expulsion of the plasma. (b) A tokamak: a toroidal current induced in the plasma generates a poloidal field. The field lines become helical and make plasma confinement possible.*

Since in a toroidal configuration the magnetic field is non-uniform, particle drifts in the vertical direction arise, which are in opposite direction for ions and electrons, as explained in Chapt. 3. The electric field resulting from charge separation leads eventually to the expulsion

---

[4] A relativistic description is sometimes needed in order to properly account for suprathermal electrons, in particular those developing in heating processes and runaway events.

[5] Unless explicitly stated, c.g.s. units are used in this work. The electron charge is $-e$, i. e. $Z = -1$.

of the plasma in the direction $\mathbf{E} \times \mathbf{B}$ perpendicular to both the vertical electric field and the toroidal magnetic field. To avoid this problem, two main solutions have been proposed since the early days of magnetic-confinement fusion. The first concept is based on the generation an additional ("poloidal") magnetic field component through a current flowing toroidally in the plasma. This current is generated by a toroidal electric field induced by a change of magnetic flux through the torus, the plasma acting as the secondary winding of a transformer. The superposition of the poloidal field with the toroidal field generated by the coils gives rise to helical field lines (Fig. 2b), describing nested toroidal surfaces called magnetic surfaces or flux surfaces. This configuration can be shown to compensate for the vertical drifts mentioned above, so that the plasma particles are to a good approximation forced to remain on the magnetic surfaces. This ensures a good radial confinement of the hot plasma, that can be kept in the desired shape and at a suitable distance from the material walls of the vessel. Such a confinement device is called a *tokamak* (Russian acronym for "toroidal chamber and magnetic coils"). The best performances of a magnetically-confined plasma (with a fusion gain Q just below unity) have been obtained employing this approach, that has been chosen also for the ITER reactor mentioned above. This concept, however, has the obvious disadvantage that it is intrinsically non-stationary, since a time-varying magnetic flux in the transformer cannot be provided for an indefinite time[6]. Moreover, the current flowing in the plasma is a source of free energy for possible instabilities that can endanger the confinement. The alternative concept, i. e. the so-called *stellarator*, in which the additional magnetic field needed for confinement is provided directly by non-planar coils, is free from these limitations. However, it turns out that the quality of the confinement in a stellarator is less good than in a tokamak of comparable size.

1.3 Contribution of this thesis

The problems encountered in the effort of increasing the performance of a reactor define the major current research fields in the physics of fusion plasmas. First, the achievable parameters like pressure and current are limited by large-scale instabilities, that must be avoided or at least controlled in order to operate the machine. A second area of intense activity is the explanation of the observed energy confinement time, i. e. of the physical mechanisms (mainly related to turbulence developing as a consequence of small-scale instabilities) responsible for the transport of particles and heat in a tokamak. Third, heating schemes to bring the plasma to the required temperature must be devised. This involves the study of electromagnetic waves excited by external antennas that deliver their energy to the plasma as a consequence of resonant processes, and the investigation of heating by injection of high-energy ions, releasing their energy through collisions with the plasma particles. A fourth important area, particularly in view of the construction of the first prototype of a fusion reactor, is the interaction of the burning plasma with the surrounding material walls.

The work presented here can be roughly inserted in the frame of the first big area described above. Specifically, recent progresses in the theoretical understanding of the so-called *tearing* instability in a tokamak are discussed. This is a large-scale instability arising in regions of

---

[6] In a tokamak, the plasma current is actually not entirely induced by the transformer. An additional current, roughly proportional to the pressure gradient, is provided for instance by the so-called *bootstrap* effect explained in Sec. 3.1. Moreover, a further part of the current can be driven by external means, like the injection of fast particles or electromagnetic waves, cf. next section and Sec. 5.1. The maximization of the non-inductive current fraction ("advanced scenarios") with the goal of approaching steady-state conditions is one of the most challenging research areas for tokamak operations.

the plasma prone to magnetic reconnection and causing the appearance of magnetic islands, as depicted in Fig. 3 (for a close-up view of a magnetic island see Fig. 2 of the next chapter). In the reconnected region, the magnetic field acquires a radial component, with a correspondent degradation of the radial confinement of energy and particles with respect to the case with nested flux surfaces described in the previous section. The consequent pressure loss is also shown in Fig. 3. A fully-developed tearing instability in ITER is predicted to have a significant impact on the target $Q = 10$ [4]. Moreover, the loss of confinement can also lead to a quench of the plasma current and to the disruption of the plasma discharge, with possible damage of the reactor [5, 6]. Finally, tearing modes can lead to the expulsion of fast ions, like those generated in fusion reactions or through plasma heating [7][8][9], with consequent reduction of the energy content of the plasma and erosion of the surrounding material walls. For these reasons, the conditions under which magnetic islands develop and how they can be actively controlled or avoided are intensively investigated. This will be the subject of the next chapters, as outlined in the remainder of this section with particular reference to the journal articles, listed in Appendix C, that constitute the body of this thesis.

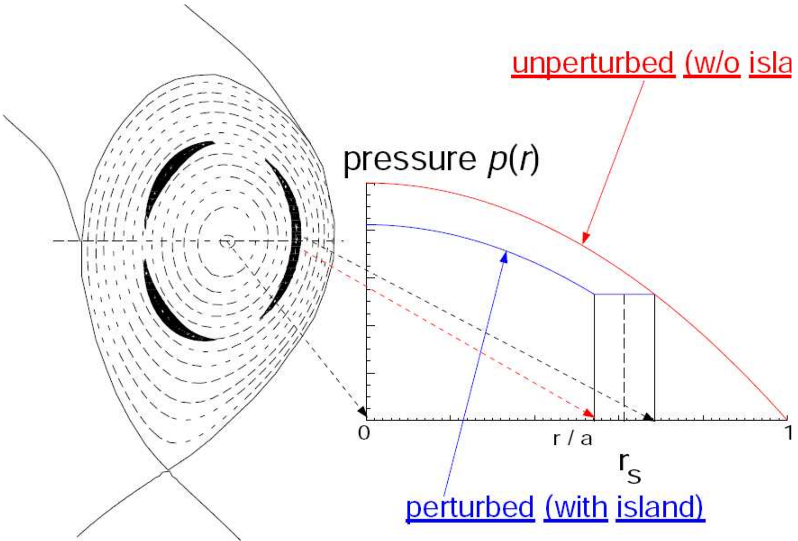

Fig. 3. *Vertical (poloidal) cross section of a tokamak plasma in the presence of a magnetic island at a radial position* $r = r_s$ *(left) and the corresponding pressure profile, showing the loss in the core due to degraded radial confinement (pressure flattening inside the island, right).*

The basic theory of the tearing mode is described in Chapt. 2 employing a simplified planar geometry and a single-fluid approach to describe the plasma behaviour. Although some of the conditions for the applicability of this model can be violated under realistic circumstances, it provides nevertheless the simplest framework to understand several fundamental features of the reconnection process (a discussion of this approach and of its extensions within a linear approximation is presented in Appendix A).

In a toroidal configuration, additional currents flowing in the region where reconnection takes place affect significantly the dynamics of a magnetic island, as explained in Chapt. 3. In particular, experimental results and theoretical modelling show that the main drive for the tearing mode in present and future tokamaks originates from the perturbation of the pressure-gradient-driven bootstrap current due to the flattening of the pressure inside the island (see again Fig. 3). The generation mechanism of the bootstrap current relies critically on the details of the particle orbits. The first set of original results presented in this thesis (Sec. 3.2) concerns the calculation of the bootstrap drive for the case of a magnetic island whose size is of comparable to the orbit width of the plasma ions, as is typically the case in the early phase of tearing modes. These "small" islands are observed to be more stable against tearing, so that the initial perturbation must often exceed a given threshold to become unstable. In this phase, the approximation of small orbit width (with respect to the island width) usually employed in analytic theories becomes invalid and a numerical approach to solve the relevant (drift) kinetic equation becomes necessary. Refs. [10, 11] report on kinetic simulations of the ion component of the bootstrap current, for which finite-orbit effects are larger (electrons having a much smaller orbit width). It is shown that the assumption of vanishing bootstrap current is not justified inside a small island. This is explained in terms of an overlap between particle orbits and the radial extension of the magnetic island, which leads to an "averaged" response of those particles that drift partly inside and partly outside it. These finite-orbit effects are found to compete with the reduction of the bootstrap drive due to finite transport across the island in increasing the stability of the plasma against tearing, and they are even stronger [11] in the case of (almost) flat core density, which is predicted to occur in ITER. Moreover, the reduction of the bootstrap drive resulting from orbit overlap yields a possible explanation [10] for the observed scaling of the plasma pressure at mode onset with the normalized Larmor radius found experimentally. The numerical approach employed to obtain these results has been extended to the case of rotating islands by including an analytic model for the electrostatic potential connected with the time-dependent magnetic perturbation. More refined simulations determining the total bootstrap current (including the electrons in a successive simulation step) in small rotating islands, presented in Ref. [12], have confirmed the enhanced stability against the bootstrap drive for islands rotating in the so-called electron diamagnetic direction, which is likely to be the rotation direction of small islands. In this case, the reduction of the drive is seen to involve the entire bootstrap current and not just the ion component.

A particularly interesting issue connected with the rotation of magnetic islands with respect to the surrounding plasma is the ion polarization current generated by the time-dependent electric field seen by the particles (Sec. 3.3). Due to its strong increase at small island widths predicted by the analytic theory, the contribution of the polarization current has been invoked as an alternative explanation for the increased stability of small islands (although its effect – whether stabilizing or destabilizing – is not known with certainty). Three aspects of this problem have been addressed in Ref. [13]. First of all, the transition to the enhanced "high-collisionality" regime of the polarization current is found to take place at unrealistically high collision frequencies. Moreover, finite-orbit effects like those described for the bootstrap drive are found to reduce the value of the polarization current at small islands with respect to analytic theory. Finally, for small (but still realistic) rotation frequencies the polarization current is found to be superseded by a contribution related to a resonance between the island rotation and the precession of part of the particle population around the torus, this contribution to the island dynamics being of different sign with respect to the polarization current. These resonance effects have been investigated in detail in Ref. [14] and an analytic explanation of the numerical results has been given in Ref. [15]. All the effects described above point towards a reduction of the role of the polarization current for the dynamics of the tearing mode. More generally, the results presented in Chapt. 3 demonstrate that a theory of magnetic islands in a tokamak must be based on a kinetic modelling, and that toroidicity effects need to be included.

These results were among the reasons for adopting an approach based on a (gyro) kinetic description of the plasma in tokamak geometry also to address another important topic for the theory of magnetic islands, namely the mutual interaction between small and large-scale instabilities. This involves a fairly complex physics, since both small and large structures contribute to the transport level (the resulting profiles back-reacting on the further growth of the instabilities) and since energy can be transferred among different scales through nonlinear coupling. Refs. [16, 17] explore the influence of a prescribed island on microturbulence. The simulations reported in Refs. [16] show the first numerical evidence of the nonlinear excitation in toroidal geometry of linearly stable large-scale electrostatic modes of the same size as the island and of the action of the related $\mathbf{E} \times \mathbf{B}$ sheared flows in "ripping apart" the turbulent eddies, thus strongly reducing the transport across the island (except for the region around the so-called X-points). In other words, the transport in the island region is found to be spatially inhomogeneous and previous modelling based on the assumption of constant transport coefficients should be revised. Employing a more refined model for the dynamics of the electrons, as reported in Refs. [17], has evidenced that the large-scale modes can appear as time-dependent "vortex modes", whose contribution to radial transport can compete with the transport due to the streaming along the field lines. Because of the sophistication of such a kinetic approach, a closure of the loop to include the feedback of small-scale modes on the evolution of the tearing mode (which involves much longer time scales than those typical of turbulence) is still computationally prohibitive, and our results can be seen as a first step towards this goal, complementing other studies that retain the feedback of small on large scales but simplify the description of turbulence and/or geometry. Nevertheless, first results showing the contribution of electromagnetic turbulence to the growth of a magnetic island have been obtained under conditions typical of a mid-size tokamak through the numerical solution of the gyrofluid equations [17]. These findings are discussed in Chapt. 4.

The issue of an active control of tearing modes in a tokamak reactor is finally addressed in Chapt. 5. The most promising strategy developed so far for the control of large scale instabilities is the localized injection of electromagnetic waves resonating with the cyclotron motion of the electrons. In this frequency range, the propagation and absorption of a wave beam can be described through asymptotic techniques. Paraxial beam tracing is an elegant method for the solution of the wave equation in the short-wavelength limit including diffraction effects, which are otherwise neglected in applications based on standard geometric optics. The underlying physics and its numerical implementation in one of the codes that are routinely employed for the calculation of plasma heating and current drive in tokamaks is presented in Ref. [18]. An antenna for active mode control/stabilization in ITER is being developed. Theory-based criteria on the amount of driven current and its localization required to achieve tearing-mode suppression have been developed. A recent account of the predictions of the system performance is presented in Ref. [19], where it is shown that the ITER antenna should not only achieve full tearing-mode suppression but also help control other large-scale instabilities and allow a synergy with the other antennas which will be installed for electron heating.

A summary of the thesis is given in Chapt. 6.

Although a constant effort is made to put each result in an appropriate context, it is stressed that this thesis does not have the goal of presenting a comprehensive review of the present knowledge on the stability of a tearing mode in a tokamak. It is rather intended to give the reader the necessary background to understand the contribution of the author to this research field, together with a summary of the main results.

Chapter 2

The tearing mode

2.1 Magnetohydrodynamics and magnetic reconnection

Magnetic reconnection is the process by which magnetic-field lines embedded in a plasma break and rearrange in a new (topologically different) configuration. An example is shown in Fig. 1, where two field lines are "pushed" towards each other. During the reconnection process they loose their original identity so that finally a new magnetic configuration emerges. This apparently simple process is responsible for some of the most spectacular observations which can be made in the Solar system. The occurrence of reconnection in both tokamak and astrophysical plasmas is discussed at the end of this section. Here, we first present the basic theoretical framework allowing a joint treatment of the dynamics of both the plasma and the magnetic field.

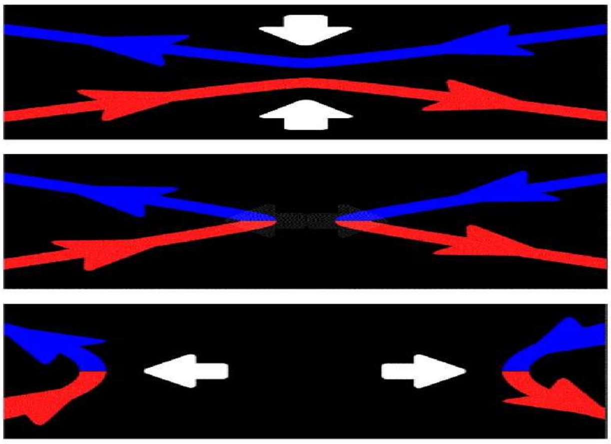

Credits: Center for Visual computing, Univ. of California Riverside

Fig. 1. *Diagram showing the reconnection of two magnetic-field lines pointing in opposite directions and the consequent change of the field topology.*

A plasma can be considered as a gas of charged particles reacting to electromagnetic fields. The simplest description of a magnetized plasma is the magnetohydrodynamic theory (MHD), according to which the motion of the plasma fluid is determined by the balance of pressure gradient and Lorentz force,

$$\rho\left(\frac{\partial}{\partial t}+\mathbf{u}\cdot\nabla\right)\mathbf{u}=-\nabla p+\frac{\mathbf{J}\times\mathbf{B}}{c}. \tag{2.1}$$

Here, ρ is the mass density and $\mathbf{u}$ the fluid velocity. The last term, that would be absent in a gas of neutral particles, introduces a coupling with the electromagnetic fields. In this term, Ampère's law is employed to determine $\mathbf{J}$ as a function of $\mathbf{B}$:

$$\mathbf{J} = \frac{c}{4\pi}\nabla \times \mathbf{B}, \tag{2.2}$$

implying that the current is solenoidal and $\nabla \cdot \mathbf{J} = 0$ expresses quasi-neutrality (for non-relativistic fluid velocities, $\partial\rho/\partial t$ in the current continuity equation and the displacement current in Ampère's law can be neglected). The magnetic field itself is the solution of the induction equation,

$$\frac{\partial \mathbf{B}}{\partial t} = -c\nabla \times \mathbf{E}. \tag{2.3}$$

A fundamental point for the description of magnetic reconnection is the equation used to determine the electric field $\mathbf{E}$ appearing in Eq. (2.3). As a first approximation, the inertia of the electrons and their friction with the ions can be neglected. The electric field is then determined by the so-called Ohm's law of ideal MHD,

$$\mathbf{E} + \frac{\mathbf{u} \times \mathbf{B}}{c} = 0, \tag{2.4}$$

which can be interpreted as a statement that in a system co-moving with a fluid element (in which the magnetic field vanishes) every electric field is compensated by the fast motion of the electrons[1]. The MHD theory obtained from substituting Eq. (2.4) into Eq. (2.3) is called ideal MHD, as in this model a current can flow without the need for an electric field to generate it. In this context, an important point to be stressed is that no electric field parallel to the magnetic field can exist in ideal MHD. One of the most impressive consequences of this model is the so-called frozen-in flux. As it was shown by Alfvén [23], Eqs. (2.3,2.4) imply that in a perfectly conducting fluid, magnetic field lines move with the medium (and vice versa), as if they were material lines frozen into it. This theorem helps explain the behaviour of the plasma under the action of the Lorentz force. Employing Eqs. (2.2,B.7) we can write $\mathbf{J} \times \mathbf{B}/c = [(\mathbf{B} \cdot \nabla)\mathbf{B} - (\nabla\mathbf{B}) \cdot \mathbf{B}]/4\pi$. Taking e. g. a small magnetic perturbation, perpendicular to $\mathbf{B}$ and periodic along $\mathbf{B}$ (as to ensure $\nabla \cdot \mathbf{B} = 0$), and linearizing, it is easy to see that the magnetic field oscillates as a violin string under the effect of tension, due to the first term, sometimes called "magnetic tension force". The "inertia" of the magnetic field line is provided by the fluid mass oscillating with it according to Alfvén's theorem. Similarly, a magnetic perturbation parallel to $\mathbf{B}$ and periodic in the direction perpendicular to $\mathbf{B}$ leads to a compression of the magnetic field (and of the fluid moving with it) described by the second term in the Lorentz force. This implies that whichever mechanism leads to tearing and magnetic reconnection, it has to act against a tension trying to "straighten" the bent magnetic field.

Actually, Alfvén's theorem also implies that the annihilation of magnetic field lines is forbidden, since it would imply the annihilation of the plasma associated with them. In other words, no magnetic reconnection can take place in the framework of ideal MHD. However,

---

[1] A more rigorous justification [20, 21] of Eq. (2.4) relies on the analysis of the various terms of the electron momentum balance [22]

$$m_e n_e \left(\frac{\partial}{\partial t} + \mathbf{u}_e \cdot \nabla\right)\mathbf{u}_e = -\nabla p_e - e n_e \left(\mathbf{E} + \frac{\mathbf{v} \times \mathbf{B}}{c}\right) - m_e n_e \nu_{ei}\left(\mathbf{u}_e - \mathbf{u}_i\right). \tag{2.5}$$

For fluid velocities of the order of the thermal velocity, under the assumptions mentioned above, together with that of a strongly magnetized plasma (small gyroradius), Eq. (2.4) is recovered. The validity of these assumptions is discussed below.

magnetic-flux conservation can be violated, i. e. field lines are allowed to shift with respect to the plasma, if the assumption leading to Eq. (2.4), i. e. that the electrons are free to move along the field lines to instantaneously short out every electric field in that direction, is relaxed. This is the case if we consider, for instance, the collisions of the electrons with the ions, i. e. if we retain the last term in Eq. (2.5). This leads to a non-zero resistivity $\eta = 4\pi\nu_{ei}/\omega_{pe}^2$, where $\omega_{pe}^2 = 4\pi n_e e^2/m_e$ is the electron plasma frequency. Ohm's law acquires the form

$$\mathbf{E} + \frac{\mathbf{u}\times\mathbf{B}}{c} = \eta\mathbf{J}, \tag{2.6}$$

showing that a parallel electric field can now arise. Using Eq. (2.2) it is easy to show that the induction law $\partial\mathbf{B}/\partial t = -c\nabla\times\mathbf{E}$ then becomes (η is supposed to be constant for the sake of simplicity)

$$\frac{\partial\mathbf{B}}{\partial t} = \nabla\times(\mathbf{u}\times\mathbf{B}) + \frac{c^2\eta}{4\pi}\nabla^2\mathbf{B}. \tag{2.7}$$

A diffusive term, absent in the ideal limit $\eta \to 0$, appears in Eq. (2.7) and describes the "defrosting" of the magnetic field, i. e. it allows for a relative motion of the magnetic field with respect to the plasma. Different time scales are associated with the two terms on the right-hand side of this equation. For a fusion plasma with $T_e = 1$ keV and $n_e = 10^{14}$ cm^{-3} one obtains (for a scale length of the order of $L = 50$ cm) a *resistive time* τ_R for the diffusion of the magnetic field

$$\tau_R \equiv \left(\frac{c^2\eta}{4\pi L^2}\right)^{-1} \simeq 6.4 \text{ s}, \tag{2.8}$$

whereas the typical ideal-MHD time (*Alfvén time*) can be estimated as

$$\tau_A \equiv \left(\frac{v_A}{L}\right)^{-1} \simeq 1.1\cdot 10^{-7} \text{ s}, \tag{2.9}$$

where in the Alfvén velocity[2] $v_A \equiv B/\sqrt{4\pi\rho}$ a field $B = 2$ T ($2\cdot 10^4$ gauss) has been taken and the mass density $\rho = n_i m_i$ has been calculated assuming a hydrogen plasma. The ratio $S \equiv \tau_R/\tau_A$ is called the magnetic Reynolds number or Lundquist number. In many applications, $S \gg 1$ (for the parameters under consideration, $S \simeq 5.6\cdot 10^7$), and the use of ideal MHD is in general well justified.

There are however situations for which the first term on the right-hand side of Eq. (2.7) vanishes, and the finite resistivity of the plasma, no matter how small, becomes important. An example which is particularly instructive for the results presented in this work is a spatially periodic small displacement $\boldsymbol{\xi} \propto \exp(i\mathbf{k}\cdot\mathbf{x})$ (with $\mathbf{u} = \partial\boldsymbol{\xi}/\partial t$) of the plasma from its equilibrium. In the frame of ideal MHD, i. e. neglecting the diffusive term, linearizing Eq. (2.7) yields for the corresponding magnetic perturbation $\tilde{\mathbf{B}} = \nabla\times(\boldsymbol{\xi}\times\mathbf{B}_0)$. Using Eq. (B.9) it is easy to show that a component of $\tilde{\mathbf{B}}$ perpendicular to $\mathbf{B}_0$ is forbidden where $\mathbf{k}\cdot\mathbf{B}_0 = 0$. This situation is illustrated on the left side of Fig. 2. If the resistive term in Eq. (2.7) is taken into account, such a component is admitted and the topology of the magnetic field lines is modified around the "resonant" surface $\mathbf{k}\cdot\mathbf{B}_0 = 0$. Magnetic surfaces are disrupted and *reconnected* forming a chain of "magnetic islands" (Fig. 2, right side).

---

[2] The Alfvén velocity is the typical speed associated to the fluid motion under the action of the Lorentz force, as can be readily estimated from Eq. (2.1), which using Eq. (2.2) to express the current density gives $\rho u^2/L \sim B^2/4\pi L$.

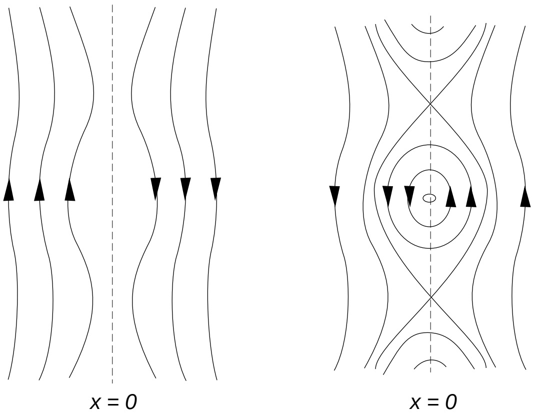

Fig. 2. *Effect of a periodic plasma displacement in ideal and resistive MHD. The condition* $\mathbf{k} \cdot \mathbf{B}_0 = 0$ *is supposed to be satisfied at* $x = 0$.

The perturbation associated with the formation of magnetic islands is called the tearing mode. From an energetic point of view, it can be shown by taking the scalar product of Eq. (2.7) with $\mathbf{B}/4\pi$ that magnetic reconnection leads to dissipation of magnetic-field energy $B^2/8\pi$ through a term ηJ^2 (absent in ideal MHD) and is therefore energetically favorable. However, since the tearing configuration requires bending of the field lines, i. e. to work against the field-line tension, a source of free energy must be available. If this is the case, the tearing mode becomes unstable.

As a final remark, it is important to stress that violation of the frozen-flux theorem does not necessarily imply that a finite resistivity must be assumed. Other terms in Eq. (2.5) can also lead to a breakdown of the ideal MHD law $\mathbf{E} + \mathbf{u} \times \mathbf{B}/c = 0$ and hence to magnetic reconnection. These terms can be more important than resistivity if the collision frequency is low, as is the case in a high-temperature plasma. Generally speaking, the physical mechanism determining the width of the "reconnection layer" where $E_{\|}$ does not vanish has a significant impact on the time and space scales involved in the reconnection process. In particular, at low collisionalities the response of the plasma is dominated by the electrons alone and the width of the reconnection layer falls below the ion gyroradius, making a separate treatment of ions and electrons mandatory. This instructive analysis is presented in Appendix A, in a linear approximation, for the planar sheet-pinch model discussed in Sec. 2.2. In the remainder of this chapter, for the purpose of illustrating the basic features of magnetic reconnection we will stick to the single-fluid MHD model outlined above. The consequences of different collisionality regimes for the tearing mode in a tokamak are briefly addressed at the end of Sec. 2.3.

To conclude this section, we present some examples of magnetic reconnection, taken from the two main research areas of plasma physics, namely astrophysics and nuclear fusion.

2.1.1 Reconnection in astrophysics

Magnetic reconnection is involved in several processed observed in stellar and interplanetary plasmas, playing a crucial role solar flares, in the magnetotail and the magnetosphere-solar wind interface [24, 25, 26]. The reconnection event is forced by the flow of the plasma as depicted in Figs. 1 and 3. Opposite field lines are crushed so closely together and the region between them becomes so narrow that the current density increases to a point where the resistive term on the right-hand side of Eq. (2.6) is no longer negligible, even for high Lundquist number $S \gg 1$. Once reconnection has occurred, the magnetic pressure and the tension of the new field lines cause the field to unfold and the plasma to accelerate out of the ends of the current layer. In the process, the magnetic energy is lowered and the kinetic energy of the plasma increases, and can be visible in the form of particle acceleration or radiation.

The reference model to estimate the reconnection rate under these conditions is due to Sweet [27] and Parker [28, 29]. They recognized that the reconnection rate is determined not only by the strength of the non-ideal term in the diffusion equation for the magnetic field lines, but also by the rate at which the plasma conveyed into the layer can leave it at its ends, cf. Fig. 3a.

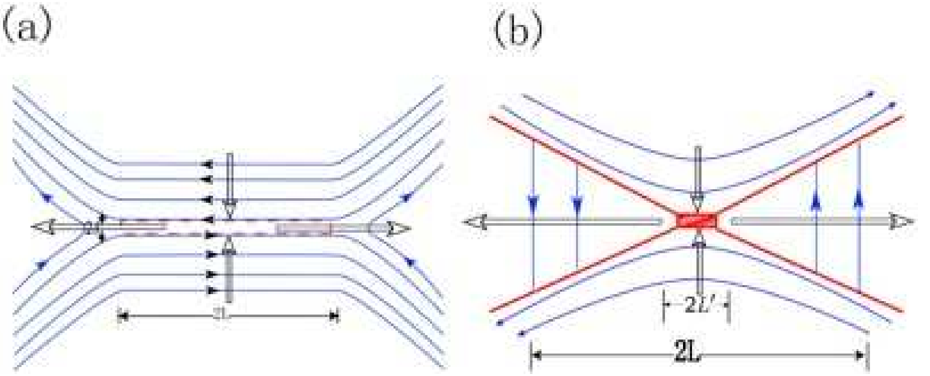

Fig. 3. *Sweet-Parker (a) and Petschek (b) reconnection models. The parameter δ in the left figure corresponds to the tearing-layer width denoted by Δ in the text. The plasma is advected into the reconnection layer in the vertical direction and leaves it in the horizontal direction.*

From Eqs. (2.7,2.16) the annihilated flux per unit length ψ at a singular layer of width Δ can be estimated as

$$\frac{\partial \psi}{\partial t} = -\frac{c^2 \eta}{4\pi} \frac{B}{\Delta}.$$

The velocity of the ejection of the plasma from the singular layer is determined by the increase of magnetic energy in the layer and is hence of the order of the Alfvén speed v_A. The reconnection velocity v_R, defined through the equation $\partial\psi/\partial t = -v_R B$, can be related to the outflow velocity under the hypothesis of incompressibility as $v_R/\Delta = v_A/L$, where L is the length of the layer. Equating both expressions for $\partial\psi/\partial t$ we can determine the reconnection velocity as

$$v_R^2 = \frac{c^2 \eta}{4\pi} \frac{v_A}{L} \Rightarrow v_R = v_A/\sqrt{S} \Rightarrow \Delta = L/\sqrt{S}.$$

Substituting in these formulas the values typical e. g. of solar flares, it is found that the reconnection rate predicted by this model is too slow by several orders of magnitude. Petschek [30] showed that a much larger reconnection rate is achieved if it is supposed that the merging of the filed lines occurs in smaller regions of the reconnection layer characterized by a length $L' \ll L$ (Fig. 3b). The remaining length of the layer is occupied by slow shocks that accelerate the plasma up to v_A almost instantaneously [31]. As a result, the reconnection rate is given by the previous formulas but with L replaced L' and is hence much higher[3]. According to the recent developments of astrophysical reconnection studies, two-fluid (Hall) effects and turbulent enhancement of the plasma resistivity are the most likely candidates to explain the observed energy release times in space plasmas.

---

[3] Petschek's model is highly controversial. For an account of the status of the discussion see for instance Ref. [26].

2.1.2 Reconnection in a tokamak

The tokamak configuration implies periodicity of every physical quantity with respect to the poloidal angle θ and the toroidal angle φ. For a magnetic perturbation varying as $\exp[i(m\theta - n\varphi)]$, the condition $\mathbf{k} \cdot \mathbf{B}_0 = 0$ becomes

$$\frac{m}{r} B_p - \frac{n}{R} B_t = 0 \tag{2.10}$$

(B_p and B_t are the poloidal and toroidal components of $\mathbf{B}_0$, respectively) since $\nabla\theta = 1/r$ and $\nabla\varphi = 1/R$. The safety factor $q(r)$, describing the number of toroidal turns necessary to complete a poloidal turn of the torus while following a field line, can be written approximately as $q = rB_t/RB_p$ and varies in a typical discharge between $q \lesssim 1$ in the centre and $q \gtrsim 3$ at the edge of the plasma. This implies that the previous resonance condition can be written $m/n - q(r) = 0$, i. e. the mode can occur on "rational" surfaces. In particular, since long-wavelength modes are more likely unstable with respect to tearing (see also Sec. 2.2.1), magnetic islands can arise on rational surfaces with low mode numbers (m, n).

In a tokamak, the observed mode numbers are typically $(1, 1)$, $(3, 2)$ and $(2, 1)$. The development of a magnetic island on the surface corresponding to $q(r) = 1$ exhibits some peculiar features, as reconnection is in this case usually forced by an internal kink of the plasma column, pushing the hot plasma core inside the $q = 1$ surface as illustrated in Fig. 4.

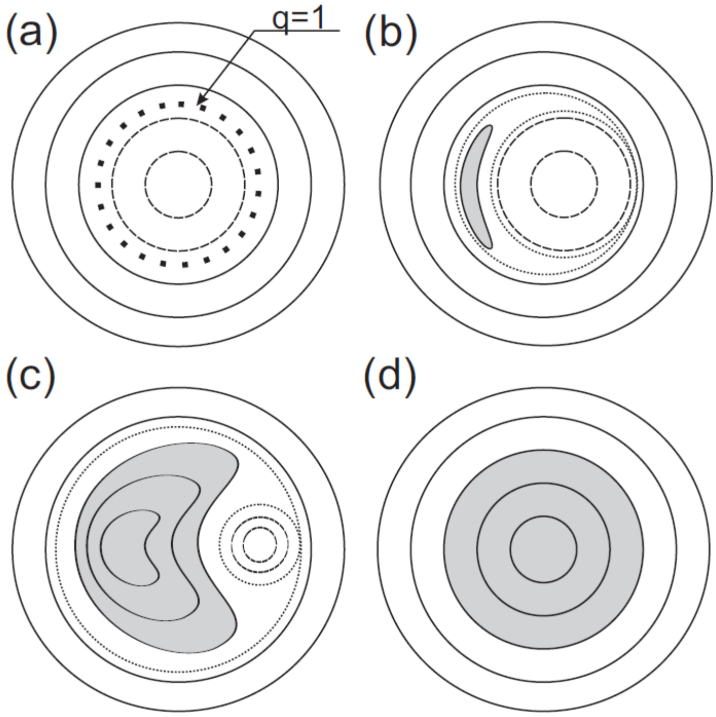

Fig. 4. *Schematic evolution of the sawtooth instability. The plasma inside $q = 1$ (a) is shifted by a kink and forces reconnection (b), the resulting magnetic island grows (c) and eventually expels the initial hotter core taking its place (d).*

According to the model proposed by Kadomtsev [32], after the reconnection event, a fast heat transfer from inside to outside the $q = 1$ surface occurs, the temperature profile inside this surface flattens and the current profile becomes uniform. This removes the cause of the kink and temperature and current start to peak again. The temporal trace of the temperature (with a slow rise and a sudden drop) gives this process the name of sawtooth instability. Like for the case of astrophysical plasmas, experimental observations usually report a much faster reconnection rate than predicted by the Kadomtsev model and two-fluid effects are often indicated as a possible explanation of this fact [33].

On the other rational surfaces mentioned above, $(3, 2)$ and $(2, 1)$, reconnection is rather a "spontaneous" event, triggered by another instability at the edge or in the centre of the plasma (as the sawtooth crash described above [34, 35]). Also tearing modes with no clear trigger have been observed. The growth of $(3, 2)$ or $(2, 1)$ tearing modes leads to the confinement degradation mentioned at the end of Sec. 1.3. They are the subject of this thesis. The results presented in the following chapters do not focus on the initial reconnection trigger, but rather on the different contributions to the dynamics of a tearing mode once it has been excited.

2.2 Linear MHD theory

A simple planar configuration, called the sheet pinch, is particularly relevant for the study of the tearing mode. The equilibrium magnetic field $\mathbf{B}_0$ has a strong homogeneous component B_{0z} in the z direction and a smaller y component $B_{0y}(x)$, varying in the x direction and changing sign across the position $x = 0$. The z direction is supposed to represent a symmetry direction of the system, so that no physical quantity depends on z. This form of the magnetic field implies by Ampère's law a current $J_{0z}(x) = (c/4\pi)\partial B_{0y}/\partial x$. For this reason, this configuration is also called a "current slab". A typical current profile and the corresponding magnetic field profile are shown in Fig. 5.

The projection of the magnetic field onto the xy plane reflects the situation described in Sec. 2.1 (Fig. 2). A periodic displacement in the y direction ($\mathbf{k} = k_y\hat{\mathbf{y}}$) satisfies then the condition $\mathbf{k} \cdot \mathbf{B}_0 = 0$ at $x = 0$, since $\mathbf{B}_{0y}(x = 0) = 0$. We want to investigate under which conditions the sheet pinch is unstable against the tearing mode.

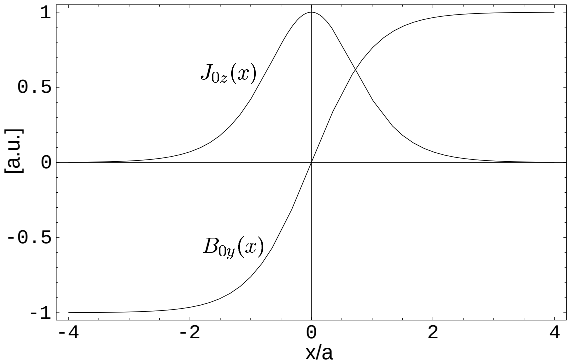

Fig. 5. *Sketch of the equilibrium magnetic field* $B_{0y}(x) \propto \tanh(x/a)$ *as a function of* x/a *and of the corresponding current density* $J_{0z}(x) \propto \partial B_{0y}/\partial x$ *in a sheet pinch.*

The velocity field $\mathbf{u}$ and the magnetic field $\mathbf{B}$ are conveniently written in terms of the electrostatic potential ϕ and of the vector potential A_z (the y component of the vector potential $A_{0y} = xB_0$ representing the homogeneous guiding field $B_0\hat{\mathbf{z}}$),

$$\mathbf{u} = c\,\frac{\hat{\mathbf{z}} \times \nabla\phi}{B}$$
$$\mathbf{B} = \nabla A_z \times \hat{\mathbf{z}}.$$

Taking the z component of the curl of Eq. (2.1) one obtains

$$\rho\left(\frac{\partial}{\partial t}+\mathbf{u}\cdot\nabla\right)\nabla_\perp^2\phi=\left(\frac{B_0}{c}\right)^2\nabla_\parallel J_z \tag{2.11}$$

($\nabla_\parallel=(\mathbf{B}/B)\cdot\nabla$ being the parallel gradient operator and $\nabla_\perp^2=\nabla^2-\nabla_\parallel^2$), whereas from Eq. (2.7)

$$\frac{\partial A_z}{\partial t}=-c\nabla_\parallel\phi-c\eta J_z. \tag{2.12}$$

In both equations,

$$J_z=-\frac{c}{4\pi}\nabla_\perp^2 A_z, \tag{2.13}$$

see Eq. (2.2).

The problem is solved by means of a boundary-layer approach. Following the seminal paper by Furth et al. [36], we distinguish two regions in the plasmas. In a narrow (in the sense specified below) layer around $x=0$, non-ideal effects are important and $E_\parallel$ can be non-zero. The width Δ of this layer is determined as a result of the analysis. The outer domain is defined as the region where ideal MHD is supposed to hold. The solutions obtained in the two regions must be matched at their boundary. We address first the outer region, where non-ideal effects are negligible.

2.2.1 The outer layer

In a linear analysis, the unknown quantities ϕ and A_z are written as the sum of a zero-order term (denoted by a subscript 0) and a perturbed part (denoted by a tilde). We investigate the response of the plasma to a perturbation $\tilde{A}_z(x,y,t)=\tilde{A}_z(x)\exp[ik_y y-\gamma t]$, a similar expression holding for $\tilde{\phi}$. Here, we will suppose that the equilibrium fluid velocity $\mathbf{u}_0$ vanishes. Correspondingly, $\phi_0=0$. Turning to Eq. (2.11), it is noted that the response time $1/\gamma$ characterizing the variation of $\tilde{\phi}$ on the left-hand side is much slower (since it involves the resistive time scale[4]) than the Alfvén time characterizing the ideal response to the bending of the field lines described by the right-hand side. Eq. (2.11) reduces then to the linearized form of $\nabla_\parallel J_z=0$, namely

$$B_{0y}\frac{\partial\tilde{J}_z}{\partial y}+\tilde{B}_x\frac{\partial J_{0z}}{\partial x}=0. \tag{2.14}$$

Eq. (2.14) relates the wavelength of the current perturbation to the gradient of the equilibrium current. A stronger bending of the field lines is possible in the presence of a stronger peaking of the current profile. Employing Eq. (2.13) with $\nabla_\perp^2=\partial^2/\partial x^2-k_y^2$ we can recast the previous equation in the form

$$B_{0y}\left(\frac{\partial^2}{\partial x^2}-k_y^2\right)\tilde{A}_z-\frac{\partial^2 B_{0y}}{\partial x^2}\tilde{A}_z=0.$$

Assuming $B_{0y}(x)\propto\tanh(x/a)$ (see Fig. 5), the previous equation can be integrated on both sides of the layer $|x|<\Delta\to 0$ with the boundary condition $A_z(x)\to 0$ for $|x|\to\infty$. The result is

$$\tilde{A}_z(x)=Ce^{-k_y|x|}\left[1+\frac{1}{k_y a}\tanh\left|\frac{x}{a}\right|\right]. \tag{2.15}$$

---

[4] The calculation of the growth rate requires the analysis of the inner layer and is presented in the next section.

Taking the limit for $x \to 0$ of this solutions shows that, although $\tilde{A}_z$ is continuous across the inner layer, its derivative is not. This discontinuity can be easily understood. Within the layer, $\tilde{E}_z \neq 0$ generates a current perturbation. This current produces a discontinuity in $\tilde{B}_y$ which can be estimated by integrating the z component of Ampère's equation to give

$$\tilde{B}_y \Big|_{-\Delta}^{\Delta} = \frac{4\pi}{c} \Delta\ \tilde{J}_z(x=0). \tag{2.16}$$

The same discontinuity holds for the derivative of the vector potential, since $\tilde{B}_y = -\partial \tilde{A}_z / \partial x$. As shown in the next section, a crucial role in the stability of the tearing mode is played by the parameter Δ' defined as the jump in the logarithmic derivative of $\tilde{A}_z$ across the layer:

$$\Delta' = \lim_{\Delta \to 0} \left[\frac{1}{\tilde{A}_z(0)} \frac{\partial \tilde{A}_z}{\partial x} \right]_{-\Delta}^{\Delta}. \tag{2.17}$$

In particular, we will see that the sign of Δ' determines the stability of the mode, positive sign corresponding to instability. Explicit evaluation of Δ' using Eq. (2.15) yields

$$a\Delta' = 2 \left(\frac{1}{ak_y} - ak_y \right).$$

As expected, the tearing mode is found to be unstable for long wavelengths (small k_y) or steep current profiles (small a). Fig. 6 shows the perturbed vector potential $\tilde{A}_z$ corresponding to a stable ($k_y a = 2$) or unstable ($k_y a = 1/2$) situation.

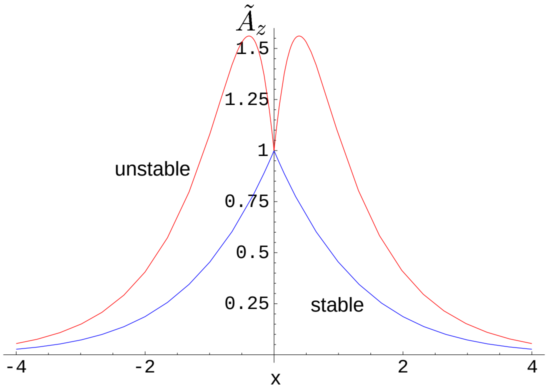

Fig. 6. *Perturbed vector potential in a stable (blue) and unstable (red) tearing mode.*

Finally, it is observed that Eq. (2.16) can be written also as

$$\Delta' \tilde{A}_z(0) = -\frac{4\pi}{c} \Delta\ \tilde{J}_z(x=0). \tag{2.18}$$

Since the left-hand side is entirely determined by the solution in the outer region, the total current flowing in the central layer (proportional to $\Delta\ \tilde{J}_z(x=0)$) is also independent of the detailed processes occurring there. This means that an increase of the linear layer width implies a decrease of the current density $\tilde{J}_z(x=0)$.

2.2.2 The inner layer

The extension Δ of the central layer for a given magnetic equilibrium is determined by how quick the electrons can respond to the electric field induced by the growing tearing mode. In the

MHD model considered here, collisions are supposed frequent enough to hinder the electrons accelerated by the electric field from diffusing along the field lines. There is consequently a periodic variation of the electron density in the y direction and an electrostatic potential arises, which at a distance Δ from $x = 0$ leads to a complete short-circuit of the induced field and hence to $\tilde{E}_\parallel = 0$ [37]. For lower collision frequencies, the mechanism responsible for the violation of the ideal MHD constraint $\tilde{E}_\parallel = 0$ can be different, as mentioned above and explained in Appendix A. To evaluate the time scales related to the reconnection process, the first step is to determine the length an electron needs to travel along the field lines to move by a wavelength in the y direction. For $\Delta \ll a$ (which will be shown below to be the case) we can approximate $B_{0y}(x) \simeq B'_{0y} x = B_0 x/L_s$ where the shear length $L_s = B_0/B'_{0y}$ has been introduced. To the lowest order, the parallel-gradient operator is then $\nabla_\parallel \simeq (x/L_s)\partial/\partial y$. Substituting $\partial/\partial y \sim k_y$ an expression for the parallel wave vector is obtained,

$$k_\parallel = k_y x/L_s. \tag{2.19}$$

In other words, for a given wavelength, the connection length along a field line decreases as we move away from the singular layer $x = 0$.

In the narrow region around $x = 0$ one can take $\partial^2/\partial x^2 \gg k_y^2$. Eqs. (2.11,2.12) become

$$\begin{aligned} \rho \frac{\mathrm{d}}{\mathrm{d}t} \frac{\partial^2 \tilde{\phi}}{\partial x^2} &= \frac{B_0^2}{c^2} \nabla_\parallel \tilde{J}_z \\ \frac{\partial \tilde{A}_z}{\partial t} &= -c \nabla_\parallel \tilde{\phi} - c\eta \tilde{J}_z \end{aligned}$$

Linearizing, eliminating $\tilde{\phi}$ from the previous equations (estimating $\nabla_\perp^2 \tilde{\phi} \approx -\tilde{\phi}/x^2$) and using Ampère's law (2.13) for $\tilde{J}_z$ we obtain

$$\gamma \tilde{A}_z = \left(\frac{k_y^2 x^4}{\gamma \tau_A^2} + \frac{L_s^2}{\tau_R} \right) \frac{\partial^2 \tilde{A}_z}{\partial x^2},$$

with the definitions of resistive and Alfvénic time as in Eqs. (2.8,2.9) with $L \rightarrow L_s$. The integration of this equation across the central layer can be simplified by observing that, as it was shown in the analysis of the outer region, $\partial \tilde{A}_z/\partial x$ is discontinuous across $x = 0$ but $\tilde{A}_z$ is continuous and can be approximated by its central value (constant-ψ approximation [36])

$$\left. \frac{\partial \tilde{A}_\parallel}{\partial x} \right|_{-\Delta}^{\Delta} = \frac{\gamma \tau_R}{L_s^2} \tilde{A}_z(0) \int_{-\Delta}^{\Delta} \frac{\mathrm{d}x}{1 + \left(\tau_R k_y^2/\gamma \tau_A^2 L_s^2 \right) x^4}. \tag{2.20}$$

Matching this equation to the external solution implies that the jump in the first derivative of $\tilde{A}_z$ on the left-hand side equals $\Delta' \tilde{A}_z(0)$, see Eq. (2.17). The width Δ of the inner layer is determined as the region in which the function on the right-hand side significantly contributes to the integral, i. e. $\Delta^4 \approx \gamma \tau_A^2 L_s^2/\tau_R k_y^2$. Physically, Δ corresponds to the distance from $x = 0$ at which the parallel electrostatic field (proportional to $k_\parallel$) becomes strong enough to compensate the inductive field, restoring $\tilde{E}_\parallel = 0$.

Extending the integral in Eq. (2.20) from $-\infty$ to $+\infty$ introduces just a small error and allows us to write (omitting the factor $\sqrt{\pi}/2$ arising from integration) the growth rate as

$$\gamma^{5/4} = \frac{\Delta' L_s^2}{\tau_R} \left(\frac{\tau_R k_y^2}{\tau_A^2 L_s^2} \right)^{1/4} \Rightarrow \gamma = \left(\Delta'\right)^{4/5} k_y^{2/5} L_s^{6/5} \tau_A^{-2/5} \tau_R^{-3/5}, \tag{2.21}$$

i. e., the growth of the tearing mode occurs at a rate which is intermediate between the fast Alfvénic scale and the slow resistive scale. This expression shows that the sign of the stability parameter Δ' calculated in the outer region, Eq. (2.17), determines the sign of the growth rate, i. e. the stability of the mode. The mode grows if the magnetic perturbation $\tilde{B}_y$ in the inner layer correctly matches the magnetic perturbation in the outer region [38]. It is easy to check that this is the case if $\Delta' > 0$, as the sign of $\tilde{B}_y$ in the outer region is related to that of $\partial \tilde{A}_z / \partial x$, cf. Fig. 6.

2.3 Nonlinear theory

The linear theory is valid as long as the magnetic-field perturbations within the region of particle acceleration are small, i. e. if the width W of the magnetic island is much smaller than the linear layer width. When $W \gtrsim \Delta$, the electron orbits are strongly altered by the magnetic topology in the reconnected region, the electrons within the separatrix being constrained to move along the island. Since the magnetic-island geometry plays a fundamental role in this context, we introduce here the basic notation which will be used in the remainder of this work.

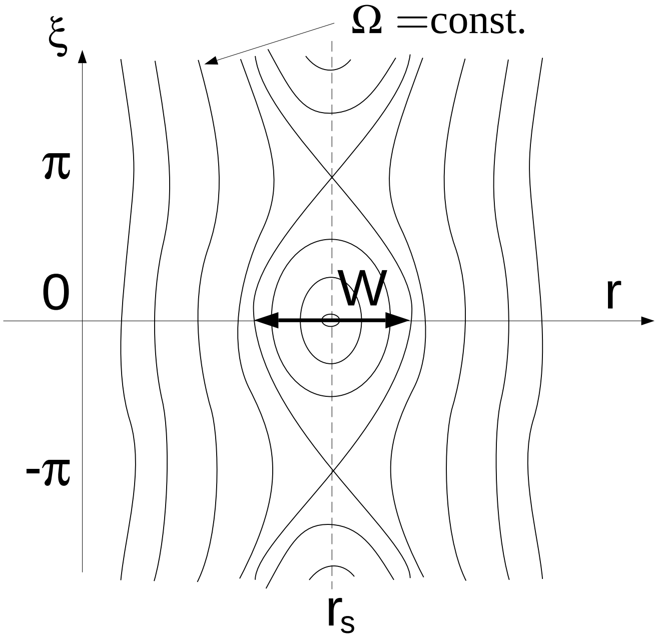

Fig. 7. *Sketch of a magnetic island showing the coordinates Ω and ξ.*

With reference to Fig. 7, the angular coordinate along the island is denoted by ξ, so that in one wavelength the X-points are located at $\xi = \mp\pi$ and the O-point at $\xi = 0$. Anticipating the usage of the next chapters, we write $\xi = m\theta - n\varphi$ (cf. Sec. 2.1.2), while the x coordinate used above is intended as the distance $r - r_s$ from the radial location r_s at which the magnetic island develops. The label Ω of the perturbed magnetic surfaces is easily found by adding the vector potential $A_z = -B_0 x^2 / 2L_s$ of the equilibrium field $B_{0y} \approx x B'_{0y}$ with the island perturbation $\tilde{A}_z = \tilde{\psi} \cos\xi$. Normalizing to $-\tilde{\psi}$ (assumed again to be constant in the island region [36]):

$$\Omega = \frac{B_0}{2\tilde{\psi} L_s} x^2 - \cos\xi. \tag{2.22}$$

Since in the xy plane $\mathbf{B} \propto \nabla\Omega \times \hat{\mathbf{z}}$, by construction we have

$$\mathbf{b} \cdot \nabla\Omega = k_\parallel \left. \frac{\partial}{\partial \xi} \right|_{\Omega} \Omega = 0, \tag{2.23}$$

with $k_\parallel$ defined in Eq. (2.19). From Eq. (2.22) follows immediately the full width of the magnetic island $W = 4\sqrt{\tilde{\psi} L_s / B_0}$.

The nonlinear theory of the tearing mode was developed first by Rutherford [38] for the collisional case and extended to lower collisionalities by Drake and Lee [39]. The main result is that the exponential growth of the linear theory is replaced by an algebraic growth. Here we sketch the derivation given by Rutherford, which has been widely used in the subsequent literature to extend his results to different contributions to the current perturbation, as discussed in Chapts. 3 and 5.

As in the nonlinear regime the electrons are forced to move along the island field lines, it is assumed that the perturbed current is a flux-surface quantity, i. e. $J_z = J_z(\Omega)$, cf. Eq. (2.23). In other words, the inertia term, right-hand side of Eq. (2.11), is neglected altogether, as discussed in Ref. [38]. This suggests to act on Eq. (2.12) with the flux-surface average operator

$$\langle \ldots \rangle_\Omega = \oint \frac{\mathrm{d}\xi}{2\pi} \frac{\ldots}{\sqrt{\Omega + \cos\xi}} \tag{2.24}$$

that annihilates the parallel gradient operator, cf. Eqs. (2.19,2.22,2.23). The result is

$$\frac{1}{c}\frac{\partial \tilde{\psi}}{\partial t} \langle \cos\xi \rangle_\Omega = -\eta J_\parallel \langle 1 \rangle_\Omega . \tag{2.25}$$

The contribution of the current perturbation to the dynamics of the mode can be linked to the tearing-mode parameter Δ' as in Eqs. (2.16-2.18). Multiplying Ampère's law (2.13) by $\cos\xi$ and integrating across the tearing layer taking into account Eq. (2.22) yields

$$\oint \frac{\mathrm{d}\xi}{2\pi} \int_{r_s^-}^{r_s^+} \mathrm{d}r \, \frac{\mathrm{d}^2 \tilde{\psi}}{\mathrm{d}r^2} \cos^2\xi = -\frac{4\pi}{c} \, 2 \, \frac{W}{4\sqrt{2}} \int_{-1}^{\infty} \mathrm{d}\Omega \oint \frac{\mathrm{d}\xi}{2\pi} \frac{J_\parallel \cos\xi}{\sqrt{\Omega + \cos\xi}},$$

where the factor 2 on the right-hand side accounts for both sides of the layer and the integration over Ω is extended to ∞ assuming that this implies a small error as in the linear calculation. The integral on the left-hand side yields $\tilde{\psi}\Delta'/2$, cf. Eq. (2.17). We can adopt the same procedure in Eq. (2.25), i. e. multiply it by $\cos\xi$, take the flux-surface average and integrate over Ω with the result

$$I_1 \frac{4\pi}{\eta c^2} \frac{\mathrm{d}W}{\mathrm{d}t} = \Delta',$$

where $I_1 = \sqrt{2} \int \mathrm{d}\Omega (\langle \cos\xi \rangle_\Omega^2 / \langle 1 \rangle_\Omega) \simeq 0.82$ and the relation between the island width W and the vector-potential perturbation $\tilde{\psi}$ has been used. This equation is usually written in dimensionless form as

$$\frac{\tau_R}{r_s} \frac{\mathrm{d}W}{\mathrm{d}t} = \Delta' r_s \tag{2.26}$$

(with respect to Eq. (2.8), the numerical factor I_1 has been included in the definition of the resistive time). The Rutherford equation (2.26) shows that in the non-linear regime of the tearing mode in a sheet pinch, the exponential growth of the linear phase is replaced by an algebraic growth, as anticipated.

As a final remark, it is noted that the result $\mathrm{d}W/\mathrm{d}t \propto \Delta'$ remains valid also for the nonlinear evolution of the tearing mode in the so-called semi-collisional regime [39], which is more realistic in the case of present and future tokamak experiments. In a toroidal device, however, other contributions to the current perturbation in the island region significantly change the picture outlined above. This subject is discussed in the remaining chapters.

Chapter 3

The tearing mode in a tokamak: neoclassical effects

3.1 Neoclassical currents

As shown in the previous chapter, the evolution of a tearing mode depends crucially on the current distribution in the region prone to tearing. In the theory presented so far, the current perturbation associated with the tearing mode is driven by the electric field induced by the growth of the magnetic field of the island. However, additional (non inductive) contributions to the current could be present in the system. In a tokamak, a decisive role for the island dynamics is played by the perturbation of those currents resulting from so-called neoclassical processes [40, 41, 42]. These are a peculiarity of a toroidal configuration and arise as a consequence of the particular orbits of the particles in the toroidal field and their scattering due to Coulomb collisions[1].

The neoclassical effects on the island evolution are the subject of the present chapter. Before turning to the island-specific aspects, we give a short overview of the contributions that are particular relevant for our investigations. First of all, the strength of a magnetic field generated by a toroidal coil system (cf. Fig. 2a of Chapt. 1) varies with the distance R from the axis of the tokamak as $1/R$, as can be immediately verified taking the flux of Ampère's law through a circle of radius R. For this reason, a high-field side (at smaller R) and a low-field side (at larger R) of the plasma can be distinguished. Particles following the helical field lines of a tokamak (cf. Fig. 2b of Chapt. 1) move from the low to the high-field side, thus experiencing a magnetic-mirror force $F_{\|} = -\mu \nabla_{\|} B$, where the magnetic moment $\mu = m v_{\perp}^2 / 2B$ is an adiabatic invariant of the system. From conservation of energy and magnetic moment it is immediate to show that for particles with a parallel-to-perpendicular velocity ratio on the low-field side

$$\frac{v_{\|}}{v_{\perp}} \lesssim \sqrt{\frac{2r}{R}} \tag{3.1}$$

(where r is the minor radius of the plasma) the mirror force is so strong that they do not reach the high-field side, being *trapped* in the outer part of the torus. Particles which can complete a poloidal orbit following the field lines are called *passing*. Due to the finite magnetic-drift

---

[1] The collisional transport in toroidal geometry is called neoclassical to distinguish it from its counterpart in a homogeneous field (called classical transport).

velocity mentioned in Chapt. 1, which can approximately be written as

$$\mathbf{v}_D = \left(\frac{mv_\perp^2}{2} + mv_\parallel^2\right)\frac{\mathbf{B}\times\nabla B}{ZeB^3}, \tag{3.2}$$

the particles do not stick to the field lines (or to the magnetic surfaces) but slightly drift with respect to them. The typical orbit of a trapped particle is sketched in Fig. 1. When projected onto a poloidal plane it exhibits a characteristic banana shape[2].

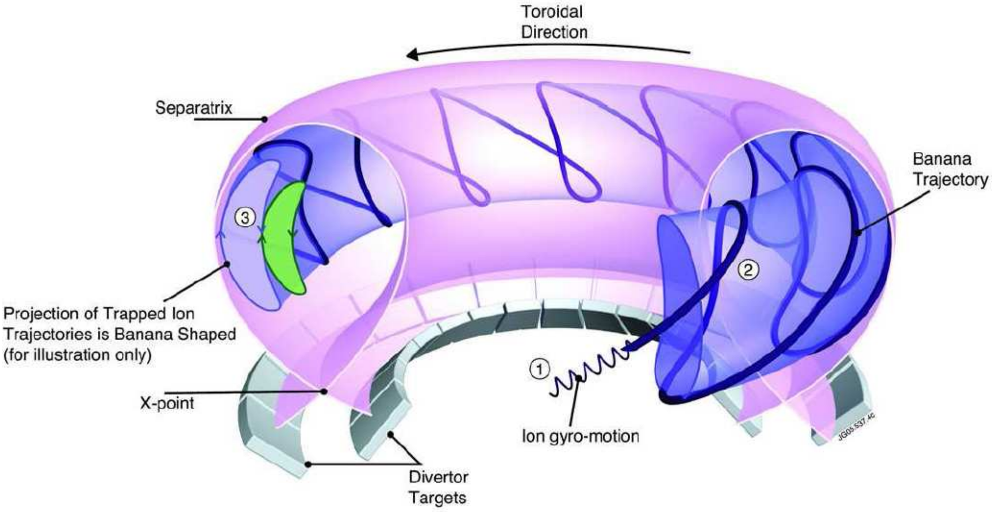

Fig. 1. *Schematic representation of the orbit of a trapped particle in a tokamak, showing its gyromotion (1), the effect of the mirror force (2) and the typical banana shape of its poloidal projection (3), together with its precession in the toroidal direction. If there are more (or faster) particles on the inner orbit than on the outer orbit (see point ③), a banana current is generated, which provides the "seed" for the bootstrap current* [Courtesy EFDA-JET].

The presence of a population of trapped particles has several significant consequences, some of which are relevant for the dynamics of the tearing mode. In particular, the trapped particles are the seed of a part of the toroidal current, that adds to the Ohmic current produced by the transformer. The generation of this current, called the bootstrap current [43], is illustrated again in Fig. 1, where the orbits of two trapped particles drifting through the same point (denoted as ③) with opposite sign of the parallel velocity are shown. In the presence of a density (temperature) gradient directed towards the centre of the plasma, there will be more (faster) particles on the inner orbit than on the outer orbit. The difference between the flows related to the inner and outer orbits gives the so-called banana current [44] at the point under consideration. This banana flow is transferred by collisions to the passing particles, which carry the largest part of the (bootstrap) current. This picture is true for both electrons and ions considered independently from each other. Due to the collisional friction with the much heavier ions, the electrons are dragged in the ion direction. The total current is of course given by the algebraic sum of the two flows and can be approximated as

$$j_{\mathrm{bs}} = 1.46\sqrt{\frac{r}{R_0}}\frac{c}{B_p}\frac{\mathrm{d}p}{\mathrm{d}r}. \tag{3.3}$$

---

[2] Details on particle orbits in a toroidal device are reported in many textbooks and by Wesson [2]. Notice that, for thermal particles, v_d is a factor of the order ρ/R smaller than the thermal velocity. The $\mathbf{E}\times\mathbf{B}$ velocity defined below, Eq. (3.4), is supposed in this chapter to be of the same order as v_d.

Assuming that the pressure profile flattens inside the island as a consequence of the fast streaming of the particles along the perturbed field lines implies that the bootstrap current vanishes inside the island. In a tokamak, where the safety factor q is usually increasing from the centre to the edge, cf. Sec. 2.1.2, this bootstrap-current perturbation leads to a growth of the island and is believed to be the main drive for the tearing mode in present and future tokamaks (see Sec. 3.2). Due to the neoclassical origin of the drive, the mode is termed *neoclassical tearing mode* (NTM).

A second effect connected with the presence of trapped particles discussed in this chapter is the modification of their orbit in the presence of a time dependent radial electric field E_r. If the particles are confined by a magnetic field, the effect of an electric field on their motion is a drift

$$\mathbf{v}_E = c\frac{\mathbf{E}\times\mathbf{B}}{B^2}, \tag{3.4}$$

perpendicular to both $\mathbf{E}$ and $\mathbf{B}$, as already noted in Chapt. 1. Notice that this drift, unlike the drift due to the magnetic-field inhomogeneity, Eq. (3.2), is independent of the mass and of the charge of the particles. Writing the velocity v_p of a trapped ion in the poloidal direction as the sum of the relevant projections of $\mathbf{v}_D$, $\mathbf{v}_E$ and $v_\parallel\mathbf{b}$ yields

$$v_p = -v_D\cos\theta - c\frac{E_r}{B} + \frac{B_p}{B}v_\parallel,$$

where θ is the poloidal angle as in Sec. 2.1.2. Averaging over one *bounce* period and applying the constraint $\langle v_p\rangle_{\text{bounce}} = 0$ for trapped particles gives

$$\langle v_\parallel\rangle_{\text{bounce}} = \frac{B}{B_p}\langle v_D\cos\theta\rangle_{\text{bounce}} + c\frac{E_r}{B_p}. \tag{3.5}$$

The first term is the toroidal precession due to the magnetic field inhomogeneity[3], while the second term describes the precession related to the radial electric field, which is of interest here. Conservation of the canonical angular momentum in toroidal direction $P_\varphi = (Ze/c)RA_\varphi + mv_\parallel R$ due to axisymmetry (with $RA_\varphi = -R_0\int \mathrm{d}rB_p(r)$; the contribution of the toroidal electric field induced by the transformer is not considered here) gives after differentiation

$$v_r = \frac{\mathrm{d}r}{\mathrm{d}t} = \frac{mc}{ZeB_p}\frac{\mathrm{d}}{\mathrm{d}t}\left[\left(1+\frac{r}{R_0}\cos\theta\right)v_\parallel\right],$$

with $R = R_0 + r\cos\theta$. Neglecting the term $r/R_0 \ll 1$

$$\langle v_r\rangle_{\text{bounce}} = \frac{mc}{ZeB_p}\frac{\mathrm{d}}{\mathrm{d}t}\langle v_\parallel\rangle_{\text{bounce}}, \tag{3.6}$$

where $\langle v_\parallel\rangle_{\text{bounce}}$ is given by Eq. (3.5), we obtain the neoclassical radial polarization drift [45]. In the presence of a magnetic island, a time-varying (nearly) radial electric field is associated with the rotation of the mode with respect to the surrounding plasma and can lead to a (nearly) radial polarization current (mostly due to the ions, which are much heavier than the electrons). The role of the resulting parallel electron current, which flows to ensure quasi-neutrality, $\nabla\cdot\mathbf{J} = 0$, is highly debated [46]. Some aspects of this problem are discussed in Sec. 3.3.

We conclude this section by noting that the most natural framework to treat effects related to the different motion of the particles depending on their velocity is kinetic theory. In this

---

[3] More rigorously, this precessional motion should include a term due to the radial variation of the safety factor, i. e. to magnetic shear.

case, the information about the phase-space behaviour of each particle species α is contained in the distribution function f_α, that satisfies the kinetic (Boltzmann) equation

$$\frac{\partial f_\alpha}{\partial t} + \mathbf{v} \cdot \frac{\partial f_\alpha}{\partial \mathbf{r}} + \frac{Z_\alpha e}{m_\alpha} \left(\mathbf{E} + \frac{\mathbf{v} \times \mathbf{B}}{c} \right) \cdot \frac{\partial f_\alpha}{\partial \mathbf{v}} = C\left(f_\alpha\right), \tag{3.7}$$

where the term on the right-hand side is the collision operator that describes the rearrangement of the particle velocities due to binary Coulomb interaction. The fields **E** and **B** appearing in Eq. (3.7) are to be determined from Maxwell's equations, where the charge and current densities are determined as moments of the distribution function. Different approaches have been developed to solve the Boltzmann-Maxwell set of equations in a magnetized plasmas, depending on the geometry of the problem and on the space and time scales under consideration. Some of them are briefly described and applied in this and in the following chapters. However, a detailed discussion of the methods employed for the analytic derivation and the numerical solution of the corresponding equations is outside the scope of this thesis.

3.2 Contribution of the bootstrap current

The contribution of the non-inductive currents to the nonlinear dynamics of the tearing mode can be incorporated into the theory presented in the previous chapter by simply operating the substitution $J_z \to J_z - J_z^{n.i.}$ on the right-hand side of Eq. (2.12). For an easier comparison with a typical tokamak scenario, where the safety profile increases monotonically with radius, it is convenient to reverse the sign of the vector potential A_z with respect to Sec. 2.3. Eq. (2.25) is then extended to

$$\frac{1}{c}\frac{\partial \tilde{\psi}}{\partial t} \langle \cos\xi \rangle_\Omega = \eta \left(J_\parallel \langle 1 \rangle_\Omega - \langle J_\parallel^{n.i.} \rangle_\Omega \right). \tag{3.8}$$

Following the same procedure as for the derivation of Eq. (2.26) we obtain with $L_s = R_0 q_s L_q / r_s$ (where $1/L_q = (1/q)\mathrm{d}q/\mathrm{d}r$) the equation

$$\frac{\tau_R}{r_s}\frac{\mathrm{d}W}{\mathrm{d}t} = \Delta' r_s - \frac{4\pi}{c}\frac{8\sqrt{2} r_s}{W}\frac{L_q}{B_p}\int_{-1}^{\infty} \mathrm{d}\Omega \frac{\langle \cos\xi \rangle_\Omega}{\langle 1 \rangle_\Omega}\, \langle J_\parallel^{n.i.} \rangle_\Omega, \tag{3.9}$$

where the coordinates Ω and ξ have been defined in Sec. 2.3. This equation is the starting point for the extension of Rutherford's nonlinear theory to include a generic non-inductive current perturbation.

In this section, we consider the impact of the bootstrap-current perturbation on the dynamics of the tearing mode, first calculated in Refs. [47, 48] under the assumption of complete pressure flattening inside the island. The corresponding current perturbation can be written as [49]

$$\langle j_{\mathrm{bs}} \rangle_\Omega = 1.46 \sqrt{\frac{r}{R_0}} \frac{c}{B_p} \frac{\mathrm{d}p}{\mathrm{d}r} \langle 1 \rangle_\Omega \tag{3.10}$$

inside the island ($-1 \leq \Omega \leq 1$) and

$$\langle j_{\mathrm{bs}} \rangle_\Omega = 1.46 \sqrt{\frac{r}{R_0}} \frac{c}{B_p} \frac{\mathrm{d}p}{\mathrm{d}r} \left[-\frac{\pi\sqrt{2}}{4\sqrt{(\Omega+1)/2}\,E\left(2/(\Omega+1)\right)} + \langle 1 \rangle_\Omega \right] \tag{3.11}$$

outside the island ($\Omega > 1$), $E(k)$ being the complete elliptic integral of the second kind. Substituting Eqs. (3.10,3.11) into Eq. (3.9), on account of the fact that $\int_{-1}^{\infty} \mathrm{d}\Omega \langle \cos\xi \rangle_\Omega = 0$, yields

$$\frac{\tau_R}{r_s}\frac{\mathrm{d}W}{\mathrm{d}t} = \Delta' r_s + 6.34 \frac{4\pi}{c} \frac{L_q j_{\mathrm{bs}}}{B_p} \frac{r_s}{W}. \tag{3.12}$$

In present and future tokamaks the current profile is in general classically stable against tearing, i. e. $\Delta' < 0$. The mode is rather driven by the hole in the bootstrap current due to the pressure flattening inside the island, as it was recognized first in TFTR discharges [50].

Eq. (3.12) describes correctly the neoclassical drive only if the pressure flattening inside the island is complete, so that the bootstrap current vanishes altogether inside the island. There are several physical effects, however, that can cause a residual bootstrap current to survive inside the island and hence reduce the island drive. First of all, the degree of flattening of, say, the temperature profile is governed under steady state conditions by the equation

$$\chi_\parallel \nabla_\parallel^2 T + \chi_\perp \nabla_\perp^2 T = 0, \tag{3.13}$$

where $\chi_\parallel$ and $\chi_\perp$ are the parallel and perpendicular heat conductivities, respectively. A similar equation governs the degree of density flattening, with the heat conductivities substituted by the corresponding particle diffusivities $D_\parallel$ and $D_\perp$. Since the particles flow much faster along the field lines than they drift across them, as a first approximation one can take the limit $\chi_\parallel/\chi_\perp \to \infty$, neglect the second term of Eq. (3.13) and conclude that T is a flux-surface function (i. e. a function of Ω). Flattening inside the island comes from symmetry reasons, supposing that no sources are present. This is the limit assumed in the derivation of Eqs. (3.10,3.11). A condition for the validity of this approximation can be obtained from Eq. (3.13) recalling Eq. (2.19) and estimating $\nabla_\perp^2 \sim 1/x^2$. This yields a critical width[4] $W_c \sim (\chi_\perp/\chi_\parallel)^{1/4}(L_s r_s/m)^{1/2}$, below which the parallel transport is not effective enough in ensuring flattening against a finite perpendicular transport [49]. For islands below this critical width, the bootstrap drive turns out to be proportional to W rather than to $1/W$ as in Eq. (3.12) and thus tends to zero for $W \to 0$. For negative values of Δ', this implies that the tearing mode is destabilized only if there is some physical effect that forces the island width above the critical value. For realistic tokamak parameters, the ratio $\chi_\perp/\chi_\parallel$ is in the range 10^{-8}–10^{-10} and the critical width is of the order of a centimetre. This is compatible with the threshold behaviour observed in several experiments [51, 52, 53].

The competition between perpendicular and parallel transport, however, is not the only candidate to explain the increased stability of small islands. The fast streaming along the field lines of the islands responsible for the flattening of density and temperature profiles does not affect directly the trapped particles. A flattening in the trapped-particle population establishes because of collisions, that force the distribution function to relax to an isotropic Maxwellian. The time scale related to scattering from the trapped to the passing domain is $r/\nu R_0$, where ν is the collision frequency[5]. On the other hand, as we have seen before, transport across the island separatrix acts to maintain a gradient and this mechanism is much more efficient for trapped than for passing particles. Estimating the transport time scale across the island as $W^2/2D_\perp$, we see that the two mechanism compete if $W \sim \sqrt{2D_\perp r_s/\nu R_0}$ and a trapped-particle gradient survives for islands below this value [54]. A more complete kinetic modelling confirms this estimate [55]. For realistic values of the parameters[6], this threshold value is again of the order of a centimetre.

There is a further subtlety associated with the orbit of trapped particles in the vicinity of a magnetic island. The width w_b of a banana orbit is often comparable to the initial island

---

[4] Here and in the following, m denotes the poloidal mode number, as in Eq. (2.10).

[5] The collision frequency is defined as the inverse of the time required for a 90° scattering in velocity space. The crossing of the boundary between the trapped and the passing domain just requires scattering across the trapping condition, Eq. (3.1).

[6] In present tokamaks, the transport is dominated by turbulent diffusion, as discussed in Chapt. 4, with diffusion coefficients of the order of (a few) m^2/s. The electron collision frequency depends on density and temperature, but for a first estimate can be assumed to be of the order of tens of kHz.

size observed in the experiments. This means that there are particles drifting partly inside and partly outside the island, so that one can expect that the unbalance between the contribution from particles drifting in opposite direction at the origin of the bootstrap current (see Sec. 3.1) is at least partly preserved inside the island. An analytic estimate of this effect is made difficult by the fact that in the frame of standard neoclassical theory the ratio between w_b and the radial inhomogeneity length L of the system is supposed to be small. This allows an expansion of the distribution function in powers of $w_b/L \ll 1$. The relevant equation is the drift kinetic equation, which can be derived from the Boltzmann equation (3.7) [56, 57] averaging away the fast (compared to the scales of interest) gyromotion and considering the drift velocities discussed in Sec. 3.1,

$$\frac{\partial f_\alpha}{\partial t} + \left(v_{\parallel\alpha}\hat{\mathbf{b}} + \mathbf{v}_{d\alpha} + \mathbf{v}_E\right) \cdot \frac{\partial f_\alpha}{\partial \mathbf{r}} - \frac{Z_\alpha e}{m_\alpha} \frac{\mathbf{v}_{d\alpha} \cdot \nabla\Phi}{v} \frac{\partial f_\alpha}{\partial v} = C(f_\alpha) \tag{3.14}$$

(Φ is the electrostatic potential associated with the electric field $\mathbf{E}$). A numerical solution of the drift kinetic equation for the ions[7] in the presence of an island has been achieved employing the Hamiltonian code HAGIS [58] augmented by a pitch-angle scattering operator which includes a procedure to ensure momentum conservation [59]. Fig. 2 shows the ion component of the bootstrap current inside a magnetic island as a function w_b/W.

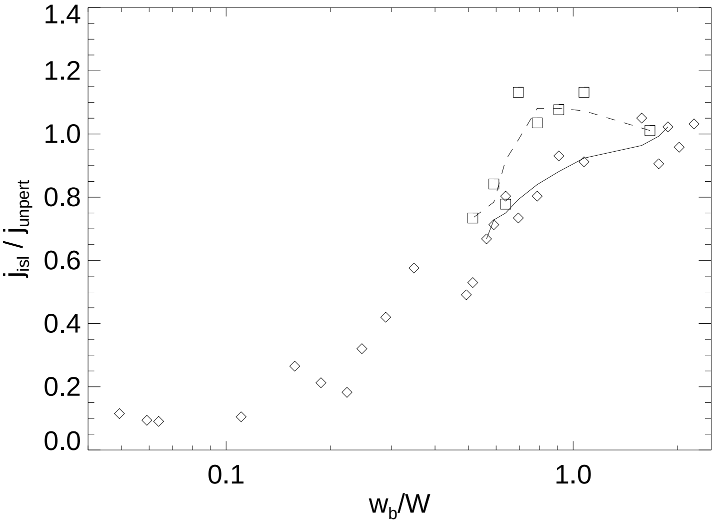

Fig. 2. *Ion bootstrap current in the centre of a magnetic island (normalized to its unperturbed value when the island is absent) as a function of the ratio between banana width and island width (the left part of the plot corresponds to large islands, the right part to small islands). Squares correspond to simulations with flat equilibrium density. The fitting curves in the region of small islands are shown to guide the eye.*

In the case of a big island the bootstrap current drops to zero, consistenlty with the usual picture of the neoclassical drive. If the island is small (island width of the order of or below the thermal ion banana width) the reconnected region hardly affects the ion motion and hence the ion bootstrap current, which stays at the same value inside and outside the island [10]. Thus we see that islands below the ion banana width exhibit an increased stability against the neoclassical drive, which is even stronger (see again Fig. 2 and Ref. [11]) if the density gradient is flat and the bootstrap current is caused mainly by the temperature gradient (rather flat density profiles are expected in ITER).

---

[7] Finite-banana-width effects are much less significant for electrons, since the banana width, like the gyroradius, scales with the square root of the mass.

These finite-orbit effects yield a possible explanation for the scaling of the plasma pressure (normalized to the pressure of the poloidal magnetic field) with the poloidal gyroradius (i. e., the gyroradius calculated with the poloidal field, normalized to the major radius of the machine R_0) which has been observed for islands whose widths remained nearly constant after the onset [60]. Taking into account the stabilization due to finite-orbit effects in the Rutherford equation by means of a factor obtained from a fit of the simulations and expressing the normalized pressure as a function of the other parameters for nearly stable islands ($\mathrm{d}W/\mathrm{d}t \simeq 0$), a linear scaling of the pressure with the poloidal gyroradius is found [10], in agreement with experiment findings [61].

The results discussed before have been obtained for the case of a static island. However, a magnetic island is in general rotating with respect to the surrounding plasma under the torque [62] provided by the the out-of-phase currents (i. e. the components of the current proportional to $\sin\xi$), which do not contribute to island growth, governed by the $\cos\xi$ harmonics, see Eq. (3.9)[8]. The electrostatic potential connected to this rotation can be easily calculated in the ideal MHD limit $E_\parallel = 0$ (which in the nonlinear theory is violated only in a narrow layer around the separatrix), as shown in Sec. 3.3, Eq. (3.15). The investigation of finite-banana-width effects on the bootstrap current in small islands can be extended to the case of rotating islands simply by including this potential and the corresponding electric field in Eq. (3.14) (these terms were set to zero in the case of a static island). The resulting $\mathbf{E} \times \mathbf{B}$ velocity forces the plasma inside the island to co-rotate with the island to satisfy Alfvén's frozen-in law. The potential Φ has therefore a different sign depending on the direction of the island rotation. It is found that in a region extending for about a banana width around the separatrix (i. e. comparable to the island width for $w_b \approx W$) the ion density exhibits a tendency to respond adiabatically [64] to the potential ($\tilde{n}/n = -Ze\Phi/T_i$), as shown in Fig. 3.

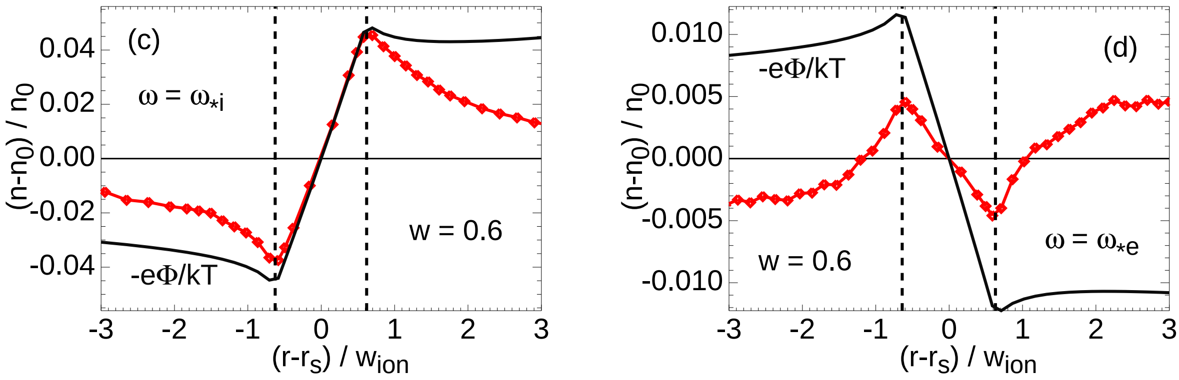

Fig. 3. *Density perturbation* $(n - n_0)/n_0$ *(red symbols), in an island rotating at the ion diamagnetic frequency (left) and at the electron diamagnetic frequency (right). Also shown is the normalized potential* $-e\Phi/T_i$ *(solid black lines). The island width is normalized to the thermal ion banana width. A density perturbation which is negative on the inner side and positive on the outer side of the island (left) corresponds to density flattening, the opposite situation (right) to steepening.*

Due to the different sign of the potential, the adiabatic response pushes the ion density profile towards flattening for island rotation in the direction of the ion diamagnetic rotation or towards steepening for rotation in the electron diamagnetic direction [12]. The bootstrap

---

[8] A typical example is given by the currents associated with background pressure gradients and the related drifts, cf. Ref. [63] and Sec A.2 for the linear case and Sec. 4.1 for a description of the drift wave.

current profile[9] is found to follow the analytic (small-orbit) prediction if the profile perturbations are included. In other words, the density profile due to the particle response to the electric field of a small rotating island leads to an additional current, that flows in the same direction as the unperturbed bootstrap current if the island rotates in the electron diamagnetic direction, while it has opposite direction in the case of rotation in the ion direction. The direction of rotation of the island with respect to the plasma is still not known with certainty [46], although there are good reasons to believe that small islands rotate in the electron diamagnetic direction [65] and are thus more stable against tearing (reduced bootstrap destabilization) than in the standard theory, the surviving drive being related mainly to the residual flattening in the electron temperature profile. (A confirmation of the validity of this statement comes from recent (gyro)kinetic simulations of small rotating islands, in which Φ is calculated self-consistently from the particle response to a given island rotation rather than from the analytic solution of the electron parallel momentum balance, showing that quasi-neutrality forces the electron density to follow the ion density, which is dominated by the adiabatic response described above [66]).

3.3 Contribution of the polarization current

As mentioned in the previous section, if the island is rotating with respect to the plasma there must be an electrostatic potential Φ connected to the rotation such that the ideal MHD condition $E_\parallel = 0$ is satisfied and the plasma is forced to move with the perturbed field lines in the reconnected region. Integration of $c\nabla_\parallel \Phi + \partial \tilde{A}_\parallel / \partial t = 0$ in toroidal geometry gives a potential of the form [67, 68]

$$\Phi = \frac{\omega R B_p}{nc} \left[r - r_s - h(\Omega) \right], \tag{3.15}$$

where ω is the island rotation frequency, n is the toroidal mode number as in Sec. 2.1.2 and $h(\Omega)$ is an integration "constant" with vanishing parallel derivative, cf. Eq. (2.23). It is usually determined assuming density flattening inside the island, so that $h(\Omega)$ vanishes for $-1 \leq \Omega \leq 1$. A simple expression [67], implemented in the numerical drift kinetic simulations presented in the previous section and here below, that obeys the boundary condition of vanishing electric field the former case, decreasing in the latter. This can be easily understood considering a reference frame in which the island is at rest, see Fig. 4a. The plasma can be thought as being accelerated in the Laval nozzle formed by the perturbed flux surfaces outside the separatrix. The ion polarization current flows perpendicularly to the magnetic surfaces and has roughly a $\sin\xi$ dependence on the helical angle. It averages to zero when integrated along the whole island. The interest of the polarization current for the island dynamics is related to the fact that it is not divergence free, so that a parallel current (mainly carried by the electrons) must flow to enforce $\nabla_\parallel J_\parallel = -\nabla_\perp \cdot \mathbf{J}_\perp$. Integrating this equation with the parallel gradient operator given by Eq. (2.23) shows immediately that the closure parallel current varies as $\cos\xi$ and hence contributes to the nonlinear island evolution determined by Eq. (3.9). An analytic drift kinetic calculation assuming density flattening inside the island and $w_b \ll W$ [68] yields

$$J_\parallel = -104 \left(\frac{r}{R_0} \right)^{3/2} \frac{\rho_p^3 L_q}{W^2 L_n^2} \, \frac{1}{W^2} \, \frac{\mathrm{d}h}{\mathrm{d}\Omega} \, \frac{\mathrm{d}^2 h}{\mathrm{d}\Omega^2} \, \frac{\omega(\omega - \omega_{*pi})}{\omega_{*i}^2} \left[\cos\xi - \frac{\langle \cos\xi \rangle_\Omega}{\langle 1 \rangle_\Omega} \right] Z e n_e v_{\mathrm{th},i}, \tag{3.16}$$

---

[9] The simulations presented in Ref. [12] were performed in two steps, first for the ions (whose scattering against electrons is negligible) and then for electrons, including the drag due to the ion flow – calculated in the previous step – as a shift in the background distribution function. This makes possible to reconstruct the total bootstrap current, cf. Sec. 3.1.

where ω_{*pi} is the diamagnetic ion frequency that includes the contribution from the temperature gradient. Since $h(\Omega) \propto W$, $J_\parallel$ in Eq. (3.16) scales as $1/W^2$ and the corresponding term in Eq. (3.9) scales as $1/W^3$. The polarization term thus has potentially a strong impact on the dynamics of small islands (the neoclassical drive scales with the island width as $1/W$). Whether this contribution is stabilizing or destabilizing depends on the island rotation frequency ω, being destabilizing for islands rotating in the electron diamagnetic direction or at frequencies exceeding ω_{*pi} in the ion direction (the neglect of the contribution of the steep current gradients towards the centre of the island, cf. Fig. 4b, led to the opposite conclusion in Ref. [68]). If stabilizing, the polarization current could provide an additional explanation for the NTM threshold discussed above, compatible with the linear scaling of the pressure at mode onset with the normalized poloidal gyroradius.

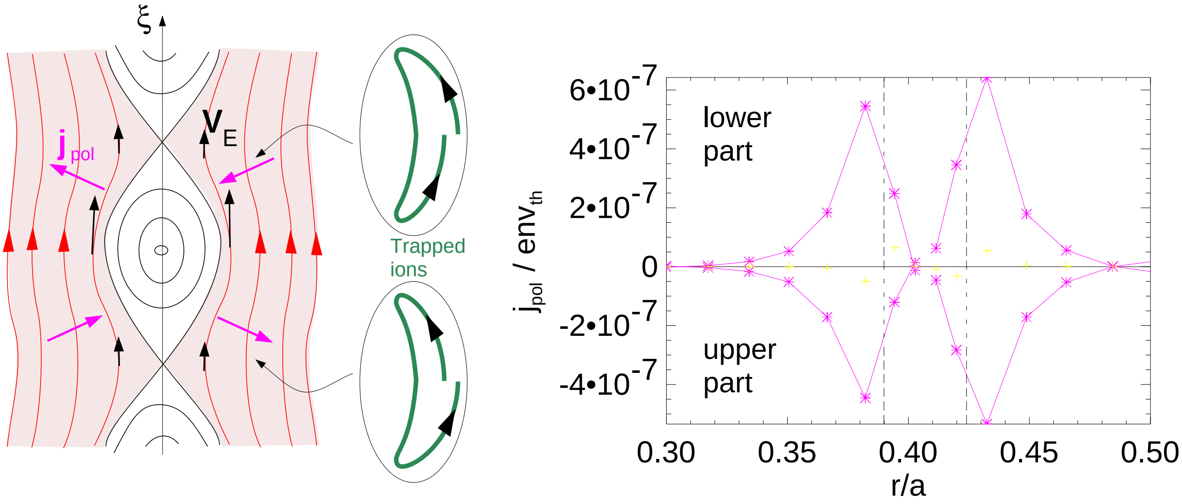

Fig. 4. *Polarization drift of trapped ions in the island rest frame (a) and typical polarization current profiles obtained from kinetic simulations in the lower and upper part of the island (b). The dashed vertical lines highlight the island region.*

An interesting feature of the polarization-current contribution expressed by Eq. (3.16) is the factor $(r/R_0)^{3/2}$, that depends on the collisionality regime. The polarization drift described in Sec. 3.1 involves the trapped ions. If the detrapping frequency is higher than the island rotation frequency ($\nu \gg (r/R_0)\omega$), however, the drift can be transferred locally, i. e. at a given position along the island, to the passing particles. In this case, the whole parallel flow (involving trapped and passing particles), which is of magnitude cE_r/B_p, varies along the island. In the opposite low-collisionality case, the trapped particles orbit the island several times before experiencing a collision, so that the part of the flow due to the passing particles averages to a constant value on a flux surface and does not contribute to the polarization drift, Eq. (3.6) [68, 69]. Eq. (3.16) is valid for low collisionalities, $\nu \ll (r/R_0)\omega$, whereas the factor $(r/R_0)^{3/2} \ll 1$ is substituted by unity in the high-collisionality regime. To evaluate the role of the polarization current for the stability of an island in a tokamak, it appears therefore important to understand where the transition between these two regimes occurs. Numerical calculations [70] performed with the code HAGIS employing the potential derived above, Eq. (3.15), and flat density and temperature gradients to suppress radial neoclassical transport, show good agreement with the analytic prediction of Ref. [71] and demonstrate that the transition occurs for $\nu \approx \omega$, so that the high-collisionality regime is reached only at even higher frequencies. Assuming the island rotation frequency to be of the order of the diamagnetic frequency, it follows that in large tokamaks with high plasma temperature the high-collisionality regime can hardly be attained.

Besides the collisionality scaling, drift kinetic numerical simulations have uncovered several new features with respect to the picture of the polarization current described above. First of all, when the island width becomes comparable or smaller than the ion banana width, the parallel velocity cE_r/B_p exhibits a similar behaviour as the bootstrap current, cf. Sec. 3.2, i. e. the motion of the trapped particles depends on the variation of the plasma properties (the electrostatic potential in this case) across the island separatrix. A reduction of the polarization current is observed for island widths $W \lesssim 2w_b$ [13]. For islands below the ion banana width, we are beyond the range of validity of Eq. (3.15) for the island potential and a self-consistent calculation of Φ is necessary. Recently, it has been stressed that a further possible reason for a reduction of the polarization current is a finite radial diffusion across the island separatrix that lowers the local current gradients [72].

Kinetic effects can also change significantly the scaling of the polarization current with the island rotation frequency, which according to Eq. (3.16) should be proportional to ω^2 (and always destabilizing) in the limit of vanishing density and temperature gradients, i. e. $\omega_{*pi} \rightarrow 0$ in Eq. (3.16). For frequencies close to or below $k_\parallel v_{\mathrm{th},i}$ (which can be shown to be a plausible value for ω under experimental conditions) the perpendicular current exhibits four roots instead of the expected two coinciding roots at $\omega = 0$, see Fig. 5 [14].

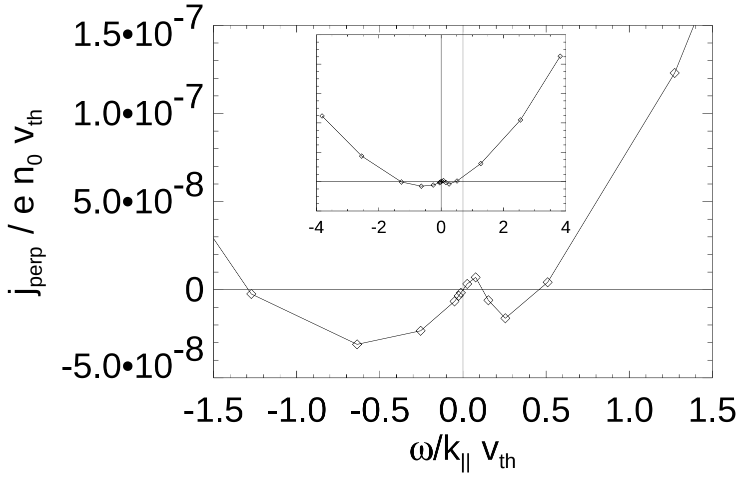

Fig. 5. *The perpendicular ion current as a function of the island rotation frequency* ω *(normalized to the parallel streaming frequency* $k_\parallel v_{th,i}$*) for flat background density and temperature gradients. The four zeros of* $\mathbf{J}_\perp$ *are shown, together with the nearly quadratic behaviour at large frequencies (inset).*

This behaviour is related to the precession of the trapped particles in the toroidal direction described by Eq. (3.5). Since the magnetic precession velocity, first term in Eq. (3.5), scales quadratically with the particle velocity, cf. Eq. (3.2), there are trapped particles whose precessional motion can be in resonance with the island rotation over a quite large frequency range. In this case, the drift across the perturbed flux surfaces is dominated by the increase or decrease of the toroidal precession due to the island field and the consequent density perturbation. This precessional current, which has been calculated analytically in the usual neoclassical limit $w_b \ll W$ [15], has a stabilizing effect on the island evolution, except for a frequency band between zero and approximately the toroidal precession frequency (the exact value depending on the collision frequency). When $\omega \gg k_\parallel v_{\mathrm{th},i}$ the standard behaviour of the polarization current ($\propto \omega^2$) is recovered and this explains the sign reversal when $\omega/k_\parallel v_{\mathrm{th},i}$ is of order unity. A kinetic treatment that retains the effects of toroidal geometry is thus mandatory to determine whether the currents due to the island potential produce a stabilizing or destabilizing contribute to the island dynamics. The same major conclusion applies in general to all the neoclassical contributions to the evolution of a magnetic island in a tokamak.

Chapter 4

The tearing mode in a tokamak: interaction with turbulence

4.1 Plasma turbulence

The radial transport of heat and particles in today's tokamak reactors is to a large extent determined by turbulent processes developing on small scales (typically of the order of the ion gyroradius) [73, 74]. The experimental characterization of the turbulence and the quantitative prediction of the associated transport levels is one of the big challenges in present tokamak research. From a computational point of view, the simulation of turbulence in toroidal plasmas turns out to be extremely demanding. This is due to the fact that one has to resolve in space (and in velocity space in the case of a kinetic approach) a complex nonlinear dynamics which is strongly anisotropic in the direction parallel and perpendicular to the magnetic field and occurs on different time scales for ions and electrons [75].

Small-scale instabilities (leading to turbulence) and large-scale instabilities (such as the tearing mode) can interact in several ways, and a complete understanding of the tearing-mode dynamics requires the study of such an interaction. Recently, this subject has received a growing interest. Although some aspects of the problem have been known for some decades, the availability of high-performance computing tools allows now direct numerical simulations for more and more realistic parameters. Turbulence can affect the growth of a magnetic island through a modification of the resistivity (and viscosity) of the plasma [76, 77, 78, 79, 80] and providing "seed islands" that can trigger the mode [81]. Moreover, as the turbulent transport is one of the fundamental players in determining the density and temperature profiles across the island, it influences the contribution of the bootstrap [49] and polarization [82] currents discussed in the previous chapter. On the other hand, a tearing mode affects the dynamics of the turbulence, first of all because the pressure flattening inside the island reduces the drive for the small-scale fluctuations, and moreover because the plasma flows developing along the perturbed magnetic surfaces turn out to regulate the level of the turbulence. In this chapter, we focus mainly on the latter aspect. Some basic concepts required for a physical understanding of the turbulence in a magnetized plasma and the possible role of a magnetic island are presented in this section. Secs. 4.2 is devoted to the presentation of the results of numerical simulations in toroidal geometry.

The paradigm for the description of small-scale instabilities leading to turbulent transport in magnetized plasmas is represented by the drift wave, whose origin is explained in Fig. 1.

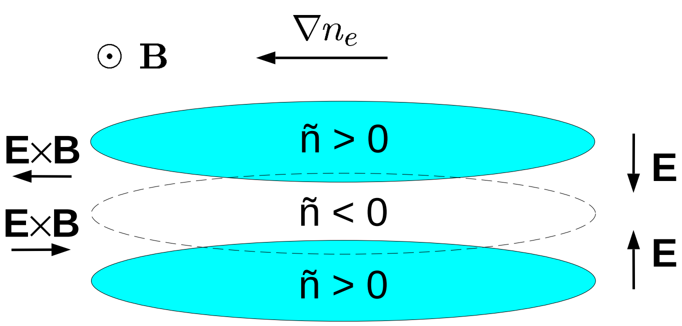

Fig. 1. *Generation of a drift wave. A periodic density perturbation in the y direction (vertical) in the presence of a gradient in the x direction (horizontal) leads to an* **E** × **B** *convection of plasma as shown and a consequent drift of the initial perturbation in the y direction.*

In the presence of a periodic density perturbation, the electrons rapidly flow along the magnetic-field lines generating an electric field, directed from the regions of increased density to those of decreased density, which balances the parallel pressure gradient. The relation between the electrostatic potential and the density perturbation is the Boltzmann response $\tilde{n}_e/n_e = e\phi/T_e$, as can be seen from the parallel component of Eq. (2.5) equating the first two terms on the right-hand side. The subsequent $\mathbf{E}\times\mathbf{B}$ velocity convects plasma alternately from the left or from the right side. This leads to a drift of the initial density disturbance, from the bottom to the top in the figure. The frequency of the drift wave can be immediately derived from the ion continuity equation

$$\frac{\partial n_i}{\partial t} = -\nabla\cdot(\mathbf{v}_i n_i)$$

under the assumption that the parallel phase velocity of the wave is much larger than the thermal velocity of the ions ("cold" ions) and that the magnetic field is uniform, so that the $\mathbf{E}\times\mathbf{B}$ velocity is incompressible[1]. The previous equation reduces for a perturbation of the form $\exp[i(k_y y - \omega t)]$ to

$$-i\omega\tilde{n}_e = \frac{c}{B}\left(ik_y \frac{T_e}{e}\frac{\tilde{n}_e}{n_e}\right)\frac{\mathrm{d}n_e}{\mathrm{d}x}$$

where quasi-neutrality $\tilde{n}_e \simeq \tilde{n}_i$ has been imposed and the electrostatic potential in the $\mathbf{E}\times\mathbf{B}$ velocity is taken from the Boltzmann response. The wave frequency is hence the electron diamagnetic frequency $\omega_* = k_y c T_e/eBL_n$, cf. Sec. A.2, with $L_n = -(1/n)\mathrm{d}n/\mathrm{d}x$.

This features are captured by the model proposed by Hasegawa and Mima in 1978 [83], who derived the relevant equation for the electrostatic potential,

$$\frac{\mathrm{d}}{\mathrm{d}t}\left[\frac{e\phi}{T_e} - \rho_s^2\nabla_\perp^2\left(\frac{e\phi}{T_e}\right)\right] + u_{*y}\frac{\partial}{\partial y}\left(\frac{e\phi}{T_e}\right) = 0$$

(with $u_{*y} = \omega_*/k_y$), which can be easily obtained from Eqs. (A.1,A.2), neglecting the magnetic fluctuations (along with collisions and electron inertia) in Eq. (A.3) to derive the Boltzmann response for the electrons. Writing the total time derivative explicitly, the previous equation can be cast in the form

$$\frac{\partial}{\partial t}\left[\frac{e\phi}{T_e} - \rho_s^2\nabla_\perp^2\left(\frac{e\phi}{T_e}\right)\right] - \rho_s^2\left(\mathbf{u}_E\cdot\nabla\right)\nabla_\perp^2\left(\frac{e\phi}{T_e}\right) + u_{*y}\frac{\partial}{\partial y}\left(\frac{e\phi}{T_e}\right) = 0. \tag{4.1}$$

The Hasegawa-Mima equation (4.1) is very similar to the two-dimensional Navier-Stokes equation for an incompressible fluid. In particular, the nonlinear term is identical for both equation.

---

[1] The diamagnetic flux is divergence-free in this model and does not contribute to the oscillation.

With respect to the Navier-Stokes equation, however, there is an extra term appearing in Eq. (4.1), namely the first one on the left-hand side which expresses the compressibility due to the parallel electron motion [83]. This term dominates for perturbations whose wavelength exceeds the ion sound radius ρ_s, as can be seen from the dispersion relation following from the substitution of a plane-wave *ansatz* in the linearized form of Eq. (4.1):

$$\omega = \frac{\omega_*}{1 + \rho_s^2 k_\perp^2}.$$

This corresponds to the result derived above in the limit $\rho_s^2 k_\perp^2 \ll 1$.

It has to be noticed that according to this model the drift wave is stable, i. e. its amplitude is neither growing nor damped. This is a consequence of the assumption of adiabatic electrons, which leads to a perfect overlap of density and potential perturbations. Relaxing the assumption of perfect adiabaticity (e. g. introducing collisions) it is easy to see that the drift wave can become unstable. This can be understood referring again to Fig. 1 and supposing that the $\mathbf{E} \times \mathbf{B}$ velocity is now phased in such a way that it convects plasma from the left "high-density" side into the region where $\tilde{n}_e > 0$ and from the right "low-density" side into the region where $\tilde{n}_e < 0$, thus reinforcing the initial perturbation and leading to a net transport from left to right.

In the nonlinear problem, the various Fourier harmonics become coupled and turbulence arises. In the investigation of tokamak turbulence, a particular role is played by so-called *zonal* perturbations with vanishing parallel wavenumber[2]. The dynamics of the zonal modes is not captured by the Hasegawa-Mima model, since for $k_\parallel = 0$ there is no parallel electric field and the density perturbation is zero rather than Boltzmann. A way to include this effect in the two-dimensional model discussed here is to repeat the derivation of Eq. (4.1) writing the potential as $\phi = \phi_{DW}(x, y) + \phi_{ZF}(x)$ and the density as $\tilde{n} = \tilde{n}_{DW}$ (where the subscripts stand for drift wave and zonal flows, respectively, and the fact that $\tilde{n}_{ZF} = 0$ has been used). This leads to the replacement of Eq. (4.1) with [85]

$$\left(\frac{\partial}{\partial t} + u_{Ey,ZF}\frac{\partial}{\partial y}\right)\frac{e\phi_{DW}}{T_e} - \rho_s^2\left(\frac{\partial}{\partial t} + \mathbf{u}_{E,DW}\cdot\nabla + u_{Ey,ZF}\frac{\partial}{\partial y}\right)\nabla_\perp^2\left(\frac{e\phi}{T_e}\right) + u_{*y}\frac{\partial}{\partial y}\left(\frac{e\phi_{DW}}{T_e}\right) = 0.$$

Averaging this equation over the small-scale drift-wave oscillations (this operation is denoted by a bar) leads to an equation for the zonal potential

$$\frac{\partial}{\partial t}\nabla_\perp^2\phi_{ZF} = -\overline{\mathbf{u}_{E,DW}\cdot\nabla\nabla_\perp^2\phi_{DW}}, \tag{4.2}$$

showing that the large-scale zonal flows are driven through nonlinear coupling by the small-scale drift fluctuation via the Reynolds stress forces (the right-hand side of Eq. (4.2) can be easily transformed into a term proportional to $\nabla^2(\overline{u_{Ex,DW}u_{Ey,DW}})$). Using Eq. (4.2) it is possible to show that the envelope of the drift-wave intensity is unstable against e. g. modulation by a seed zonal velocity shear [84] and that energy is transferred by this mechanism from small to large scales.

A similar situation occurs in the presence of a magnetic island, the main difference consisting in the fact that the perturbed flux surfaces are not characterized by the mode numbers $m =$

---

[2] In a tokamak with nested flux surfaces, a zonal perturbation, constant on magnetic surfaces, is characterized by the mode numbers $m = n = 0$, cf. Eq. (2.10). Its importance is related to the fact that the $\mathbf{E} \times \mathbf{B}$ flows due to a potential varying only in the radial direction are mainly in the poloidal direction. These zonal flows [84] can significantly lower the turbulence level, ripping apart the eddies, thus reducing their correlation times and lengths, and depleting the energy in the turbulent modes.

$n = 0$. The extension of the analysis sketched above to the island case has been developed by McDevitt and Diamond [79]. In a tokamak, we can expect a nonlinear coupling between turbulent modes with high wavenumbers and modes with low wavenumbers corresponding to a given magnetic island. Moreover, on can infer that a similar nonlinear coupling occurs not only for the electrostatic part of the turbulence, but also for its magnetic component, so that "zonal fields" can be nonlinearly excited like the zonal flows (in the case of an island, long-wavelength fields that can amplify a seed island).

As mentioned at the beginning, a considerable progress in the field of the interaction between small and large-scale fluctuations has been achieved recently [82, 86, 87, 88], through fluid simulations showing the importance of the mutual interaction of small and large scales, including the nonlinear excitation and amplification of magnetic islands [89, 90]. In this thesis, we focus on a description that retains both kinetic effects and a tokamak geometry. Under these conditions, a complete (self-consistent) kinetic description of the problem, resolving both the time scale typical of the turbulence development and that typical of the island growth, is still not feasible. Thus, we first present electrostatic (gyro)kinetic simulation that investigate the influence of the island geometry on the turbulence, discarding island evolution. At the end of the section, we discuss the first results of electromagnetic (gyro)fluid simulations with self-consistent island evolution in toroidal geometry.

4.2 Tokamak turbulence in the presence of a magnetic island

Under conditions typical of today's tokamaks, the mechanism leading to turbulent transport is slightly different with respect to the model presented in the previous section. One of the most common small-scale instabilities (sometimes named also microinstabilities) is the so-called toroidal ion-temperature-gradient (ITG) mode [91]. Fig. 2 describes the instability mechanism.

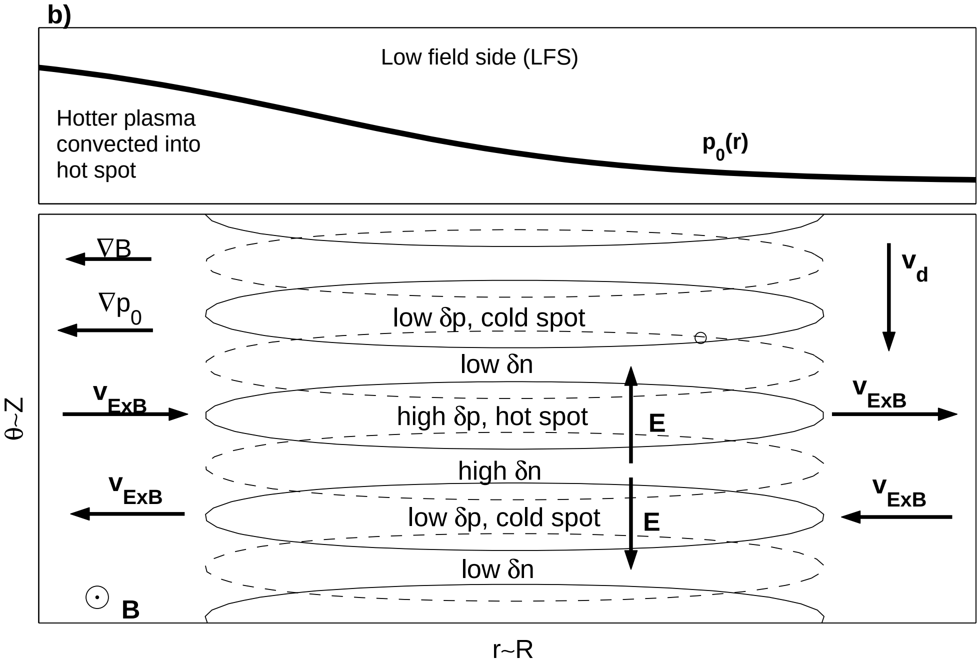

Fig. 2. *Generation of the ITG instability on the low-field side of a toroidal confinement device* (reprinted from Ref. [92]).

In this case, an initial ion-temperature perturbation leads to a density perturbation because of the fact that the magnetic-drift velocity, Eq. (3.2), is proportional to the energy of the particles and is therefore on average higher where the temperature is higher. As in the case of the drift wave, the electron response to the density perturbation leads to an electric field directed from the regions of higher density to those of lower density. The consequent $\mathbf{E} \times \mathbf{B}$ velocity conveys hot plasma into the hot region and cold plasma into the cold region, thus amplifying the initial perturbation (actually, this is the case only on the low-field side of the tokamak; on the high-field side the $\mathbf{E} \times \mathbf{B}$ flows damp the initial temperature perturbation). With respect to the case of an unstable drift wave described in the previous section, in the case of the ITG mode the source of free energy for the instability is the temperature gradient rather than the density gradient. Moreover, the ITG is a reactive instability, in the sense that no dissipation (like the collisions in the drift-wave case) is required to make the mode unstable, whereas perpendicular compressibility becomes important.

In order to model this kind of instabilities, advantage can be taken from the fact that the time scales associated with turbulence are much longer than those connected with the gyromotion of the particles. An average of the kinetic equation over the gyrophase allows one to reduce the number of variables in phase space from six to five, as in the case of the drift kinetic modelling considered in the previous chapter. For a consistent treatment of the microinstabilities, however, the variation of the electromagnetic disturbances on the scale of the ion gyroradius must be retained. This approach leads to the gyrokinetic model [93, 94] and its gyrofluid counterpart [95, 96]. Neglecting collisions, the gyrokinetic equation can be written in the form

$$\frac{\partial f}{\partial t} + \frac{\mathrm{d}\mathbf{R}}{\mathrm{d}t} \cdot \frac{\partial f}{\partial \mathbf{R}} + \frac{\mathrm{d}v_\parallel}{\mathrm{d}t}\frac{\partial f}{\partial v_\parallel} + \frac{\mathrm{d}\mu}{\mathrm{d}t}\frac{\partial f}{\partial \mu} = 0, \tag{4.3}$$

with the nonlinear characteristics

$$\begin{aligned}
\frac{\mathrm{d}\mathbf{R}}{\mathrm{d}t} &= v_\parallel \mathbf{b} + \frac{1}{B_\parallel^*}\left[\frac{\mu B + v_\parallel^2}{\Omega}\mathbf{b} \times \nabla B - \frac{v_\parallel^2}{\Omega}\mathbf{b} \times (\mathbf{b} \times \nabla \times \mathbf{B}) - \nabla\langle\phi\rangle_g \times \mathbf{b}\right], && (4.4)\\
\frac{\mathrm{d}v_\parallel}{\mathrm{d}t} &= -\mu\left[\mathbf{b} - \frac{v_\parallel}{B_\parallel^*\Omega}\mathbf{b} \times (\mathbf{b} \times \nabla \times \mathbf{B})\right] \cdot \nabla B && (4.5)\\
&- \frac{q}{m}\left\{\mathbf{b} + \frac{v_\parallel}{B_\parallel^*\Omega}\left[\mathbf{b} \times \nabla B - \mathbf{b} \times (\mathbf{b} \times \nabla \times \mathbf{B})\right]\right\} \cdot \nabla\langle\phi\rangle_g, &&\\
\frac{\mathrm{d}\mu}{\mathrm{d}t} &= 0. && (4.6)
\end{aligned}$$

In the previous equations, $\mathbf{R}$ is the position *of the gyrocentre*, $v_\parallel$ its velocity component along the magnetic field, $\mathbf{b}$ the unit vector along the magnetic field $\mathbf{B}$, μ the magnetic moment, $B_\parallel^* = B + (m/q)v_\parallel \mathbf{b} \cdot \nabla \times \mathbf{b}$ and $\langle\phi\rangle_g$ the perturbed potential averaged over the gyroperiod, solution of the gyrokinetic Poisson equation

$$\nabla^2\phi = 4\pi q_i \left\{n_e - \int \left[f + \frac{q_i}{m_i B}(\phi - \langle\phi\rangle_g)\frac{\partial f}{\partial \mu}\right]\delta(\mathbf{R} + \rho - \mathbf{r})\mathrm{d}^6\mathbf{Z}\right\}, \tag{4.7}$$

where ρ is a vector directed from the gyrocentre to the position of the particle.

In the gyrokinetic studies presented below, the codes ORB5 [97] and GKW [98] have been employed. They adopt two different approaches for the solution of the gyrokinetic equation. ORB5 is based on the PIC method, consisting in a discretization of phase space through a number of numerical particles that follow the nonlinear characteristics. The self-consistent electromagnetic fields are calculated projecting the charge and current connected to each tracer onto a fixed spatial grid (this is called a Lagrangian approach). GKW solves the gyrokinetic equation on a five-dimensional grid (Eulerian or Vlasov approach) in the flux-tube approximation [99]. A finite domain of the plasma around a given field line is considered and the deviation of the distribution function from its equilibrium value is assumed to be small over the region of interest, whereas its gradients can be comparable to the equilibrium gradients.

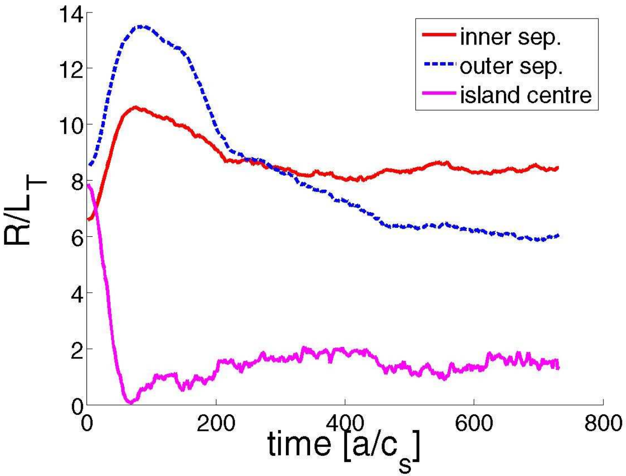

Fig. 3. *Time evolution of the temperature gradient in the island region for a typical ORB5 simulation.*

The implementation of a magnetic island in these codes is correspondingly different. In a PIC approach, the equations of motion of the particles are modified including the radial magnetic field produced by a magnetic island of assigned helicity [16]. In GKW, the computational box is set around the rational surface of interest and a parallel vector potential corresponding to a mode of desired amplitude is imposed (in the case of a static island, Ampère's law is not solved) [54]. In the gyrokinetic results presented below for a $m = 3$, $n = 2$ island, only electrostatic perturbations are considered. The plasma parameters are similar to those of the so-called Cyclone base case, characterized by ITG turbulence [100].

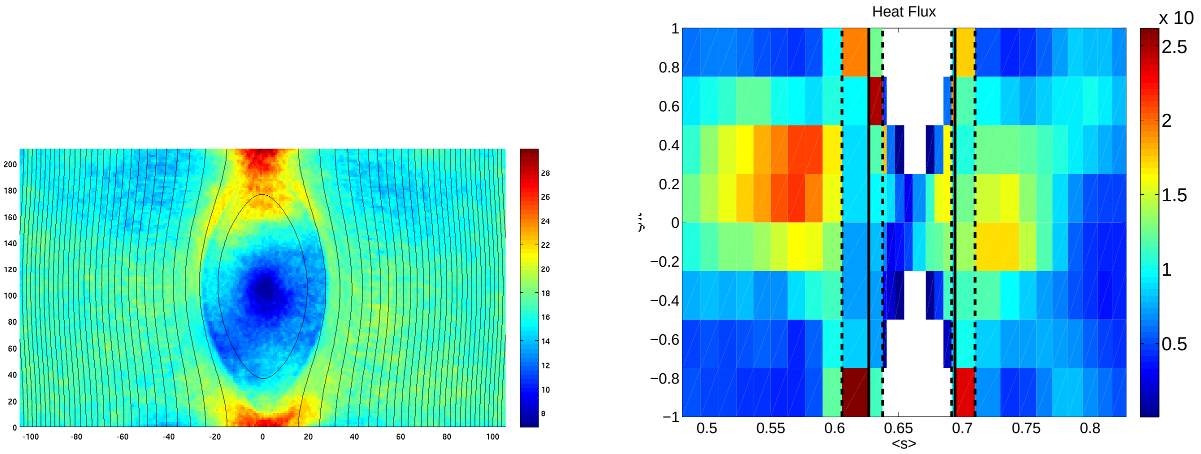

Fig. 4. *Contour plot of the density fluctuations (left, GKW simulations) and of the heat flux (right, ORB5 simulations) in the island region. The horizontal axis is the radial position, the vertical axis is the helical angle along the island. The drift direction is from top to bottom in the left figure and from bottom to top in the right figure.*

Since in turbulence runs including a static magnetic island the profiles are initialized with a finite gradient and as functions of the unperturbed radial coordinate, the first effect seen in the simulations is the flattening inside the island shown in Fig. 3. In the centre of a sufficiently big island, the temperature gradient almost vanishes, whereas it initially increases just outside the island because of the "compression" of the flux surfaces. In this first phase, where the temperature profile relaxes to the perturbed magnetic geometry due to the island, turbulent modes are filtered out. When turbulence is switched on, a significant transport sets in, until the profiles reach a quasi-steady state. The radial heat flux driven by the turbulence is found to be highly inhomogeneous in the island region. ORB5 and GKW simulations consistently show that transport across the island region occurs mainly at the X-points (Fig. 4).

Turbulent eddies can also penetrate inside the island through convection in the drift direction of the instability. This mechanism seems to be more effective than turbulence spreading [101] in conveying the turbulence towards linearly stable regions inside the island. On the contrary, at the level of the O-point ($\xi = 0$) the transport across the separatrix is strongly suppressed. This behaviour is interpreted in terms of the sheared flows due to long-wavelength modes mentioned in the previous section. These modes are particularly strong at the island separatrix and inside and reduce the transport level as known from zonal flows in unperturbed equilibria. This is confirmed by the local turbulence spectra [17] plotted in Fig. 5.

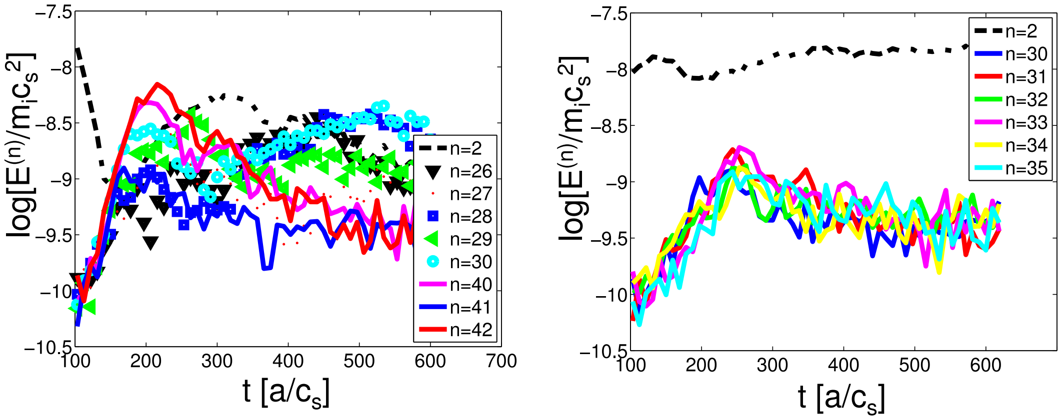

Fig. 5. *Time evolution (in units of minor radius over sound speed) of the energy spectrum outside the island (left) and at the island separatrix, core side (right). In the latter case, only long-wavelength modes corresponding to the island helicity are excited.*

In particular, the left figure clearly shows the nonlinear coupling between modes with high toroidal numbers and the harmonic $n = 2$ corresponding to the magnetic island. The $n = 2$ mode, initially decaying after the turbulence-free phase ($t \lesssim 100a/c_s$, not shown in the figure), rises again, pumped by high-n modes satisfying a three-wave coupling condition. At the island separatrix (right figure), the $n = 2$ clearly dominates the other modes and the transport is suppressed[3]. The low-n mode can appear in the form of a vortex mode [103], i. e. as an electrostatic potential developing in the centre of the island (with periodic sign reversals) with contour levels coinciding with the island flux surfaces, as shown in Fig. 6. The $\mathbf{E} \times \mathbf{B}$ heat flux connected to a vortex mode at its peak intensity can largely exceed the flux due to the parallel motion along the magnetic-field lines of the island [54]. On average, these two fluxes are found to give a comparable contribution to the total heat transport. From these results a

---

[3] Unfortunately, the simulations performed so far do not allow a clear statement on the role of the shear fluxes associated with small islands as a possible explanation for the improved confinement sometimes observed in the vicinity of rational surfaces [102].

new picture of the transport across the rational magnetic surface where a magnetic island is present emerges, which is more complex than the "standard" paradigm, based on homogeneous heat conductivities and Fick's law, on which the calculation of the "transport threshold" for the neoclassical drive [49, 104] discussed in the previous chapter is based.

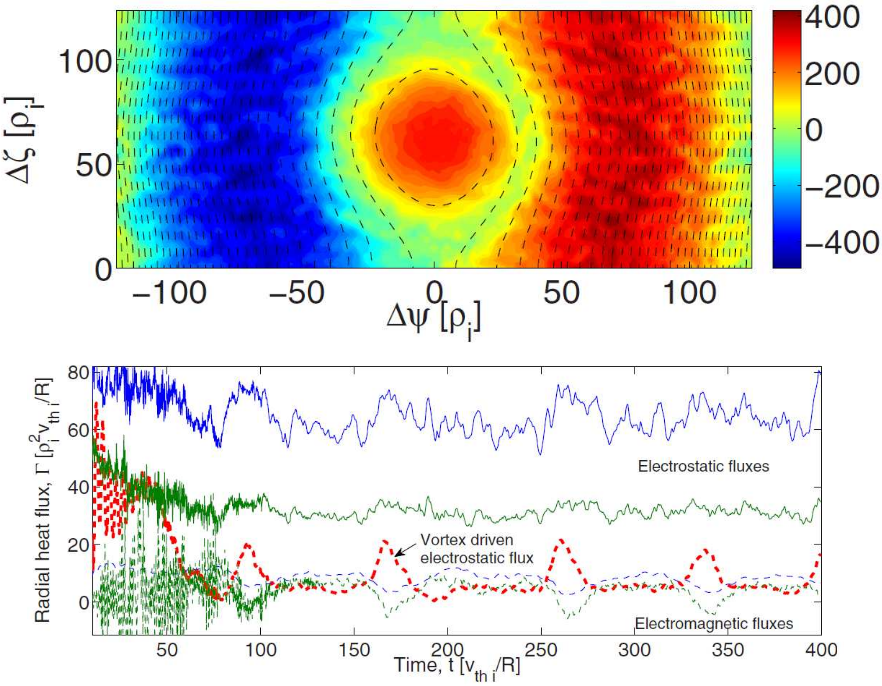

Fig. 6. *Electrostatic potential (top) and time evolution of the heat fluxes integrated over the simulation volume (bottom) in the presence of a vortex mode. Dark blue lines represent the ion contribution, light green lines the electron contribution; solid lines the flux due to* $\mathbf{E}\times\mathbf{B}$ *convection, dashed lines the fluxes along the perturbed field lines.*

We conclude this chapter quoting the first fully electromagnetic simulations, performed for realistic tokamak parameters, resolving both the turbulence time scales and the much slower island growth. The runs have been performed with the code GEMZ, that solves the gyrofluid equations as formulated in Ref. [105]. These are time dependent equations for six gyrofluid moment variables (density, parallel velocity, parallel and perpendicular temperatures and parallel and perpendicular heat fluxes for each species), solved in field-aligned conformal coordinates [106]. In the simulations, a small island is initialized in a random bath of turbulent density fluctuations for parameters typical of a mid-size tokamak like ASDEX Upgrade with different current profiles. As already mentioned, current profiles in present tokamaks are usually stable against tearing ($\Delta' < 0$) but also a tearing-unstable profile taken from Wesson [2] has been considered. The bootstrap current is not switched on in the equations, so that no neoclassical drive is included. On the contrary, the tearing mode is stabilized by toroidicity effects as discussed in Ref. [107]. In spite of this effect, the island if found to be not only maintained but increased during the turbulence. In the runs with the tearing-unstable current profile, a more clear and more coherent island is found, but also for a more realistic current profile the island persists [17]. Also simulations without any island initialization lead to similar results. The analysis of the energy-transfer channels has still to be performed. Further investigations are required to assess the relevance of the interaction between turbulence island for the seeding process and the island evolution in tokamaks.

Chapter 5

Active stabilization of tearing modes by electron cyclotron current drive

5.1 Electron cyclotron waves

To limit the deleterious impact of tearing modes on the performance of a tokamak reactor, strategies for their active control are being developed. One of the most promising methods is based on the injection of electromagnetic waves with a frequency in the range of the electron cyclotron (EC) frequency[1]. For a proper choice of frequency and polarization, EC waves are resonantly absorbed in a very localized region, comparable with the radial extension of the magnetic island. This opens the possibility of controlling the tearing mode through local change of the magnetic shear (i. e. acting on the Δ' parameter defined in Chapter 2) or the generation of a current inside the island to replace the missing bootstrap current (see Chapter 3). The latter mechanism, which is predicted to dominate the stabilization process under ITER conditions [108, 109], is discussed in Sec. 5.2 and 5.3.

A brief summary of some properties of the interaction between wave and plasma is presented in the remainder of this section, to supply the basic information necessary to understand the strategy for present and future NTM control via EC waves.

5.1.1 The plasma response

The plasma response to the field of a propagating electromagnetic wave can be calculated by solving the relevant kinetic equation, coupled with Maxwell's equations, and deriving the associated dielectric tensor [110, 111, 112, 113]. If the wave frequency is in the range of the cyclotron frequency of a given particle species, the assumption of scale separation between wave oscillation and gyration motion adopted in the previous chapters is of course invalid and no simplification can be obtained at this level. However, the derivation of the dielectric tensor is made easier by the fact that for realistic wave energies nonlinear effects can be usually neglected [114]. Moreover, in the calculation of the linear response, the plasma can be treated as locally homogeneous and collisions can be neglected, as they occur on a much slower time scale.

Here only waves in the range of the EC frequency are discussed. The ions can be assumed to constitute a constant neutralizing background and do not take part in the dynamics, which

---

[1] The cyclotron frequency of electrons can be calculated using the simple formula $\Omega/2\pi$ [GHz]= $28B$ [T]. For $B = 5.3$ T, as foreseen for ITER, the EC frequency is approximately 148 GHz.

is determined by the linearized Vlasov equation[2]

$$\frac{\mathrm{d}\tilde{f}}{\mathrm{d}t} = e\left(\tilde{\mathbf{E}} + \frac{\mathbf{v}\times\tilde{\mathbf{B}}}{c}\right)\cdot\frac{\partial f_0}{\partial \mathbf{p}}$$

where $\mathrm{d}/\mathrm{d}t$ denotes the total derivative along the unperturbed (no wave) orbits of the electrons and f_0 is the background electron distribution, assumed here to be a relativistic isotropic Maxwellian $f_0 = f_0(p)$. The formal solution to this equation can be written for each Fourier component as

$$\hat{f}e^{i(\mathbf{k}\cdot\mathbf{r}-\omega t)} = e\int_{-\infty}^{t}\mathrm{d}t\; e^{i(\mathbf{k}\cdot\mathbf{r}'-\omega t')}\left(\hat{\mathbf{E}} + \frac{\mathbf{v}'\times\hat{\mathbf{B}}}{c}\right)\cdot\frac{\mathbf{p}'}{p'}\frac{\partial f_0}{\partial p'}.$$

To ensure convergence of this integral, $\mathrm{Im}[\omega] > 0$ should be assumed. The solution can be generalized to the case $\mathrm{Im}[\omega] \leq 0$ through analytic continuation following Landau's prescription for the integration of the poles, see below. To obtain a treatable expression for $\hat{f}$, the (relativistic) unperturbed trajectories are substituted in $\mathbf{r}(t) - \mathbf{r}(t')$ and $\mathbf{p}(t')$. The term proportional to $\mathbf{v}'\times\hat{\mathbf{B}}$ is perpendicular to $\mathbf{p}'$ and does not contribute, so that the result is

$$\hat{f} = e\int_{0}^{\infty}\mathrm{d}\tau\; e^{i\Phi(\tau)}\frac{\hat{\mathbf{E}}\cdot\mathbf{p}'}{p'}\frac{\partial f_0}{\partial p'},$$

with $\tau = t - t'$ and

$$\Phi(\tau) = (\omega - k_{\|}v_{\|})\tau + \frac{k_{\perp}p_{\perp}}{m_e\Omega_e}\left[\sin\left(\phi - \frac{\Omega}{\gamma}\tau\right) - \sin\phi\right]$$

(ϕ is the gyrophase at $t' = t$ and $\gamma = (1 - v^2/c^2)^{-1/2}$ is the relativistic Lorentz factor). The last step is to use Jacobi-Anger expansion for the exponential of the trigonometric function. Choosing a Cartesian reference frame such that $\mathbf{B}_0 = B_0\hat{\mathbf{z}}$ and $\mathbf{k} = (k_{\perp}, 0, k_{\|})$, we can cast the solution for $\hat{f}$ in the form

$$\hat{f} = e\int_{0}^{\infty}\mathrm{d}\tau\;\frac{1}{p'}\frac{\partial f_0}{\partial p'} \tag{5.1}$$
$$\left[\sum_{m=-\infty}^{+\infty}\sum_{n=-\infty}^{+\infty}\left(e^{i(\omega-k_{\|}v_{\|}-n\Omega_e/\gamma)\tau+i(n-m)\phi}\left(\frac{np_{\perp}J_n(b)}{b}\hat{\mathbf{E}}_x + ip_{\perp}J_n'(b)\hat{\mathbf{E}}_y + p_{\|}J_n(b)E_{\|}\right)\right)\right],$$

where $b = k_{\perp}p_{\perp}/m_e\Omega_e$.

The integration of the previous equation with respect to time has now become trivial and leads to a factor $i/(\omega - k_{\|}v_{\|} - n\Omega_e/\gamma)$. When the *cyclotron resonance condition*

$$\omega - k_{\|}v_{\|} - n\Omega_e/\gamma = 0 \tag{5.2}$$

is satisfied, a singularity appears in Eq. (5.1). In practical applications, we are often interested in the case of moderate absorption, $\mathrm{Im}[\omega] \ll \mathrm{Re}[\omega]$, for which we can use the formula (to be understood as a prescription when performing the integral over $v_{\|}$)

$$\frac{1}{\omega - k_{\|}v_{\|} - n\Omega_e/\gamma} = \mathcal{P}\frac{1}{\omega - k_{\|}v_{\|} - n\Omega_e/\gamma} - i\pi\delta(\omega - k_{\|}v_{\|} - n\Omega_e/\gamma)$$

where $\mathcal{P}$ denotes the principal part and the last term represents the contribution of the resonances. Due to the expansion in Bessel functions, a wave-particle resonance occurs at all

---

[2] The Vlasov equation is the collisionless limit of the kinetic equation (3.7) presented in Sec. 3.1.

cyclotron harmonics. Physically, harmonics appear because the motion of the particles in the wave is not purely sinusoidal but rather overlays with the thermal gyration motion.

This expression for $\hat{f}$ can be used to express the perturbed current density generated by the wave as a function of the wave field

$$\hat{J}_i = -e \int v_i \hat{f} \mathrm{d}^3\mathbf{p} = \sigma_{ij} \hat{\mathbf{E}}_j .$$

This formula defines the conductivity tensor (in Fourier space), which in turn determines the dielectric tensor $\varepsilon_{ij} = \delta_{ij} + (4\pi i/\omega)\sigma_{ij}$ expressing the response of the medium in the wave equation (5.3). Mathematically, the contribution of the resonances is the appearance of a Hermitian part of the conductivity tensor and consequently of a anti-Hermitian part of the dielectric tensor.

5.1.2 Short-wavelength approximation

The propagation of an electromagnetic wave in a homogeneous plasma is described by the (Fourier transformed) wave equation for a linear medium

$$\mathbf{k} \times \left(\mathbf{k} \times \hat{\mathbf{E}}\right) + \frac{\omega^2}{c^2} \boldsymbol{\varepsilon} \cdot \hat{\mathbf{E}} = 0. \tag{5.3}$$

Writing the first term in dyadic notation as $(-k^2\mathbf{I} + \mathbf{k}\mathbf{k}) \cdot \hat{\mathbf{E}}$ allows us to put the wave equation in the form $\boldsymbol{\Lambda} \cdot \hat{\mathbf{E}} = 0$, where $\boldsymbol{\Lambda}$ is called the dispersion tensor. The condition for non-trivial solutions yields the dispersion equation $H \equiv \det[\boldsymbol{\Lambda}] = 0$, whose roots determine the modes of propagation, i. e. the waves supported by the system. In the case of weak inhomogeneity, $\lambda \ll L$ (where λ is the wavelength and L is the inhomogeneity scale of the medium), Eq. (5.3) remains valid to the lowest order in λ/L. The assumption $\lambda/L \ll 1$ is usually well satisfied for waves in the EC frequency range in a tokamak, so that asymptotic techniques for the solution of the wave equation can be adopted. The most common method is geometrical optics, or ray tracing [115, 116]. The dispersion equation $H(\mathbf{k}, \mathbf{r}) = 0$ is satisfied along the curves (rays) determined by the Hamiltonian equations

$$\frac{\mathrm{d}\mathbf{r}}{\mathrm{d}s} = \frac{\partial H}{\partial \mathbf{k}}, \qquad \frac{\mathrm{d}\mathbf{k}}{\mathrm{d}s} = -\frac{\partial H}{\partial \mathbf{r}}, \tag{5.4}$$

where s is the arclength along the ray. According to this method, the wave front is decomposed into several rays, each of them traced independently[3] through the plasma. It can be shown that the energy carried by a wave beam propagates in the direction parallel to the rays, i. e. in the direction of the group velocity, and is absorbed in the region where the resonance condition is satisfied. Although the solution of Eqs. (5.4) in tokamak geometry usually requires a numerical approach, the computational effort is significantly reduced with respect to the numerical solution of the original wave equation. Some fundamental features of the absorption process can be understood by a closer inspection of the resonance condition (5.2). In the case of perpendicular propagation ($k_\parallel = 0$), Eq. (5.2) can be written (e. g. for the fundamental cyclotron harmonic $n = 1$) as $\Omega_e(R) = \gamma\omega$, where in a tokamak $\Omega_e \propto B_0 \propto 1/R$. In the cold-plasma limit, $\gamma = 1$,

---

[3] Several methods have been developed in order to allow for wave phenomena (diffraction), neglected when the rays are traced independently from each other, taking advantage from the short-wavelength condition. Here we mention only two techniques base on a complex-eikonal ansatz, namely the quasi-optical ray tracing [117, 118] and the paraxial beam tracing [119, 120][121, 122], which have been implemented respectively in the codes GRAY [123] and TORBEAM [18]. These codes have been thoroughly benchmarked [124, 125] and are used in the analysis presented in Sec. 5.3.

all the particles would be resonant at the position R_c where $\Omega_e(R_c) = \omega$. Since $\gamma \geq 1$, thermal effects broaden the resonance towards the high-field side (smaller R). If wave with a finite $k_\parallel$ is injected, typically orienting the antenna at a finite angle in the toroidal direction, the Doppler shift leads to a further broadening of the resonance layer (increasing with $k_\parallel$) and to a shift towards the low-field side (larger R). An important effect is that in this case the absorption of the wave is asymmetric with respect to $v_\parallel$, i. e. electrons travelling in a given direction are heated preferentially. The resulting asymmetry in the distribution function corresponds to a finite current driven in the plasma by the EC wave. This current can be used to replace the missing bootstrap current inside the magnetic island and thus reduce or completely stabilize a neoclassical tearing mode. Despite of the broadening mentioned above, the optical thickness of the plasma for waves injected especially with frequencies around the $n = 1$ and $n = 2$ harmonics (in the so-called ordinary and extraordinary mode, respectively) is high, implying very localized absorption, so that local control of MHD activity (and NTM in particluar) has become one of the main fields of application of EC waves [126].

5.2 Stabilization criteria

The contribution of the EC-driven current J_{CD} to the dynamics of the island can be calculated [127] in analogy to the neoclassical contribution discussed in Chapter 3, i. e. including J_{CD} in the non-inductive current on the right-hand side of Eq. (3.9). The resulting generalized Rutherford equation can be used to derive a quantitative estimate of the current necessary to compensate the driving terms. To this aim, we can first neglect the effects that determine the stability of small islands, which are relatively poorly known, as discussed in the previous chapters. The Rutherford equation (3.12) can be extended in the form [128]

$$\frac{\tau_R}{r_s}\frac{\mathrm{d}W}{\mathrm{d}t} = r_s\Delta' + c_{\mathrm{sat}} f_{GGJ}\, 6.34\frac{4\pi}{c}\frac{L_q j_{\mathrm{bs}}}{B_p}\frac{r_s}{W} - c_{\mathrm{stab}}\frac{32\sqrt{\pi}}{2}\frac{4\pi}{c}\frac{L_q j_{\mathrm{CD}}}{B_p}\frac{r_s w_{CD}}{W^2}\eta_{CD}, \tag{5.5}$$

where the ECCD current profile is assumed to have a Gaussian shape $J_{\mathrm{CD}} = j_{\mathrm{CD}} \exp[-4(r - r_s)^2/w_{CD}^2]$ and the current-drive efficiency η_{CD}, defined as [129]

$$\eta_{CD} = \frac{\int_{-1}^{\infty} \mathrm{d}\Omega \langle 1\rangle_\Omega^{-1}\langle\cos\xi\rangle_\Omega\langle J_{\mathrm{CD}}\rangle_\Omega}{\int_{-1}^{\infty} \mathrm{d}\Omega\langle J_{\mathrm{CD}}\rangle_\Omega},$$

weights the component of the driven current with the correct helicity for mode stabilization ($\eta_{CD} = 1$ if the ECCD profile is a δ-function centred at the O-point of the island). The flux-surface average operator has been defined in Eq. (2.24). Uncertainties in the size of the drive and stabilization terms, due for instance to the realistic tokamak geometry, can be included through the two coefficients of order unity, c_{sat} and c_{stab} in Eq. (5.5), that are to be determined from experimental measurements [130]. The factor $f_{GGJ} = 1 - 1.37(q^2 - 1)/q^2(L_q r_s^{1/2})/R_0^{3/2}$ represents the reduction of the bootstrap drive due to geodesic-curvature effects [131, 107] (this contribution also scales as $1/W$ for sufficiently large island widths). To derive the conditions for the ECCD current required for tearing-mode stabilization it is useful to introduce the saturated island width

$$W_{\mathrm{sat}} = c_{\mathrm{sat}}\frac{f_{GGJ}}{(-\Delta')}\frac{6.34\,4\pi}{c}\frac{L_q j_{\mathrm{bs}}}{B_p},$$

so that the second term on the right-hand side of Eq. (5.5) becomes simply $-r_s\Delta' W_{\mathrm{sat}}/W$. The saturated island width is determined by a balance between the stabilizing effect of the equilibrium current profile ($\Delta' < 0$) and the neoclassical drive. With this definition, the stationarity condition $\mathrm{d}W/\mathrm{d}t = 0$ can be formulated as

$$0 = -\frac{W}{W_{\mathrm{sat}}} + 1 - 5\frac{c_{\mathrm{stab}}}{c_{\mathrm{sat}} f_{GGJ}} \frac{\eta_{CD} j_{\mathrm{CD}}}{j_{\mathrm{bs}}} \frac{w_{CD}}{W}. \tag{5.6}$$

Requiring that no root exists (unconditional stability), i. e. that the discriminant of the previous equation is negative, leads to the following criterion for island stabilization:

$$\frac{\eta_{CD} j_{\mathrm{CD}}}{j_{\mathrm{bs}}} \frac{w_{CD}}{W_{\mathrm{sat}}} > \frac{1}{20} \frac{f_{GGJ} c_{\mathrm{sat}}}{c_{\mathrm{stab}}}. \tag{5.7}$$

It is useful to distinguish between the case in which the ECCD profile is narrower or broader than the typical island width W_{marg} at which stabilization occurs. In the former case ($w_{CD} < W_{\mathrm{marg}}$) the current-drive efficiency can be shown to be in the range $\eta_{CD} \lesssim 0.4$ for both continuous injection and 50%-duty-cycle modulation. Eq. (5.7) becomes then

$$\frac{j_{\mathrm{CD}}}{j_{\mathrm{bs}}} \frac{w_{CD}}{W_{\mathrm{sat}}} > \frac{1}{8} \frac{f_{GGJ} c_{\mathrm{sat}}}{c_{\mathrm{stab}}}. \tag{5.8}$$

On the other hand, if $w_{CD} > W_{\mathrm{marg}}$ modulation becomes important and the current drive efficiency can be approximated as $\eta_{CD} \simeq 0.15W/w_{CD}$ for modulated injection and $\eta_{CD} \simeq W^2/8w_{CD}^2$ for continuous injection. To express the stabilization condition it is more practical to exploit the fact that in general W_{marg} is much smaller than W_{sat}, so that the first term on the right-hand side of Eq. (5.6) can be dropped. The result in case of modulated injection is that stabilization is achieved if

$$\frac{j_{\mathrm{CD}}}{j_{\mathrm{bs}}} > \frac{4}{3} \frac{f_{GGJ} c_{\mathrm{sat}}}{c_{\mathrm{stab}}}. \tag{5.9}$$

Since for typical tokamak parameters f_{GGJ} is around $0.7 - 0.8$, we see that stabilization is achieved when the driven current density is larger than the bootstrap current density. In fact, the criterion

$$\eta_{NTM} \equiv \frac{j_{\mathrm{CD}}}{j_{\mathrm{bs}}} > 1.2 \tag{5.10}$$

has been adopted as a requirement for the ITER ECCD system for NTM stabilization (described in the next section), since ITER is predicted to be in the regime $w_{CD} > W_{\mathrm{marg}}$ [132]. For continuous injection, the previous formula must be replaced by

$$\frac{j_{\mathrm{CD}}}{j_{\mathrm{bs}}} > \frac{8}{5} \frac{f_{GGJ} c_{\mathrm{sat}}}{c_{\mathrm{stab}}} \frac{w_{CD}}{W},$$

i. e. complete stabilization ($W \to 0$) can be achieved only with an infinite ECCD current (no effects leading to stability of small islands are considered in the above derivation).

More recently, the criterion for NTM stabilization has been revised through a more detailed analysis, taking into account different models for the stability of small islands, namely the reduction of the bootstrap drive due to incomplete pressure flattening in the island [49] and the polarization current [67] already discussed in Chapt. 3. Moreover, the effect of confinement deterioration on the driving term, which is reduced by an amount proportional to the island width, has been included [4]. Most importantly, the condition $w_{CD} > W_{\mathrm{marg}}$ has been relaxed. If the EC deposition width becomes comparable or falls below the marginal island width, no advantage derives from further focusing, and better stabilization is achieved by increasing the total driven current, even at the expenses of the peak current density [133], see the discussion in Sec. 5.3. For ITER, this leads to the criterion [4, 133]

$$w_{CD} j_{\mathrm{CD}}/j_{\mathrm{bs}} \gtrsim 5\ \mathrm{cm}\ \text{and}\ w_{CD} \lesssim 5\ \mathrm{cm}. \tag{5.11}$$

Indeed, for $w_{CD} < W_{\mathrm{marg}}$, Eq. (5.8) should be used instead of Eq. (5.9). Taking typical values predicted for the saturated island size for ITER (32 cm for the $(2, 1)$ mode) one arrives at a similar conclusion as in Eq. (5.11).

It is remarked that, although the control and suppression of tearing modes by EC waves has been demonstrated and is routinely performed in several tokamak experiments [134, 135, 136], a direct experimental verification of the validity of the stabilization criteria derived above is far from easy. On the one hand, the detection of magnetic islands close to their marginal width becomes increasingly challenging, on the other hand the injected power is seldom tuned to be the minimum required power for mode stabilization. Moreover, the actual value of the EC current density could deviate from that calculated by beam tracing codes and its experimental determination is again very demanding.

5.3 Active NTM stabilization in ITER

In the ITER tokamak, the EC launchers devoted to the control of MHD activities (primarily NTMs) will be located in four access ports in the upper part of the vacuum vessel [137, 138]. From each port, eight beams will be aimed at the plasma from two rows. The total installed power is planned to be 24 MW. Subtracting the losses along the transmission lines, a maximum of 20 MW should reach the plasma. Alternatively, this power can be injected from an equatorial port to heat and drive a part of the plasma current near the centre of the plasma column. At the time of writing, the system is entering its final design phase.

The first requirement to be fulfilled by the upper launcher (UL) is that the stabilization criterion $\eta_{NTM} > 1.2$, Eq. (5.10), is satisfied at full injected power, for a selected number of ITER plasma scenarios which are assumed to be prone to NTMs. Depending on the plasma parameter, the location of the $q = 3/2$ and $q = 2$ surfaces and its intersection with the resonance layer can shift in space with respect to the antenna position. An optimal design requires that the mirrors steering the beams onto the corresponding surfaces ensure a sufficient focusing to generate a high current density. Priority is given to full stabilization of NTMs developing on the $q = 2$ surfaces (where NTMs are most deleterious for confinement loss and as disruption precursors) for Scenario 2, which is designed to achieve the main mission of ITER, namely a gain factor $Q = 10$ (see Ref. [3] for a discussion of the scenarios presently considered for ITER). The spatial arrangements of the UL beams and the plasma for ITER Scenario 2 can be seen in Fig. 1. For a nominal magnetic field on axis $B = 5.3$ T and an injected frequency $\omega/2\pi = 170$ GHz, the cold resonance (for the fundamental cyclotron harmonic $n = 1$) lies slightly on the high-field side of the magnetic axis.

The beam steering is planned to occur in the poloidal direction at a fixed optimal toroidal injection angle. This optimal angle has been found to be around 20° [139] and results from a compromise between a high total driven current (which increases with $k_\parallel$ and hence with the toroidal angle, as long as the resonance is met) and a good localization of the absorption profile, which deteriorates at large angles due to the large Doppler shift, leading to a drop in the current density even if the total current still increases. The final value of the toroidal angle of the UL will result from a refined analysis, including a more comprehensive performance criterion (see end of Sec. 5.2), a more accurate evaluation of the driven current to include momentum conservation in collisions of fast resonant electrons with the thermal bulk [140, 141], and the detailed launcher design, yielding the degree of superposition of the beams injected from a given row [142].

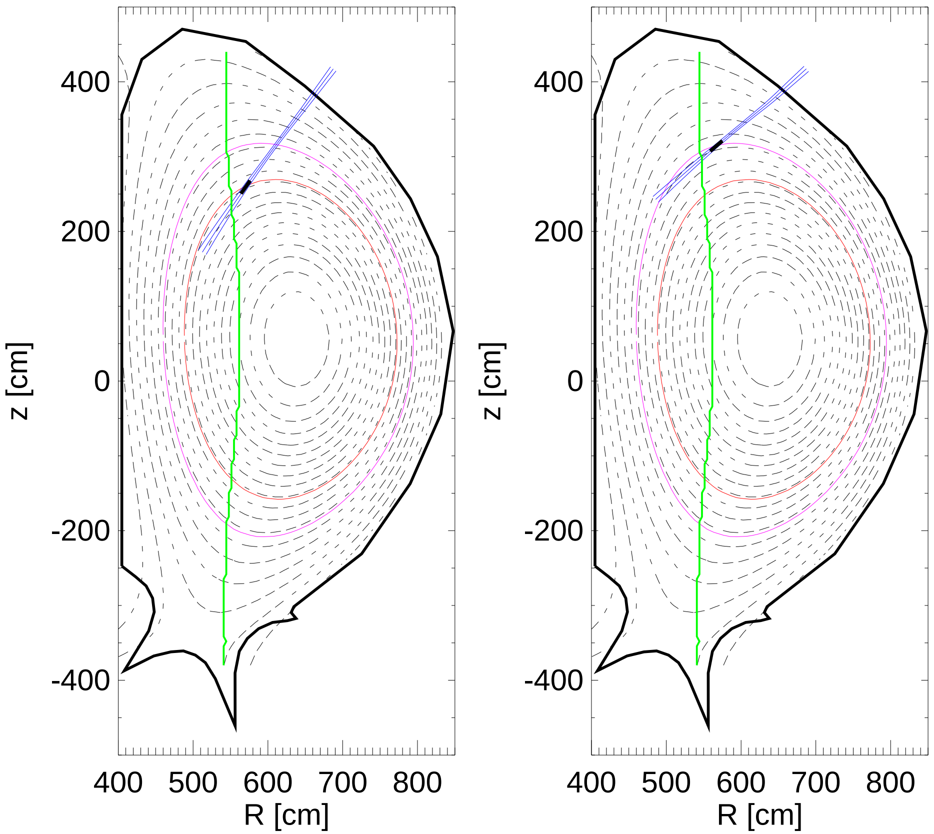

Fig. 1. *Beam paths for injection from the ITER Upper Launcher towards the* $q = 1.5$ *surface (left, red contour) and* $q = 2$ *surface (right, violet contour). Also shown is the location of the cold resonance (nearly vertical green line). The location of beam absorption is highlighted as a thicker region along the beam axis* (TORBEAM [18] *runs*).

The first result of the performance analysis carried out according to the criteria explained above was that the original idea of a beam steering operated without moving components facing the plasma (remote steering [143]) had to be abandoned, although technically attractive, since a sufficient steering range could be achieved only at the expenses of an unacceptable loss of beam focusing [132]. On the contrary, an antenna based on the front-steering design subsequently developed has been shown to satisfy the criterion $\eta_{NTM} > 1.2$ with a large margin for all the plasma scenarios included in the analysis, bringing the power requirement down to approximately 2/3 of the 20 MW mentioned before [144]. This means that the constraint on beam focusing, i. e. on current density, could be relaxed. This flexibility has been exploited to increase steering range of the antenna, thus allowing a synergy with the equatorial launcher and extending the range of possible physical applications [19]. In particular, driving EC current in the vicinity of appropriate flux surfaces can be used to induce localized changes in the plasma current profile that can be used to control the period of the sawtooth instability (injection around $q = 1$ [145]), which is often found to act as a trigger for the NTM instability (cf. Sec. 2.1.2), or to enter the frequently-interrupted-regime of NTMs, in which the mode does not grow to its saturated width due to a coupling with a $m + 1$, $n + 1$ ideal mode (demonstrated for current drive around the $q = 4/3$ surface [146]).

According to this “extended physics” approach, at the actual design stage the tasks of the UL are split between the two steering mirrors, upper and lower, mounted in each port (one mirror for each row of four beams). There is thus a maximum of 16 beams reaching the plasma from the four lower mirrors or from the four upper mirrors. Assuming that each beam line is connected to a 1 MW EC-wave generator (gyrotron) and a transmission loss of 5/6 as before, the maximum power injected from each row is 13.3 MW. The lower mirrors should cover the outer region of the plasma (the most critical for NTMs), whereas the upper mirrors have an increases steering range to reach down to the $q = 1$ surface. The UL performance calculated for scenario 2 in terms of the figures of merit discussed in the previous section, Eqs. (5.10,5.11), is shown in Table 1.

q	η_{NTM}	w_{cd} [cm]	$\eta_{NTM} w_{cd}$ [cm]
2	2.8	2.4	6.7
3/2	1.8	3.8	6.8

Table 1. *Figures of merit for NTM stabilization employing the ITER Upper Launcher (scenario 2).*

For other scenarios, where the resonant surfaces move outwards or inwards with respect to scenario 2, the figures of merit for NTM stabilization are still satisfied, although with a reduced margin [19].

The whole discussion reported above is focused on the requirements on the EC system in order to achieve full NTM stabilization (vanishing island width). In fact, the presence of a magnetic island implies a confinement deterioration, as already mentioned in Chapt. 1. The reduction of the energy confinement time τ_E is usually quantified in terms of the so-called belt model [147], according to which $\Delta\tau_E/\tau_E = 4Wr_s^3/a^4$ (the confinement decreases linearly with the island width and with the third power of the minor radius of the resonant surface), so that a complete stabilization of the mode looks meaningful. In ITER, however, this is not necessarily always the best choice to minimize the impact of the tearing modes on the fusion gain Q, as the injected EC power itself leads to a deterioration of the power balance, i. e. to a decrease of the fusion gain Q, cf. Eq. (1.2). In this sense, it could be not beneficial to have the EC waves turned on the whole time. The best strategy will be a trade-off between several factors: besides the impact of the injected EC power on Q, also the frequency of the trigger events (and the possibility to influence it) and the time required to stabilize the mode. This in turn depends critically on the strength of the various stabilizing and destabilizing mechanisms, on the size of the initial (seed) island and on the delay between mode detection and the start of the suppression process. Our ability to determine or constrain these parameters through simulations and dedicated experiments in present tokamaks will be of crucial importance for a successful planning of the best approach to tearing mode control on ITER.

Chapter 6

Synopsis

Good confinement of particles and energy in a toroidal fusion reactor is based on the presence of nested toroidal magnetic surfaces, which to a large degree inhibit the plasma particles from escaping radially from the hotter and denser core to the edge. This desirable configuration can be lost at radial positions that are prone to magnetic reconnection, since the radial magnetic field related to the appearance of a magnetic island allows the particles to stream across the reconnected region. For this reason, and because of their role as precursors of disruption events, magnetic islands represent a threat for the confinement of the plasma in a tokamak and even for its very safety. Understanding under which conditions magnetic islands appear and grow, and how their evolution can be actively controlled is thus a crucial task to achieve the targeted performance in a fusion device.

The stability of the tearing mode is determined by the interplay of disparate phenomena, taking place on different space and time scales and no theory is presently able to give a complete description of the evolution of tearing modes in present and future machines. In particular, the characterization of the stability of a small island, i. e. of the processes leading to its initial growth or suppression, is still a challenge for both theory and experiment. In this thesis, it has been shown that while a qualitative description of the tearing mode can be obtained in the frame of a fluid theory employing a simplified planar geometry, the explanation of the behaviour observed in a tokamak requires a more sophisticated approach. Thus, the results presented in Chapt. 3 and 4 are based on a kinetic description, that retains the different response of the particles to the island perturbation depending on their position in velocity space. Moreover, the toroidal geometry typical of a tokamak, with its magnetic-field inhomogeneity and the connected change of the particle orbits with respect to the planar case, has been included in all our numerical simulations.

A main focus of this thesis has been on the neoclassical contributions to the island dynamics (bootstrap and polarization current) at island widths comparable with the radial orbit width of the particles. This situation, encountered under experimental conditions in the early phase of the tearing instability in a tokamak, is outside the range of validity of the standard analytic treatment but is accessible to a numerical study. The drive of the mode, due to the drop of the bootstrap current inside the island, is found to be strongly modified with respect to a simple extrapolation of the large-island theory. Ions drifting across the island restore part of the missing current inside it. If the mode rotates, the ion response to the related electrostatic potential leads to a density perturbation. The consequent current perturbation acts as stabilizing if the island rotates in the electron diamagnetic direction. This leads to the general conclusion that small magnetic islands are more stable against the neoclassical drive than assumed neglecting finite-orbit effects. Such effects also reduce the neoclassical polarization current produced by the island rotation and hence its impact on the tearing mode, whether stabilizing or destabilizing. Moreover, kinetic studies have shown that resonances between the precession of the trapped particles around the torus and the island rotation can overcome the polarization current, yielding an opposite contribution to the island evolution. A further key aspect discussed here is the coupling between small-scale and large-scale fluctuations in the presence of an island under typical tokamak conditions. The growth of long-wavelength components of the electrostatic potential (corresponding to the angular extension of the island) through turbulent fluctuations has been shown to lead to a feedback on transport, reducing in particular the flows across the separatrix at the O-point level and favouring X-point fluxes. This means that the usual calculation of diffusion across the island region, based on constant diffusion coefficients, is only qualitatively valid. Moreover, large-scale electrostatic fluctuations can give a contribute to the radial transport which is comparable to the radial transport along the perturbed magnetic field. Finally, these simulations represent a first step towards a simultaneous description of turbulence and island dynamics in a torus.

Indeed, in the present work a price has been paid for retaining the details of phase-space behaviour of the particles in a realistic tokamak a geometry. Most of the results concern the influence of an island with prescribed width and rotation frequency (and associated potential) on the evolution of the electric currents and fields in its vicinity, but do not close the feedback loop on the evolution of the island itself. Studies to fill this gap have already been started. The investigation of the island potential as derived from a numerical solution of the gyorkinetic Poisson equation is under way, as reported at the end of Sec. 3.2, and first results confirm the validity of the conclusions on the stability of small island discussed above. The feasibility of simulations resolving both turbulence and island time scales and the related nonlinear interaction between small and large scales has been demonstrated for realistic tokamak turbulence in gyrofluid simulations, cf. Sec.4.2. With the present progress of the physical understanding, of the numerical tools and of the computer resources, self-consistent gyrokinetic simulations of magnetic islands capable to resolve both turbulence and MHD scales involved in the problem could be within reach in the next few years.

In Chapt. 5 it has been finally shown that much progress has been achieved also in the field of an active control of magnetic islands. In particular, injection of electron cyclotron waves in the island region can be used to replace the missing plasma current inside the island and hence reduce or suppress the tearing mode. A launcher dedicated to the control of MHD instabilities in general and tearing modes in particular is being developed for ITER. Preliminary results based on the present design show that the required stabilization criteria can be met.

Appendix A

Collisionality regimes in the linear theory of the tearing mode

A deeper insight into the linear dynamics of the tearing mode can be gained by distinguishing between different collisionality regimes, as this clarifies the role of ions and electrons and the assumptions underlying the MHD description presented in Sec. 2.2.

The model adopted in this appendix involves three equations for the unknown functions $\tilde{n}$ (perturbed electron density), $\tilde{\phi}$ (electrostatic potential) and $\tilde{A}_\parallel \simeq \tilde{A}_z$ (perturbed parallel vector potential):

$$\frac{\mathrm{d}}{\mathrm{d}t}\left(\frac{\tilde{n}}{n_0}\right) = -\frac{cT_e}{eBL_n}\frac{\partial}{\partial y}\left(\frac{e\tilde{\phi}}{T_e}\right) + \nabla_\parallel\left(\frac{\tilde{J}_\parallel}{en_0}\right) \tag{A.1}$$

$$\frac{\mathrm{d}}{\mathrm{d}t}\left[\rho_s^2\nabla_\perp^2\left(\frac{e\tilde{\phi}}{T_e}\right)\right] = \nabla_\parallel\left(\frac{\tilde{J}_\parallel}{en_0}\right) \tag{A.2}$$

$$\begin{aligned}&\beta_e\frac{\partial}{\partial t}\left(\frac{\tilde{A}_\parallel}{\beta_e\rho_s B_0}\right) + \frac{m_e}{m_i}\frac{\mathrm{d}}{\mathrm{d}t}\left(\frac{\tilde{J}_\parallel}{en_0c_s}\right) = \\ &c_s\nabla_\parallel\left(\frac{\tilde{n}}{n_0} - \frac{e\tilde{\phi}}{T_e}\right) - \frac{cT_e}{eBL_n}\frac{\partial}{\partial y}\left(\frac{\tilde{A}_\parallel}{\beta_e\rho_s B_0}\right) - \frac{m_e}{m_i}\nu_e\frac{\tilde{J}_\parallel}{en_0c_s}.\end{aligned} \tag{A.3}$$

In these equations, n_0 is a constant background density used for normalization, $c_s^2 = T_e/m_i$ is the square of the sound speed, $\rho_s = c_s/\Omega_i$ is the sound Larmor radius, $1/L_n = -(1/n_0)\mathrm{d}n_0/\mathrm{d}x$ is the scale length of the density profile, $\beta_e = 4\pi n_0 T_e/B^2$ measures the ratio between kinetic and magnetic pressure and

$$\rho_s^2\nabla_\perp^2\left(\frac{\tilde{A}_\parallel}{\beta_e\rho_s B}\right) = -\frac{\tilde{J}_\parallel}{en_0c_s}, \tag{A.4}$$

which is identical to Eq. (2.13). This three-field model, that allows us to reproduce the phenomenology described by Drake and Lee [37], can be derived from the two-fluid equations [22] with cold ions ($T_i \ll T_e$) and isothermal electrons and correspond to the set discussed by Scott *et al.* [148], under the additional assumption of slow parallel ion motion, i. e. that sound waves are negligible ($k_\parallel c_s \ll \omega$). Physically, Eqs. (A.1-A.3) represent electron continuity, quasi-neutrality and Ohm's law (parallel momentum balance for electrons) respectively. The first term on the right-hand side of Eq. (A.1) represents the contribution of the background density gradient to the density advection ($\mathbf{v}_E \cdot \nabla n_0$) and in the last term the fact that the parallel current is carried only by the electrons has been taken into account (Eq. (A.4) is used to express $\tilde{J}_\parallel$ in terms of

$\tilde{A}_\parallel$). The form left-hand side of Eq. (A.2) is due to the fact that in this slab model the only contribution to $-\nabla_\perp \cdot \tilde{\mathbf{J}}_\perp$ is due to the polarization current $\mathbf{J}_{pol} = -(m_i n_0 c^2/B^2)\mathrm{d}/\mathrm{d}t(\nabla_\perp \phi)$, see Eq. (3.6) for its neoclassical counterpart (which is larger by a factor B^2/B_p^2). Eq. (A.3) reproduces the parallel component of Eq. (2.5), with the electric field split into its inductive and electrostatic components and the contribution of the perturbed magnetic field to the parallel gradient appearing in the term before last.

A.1 Linear two-fluid analysis and collisionality regimes

The linear dynamics of the tearing mode depends on whether the frequency ω_e at which the electrons drift by one wavelength while streaming along the field lines is faster or slower than the growth rate γ of the mode [37]. If $\omega_e \gg \gamma$, the physics is governed by the electrons only, since they average out during their motion the periodic field $\tilde{E}_\parallel$ induced by the growing magnetic perturbation. If the electron-ion collision frequency ν_e is much smaller than γ, the only effect which prevents the electrons from flowing infinitely fast along the field lines is their finite mass (inertia) and $\omega_e = k_\parallel v_{\mathrm{th},e}$. This regime is called *collisionless* and the condition $\tilde{E}_\parallel = 0$ is reached at a distance $x \approx \Delta$ from $x = 0$ where $k_\parallel v_{\mathrm{th},e}$ starts to exceed γ. If, on the other hand, $\gamma \ll \nu_e$, the electrons diffuse along the field lines, rather than freely stream along them, with a diffusion coefficient $D = v_{\mathrm{th,e}}^2/\nu_e$ and the width of the layer is determined by $\omega_e = k_\parallel^2 v_{\mathrm{th,e}}^2/\nu_e \approx \gamma$ (*semi-collisional* regime). At high collisionality, the motion of the electrons is strongly inhibited and ω_e becomes smaller than γ. In this case, charge separation occurs and an electrostatic potential develops. The tearing-layer width is then the distance from $x = 0$ at which the electric field $-ik_\parallel\tilde{\phi}$ is strong enough to compensate the induced field $-\gamma\tilde{A}_\parallel/c$. This *collisional* case, in which the ion dynamics becomes important, has already been described through the equations of resistive MHD (to which Eqs. (A.1-A.3) reduce under these conditions, see below) in Sec. 2.2. To account for the collisionless and semi-collisional regime, we need the more refined model presented above, which is able to account for electron and ion continuity separately. We start neglecting the terms proportional to the equilibrium density gradient, which will be considered in Sec. A.2:

$$\frac{\mathrm{d}}{\mathrm{d}t}\left(\frac{\tilde{n}}{n_0}\right) = \nabla_\parallel\left(\frac{\tilde{J}_\parallel}{en_0}\right) \tag{A.5}$$

$$\frac{\mathrm{d}}{\mathrm{d}t}\left[\rho_s^2\nabla_\perp^2\left(\frac{e\tilde{\phi}}{T_e}\right)\right] = \nabla_\parallel\left(\frac{\tilde{J}_\parallel}{en_0}\right) \tag{A.6}$$

$$\beta_e\frac{\partial}{\partial t}\left(\frac{\tilde{A}_\parallel}{\beta_e\rho_s B_0}\right) + \frac{m_e}{m_i}\frac{\mathrm{d}}{\mathrm{d}t}\left(\frac{\tilde{J}_\parallel}{en_0c_s}\right) = c_s\nabla_\parallel\left(\frac{\tilde{n}}{n_0} - \frac{e\tilde{\phi}}{T_e}\right) - \frac{m_e}{m_i}\nu_e\frac{\tilde{J}_\parallel}{en_0c_s}. \tag{A.7}$$

Eqs. (A.5-A.7) are the starting point of the linear investigation of the tearing mode presented in this section, where only the imaginary part of ω (i. e. the growth rate γ) is retained, since the analysis will show that the currents which develop in the sheet pinch when background density gradients are neglected only contribute to the growth of the tearing mode and not to its drift.

A.1.1 Collisionless regime

As discussed previously, in the collisionless regime we have $\gamma \gg \nu_e$ and the quickness of the response of the electrons to the induced parallel electric field is just determined by their inertia. Moreover, we have no charge separation and we can neglect the electrostatic potential $\tilde{\phi}$

altogether. Eqs. (A.5-A.7) reduce to

$$
\begin{aligned}
\frac{\mathrm{d}}{\mathrm{d}t}\left(\frac{\tilde{n}}{n_0}\right) &= \nabla_\parallel \left(\frac{\tilde{J}_\parallel}{en_0}\right) \\
\beta_e \frac{\partial}{\partial t}\left(\frac{\tilde{A}_\parallel}{\beta_e \rho_s B_0}\right) &= c_s \nabla_\parallel \left(\frac{\tilde{n}}{n_0}\right) - \frac{m_e}{m_i}\frac{\mathrm{d}}{\mathrm{d}t}\left(\frac{\tilde{J}_\parallel}{en_0 c_s}\right).
\end{aligned}
$$

In a linear analysis, substituting $\partial/\partial t \to \gamma$ and $\nabla_\parallel \to ik_\parallel$, it is immediate to eliminate $\tilde{n}$ from the previous equations. In the central layer, the derivatives along y are neglected with respect to those in the x direction, $\nabla_\perp^2 \simeq \partial^2/\partial x^2$. Recalling Eqs. (2.19,A.4), the equation for $\tilde{A}_\parallel(x)$ is:

$$
\frac{c^2}{\omega_{pe}^2}\frac{\partial^2 \tilde{A}_\parallel}{\partial x^2} = \frac{\tilde{A}_\parallel}{1 + \left(v_{\mathrm{th},e} k_y/\gamma L_s\right)^2 x^2},
$$

where $\omega_{pe}^2 = 4\pi n_0 e^2/m_e$ is the electron plasma frequency and the relations $m_e \rho_s^2/m_i \beta_e = c^2/\omega_{pe}^2$ and $m_i c_s^2/m_e = v_{\mathrm{th},e}^2$ have been used. The integration of this equation across the central layer can be simplified by observing that, as shown in the analysis of the outer region (Sec. 2.2.1), $\partial \tilde{A}_\parallel/\partial x$ is discontinuous across $x = 0$ but $\tilde{A}_\parallel$ is continuous and can be approximated by its central value (constant-ψ approximation [36]):

$$
\frac{c^2}{\omega_{pe}^2}\left.\frac{\partial \tilde{A}_\parallel}{\partial x}\right|_{-\Delta}^{\Delta} = \tilde{A}_\parallel(0)\int_{-\Delta}^{\Delta}\frac{\mathrm{d}x}{1 + \left(v_{\mathrm{th},e} k_y/\gamma L_s\right)^2 x^2}. \tag{A.8}
$$

Matching this equation to the external solution implies that the jump in the first derivative of $\tilde{A}_\parallel$ on the left-hand side equals $\Delta' \tilde{A}_\parallel(0)$, see Eq. (2.17). The width Δ of the inner layer is determined as the region in which the function on the right-hand side significantly contributes to the integral, i. e. $\Delta \approx \gamma L_s/v_{\mathrm{th},e} k_y$. Physically, Δ corresponds to the distance from $x = 0$ at which $\gamma = k_\parallel v_{\mathrm{th},e}$, as anticipated above. Extending the integral from $-\infty$ to $+\infty$ introduces just a small error and allows us to write (omitting the factor π resulting from the integral)

$$
\gamma = \frac{\Delta' k_y v_{\mathrm{th},e}}{L_s k_0^2} \equiv \gamma_{cl} \tag{A.9}
$$

(where $1/k_0 = c/\omega_{pe}$ is the collisionless skin depth). Substituting Eq. (A.9) into the expression for Δ yields

$$
\Delta = \frac{\Delta'}{k_0^2} \equiv \Delta_{cl}. \tag{A.10}
$$

As shown by Eq. (2.17), Δ' scales as $1/a$. Since typically $k_0 a \gg 1$, the width of the central layer is much smaller than $1/k_0$ and hence $\Delta_{cl} \ll \rho_i$, since in most fusion plasmas the ion Larmor radius is larger than the collisionless skin depth.

A.1.2 Semi-collisional regime

If the collision frequency exceeds the growth rate, the electron diffuse along the field lines rather than freely streaming along them. As in the collisionless case, no electrostatic potential is generated, but now the collision term in Eq. (A.7) replaces the electron inertia:

$$
\begin{aligned}
\frac{\mathrm{d}}{\mathrm{d}t}\left(\frac{\tilde{n}}{n_0}\right) &= \nabla_\parallel \left(\frac{\tilde{J}_\parallel}{en_0}\right) \\
\beta_e \frac{\partial}{\partial t}\left(\frac{\tilde{A}_\parallel}{\beta_e \rho_s B_0}\right) &= c_s \nabla_\parallel \left(\frac{\tilde{n}}{n_0}\right) - \frac{m_e}{m_i}\nu_e \frac{\tilde{J}_\parallel}{en_0 c_s}.
\end{aligned}
$$

After linearizing and eliminating $\tilde{n}$ from the previous equations we find that in the semi-collisional regime Eq. (A.8) is substituted by

$$\frac{c^2}{\omega_{pe}^2}\left.\frac{\partial \tilde{A}_\parallel}{\partial x}\right|_{-\Delta}^{\Delta} = \frac{\gamma}{\nu_e}\tilde{A}_\parallel(0)\int_{-\Delta}^{\Delta}\frac{\mathrm{d}x}{1+\left(v_{\mathrm{th},e}^2 k_y^2/\gamma\nu_e L_s^2\right)x^2}, \tag{A.11}$$

which implies a width of the inner layer $\Delta \approx (\gamma\nu_e)^{1/2}L_s/k_y v_{\mathrm{th},e}$. Proceeding as in the collisionless case and ignoring again the factor π resulting from the integral on the left-had side, Eq. (A.11) becomes $\Delta'/k_0^2 = (\gamma\nu_e)\Delta$, so that the growth rate

$$\gamma_{sc} = \nu_e^{1/3}\gamma_{cl}^{2/3} \tag{A.12}$$

and the layer width

$$\Delta_{sc} = \frac{\nu_e^{1/2}L_s}{k_y v_{\mathrm{th},e}}\nu_e^{1/6}\gamma_{cl}^{1/3} = \left(\frac{\nu_e}{\gamma_{cl}}\right)^{2/3}\Delta_{cl}. \tag{A.13}$$

immediately follow. Since in the semicollisional regime discussed here it is supposed that the collision frequency exceeds the growth rate, Eq.(A.13) shows that collisions broaden the region of particle acceleration (correspondingly reducing the current density within the layer, as explained in Sec. 2.2.1). From Eq.(A.12) it follows that also the growth rate increases in the semi-collisional case as compared to the collisionless case.

A.1.3 Collisional regime

If the collisionality is high enough, electrons alone cannot short out $\tilde{E}_\parallel$ on a scale faster than γ and an electrostatic potential arises from charge separation. To describe the electrostatic ion response, Eqs. (A.5-A.7) are appropriate only if $\Delta \gg \rho_i$, as they hold only for magnetized ions, for which the basic perpendicular drift is due to polarization, i. e. to a time dependent $\mathbf{E}\times\mathbf{B}$ velocity. The assumption $\Delta \gg \rho_i$ will be verified once Δ has been calculated. The electron current is, in this case, due to quasi-neutrality rather than electron continuity and the equations to be solved are

$$\begin{aligned}
\frac{\mathrm{d}}{\mathrm{d}t}\left[\rho_s^2\nabla_\perp^2\left(\frac{e\tilde{\phi}}{T_e}\right)\right] &= \nabla_\parallel\left(\frac{\tilde{J}_\parallel}{en_0}\right)\\
\beta_e\frac{\partial}{\partial t}\left(\frac{\tilde{A}_\parallel}{\beta_e\rho_s B_0}\right) &= -c_s\nabla_\parallel\left(\frac{e\tilde{\phi}}{T_e}\right) - \frac{m_e}{m_i}\nu_e\frac{\tilde{J}_\parallel}{en_0c_s}.
\end{aligned}$$

which are perfectly equivalent to the collisional MHD equations (2.11,2.12) since $\eta = 4\pi\nu_e/\omega_{pe}^2$. Following the linearization procedure described for the collisionless and semicollisional regimes and eliminating $\tilde{\phi}$ from the previous equations (simplifying $\nabla_\perp^2\tilde{\phi} \approx -\tilde{\phi}/x^2$) the dispersion relation is obtained in the form

$$\frac{c^2}{\omega_{pe}^2}\left.\frac{\partial \tilde{A}_\parallel}{\partial x}\right|_{-\Delta}^{\Delta} = \frac{\gamma}{\nu_e}\tilde{A}_\parallel(0)\int_{-\Delta}^{\Delta}\frac{\mathrm{d}x}{1+\left(v_{\mathrm{th},e}^2 k_y^2/\gamma\nu_e\rho_s^2 L_s^2\right)x^4}, \tag{A.14}$$

which leads to the estimate for the layer width $\Delta \approx (\gamma\nu_e/\Omega_i\Omega_e)^{1/4}(L_s/k_y)^{1/2}$ and (again neglecting a factor $\sqrt{\pi}/2$ arising from integration) to the growth rate

$$\gamma^{5/4} = \frac{\Delta'}{k_0^2}\left(\frac{k_y}{L_s}\right)^{1/2}\left(\nu_e^3\Omega_e\Omega_i\right)^{1/4} \Rightarrow \gamma_c = \left(\frac{\Delta_{cl}}{\rho_i}\right)^{2/5}\gamma_{cl}^{2/5}\nu_e^{3/5}. \tag{A.15}$$

The layer width can now be written

$$\Delta_c = \left(\frac{\nu_e}{\gamma_{cl}}\right)^{2/5} \rho_i^{2/5} \Delta_{cl}^{3/5}. \tag{A.16}$$

The previous results for γ_c and Δ_c of course coincide with the expressions obtained in Sec. 2.2.2.

This analysis shows that both γ and Δ increase monotonically with the collision frequency ν_e. In particular, Δ ranges from a value well below the ion Larmor radius (collisionless regime) to a level $\Delta \gg \rho_i$ in the collisional regime, the condition $\Delta \approx \rho_i$ denoting the transition between the semi-collisional and the collisional regime. Eqs. (A.9,A.12,A.15) clearly show that the sign of the stability parameter Δ' calculated in the outer region, Eq. (2.17), determines the sign of the growth rate, i. e. the stability of the mode.

A.2 Drift tearing modes

In the presence of a background density gradient, the term proportional to L_n^{-1} must be retained on the right-hand side of both Eqs. (A.1) and (A.3). These terms change qualitatively the dynamics of the tearing instability, since they introduce a rotation of the mode which was absent in the picture presented in the previous section. This rotation is associated with a fundamental plasma oscillation called the drift wave (or, if also the vector potential is involved, the drift Alfvén wave), cf. Sec 4.1. For this reason, rotating tearing modes are also called drift tearing modes.

As an example, the collisionless regime is discussed here. For $\gamma \gg \nu_e$, the starting point are following equations:

$$\frac{\mathrm{d}}{\mathrm{d}t}\left(\frac{\tilde{n}}{n_0}\right) = \nabla_\parallel \left(\frac{\tilde{J}_\parallel}{en_0}\right)$$

$$\beta_e \frac{\partial}{\partial t}\left(\frac{\tilde{A}_\parallel}{\beta_e \rho_s B_0}\right) = c_s \nabla_\parallel \left(\frac{\tilde{n}}{n_0}\right) - \frac{m_e}{m_i}\frac{\mathrm{d}}{\mathrm{d}t}\left(\frac{\tilde{J}_\parallel}{en_0 c_s}\right) - \frac{cT_e}{eBL_n}\,\beta_e \frac{\partial}{\partial y}\left(\frac{\tilde{A}_\parallel}{\beta_e \rho_s B_0}\right).$$

Linearizing as before, substituting $\partial/\partial t \to -i\omega$, $\partial/\partial y \to ik_y$ and introducing the diamagnetic frequency $\omega_* = k_y cT_e/eBL_n$, a dispersion relation similar to Eq. (A.8) is obtained

$$\frac{c^2}{\omega_{pe}^2}\frac{\partial \tilde{A}_\parallel}{\partial x}\bigg|_{-\Delta}^{\Delta} = \tilde{A}_\parallel(0)\frac{\omega - \omega_*}{\omega}\int_{-\Delta}^{\Delta} \frac{\mathrm{d}x}{1 - \left(v_{\mathrm{th},e}k_y/\omega L_s\right)^2 x^2}. \tag{A.17}$$

Writing the width of the inner layer as $\Delta \approx -i\omega L_s/k_y v_{\mathrm{th},e}$, the previous equation becomes

$$\frac{\Delta'}{k_0^2} = \frac{\omega - \omega_*}{\omega}\left(\frac{-i\omega L_s}{k_y v_{\mathrm{th},e}}\right)\pi.$$

Separating real and imaginary part, we obtain $\omega_r = \omega_*$ and $\gamma = \Delta' k_y v_{\mathrm{th},e}/\pi L_s k_0^2$. In the collisionless regime, the growth rate of the mode is not influenced by the density gradient, cf. Eq. (A.9) and the rotation frequency is given by the diamagnetic frequency. The treatment of the singularity on the right-hand side of Eq. (A.17), that has been removed simply with a convenient definition of Δ, relies on the kinetic analysis presented in the next section.

A.3 Linear kinetic description

In a kinetic approach, the source terms in Poisson and Ampère equations, i. e. the charge density and the current density, are calculated as the zeroth and first-order moments of the distribution function, that satisfies the kinetic equation. As in the two previous sections, the analysis developed here concerns the central layer, and the solution for $\tilde{A}_z$ has to be matched again with that obtained in the outer region (some comments on the outer layer are made at the end of the section). In the inner layer, the derivatives with respect to y are neglected with respect to those in the x direction and the relevant Maxwell equations read

$$\frac{\partial^2 \tilde{\phi}}{\partial x^2} = 4\pi e\left(\tilde{n_e} - Z\tilde{n}_i\right) \tag{A.18}$$

$$\frac{\partial^2 \tilde{A}_z}{\partial x^2} = -\frac{4\pi}{c}\tilde{J}_z. \tag{A.19}$$

In the determination of the current, only the motion of the much more mobile electrons is considered. Correspondingly, only the kinetic equation for the electrons is addressed explicitly here. It was shown in Sec. A.1 that in the collisionless and semicollisional regime the ions do not contribute to the tearing mode dynamics. Explicit results are known for the ion response needed for the collisional regime [149]. In this section, only the solution for the collisionless tearing mode is derived and compared to that found in the previous section.

In a current slab, equilibrium quantities depend on the x coordinate only. The equilibrium distribution function can be written as a shifted Maxwellian

$$f_0 \approx f_M\left(1 + \frac{m v_z u_z}{T}\right),$$

where the velocity in the z direction $u_z = -(c/4\pi)B_0/en_0L_s \ll v_{\mathrm{th},e}$ yields the equilibrium current that generates the equilibrium field $B_{0y} = xB_0/L_s$.

The linearized kinetic equation reads

$$\frac{\partial \tilde{f}}{\partial t} + \mathbf{v}\cdot\nabla\tilde{f} + C(\tilde{f}) = -\tilde{\mathbf{v}}\cdot\hat{\mathbf{x}}\frac{\partial f_0}{\partial x} + \frac{e}{m}\left(\tilde{\mathbf{E}} + \frac{\mathbf{v}\times\tilde{\mathbf{B}}}{c}\right)\cdot\frac{\partial f_0}{\partial \mathbf{v}} \tag{A.20}$$

with the collision operator $C = -(\nu/2)(\partial/\partial\mathbf{v})\cdot(v^2\mathbf{I} - \mathbf{vv})\cdot(\partial/\partial\mathbf{v})$. Assuming again the perturbation to vary as $\exp[i(k_y y - \omega t)]$ and considering the relation between the parallel and the y direction, the previous equation becomes finally

$$\begin{aligned}&-\left[i\left(\omega - k_\parallel v_\parallel\right) + \frac{\nu}{2}\frac{\partial}{\partial \mathbf{v}}\cdot\left(v^2\mathbf{I} - \mathbf{vv}\right)\frac{\partial}{\partial \mathbf{v}}\right]\tilde{f} = \\ &\frac{ik_y c}{TB}\left(\tilde{\phi} - \frac{v_\parallel}{c}\tilde{A}_\parallel\right)\left[\frac{\mathrm{d}n_0}{\mathrm{d}x}\frac{T}{n_0} + m(v_z - u_z)\frac{\mathrm{d}u_z}{\mathrm{d}x}\right]f_M - \left(v_\parallel\tilde{E}_\parallel - \tilde{E}_z u_z + \frac{ik_\parallel v_\parallel \tilde{A}_z}{c}u_z\right)\frac{ef_M}{T},\end{aligned} \tag{A.21}$$

where the temperature gradient has been neglected to facilitate the comparison with the fluid results presented in the last section. In $\tilde{E}_z$, the electrostatic term $ik_\parallel\tilde{\phi}$ can be neglected with respect to the last term of Eq. (A.21), so that the solution of in the collisionless regime $\nu \to 0$ can be immediately written as

$$\tilde{f} = \frac{-ie\tilde{E}_\parallel v_\parallel}{\omega - k_\parallel v_\parallel}\left(1 - \frac{\omega_*}{\omega}\right)\frac{f_M}{T} + \frac{\omega_*}{\omega}\frac{e\tilde{\phi}}{T}f_M - \frac{e\tilde{A}_z}{c}\,u_z\frac{f_M}{T}. \tag{A.22}$$

In this expression, a term $(k_\parallel v_\parallel/\omega)\tilde{\phi}$ has been added and subtracted and the diamagnetic frequency $\omega_* = k_y cT/eBL_n$ is defined as in Sec. A.2. In the inner layer, the equilibrium current is assumed to be nearly constant and the term proportional to $\mathrm{d}u_z/\mathrm{d}x$ is dropped. It is important for the determination of Δ' in the outer region, since it represents the contribution of the unperturbed current-density gradient to the current perturbation, as shown at the end of this section. The last two terms on the right-hand side of Eq. (A.22) do not contribute to the perturbed electron current in the inner layer, which is therefore

$$\tilde{J}_z = -e\int v_\parallel \tilde{f}\mathrm{d}^3\mathbf{v} = \frac{ie^2\tilde{E}_\parallel}{T}\left(\frac{\omega-\omega_*}{\omega}\right)\int_{-\infty}^{\infty}\frac{v_\parallel^2 f_M}{\omega - k_\parallel v_\parallel}\mathrm{d}^3\mathbf{v}.$$

The treatment of the singularity arising for parallel velocities matching the propagation velocity of the mode can be performed by following the prescription of Landau [150], who first showed that, at the resonance, a plasma wave can be damped or driven depending on whether there are more particles with slightly lower or slightly higher velocity than the phase velocity of the wave. The physics of Landau damping is described in several textbooks and is not discussed here. The resonant integral can be expressed in terms of the plasma dispersion function [151] $Z(\omega/k_\parallel v_{\mathrm{th},e})$ employing the relation $Z'(\zeta) = -2(1+\zeta Z(\zeta))$ as

$$\tilde{J}_z = \frac{i\omega_{pe}^2}{4\pi\omega}\left(\frac{\omega-\omega_*}{\omega}\right)\tilde{E}_\parallel\left(\frac{\omega}{k_\parallel v_{\mathrm{th},e}}\right)^2 Z'\left(\frac{\omega}{k_\parallel v_{\mathrm{th},e}}\right).$$

As we know from Sec. A.1, in the collisionless regime we can neglect the contribution of $\tilde{\phi}$ to $\tilde{E}_\parallel$ and write $\tilde{E}_\parallel = i\omega\tilde{A}_\parallel/c$. Inserting the previous expression for $\tilde{J}_z$ in Eq. (A.19) and integrating across the inner layer, a dispersion relation similar to Eq. (A.17) is obtained:

$$\frac{c^2}{\omega_{pe}^2}\left.\frac{\partial\tilde{A}_\parallel}{\partial x}\right|_{-\Delta}^{\Delta} = \tilde{A}_\parallel(0)\frac{\omega-\omega_*}{\omega}\int_{-\Delta}^{\Delta}\left(\frac{\omega}{k_\parallel v_{\mathrm{th},e}}\right)^2 Z'\left(\frac{\omega}{k_\parallel v_{\mathrm{th},e}}\right)\mathrm{d}x. \tag{A.23}$$

The integral on the right-hand side yields $-2i\sqrt{\pi}\omega L_s/k_y v_{\mathrm{th},e}$, so that separating real and imaginary part we have $\omega = \omega_*$ and $\gamma = \Delta' k_y v_{\mathrm{th},e}/2\sqrt{\pi}k_0^2 L_s$, confirming the validity of the results presented in the previous section.

As mentioned before, the gradient of the equilibrium current profile is accounted for by the term containing $\mathrm{d}u_z/\mathrm{d}x$ in Eq. (A.21). As known from Sec. 2.2, this term represents the source of free energy which can lead to an instability and is fundamental to determine the stability parameter Δ' in the outer region from $\nabla_\parallel J_\parallel = 0$, see Eq. (2.14). Indeed, the outer domain is defined as the region where the electric field perturbation $\tilde{E}_z$ caused by the growing mode is shorted out, $\omega \ll k_\parallel v_\parallel$. If we neglect ω in the resonant denominator and include the $\mathrm{d}u_z/\mathrm{d}x$ term in $\tilde{f}$, Eq. (A.22), we see that this actually is the only term leading to a current perturbation in this limit,

$$\tilde{J}_z = -e\int v_\parallel \tilde{f}\mathrm{d}^3\mathbf{v} = -\frac{\tilde{B}_x}{ik_y B_{0y}}\frac{\partial J_{0z}}{\partial x}, \tag{A.24}$$

where in the last step we wrote $k_y/k_\parallel = B_0/B_{0y}$ and $\tilde{A}_z = \tilde{B}_x/ik_y$. The current given by Eq. (A.24) satisfies Eq. (2.14).

Appendix B

Useful identities

$$\mathbf{a}\cdot(\mathbf{b}\times\mathbf{c}) = \mathbf{b}\cdot(\mathbf{c}\times\mathbf{a}) = \mathbf{c}\cdot(\mathbf{a}\times\mathbf{b}) \tag{B.1}$$

$$\mathbf{a}\times(\mathbf{b}\times\mathbf{c}) = (\mathbf{a}\cdot\mathbf{c})\mathbf{b} - (\mathbf{a}\cdot\mathbf{b})\mathbf{c} \tag{B.2}$$

$$(\mathbf{a}\times\mathbf{b})\cdot(\mathbf{c}\times\mathbf{d}) = (\mathbf{a}\cdot\mathbf{c})(\mathbf{b}\cdot\mathbf{d}) - (\mathbf{a}\cdot\mathbf{d})(\mathbf{b}\cdot\mathbf{c}) \tag{B.3}$$

$$\nabla\cdot(f\mathbf{a}) = f\nabla\cdot\mathbf{a} + \mathbf{a}\cdot\nabla f \tag{B.4}$$

$$\nabla\times(f\mathbf{a}) = f\nabla\times\mathbf{a} + \nabla f\times\mathbf{a} \tag{B.5}$$

$$\nabla\cdot(\mathbf{a}\times\mathbf{b}) = \mathbf{b}\cdot\nabla\times\mathbf{a} - \mathbf{a}\cdot\nabla\times\mathbf{b} \tag{B.6}$$

$$\mathbf{a}\times(\nabla\times\mathbf{b}) = (\nabla\mathbf{b})\cdot\mathbf{a} - (\mathbf{a}\cdot\nabla)\mathbf{b} \tag{B.7}$$

$$\nabla(\mathbf{a}\cdot\mathbf{b}) = \mathbf{a}\times(\nabla\times\mathbf{b}) + (\mathbf{a}\cdot\nabla)\mathbf{b} + \mathbf{b}\times(\nabla\times\mathbf{a}) + (\mathbf{b}\cdot\nabla)\mathbf{a} \tag{B.8}$$

$$\nabla\times(\mathbf{a}\times\mathbf{b}) = \mathbf{a}(\nabla\cdot\mathbf{b}) - \mathbf{b}(\nabla\cdot\mathbf{a}) - (\mathbf{a}\cdot\nabla)\mathbf{b} + (\mathbf{b}\cdot\nabla)\mathbf{a} \tag{B.9}$$

$$\nabla\times(\nabla\times\mathbf{a}) = \nabla(\nabla\cdot\mathbf{a}) - \nabla^2\mathbf{a} \tag{B.10}$$

$$\nabla\times(\nabla f) = 0 \tag{B.11}$$

$$\nabla\cdot(\nabla\times\mathbf{a}) = 0 \tag{B.12}$$

Appendix C

Selected papers

1. E. Poli, A. G. Peeters, G. V. Pereverzev, *TORBEAM, a Beam Tracing code for Electron Cyclotron waves in tokamak plasmas*, Computer Physics Communication **136**, 90 (2001).

2. E. Poli, A. G. Peeters, A. Bergmann, S. Günter, S. D. Pinches, *Reduction of the ion drive and ρ^*_θ scaling of the neoclassical tearing mode*, Physical Review Letters **88**, 075001 (2002).

3. E. Poli, A. G. Peeters, A. Bergmann, S. Günter, S. D. Pinches, *Monte Carlo δf simulation of the bootstrap current in the presence of a magnetic island*, Plasma Physics and Controlled Fusion **45**, 71 (2003).

4. E. Poli, A. Bergmann, A. G. Peeters, *The role of kinetic effects on the polarisation current around a magnetic island*, Physical Review Letters **94**, 205001 (2005).

5. E. Poli, A. Bergmann, A. G. Peeters, L. Appel, S. D. Pinches, *Kinetic calculation of the polarization current in the presence of a neoclassical tearing mode*, Nuclear Fusion **45**, 384 (2005).

6. G. Ramponi, D. Farina, M. A. Henderson, E. Poli, G. Saibene, O. Sauter, H. Zohm, C. Zucca, *Physics analysis of the ITER ECW system for an optimized performance*, Nuclear Fusion **48**, 054012 (2008).

7. M. Siccinio, E. Poli, *Kinetic Effects on Slowly Rotating Magnetic Islands in Tokamaks*, Plasma Physics and Controlled Fusion **51**, 075005 (2009).

8. E. Poli, A. Bottino, A. G. Peeters, *Behaviour of turbulent transport in the vicinity of a magnetic island*, Nuclear Fusion **49**, 075010 (2009).

9. A. Bergmann, E. Poli, A. G. Peeters, *The bootstrap current in small rotating magnetic islands*, Physics of Plasmas **16**, 092507 (2009).

10. E. Poli, A. Bottino, W. A. Hornsby, A. G. Peeters, T. Ribeiro, B. D. Scott, M. Siccinio, *Gyrokinetic and gyrofluid investigation of magnetic islands in tokamaks*, Plasma Physics and Controlled Fusion **52**, 124021 (2010).

Computer Physics Communications 136 (2001) 90–104

Computer Physics
Communications

www.elsevier.nl/locate/cpc

TORBEAM, a beam tracing code for electron-cyclotron waves in tokamak plasmas

E. Poli [*], A.G. Peeters, G.V. Pereverzev

Max-Planck-Institut für Plasmaphysik, Boltzmannstrasse 2, D-85748 Garching bei München, Germany

Received 31 July 2000; accepted 22 December 2000

Abstract

The beam tracing technique is used to describe the propagation and absorption of Gaussian wave beams with frequencies in the electron-cyclotron frequency range in a fusion plasma. Like in the standard ray tracing method, Maxwell's equations are reduced to a set of first-order ordinary differential equation. The technique employed here, however, allows for diffraction effects, neglected by the geometrical-optics procedure. The beam is specified in terms of the trajectory of the beam axis, the evolution of both the curvature of the wave front and the width of the field profile, as well as the absorption of the wave energy by the plasma. A Fortran code is presented, which solves the beam tracing equations in a tokamak geometry for arbitrary launching conditions and for both analytic and experimentally prescribed magnetic equilibria. Examples of wave propagation, power deposition and current profiles are computed and compared with ray tracing results. © 2001 Elsevier Science B.V. All rights reserved.

1. Introduction

Electromagnetic wave beams in the frequency range of the electron-cyclotron (EC) resonance play an important role in the physics of fusion devices. They are employed for heating and current drive, as well as for diagnostic purposes. From a theoretical viewpoint, the most known and widespread technique used to perform calculations concerning propagation and absorption of EC waves is surely the geometrical optics (GO) approach [1–3]. This technique is applied whenever the radiation wavelength λ is much smaller than the inhomogeneity scale of the medium L, i.e. whenever it is possible to introduce a parameter μ, such that

$$\mu \equiv \frac{\omega L}{c} \gg 1, \tag{1}$$

where $\omega/2\pi$ is the wave frequency and c is the speed of light. This condition is usually well satisfied for the case of EC waves in tokamak plasmas. GO reduces Maxwell's equations to a set of first-order ordinary differential equations, thus greatly simplifying the solution of the problem, since it gives a simple and intuitive picture of wave propagation (in terms of rays) and allows a straightforward numerical implementation.

---

[*] Corresponding author.
E-mail address: emp@ipp.mpg.de (E. Poli).

PII: S0010-4655(01)00146-1

Unfortunately, the lowest-order GO equations do not retain typical wave effects, such as interference and diffraction. In fact, Eq. (1) is only a necessary condition for applicability of the ray method [4], but not a sufficient one. For instance, it can be shown that in a homogeneous medium the effects of diffraction can not be neglected if $W^2 \leqslant \lambda\ell$, where W is the width of the beam and ℓ is the length of the propagation path. Hence, diffraction becomes important if ℓ is sufficiently large. Moreover, if one takes $\ell \approx L$ (inhomogeneous medium), diffraction effects are significant for $W \approx \sqrt{\lambda L}$, i.e. for

$$\frac{W}{L} \approx \frac{1}{\sqrt{\mu}}. \tag{2}$$

Several methods, such as the parabolic equation [5–8] or the complex-eikonal method [9–12], have been proposed in order to solve Maxwell's equations taking advantage from condition (1) without neglecting diffraction. However, they require the solution of a set of *partial* differential equations, thus losing one of the most attractive features of GO.

In the beam tracing (BT) approach [13], on the contrary, a set of *ordinary* differential equations is obtained. These equations give the evolution of the axis of the beam and of a set of parameters connected with the curvature of the phase front and with the amplitude profile. In the code which is presented here, the BT method is applied to the significant case of a beam with a Gaussian amplitude profile, or shortly a Gaussian beam. The code allows the user to calculate the propagation of the beam in a tokamak plasma, as well as the power transferred to the plasma and the current driven by the wave. It has been shown [11,14,15] that the diffractive broadening of the beam can lead to significant deviations in the absorption profiles with respect to standard GO calculations. One of the most attractive features of EC waves is given by the possibility of producing highly collimated beams. A proper estimation of the profile of power absorption is therefore important in all those applications where a strong localization of power deposition is desirable.

In this paper, Section 2 is devoted to a brief discussion of the basic equations of the BT technique. The features of the numerical approach adopted to solve these equations are presented in Section 3. Details about the physics involved in the numerical solution are given in Sections 4, 5: in Section 4, the toroidal geometry and the plasma equilibrium which characterize a tokamak experiment are elucidated, whilst the beam description is analyzed in Section 5. The numerical results of typical test-runs are given in Section 6 and compared with the corresponding results of GO. Conclusions are summarized in Section 7.

2. Beam tracing method

2.1. Beam tracing equations

In the BT approach, a solution to the wave equation for the electric field **E**

$$\frac{c^2}{\omega^2}\nabla \times (\nabla \times \mathbf{E}) - \boldsymbol{\varepsilon} \cdot \mathbf{E} = 0 \tag{3}$$

(where $\boldsymbol{\varepsilon}$ is the dielectric tensor) is sought in the form

$$\mathbf{E}(\mathbf{r}) = A(\mathbf{r})\mathbf{e}(\mathbf{r})\mathrm{e}^{\mathrm{i}\mu(s(\mathbf{r})+\mathrm{i}\phi(\mathbf{r}))}, \tag{4}$$

where A is the amplitude and **e** the unit polarization vector. The phase of the wave $\bar{s}(\mathbf{r}) \equiv s(\mathbf{r}) + \mathrm{i}\phi(\mathbf{r})$ includes a real part, which has the same meaning as in usual GO, and an imaginary part connected with the description of the Gaussian field profile, or, in other words, with the transverse (with respect to the propagation direction) structure of the beam. The function $\phi(\mathbf{r}) \geqslant 0$, therefore, is not connected with the damping of the wave due to absorption.

As in GO, the short-wavelength limit condition (1) is supposed to hold. In addition, it is assumed that the beam width is ordered such that $\lambda \ll W \ll L$ (this is the case in a typical experimental set-up). It is recalled [cf. Eq. (2)]

that diffraction effects become significant just in this limit. Physically, it is supposed that the field amplitude $|\mathbf{E}|$ varies faster across the propagation direction (due to its Gaussian shape) than along it (due to refraction and absorption). This assumption, which is made also in the approach of parabolic equation, is exploited to simplify the quasi-optical equations [13,16] by means of a *paraxial* expansion of the wave field around the beam axis. This amounts to performing an expansion of the amplitude profile into Gaussian modes. The lowest-order term in such an expansion gives a purely Gaussian beam, which is therefore called also “Gaussian beam of the lowest order”. Because of its practical interest, only this case is considered here. It has been shown [12] that within the ordering assumed here, a Gaussian beam maintains its shape during the propagation.

From the previous discussion, it follows that the complex phase of the wave field in Eq. (4) can be expanded around the beam axis in the following way (summation over repeated indices is adopted):

$$s(\mathbf{r}) = s_0(\mathbf{r}) + K_\alpha[x_\alpha - q_\alpha] + \tfrac{1}{2}s_{\alpha\beta}[x_\alpha - q_\alpha][x_\beta - q_\beta], \tag{5}$$

$$\phi(\mathbf{r}) = \tfrac{1}{2}\phi_{\alpha\beta}[x_\alpha - q_\alpha][x_\beta - q_\beta], \tag{6}$$

where q_α and K_α are, respectively, the components of the position vector $\{x_\alpha\} \equiv \mathbf{r}$ and the wave vector $\{k_\alpha\} \equiv \nabla s$, calculated on the beam axis. The second-order coefficients $s_{\alpha\beta}$ describe the change of the wave vector along the wave front and are hence related to its curvature. The coefficients $\phi_{\alpha\beta}$ appear in the real part of the exponential factor $\exp(\mathrm{i}\mu\bar{s})$ and are then connected with the width of the amplitude profile. Their meaning is further discussed in Section 5. The quantities $q_\alpha,\ K_\alpha,\ s_{\alpha\beta}$ and $\phi_{\alpha\beta}$ are found as the solutions of the following set of *ordinary* differential equations (beam tracing equations) [13]:

$$\frac{\mathrm{d}q_\alpha}{\mathrm{d}\tau} = \frac{\partial H}{\partial k_\alpha}, \qquad \frac{\mathrm{d}K_\alpha}{\mathrm{d}\tau} = -\frac{\partial H}{\partial x_\alpha}, \tag{7}$$

$$\frac{\mathrm{d}s_{\alpha\beta}}{\mathrm{d}\tau} = -\frac{\partial^2 H}{\partial x_\alpha \partial x_\beta} - \frac{\partial^2 H}{\partial x_\beta \partial k_\gamma}s_{\alpha\gamma} - \frac{\partial^2 H}{\partial x_\alpha \partial k_\gamma}s_{\beta\gamma} - \frac{\partial^2 H}{\partial k_\gamma \partial k_\delta}s_{\alpha\gamma}s_{\beta\delta} + \frac{\partial^2 H}{\partial k_\gamma \partial k_\delta}\phi_{\alpha\gamma}\phi_{\beta\delta}, \tag{8}$$

$$\frac{\mathrm{d}\phi_{\alpha\beta}}{\mathrm{d}\tau} = -\left(\frac{\partial^2 H}{\partial x_\alpha \partial k_\gamma} + \frac{\partial^2 H}{\partial k_\gamma \partial k_\delta}s_{\alpha\delta}\right)\phi_{\beta\gamma} - \left(\frac{\partial^2 H}{\partial x_\beta \partial k_\gamma} + \frac{\partial^2 H}{\partial k_\gamma \partial k_\delta}s_{\beta\delta}\right)\phi_{\alpha\gamma}, \tag{9}$$

where

$$H \equiv \det\!\left[(c/\omega)^2(-k^2\mathbf{I} + \mathbf{k}\mathbf{k}) + \boldsymbol{\varepsilon}^h\right] = 0 \tag{10}$$

is the dispersion function of GO and like in the ray tracing method it is assumed that the anti-Hermitian part of the dielectric tensor is much smaller than the Hermitian part, so that H is real. All the derivatives of H on the right-hand sides of Eqs. (7)–(9) are to be calculated on the beam axis, the evolution of which is given by the first two Eqs. (7). Since these equations are nothing but the ray equations of standard GO, it results that the maximum of the wave field propagates like in GO. The ray given by Eqs. (7) is called the central or reference ray and is denoted by $\Re$.

According to the paraxial expansion, the damping of the wave is calculated on the reference ray only by means of the equation

$$\frac{\mathrm{d}|A|^2}{\mathrm{d}\tau} = -(\nabla \cdot \mathbf{V} + 2\gamma)|A|^2, \tag{11}$$

where $\mathbf{V} \equiv \partial H/\partial \mathbf{k}$ and $\gamma \equiv \mathbf{e}^* \cdot \boldsymbol{\varepsilon}^a \cdot \mathbf{e}$ is the absorption coefficient.

It should be finally remarked that the elements of the matrices $\{s_{\alpha\beta}\}$ and $\{\phi_{\alpha\beta}\}$ are not independent: the symmetry of the two matrices and the six constraints

$$s_{\alpha\beta}V_\beta + \frac{\partial H}{\partial x_\alpha} = 0, \tag{12}$$

$$\phi_{\alpha\beta}V_\beta = 0 \tag{13}$$

must be taken into account.

Due to the symmetry of $\{s_{\alpha\beta}\}$ and $\{\phi_{\alpha\beta}\}$, the number of equations to be solved is 6 [central ray, Eqs. (7)] + $(6+6)[\{s_{\alpha\beta}\}$ and $\{\phi_{\alpha\beta}\}$, Eqs. (8), (9)] + 1[wave amplitude A, Eq. (11)] = 19. The condition $H = 0$ (which in the BT approach holds on $\Re$ only) and the constraints (12), (13) are used here to prescribe consistent initial conditions for the beam parameters, and during the run as a check of solution accuracy. It can be noticed that, in contrast to standard GO, where $7 \times n_r$ (n_r is the number of rays traced) equations are to be solved, here $18 + n_b$ (n_b is the number Gaussian modes; in this paper, $n_b = 1$) equations are considered, showing that the BT method can be even faster than the ray tracing approach.

2.2. Dispersion function

A fundamental role in Eqs. (7)–(11) is obviously played by the dispersion function H defined by Eq. (10). Adopting the usual choice of the cold-plasma dielectric tensor $\boldsymbol{\varepsilon}^h$ [17], H can be readily calculated

$$H = \mathcal{S}N_\perp^4 + \left[\mathcal{D}^2 - \mathcal{P}\mathcal{S} - \mathcal{S}^2 + (\mathcal{P}+\mathcal{S})N_\parallel^2\right]N_\perp^2 + \mathcal{P}N_\parallel^4 - 2\mathcal{P}\mathcal{S}N_\parallel^2 + (\mathcal{S}^2 - \mathcal{D}^2)\mathcal{P}, \tag{14}$$

where

$$\mathcal{S} \equiv 1 - \frac{\omega_p^2/\omega^2}{1-\omega_c^2/\omega^2},$$
$$\mathcal{D} \equiv -\frac{\omega_c}{\omega}\frac{\omega_p^2/\omega^2}{1-\omega_c^2/\omega^2},$$
$$\mathcal{P} \equiv 1 - \frac{\omega_p^2}{\omega^2}$$

have been introduced and

$$\omega_p(\mathbf{r}) \equiv \sqrt{\frac{4\pi n(\mathbf{r})\mathrm{e}^2}{m}},$$
$$\omega_c(\mathbf{r}) \equiv \frac{eB(\mathbf{r})}{mc}$$

are the electron plasma frequency and the electron cyclotron frequency, respectively (n is the electron density, e the absolute value of the electron charge and m the electron mass). $N_\parallel$ is the component of $\mathbf{N} \equiv c\mathbf{k}/\omega$ parallel to the confinement magnetic field $\mathbf{B}$ (i.e. $N_\parallel = \mathbf{N}\cdot\mathbf{B}/B$) and $N_\perp^2 = N^2 - N_\parallel^2$. In order to avoid singularities at $\omega = \omega_c$, the dispersion function H adopted in the code is actually given by Eq. (14) multiplied by $1 - \omega_c^2/\omega^2$.

It should be remarked that no mode selection is operated in Eq. (14); with this choice, the derivatives of H can be calculated in a simpler way. The mode of the propagating wave is selected by imposing initial conditions that satisfy the dispersion equation $H_M = 0$ for the required mode M at the starting point and controlling the condition $H_M = 0$ to be then fulfilled along the whole propagation path.

3. The numerical approach

As mentioned in the introduction, the BT method is applied here to the fusion-relevant problem of propagation of EC waves in a tokamak configuration. The code presented here has therefore been called TORBEAM, since it solves the BEAM tracing equations in a TORoidally symmetric geometry. The numerical solution of the problem, however, has been performed in such a way that the user should be able to adapt the code to a different frequency range (e.g., lower hybrid waves) or to a different geometry (e.g., stellarator) in a straightforward way. To achieve this, the choice of a laboratory (fixed) Cartesian coordinate system is the most natural starting point. The connection between this system and a curvilinear coordinate system suggested by the specific nature of the problem (e.g., a set of toroidal coordinates for a tokamak geometry) is provided by separate routines. The beam tracing Eqs. (7)–(11) are therefore written in this fixed reference frame. Other important features of the numerical approach outlined here are:

- the plasma equilibrium can be prescribed both analytically and by means of experimental data (cf. Section 4);
- arbitrary initial conditions for the wave beam can be assigned and the beam can be followed in its vacuum-plasma crossing (cf. Section 5);
- power-deposition and current-drive profiles can be obtained with allowance for the diffractive broadening of the beam (cf. Section 6).

The code structure is described below. The programming language used is Fortran 77. It is to be remarked once again that the BT Eqs. (7)–(11) are a set of *ordinary* differential equations, which can be integrated by means of a standard Ordinary-Differential-Equations (ODE) solver. The main task of the code is then to supply the coefficients that appear in the equations, i.e. the first- and second-order derivatives of the dispersion function H and the absorption coefficient γ.

- The `MAIN` part of the code calls for the input data and the initial conditions for the 19 BT equations, then for the ODE solver; the results of the integration are given as output, along with absorption and current profiles (the current-drive efficiency is calculated by the subroutine `CURBA`, see below);

Initialization routines

- subroutine `INPUT` reads the input provided by the user, which involves the beam parameters as well as the plasma parameters for the case of analytic magnetic equilibrium (cf. Section 6); the experimental equilibrium is loaded by means of
- subroutine `GRID`; it reads the input data files providing the magnetic configuration of the system and density and temperature profiles (see Section 4); the derivatives of the relevant quantities are calculated by finite differences on this grid; the minimization routine `POWELL` is used to find the position of the magnetic axis, if needed;
- subroutine `INIT` returns the initial conditions for the unknown functions in Eqs. (7)–(11) satisfying the constraints (12), (13) and $H = 0$;

Core routines

- the beam tracing equations are written (Cartesian coordinates) in subroutine `EQS`; the routine is called directly by the ODE solver and calls in turn the routines `DERVAC, DERIV`;
- subroutines `DERVAC, DERIV` provide the derivatives of H (Cartesian coordinates) and the absorption coefficient in vacuum and in the plasma, respectively; on the vacuum-plasma boundary the initial conditions are re-calculated in subroutine `INTERF`;
- subroutine `OCOP` gives ω_c^2/ω^2 and ω_p^2/ω^2 and their derivatives with respect to the Cartesian reference frame; this is obtained by calling the subroutines `INVER, INVDER, MAGDER, DENDER` for the case of analytic equilibrium and the subroutine `OCPEXP` for the case of experimental equilibrium;
- subroutines `ROT, NBIG, NPAR, NPERP` calculate the components of $N_\parallel^2$, $N_\perp^2$ and their derivatives (Cartesian coordinates);

Geometry-dependent routines

- subroutine `ELTEMP` supplies the electron temperature needed by the absorption routine `DAMPBQ`;
- the numerical inversion from the Cartesian to the toroidal coordinates (cf. Section 4) is performed by subroutines `INVER, INVDER` (analytic equilibrium);
- the magnetic-field profile and the density profile, along with their derivatives, are expressed in term of the toroidal coordinates in subroutines `MAGDER, DENDER` (analytic equilibrium); in case of experimental equilibrium, they are provided by

- subroutine `OCPEXP`; it is remarked that for the case of a magnetic equilibrium prescribed by experimental data it is always possible to prescribe density and temperature profiles analytically;

Interpolation routines (experimental equilibrium)

the subroutines `IJOUT, INTPSI, INTPB, INTDAB, INTPOP, INTPTE` provide the polynomial interpolation of the various quantities loaded in `GRID` by calling

- `POLIN2, POLINT, POLCOF, DDPOLY` [18];

Auxiliary routines

- the subroutine `COEF` computes coefficients needed in the `MAIN` for current-drive calculations;
- subroutine `ELLPSE` calculates the amplitude profile of the beam;
- subroutine `PLPNTS` gives the points to be stored in a file for plotting purposes;
- subroutine `CARTES` performs the numerical transformation from poloidal to Cartesian coordinates (experimental equilibrium);
- `POWELL` [18] is a minimization routine; it calls `LINMIN, NMBRAK`;
- `GETDLP, IFBAUG` are routines used for the application of the code at ASDEX Upgrade to load experimental data files;

Absorption and current drive routines

- `DAMPBQ` (by Westerhof [19]) employs the weakly relativistic approximation for the dielectric tensor and gives the imaginary part of the wave vector k'' as output [cf. Eq. (15)];
- `CURBA` (by Cohen [20]) calculates the current drive efficiency η [defined in Eq. (16)] including effects of trapped particles, as well as ion-electron collisions and poloidal variation of the collision operator;

ODE solver

the routine employed here is `LSODE` (by Hindmarsh [21]).

It can be seen that the core of the code, which is written in Cartesian coordinates, is geometry-independent. The properties of the system that depend on the geometry are connected with the core by means of the interfacing routines called by subroutine `OCOP`.

As a concluding remark, it is mentioned that instead of Eq. (11), which gives $|A|^2 \propto U$, where U is the wave energy *density*, the evolution of the *total* wave power P is calculated by means of the equation

$$\frac{\mathrm{d}P}{\mathrm{d}\tau} = -2\mathbf{k}'' \cdot \mathbf{V}P, \tag{15}$$

which can be obtained from Eq. (11). The driven current is then obtained by means of the equation

$$I = \frac{\eta P}{2\pi \mathcal{R}_0}, \tag{16}$$

where $\mathcal{R}_0$ is the major radius of the torus (see Section 4), and η is provided by the subroutine `CURBA`.

4. Toroidal geometry

4.1. Analytic equilibrium

In the code, the fixed Cartesian coordinate system $\{x, y, z\}$ is chosen such that the vertical z-axis coincides with the axis of symmetry of the torus and the xy-plane with the equatorial plane. An analytic description of the magnetic equilibrium can be given in terms of a set of toroidal coordinates $\{\overline{x}_\alpha\} \equiv \{r, \chi, \varphi\}$ (where the minor radius

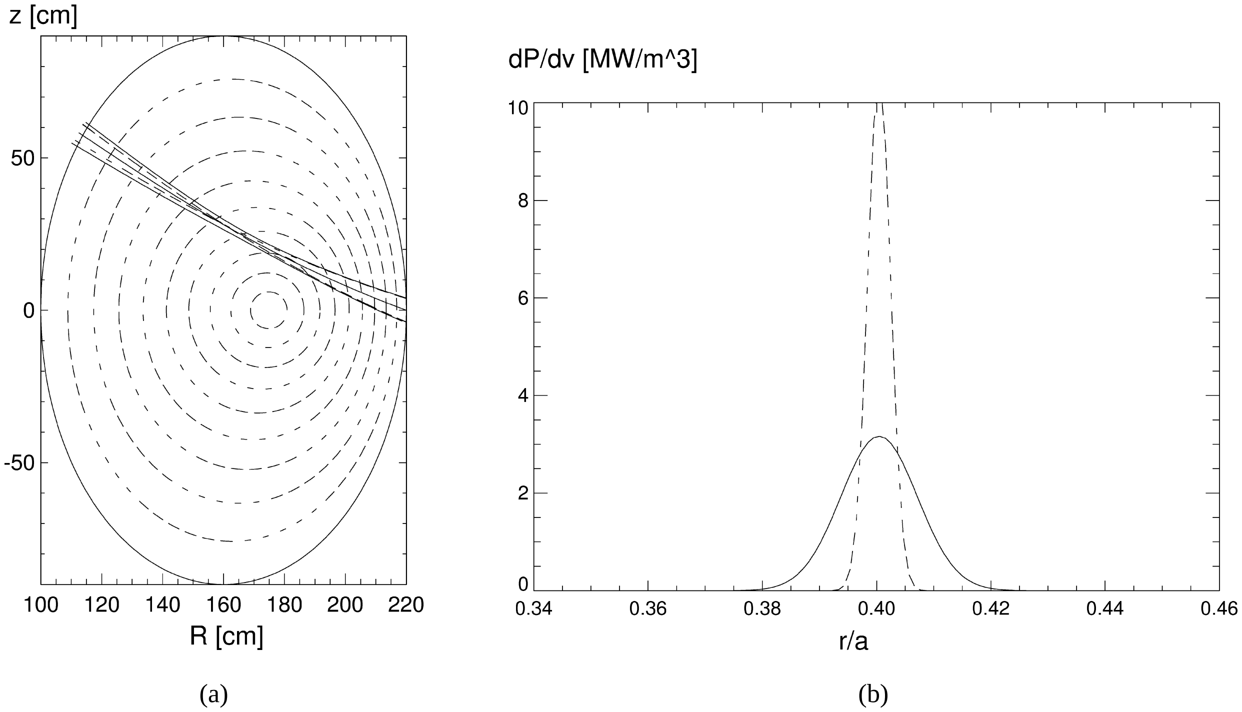

(a) (b)

Fig. 1. (a) Beam propagation (ASDEX Upgrade parameters) in the poloidal plane and (b) the corresponding power absorption profile (analytic equilibrium) in the GO approximation (dashed line) and in the BT approach (solid line).

r and the poloidal angle χ span the poloidal plane and the toroidal angle φ is a coordinate along the torus). Here, an elongated geometry with Shafranov shift [22] is considered, i.e. the Cartesian coordinates $\{x, y, z\}$ are linked to the toroidal coordinates by means of the relations

$$x = \big[\mathcal{R}_0 + r\cos\chi - \Delta(r)\big]\cos\varphi \equiv \mathcal{R}\cos\varphi, \tag{17}$$

$$y = \big[\mathcal{R}_0 + r\cos\chi - \Delta(r)\big]\sin\varphi \equiv \mathcal{R}\sin\varphi, \tag{18}$$

$$z = r\kappa(r)\sin\chi; \tag{19}$$

where $\mathcal{R}_0$ is the major radius, $\Delta(r)$ the Shafranov shift and $\kappa(r)$ the elongation. It is clearly $\mathcal{R}^2 = x^2 + y^2$. A typical tokamak configurations represented by Eqs. (17)–(19) is presented in Section 6 (Fig. 1).

Since, in general, $\omega_c, \omega_p, N_\parallel^2, N_\perp^2$ are given as functions of r, χ, φ, in order to calculate their derivatives with respect to $\{x, y, z\}$, one needs to compute the inverse Jacobian tensor

$$\{J^{-1}_{\alpha\beta}\} = \left\{\frac{\partial\overline{x}_\alpha}{\partial x_\beta}\right\} = \begin{pmatrix} \big[\kappa(r)\cos\chi\cos\varphi\big]/j & \big[\kappa(r)\cos\chi\sin\varphi\big]/j & \sin\chi/j \\ -\big[r\kappa(r)\big]'\sin\chi\cos\varphi/rj & -\big[r\kappa(r)\big]'\sin\chi\sin\varphi/rj & \big[\cos\chi - \Delta'(r)\big]/rj \\ -\sin\varphi/\mathcal{R} & \cos\varphi/\mathcal{R} & 0 \end{pmatrix},$$

where $j = j(r,\chi) \equiv \kappa(r)\cos\chi[\cos\chi - \Delta'(r)] + [r\kappa(r)]'\sin^2\chi$ and the prime $'$ denotes the derivative with respect to r. The second-order derivatives of the toroidal coordinates with respect to the Cartesian ones are also needed in the BT approach. They can be obtained by means of the formula

$$\frac{\partial^2\overline{x}_\alpha}{\partial x_\beta\partial x_\gamma} = \frac{\partial J^{-1}_{\alpha\beta}}{\partial x_\gamma} = \frac{\partial\overline{x}_\rho}{\partial x_\gamma}\frac{\partial J^{-1}_{\alpha\beta}}{\partial\overline{x}_\rho} = J^{-1}_{\rho\gamma}\frac{\partial J^{-1}_{\alpha\beta}}{\partial\overline{x}_\rho}.$$

In the previous expressions, the functions $r(x,y,z)$, $\chi(x,y,z)$, $\varphi(x,y,z)$ are calculated by numerical inversion.

The equilibrium magnetic field is the sum of a toroidal contribution $\mathbf{B}_t = B_t\mathbf{e}_\varphi$ and a poloidal contribution $\mathbf{B}_p = B_p\mathbf{e}_\chi$, with $\mathbf{e}_{\varphi,\chi} \equiv \partial\mathbf{r}/\partial(\varphi,\chi)/|\partial\mathbf{r}/\partial(\varphi,\chi)|$. The toroidal and poloidal components of the magnetic field are prescribed by specifying, besides the Shafranov shift $\Delta(r)$ and the elongation $\kappa(r)$, the value of the toroidal field B_{t0} on the geometrical axis of the torus and the profile of the safety factor $q(r)$. It can be shown [23] that for a toroidally symmetric device inside each magnetic surface it is $B_t\mathcal{R} = B_{tc}\mathcal{R}_c$ and $B_p\mathcal{R}/|\nabla r| = B_{pc}\mathcal{R}_c/|\nabla r|_c$, where the subscript c denotes the point on the surface corresponding to $\chi = \pi/2$. Introducing the inverse aspect ratio

$$\epsilon(r) \equiv \frac{r}{\mathcal{R}_c(r)} = \frac{r}{\mathcal{R}_0 - \Delta(r)},$$

the components of the magnetic field can finally be expressed as

$$B_t = \frac{\mathcal{R}_0}{\mathcal{R}} B_{t0} = \frac{B_{tc}(r)}{1+\epsilon\cos\chi},$$

$$B_p = \frac{rB_{tc}(r)}{\mathcal{R}_c(r)q(r)} \frac{[r\kappa(r)]'\sqrt{1+[\kappa^2(r)-1]\cos^2\chi}}{(1+\epsilon\cos\chi)\,j(r,\chi)}.$$

By further assigning the electron density profile (the density is supposed to be a function of the radial coordinate r)

$$n(r) = n_1\left[1-\left(\frac{r}{a}\right)^{e_1}\right]^{e_2} + n_2, \tag{20}$$

(where a is the minor radius) it is finally possible to calculate the first- and second-order derivatives of H required by the BT equations. The specification of the electron temperature $T_e(r)$ and the effective charge $Z_{\mathrm{eff}}(r) \equiv \sum_i n_i Z_i^2/n_e$ (where i runs over the ion species in the plasma) allows the calculation of the absorption coefficient and the current drive efficiency.

4.2. *Experimental equilibrium*

The magnetic configuration can be provided also numerically by assigning the (Cartesian) components of the static magnetic field $\mathbf{B}$ and a flux coordinate ψ on a grid in the poloidal plane (x,z). In the code, the magnetic field strength $B \equiv |\mathbf{B}|$ and the components of the unit vector $\mathbf{b} \equiv \mathbf{B}/B$ are needed in order to calculate the EC frequency ω_c and the parallel wave vector $N_\parallel$. Density and temperature can be also prescribed numerically; in this case they are tabulated as functions of ψ.

The first-order derivatives of the relevant functions are obtained for the case of equally spaced grid points by taking finite differences between neighboring points using the formula [24]

$$f' = \frac{1}{h}\left[\Delta f + \frac{1}{2}(2s-1)\Delta^2 f + \cdots + \frac{\mathrm{d}}{\mathrm{d}s}\binom{s}{n}\Delta^n f + \cdots\right], \tag{21}$$

where the limit $s \to 1$ is understood, h is the distance between neighboring grid points, $\Delta f \equiv f_{i+1} - f_i$, $\Delta^{k+1} f \equiv \Delta(\Delta^k f)$. For $n = 2$, Eq. (21) yields for instance

$$\left(\frac{\partial f}{\partial x}\right)_{i,j} = \frac{f_{i+1,j} - f_{i-1,j}}{x_{i+1} - x_{i-1}}, \qquad \left(\frac{\partial f}{\partial z}\right)_{i,j} = \frac{f_{i,j+1} - f_{i,j-1}}{z_{j+1} - z_{j-1}}. \tag{22}$$

The second-order derivatives are evaluated as

$$\left(\frac{\partial^2 f}{\partial x^2}\right)_{i,j} = \frac{f_{i+1,j} - 2f_{i,j} + f_{i-1,j}}{(x_{i+1} - x_i)^2}, \tag{23}$$

$$\left(\frac{\partial^2 f}{\partial x\partial z}\right)_{i,j} = \frac{f_{i+1,j+1} - f_{i-1,j+1} - f_{i+1,j-1} + f_{i-1,j-1}}{(x_{i+1} - x_{i-1})(z_{j+1} - z_{j-1})}, \tag{24}$$

$$\left(\frac{\partial^2 f}{\partial z^2}\right)_{i,j} = \frac{f_{i,j+1} - 2f_{i,j} + f_{i,j-1}}{(z_{j+1} - z_j)^2}. \tag{25}$$

If the grid points are not equally spaced (which is usually the case for the density profile), the derivatives are calculated as the average of “forward” and “backward” derivatives.

During a run, a subset of grid points close to current point $\mathbf{r}(\tau)$ is selected and the relevant quantities are found by polynomial interpolation (polynomial interpolation has been preferred to spline to avoid noise due to errors in the boundary conditions).

5. Beam description

In Section 2 it has been pointed out that a wave beam can be described in a 3D geometry by means of a set of parameters connected with the position of the beam axis, the curvature of the phase front and the amplitude profile [Eqs. (7)–(9)]. Wave damping is calculated on the reference ray by means of Eq. (15).

The physical content of Eqs. (7) is apparent, the unknown quantities $q_\alpha(\tau)$ and $K_\alpha(\tau)$ representing, respectively, the position of the beam axis and the wave vector on it, given as functions of the evolution parameter τ. In order to clarify the physical meaning of $s_{\alpha\beta}, \phi_{\alpha\beta}$ that appear in Eqs. (8), (9), it is useful to consider a Gaussian beam propagating *in vacuo* along the x-axis. Eqs. (12), (13) give immediately the constraints $s_{xx} = s_{xy} = s_{xz} = 0$ and $\phi_{xx} = \phi_{xy} = \phi_{xz} = 0$ (where $s_{xx} \equiv s_{11}$, $s_{xy} \equiv s_{12}$, etc.). As a first example, the case $s_{yz} = \phi_{yz} = 0$ can be discussed. From Eqs. (4)–(6) it results

$$\mathbf{E} \propto \exp\left\{ \mathrm{i}\mu \left[f(x) + \frac{1}{2}\bigl(s_{yy}(x)y^2 + s_{zz}(x)z^2\bigr)\right] - \frac{\mu}{2}\bigl[\phi_{yy}(x)y^2 + \phi_{zz}(x)z^2\bigr]\right\}, \tag{26}$$

where $f(x) \equiv s_0(x) + k_x x$ describes the behaviour of the wave phase along the propagation direction and has a physical meaning which is analogous to that of standard geometrical optics. The quadratic terms appearing on the right-hand side of Eq. (26) can be written in an even more transparent form by introducing the (principal) *radii of curvature* of the wave front R_α

$$s_{\alpha\alpha}(x) \equiv \frac{\omega/c}{R_\alpha(x)} \quad (\alpha = y, z;\ \text{no sum on } \alpha), \tag{27}$$

and the (principal) *beam widths* W_α

$$\phi_{\alpha\alpha}(x) \equiv \frac{2}{W_\alpha^2(x)} \quad (\alpha = y, z;\ \text{no sum on } \alpha). \tag{28}$$

It is now clear that the contour levels of the phase front and amplitude profile given by Eq. (26) are described by quadratic forms whose axes are aligned with the y- and z-axes of the laboratory system (in particular, since $\phi \geqslant 0$, the contour levels of $\phi_{\alpha\beta}x_\alpha x_\beta$ are ellipses). The case $s_{yz} \neq 0$ (or $\phi_{yz} \neq 0$) corresponds then to a rotation of the principal radii of curvature (or principal widths) with respect to the fixed reference frame [25].

In the general case of inhomogeneous media, the right-hand side of Eq. (12) is different from zero, and the connection between the phase-front curvature and the parameters $s_{\alpha\beta}$ becomes more complicated. On the contrary, the right-hand side of Eqs. (13) is always zero. Applying a rotation $\{x, y, z\} \to \{X, Y, Z\}$, where the X-axis, say, is parallel to $\mathbf{V}$, one obtains again $\phi_{XX} = \phi_{XY} = \phi_{XZ} = 0$; the physical meaning of $\phi_{YY}, \phi_{YZ}, \phi_{ZZ}$ is then the same as discussed above.

It has been already mentioned that the beam can be followed in its vacuum-plasma crossing. The initial conditions for the beam parameters are assigned in vacuo, where $s_{\alpha\beta}$ and $\phi_{\alpha\beta}$ are linked to the relevant physical quantities by means of Eqs. (27), (28). The beam propagates in vacuo till it reaches the boundary with the plasma (which is usually represented by a magnetic surface). The beam parameters inside the plasma are calculated by equating the phase of the wave on both sides of the boundary surface. This a tricky problem, because the constraints (12), (13) are to be satisfied. Nevertheless, the proper matching equations can be found [26]. They are used to re-assign the initial conditions for the unknown functions in Eqs. (7)–(11) inside the boundary surface.

The method adopted to compute absorption should finally be outlined. For each integration step i where absorption takes place, a corresponding "infinitesimal" absorption profile is calculated by assuming that it has a Gaussian shape. The maximum of this Gaussian curve is proportional to the power $\mathrm{d}P_i = P_i - P_{i-1}$ absorbed at that step and its width is given by the projection of the beam width onto the direction of ∇r. The actual absorption profile is calculated as a superposition of the infinitesimal absorption profiles (the current-drive profile is calculated in a parallel fashion). It is then clear that diffractive beam broadening can lead to a discrepancy between BT and GO profiles (cf. Section 6); on the other hand, if the propagation takes place mainly perpendicularly to the flux surface, this discrepancy is expected to be small.

6. Numerical examples

The validity of the numerical results obtained by means of the BT code has been investigated following three different criteria. First of all, the quantities $q_\alpha, K_\alpha, s_{\alpha\beta}, \phi_{\alpha\beta}$ obtained as the solution of Eqs. (7)–(9) must satisfy the dispersion equation $H = 0$ and the constraints (12), (13). In particular, $H = 0$ is a check on the integration accuracy of Eqs. (7) describing the reference ray $\Re$, whilst Eqs. (12), (13) involve also the second-order parameters in the wave phase (5), (6), and hence can be employed as a check on the integration accuracy of Eqs. (8), (9). This check is performed at each step during the run of the code; for the case of experimental equilibrium, it gives also an estimate of the accuracy of the interpolation procedure.

A second criterion which has been used to validate the code is the comparison with existing analytic solutions of the BT equations. Solutions of diffraction equations can be obtained for instance *in vacuo* and in an inhomogeneous (isotropic and anisotropic) medium with plane geometry [27]. The code can be adapted to such a geometry by simply taking the limit $\mathcal{R}_0 \to \infty$ and $\kappa(r) \to \infty$ in Eqs. (17)–(19).

Finally, the results of the code can be compared with the results obtained by means of a ray tracing code like TORAY [19,28] (see below).

Some numerical examples are now discussed. Typical running time for full absorption and current drive calculation with an experimental equilibrium is less than two minutes on a SUN Ultra 10.

The input parameters are specified by means of a namelist which is read by subroutine `INPUT`. They are

- `xrtol, xatol`: relative and absolute tolerance parameters for the ODE solver;
- `xstep`: integration step $\mathrm{d}\tau$;
- `ianexp`: switch between analytic and numerical equilibrium;
- `nni, nnj`: `nni` × `nnj` is the number of grid points;
- `nshot, xtbeg, xtend`: number of the shot to be analyzed and time parameters at which the (experimental) equilibrium is required;
- `nmod`: switch between ordinary and extraordinary mode;
- `nlnch`: selects the quantities to be plotted;
- `xf, xpw0`: wave frequency (Hz) and injected power (MW);
- `xthdeg, xphdeg`: poloidal and toroidal injection angles (degrees);
- `xxb, xyb, xzb`: coordinates of the launching point (cm);
- `xryyb, xrzzb, xwyyb, xwzzb`: initial principal radii of curvature and widths (cm) [see Eqs. (27), (28)];
- `xrmaj, xrmin`: major and minor radius of the tokamak (cm);
- `xb0, xdns, edgdns, xe1, xe2`: toroidal field on the geometrical axis (T), central and edge density (cm^{-3}), coefficients of the density profile (20) (analytic equilibrium);
- `xte0, xteedg`: central and edge electron temperature (analytic equilibrium).

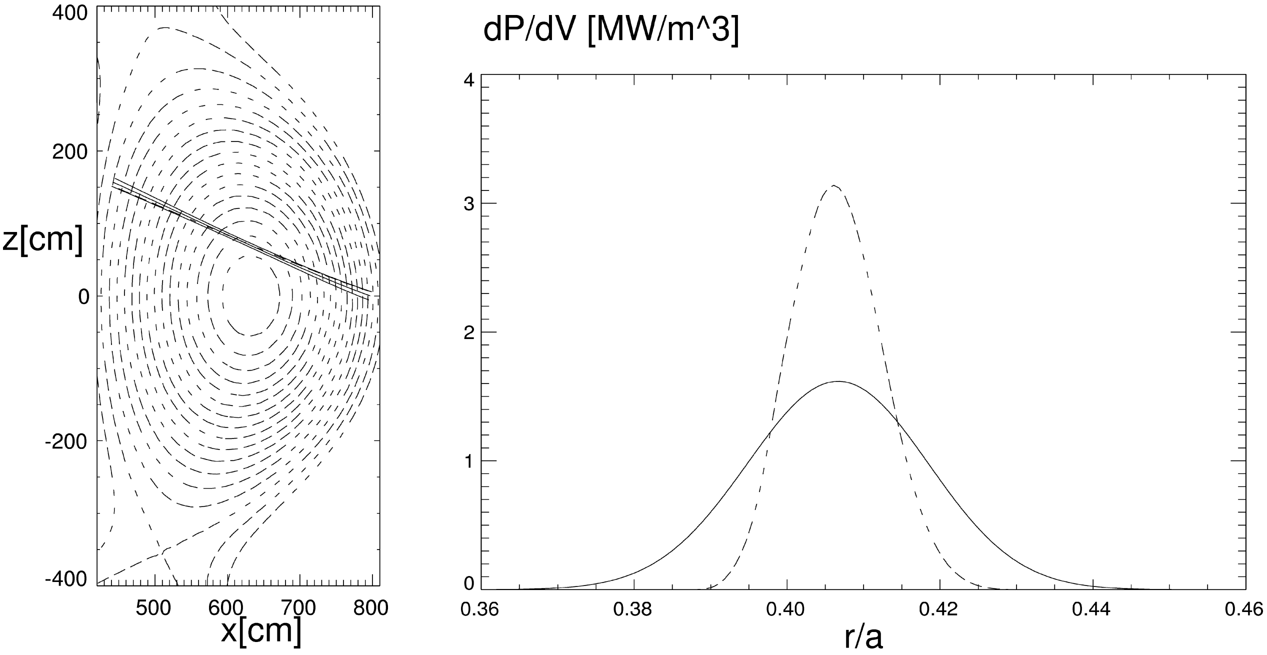

(a) (b)

Fig. 2. (a) Beam propagation (RTO/RC ITER) in the poloidal plane and (b) the corresponding power absorption profile (numerical equilibrium). Again, the dashed line corresponds to the GO calculation and the solid line to the BT calculation.

For the case of analytic equilibrium, the code also provides the functions $\Delta(r)$, $\kappa(r)$, $q(r)$ (and their derivatives) and $Z_{\text{eff}}(r)$ (cf. Section 4).

A first example obtained by running the code is shown in Fig. 1. Flux surfaces are calculated analytically as explained in Section 4 and are represented by dotted lines. The central electron density is $6 \cdot 10^{13}$ cm^{-3}, $1 \leqslant \kappa(r) \leqslant 1.5$, $-10 \leqslant \Delta(r) \leqslant 5$ cm and $1 \leqslant q(r) \leqslant 4$; $T_{\max} = 1$ keV. The wave frequency is $\omega/2\pi = 140$ GHz (which corresponds to the second EC harmonic for $B(\mathcal{R}_0) = 2.5$ T); the poloidal launching angle is 20° (the toroidal angle is zero), the initial width is 3.8 cm and the initial focusing is $1/R = 1/82$ cm. Beam and plasma parameters are in the range of interest at ASDEX Upgrade. The beam is described in the figure by means of its reference ray and its width in the plane of the plot. Dashed lines represent GO calculations, obtained by computing the central ray only (with the proper initial conditions) in two further runs. The corresponding absorption profiles are also displayed. The diffractive broadening of the beam is shown to have a significant effect on the deposition profile, since the beam is focused just in the absorption region around $\mathcal{R}_0 = 165$ cm.

In the next example, a grid in the poloidal plane supplies the magnetic configuration envisaged for the Intermediate Aspect Ratio RTO/RC ITER [29]. The major radius of IAM is $\mathcal{R}_0 = 6.20$ m, the minor radius $a = 1.90$ m, the magnetic field on the axis $B_0 = 5.51$ T. In Fig. 2, an example of propagation in the poloidal plane is shown. The beam is launched from the low-field side with a poloidal injection angle $\vartheta_0 = 20°$ (the toroidal injection angle is again zero). The wave frequency is $\omega/2\pi = 160$ GHz (first-harmonic O-mode heating is considered), the beam has an initial width $W = 6$ cm and a radius of curvature of the phase front $R = 250$ cm; the input power is 10 MW. Absorption occurs at $x \simeq 600$ cm. BT and GO calculations are again compared.

The last two figures refer to comparisons with the ray-tracing code TORAY. In these examples, only one ray, i.e. the central one, is calculated by TORAY ("one-ray" calculation; in other words, the transverse structure of the beam is neglected). The goal is to perform an easy check of the accuracy of the numerical procedure adopted in the BT code. The ray calculated by TORAY should coincide with the BT reference ray (which satisfies the same GO

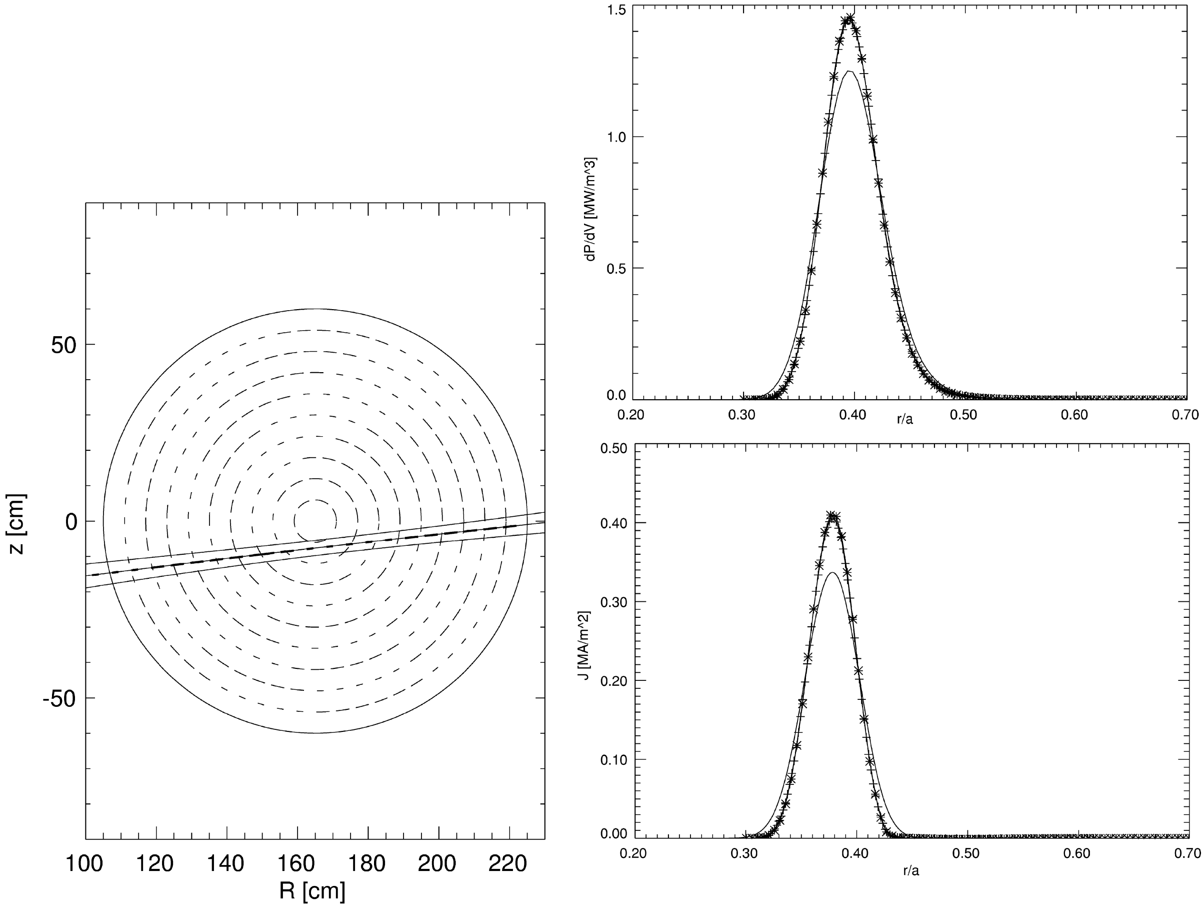

Fig. 3. Comparison with TORAY for the case of a circular equilibrium without Shafranov shift. Both power absorption and current density profiles are shown. Crosses refer to the result of TORBEAM, stars to those of TORAY.

equations). Moreover, also in the BT code absorption and current profiles can be calculated neglecting the finite width of the beam (“one-ray-like” procedure), and the results should then coincide again with those of TORAY. The plasma parameters are again in the range of interest of ASDEX Upgrade. The central density is $1.6 \cdot 10^{13}$ cm^{-3}, the magnetic field on the axis is 2.1 T and the central temperature is 2 keV. In Fig. 3, an analytic equilibrium with circular concentric flux surfaces has been considered. The BT reference ray is undistinguishable from the result of TORAY. The same feature is exhibited by the absorption and current-drive profiles, where the solid line represents the standard BT calculation (including finite beam width), the crosses give the result of the “one-ray-like” BT calculation and the stars reproduce the TORAY profiles. The figure shows a complete overlap of both “one-ray” curves. In Fig. 4, the same comparison is performed for the case of a magnetic equilibrium taken from a shot (#12257) of ASDEX Upgrade. The small discrepancy between both “one-ray” calculations of the current profile is seemingly due to the different interpolation procedures adopted in the two codes for the calculation of $\mathbf{B}$ and ω_p.

7. Conclusions

The Beam Tracing method is applied to the calculation of propagation and absorption of an electron cyclotron wave beam in a tokamak plasma. Like in standard geometrical optics, the beam is described by solving a set of

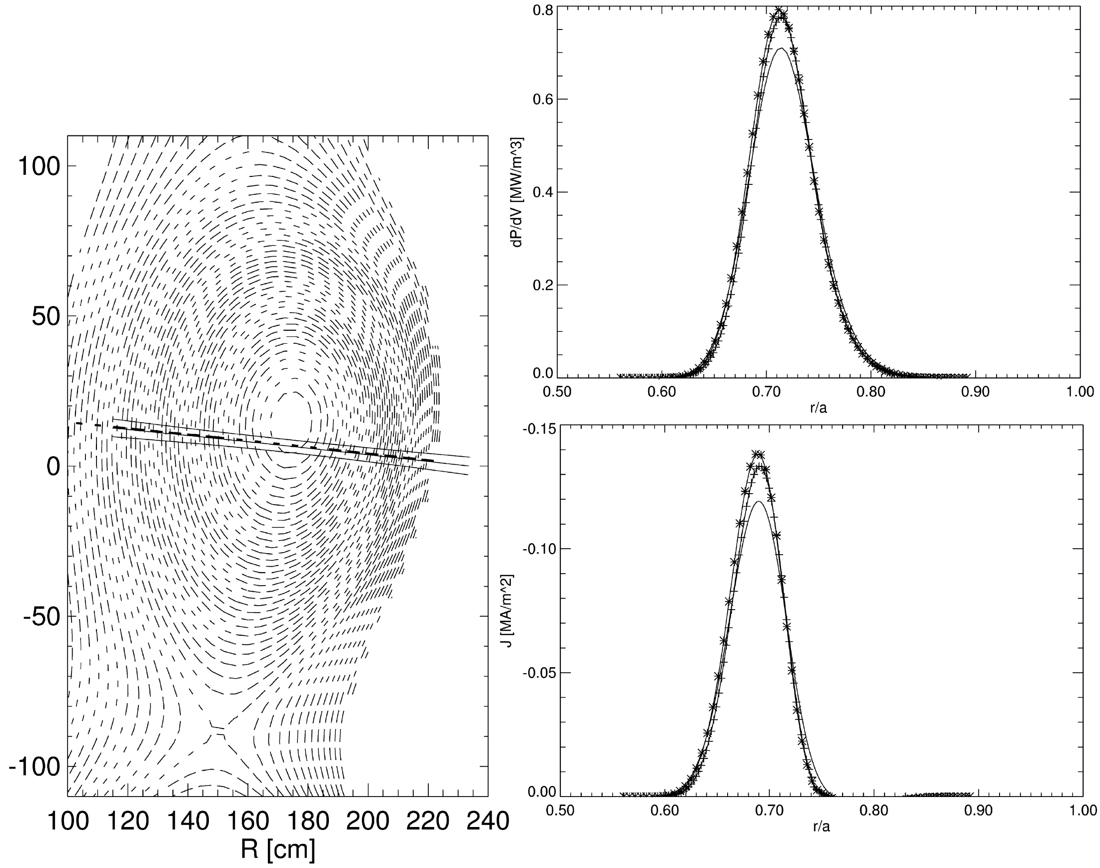

Fig. 4. Comparison with TORAY for the case of a typical ASDEX Upgrade magnetic equilibrium (cf. Fig. 3).

ordinary differential equations. The BT approach, however, allows for diffraction effects, neglected by the ray tracing procedure. The code TORBEAM presented here performs the integration of the BT equations for both analytic and experimental plasma equilibria and arbitrary launching conditions for the wave beam. The numerical implementation of the BT equations is straightforward and the solution is performed by using a standard ODE solver. Numerical examples show that diffractive broadening of the beam can change significantly the power deposition and current density profiles with respect to GO predictions.

References

[1] Yu.A. Kravtsov, Yu.I. Orlov, Geometrical Optics of Inhomogeneous Media, Springer Series on Wave Phenomena, Vol. 6, Springer, Berlin, 1990.

[2] I.B. Bernstein, Phys. Fluids 18 (1975) 320.

[3] U. Bellotti, M. Bornatici, F. Engelmann, Rivista del Nuovo Cimento 20 (5) (1997).

[4] Yu.A. Kravtsov, Yu.I. Orlov, Sov. Phys. Usp. 23 (1980) 750.

[5] V.A. Fock, Electromagnetic Diffraction and Propagation Problems, Pergamon, New York, 1965, p. 213.

[6] C.K. Phillips, F.W. Perkins, D.Q. Hwang, Phys. Fluids 29 (1986) 1608.

[7] V.M. Babič, V.S. Buldyrev, Short-Wavelength Diffraction Theory: Asymptotic Methods, Springer Series on Wave Phenomena, Vol. 4, Springer, Berlin, 1991.

[8] R.E. Aamodt, Phys. Plasmas 1 (1994) 6.

[9] S. Choudhary, L.B. Felsen, IEEE Trans. Antennas Propag. AP-21 (1973) 827.

[10] E. Mazzucato, Phys. Fluids B 1 (1989) 1855.

[11] S. Nowak, A. Orefice, Phys. Fluids B 5 (1993) 1945.

[12] A.G. Peeters, Phys. Plasmas 3 (1996) 4386.
[13] G.V. Pereverzev, Phys. Plasmas 5 (1998) 3529.
[14] E. Poli, A.G. Peeters, G.V. Pereverzev, M. Bornatici, in: Proc. 26th EPS Conference on Controlled Fusion and Plasma Physics, Maastricht, The Netherlands, June 14–18, 1999, Contributed Papers, Vol. 23J, European Physical Society, Geneva, 1999, p. 1553.
[15] E. Poli, G.V. Pereverzev, A.G. Peeters, M. Bornatici, in: Proc. 11th Joint Workshop on ECE and ECRH, Oarai, Japan, October 4–8, 1999, Invited Papers, Fus. Eng. Des. 53 (2000) 9.
[16] G.V. Pereverzev, Paraxial WKB solution of a scalar wave equation, B.B. Kadomtsev (Ed.), Rev. of Plasma Phys. 19 (1996) 1.
[17] T.H. Stix, Waves in Plasmas, American Institute of Physics, New York, 1992.
[18] W.H. Press et al., Numerical Recipes (Fortran Version), Cambridge University Press, Cambridge, 1989.
[19] E. Westerhof, Implementation of Toray at JET, Rijnhuizen Report RR-89-183, 1989.
[20] R.H. Cohen, Phys. Fluids 30 (1987) 2442.
[21] A.C. Hindmarsh, `LSODE` and `LSODI`, two new initial value ordinary differential equation solvers, ACM-Signum Newslett. 15 (4) (1980) 10.
[22] J. Wesson, Tokamaks, 2nd edn., Oxford University Press, Oxford, 1997.
[23] R.B. White, The Theory of Tokamak Plasmas, North-Holland, Amsterdam, 1989.
[24] See e.g., G.M. Phillips, P.J. Taylor, Theory and Applications of Numerical Analysis, 2nd edn., Academic Press, London, 1996.
[25] E. Poli, G.V. Pereverzev, A.G. Peeters, Phys. Plasmas 6 (1999) 5.
[26] E. Poli, A.G. Peeters, G.V. Pereverzev, Phys. Plasmas (2001), to appear.
[27] Some of these analytic solutions are discussed, e.g., in Ref. [15].
[28] A.H. Kritz, H. Hsuan, R.C. Goldfinger, D.B. Batchelor, in: C. Gormezano, G.G. Leotta, E. Sindoni (Eds.), Proc. 3rd International Symposium on Heating in Toroidal Plasmas, Varenna 1982, Vol. 2, EURATOM, Varenna, 1982, p. 707.
[29] See e.g., H. Matsumoto, D. Boucher, V. Mukhovatov, in: Proc. 26th EPS Conference on Plasma Physics and Controlled Fusion, June 14–18, 1999, Maastricht, The Netherlands, Contributed Papers, Vol. 23J, European Physical Society, Petit-Lancy, 1999, p. 1441.

TEST RUN INPUT

The input variables described in Section 6 are given in the following namelist. The values reported here have been used to produce Fig. 4.

```
Input values for beam tracing
&edata
xrtol = 1.d-7, xatol = 1.d-7, xstep = 4.d0, ianexp = 2, nni = 39, nnj = 69,
nshot = 12257, xtbeg = 3.5, xtend = 3.5, nmod = -1, nlnch = 1,
xf = 140.1d9, xthdeg = -6.15, xphdeg = -14.6, xxb = 234., xyb = 0., xzb = 0.,
xryyb = 129.4, xrzzb = 129.4, xwyyb = 2.97, xwzzb = 2.97, xpw0 = 1.,
xrmaj = 165., xrmin = 65., xb0 = 2.1, xdns = 1.6d13, edgdns = 1.4d13,
xe1 = 2., xe2 = 1., xte0 = 2., xteedg =  2.d-1
&end
```

TEST RUN OUTPUT

The output of the test run is:

```
Absorbed power (MW)    0.95446679492053        max. at rho = 0.71869060640973
Driven current (MA)    -1.0880371644799D-02    max. at rho = 0.69477110677367
```

In addition to the standard output, data files (containing informations about beam trajectory, absorbed power and driven current) can be produced.

Reduction of the Ion Drive and ρ_θ^* Scaling of the Neoclassical Tearing Mode

E. Poli, A. G. Peeters, A. Bergmann, S. Günter, and S. D. Pinches
Max-Planck-Institut für Plasmaphysik, Boltzmannstrasse 2, D-85748 Garching bei München, Germany

(Received 14 June 2001; revised manuscript received 9 August 2001; published 1 February 2002)

In the theoretical description of the neoclassical tearing mode it is usually assumed that the ion banana width w_b is much smaller than the island width W. This assumption is questionable at least for the island size at the mode onset. We show that a significant fraction of the (ion) bootstrap current survives inside the island when w_b is comparable to W. This effect also leads to a linear scaling of $\beta_\theta^{\text{onset}}$ with the normalized ion poloidal gyroradius ρ_θ^*, in agreement with the experimental results of ASDEX Upgrade.

DOI: 10.1103/PhysRevLett.88.075001 PACS numbers: 52.25.Dg, 52.30.Cv, 52.65.Pp

Neoclassical tearing modes (NTMs) have been found to often limit the energy which can be stored in the plasma of a toroidal confinement device such as a tokamak and are predicted to have a significant impact on the performance of the International Thermonuclear Experimental Reactor ITER. The NTM occurs when a sufficiently large initial magnetic perturbation, the so-called "seed island," is produced by the background magnetohydrodynamic activity. Inside the island, the reconnection of the field lines leads to a flattening of the pressure profile and, consequently, to a drop of the bootstrap current. (The bootstrap current is generated by the particles trapped in the outer side of a toroidal confinement system. In the presence of a pressure gradient, they generate a current parallel to the magnetic field.) The magnetic field associated with the "hole" in the bootstrap current in turn reinforces the perturbation and drives the instability.

The theoretical description of NTMs is based on the generalized Rutherford equation [1–5], in which the various mechanisms that can stabilize or destabilize the mode are taken into account. It is obtained by integrating Ampère's law across the island region, using Ohm's law to express the inductive contribution to the current density. The result is an evolution equation for the island half-width W:

$$\frac{4\pi}{1.22\eta c^2}\frac{dW}{dt} = \frac{\Delta'}{2} + \frac{4\sqrt{2}}{c}\frac{qR}{sBW} \times \int_{-1}^{\infty} d\Omega \oint \frac{d\xi \cos\xi}{\sqrt{\cos\xi + \Omega}}\, j_\parallel^{\text{n.i.}}. \tag{1}$$

In this equation, η is the neoclassical resistivity, Δ' is the stability index of the equilibrium current profile [1], q is the safety factor, R is the major radius, s is the magnetic shear, and B is the magnetic field strength. A helical angle $\xi \equiv m\theta - n\varphi$, where m and n are the poloidal and toroidal numbers of the resonant surface and θ and φ are the poloidal and toroidal angles, respectively, has been introduced along with a normalized helical flux $\Omega \equiv (q_s'/2q_s)(\psi - \psi_s)^2/\tilde{\psi} - \cos\xi$, where ψ is the poloidal flux, the prime denotes the derivative with respect to ψ, $\tilde{\psi}$ is the strength of the flux perturbation, and the subscript s means that a quantity is evaluted at the resonant surface. Ω is defined in such a way that $\mathbf{B} \cdot \nabla\Omega = 0$ and $\Omega = -1$ at the O point of the island and $\Omega = 1$ at the separatrix. In this Letter, the only contribution to the noninductive part of the current $j_\parallel^{\text{n.i.}}$ is supposed to be given by the bootstrap current j_{bs}, which must be calculated in the perturbed magnetic configuration and substituted in Eq. (1). This yields

$$\frac{4\pi}{1.22\eta c^2}\frac{dW}{dt} = \frac{\Delta'}{2} + a_2\sqrt{\varepsilon}\,\frac{L_q}{L_p}\frac{\beta_\theta}{W}\frac{1}{1 + (W_0/W)^2}, \tag{2}$$

where a_2 is a numerical coefficient of order one, $\beta_\theta = 8\pi p/B_\theta^2$ (p is the pressure and B_θ is the poloidal field), $1/L_q = d\ln q/dr$, $1/L_p = -d\ln p/dr$, and $\varepsilon = r_s/R$ is the inverse aspect ratio of the resonant surface. In the previous equation, the role of finite perpendicular transport in preventing a complete flattening of the pressure profile inside the island [6] has been taken into account. The corresponding reduction of the neoclassical drive is expressed by the term containing $W_0 = 2.55 r_s(\chi_\perp/\chi_\parallel)^{1/4} \times (q/ms\varepsilon)^{1/2}$. An important remark to Eq. (2) is to be made. In order to obtain an analytic expression for j_{bs} to be substituted in Eq. (1), it is supposed that the island width W is much larger than the ion banana width $w_b = \sqrt{\varepsilon}\,\rho_\theta$, where $\rho_\theta = v_T/\omega_{c\theta}$ is the ion poloidal gyroradius (v_T is the thermal velocity of the ions and $\omega_{c\theta}$ is ion cyclotron frequency calculated using the poloidal magnetic field). In this limit, the bootstrap current completely vanishes inside the magnetic island (if the aforementioned finite-$\chi_\perp$ effect is neglected). However, the opposite limit also deserves careful investigation, since at least in the early phase of a NTM it is often $w_b \approx W$. In this case, it can be thought that the particles trapped in the region around the island (where the pressure gradient is not flat) significantly overlap the island and might then provide the source for the bootstrap current also inside it. This effect is of course supposed to be larger for the ions than for the electrons, which have a much smaller banana width. Therefore, electrons are neglected in the calculations presented below.

0031-9007/02/88(7)/075001(4)$20.00

The role of the finite banana width of the ions is examined in this Letter. To this aim, the drift-kinetic equation for the ion distribution function f,

$$\frac{df}{dt} = \frac{\partial f}{\partial t} + (v_\parallel \hat{\mathbf{b}} + \mathbf{v}_d) \cdot \nabla f = C(f), \qquad (3)$$

is to be solved in the presence of an island (in this study, the width of the island is kept constant and its position in the plasma is held fixed). The limit we are interested in, $w_b \approx W$, requires a numerical solution. A physically reasonable and computationally useful choice is to employ the δf method. The solution f of Eq. (3) can be written as the sum of a time-independent term f_0 which is analytically known and a second term δf which expresses the temporal evolution of the distribution function and is to be determined numerically. In our approach, δf is represented by the distribution in the phase space of an ensemble of markers ("particles") which evolve according to a Hamiltonian set of equations of motion. If $\delta f \ll f_0$, i.e., if the final solution is a small perturbation of the background distribution function, solving for δf instead of f leads to a substantial reduction of the simulation noise, since a much smaller number of markers is required. Here f_0 is assumed to be a Maxwellian f_M; Eq. (3) then gives

$$\frac{\partial \delta f}{\partial t} + (v_\parallel \hat{\mathbf{b}} + \mathbf{v}_d) \cdot \nabla \delta f = C(\delta f) - \mathbf{v}_d \cdot \nabla f_M . \qquad (4)$$

The left-hand side of this previous equation is the total derivative of δf along the particle orbits, and the term $\mathbf{v}_d \cdot \nabla f_M$ acts as a source for δf. Equation (4) is integrated over a collisional time interval Δt_c in two steps. First, the markers evolve collision free according to the equations of motion. They are integrated using the guiding center code HAGIS [7], which solves the equations of motion in toroidal geometry in the presence of a perturbation of the magnetic equilibrium employing Boozer coordinates. In a second step, collisions are modeled by a Monte Carlo procedure [8]. The parallel velocity of the particles obtained from the first step is modified according to the pitch-angle part of the collision operator; i.e.,

$$C(f) = \frac{\partial}{\partial \lambda}(\nu \lambda f) + \frac{1}{2}\frac{\partial^2}{\partial \lambda^2}[\nu(1-\lambda^2)f], \qquad (5)$$

where $\lambda \equiv v_\parallel / v$ is the cosine of the pitch angle and $\nu(v) = (3\sqrt{2\pi}/4\tau)(v_T/v)^3 G(v/v_T)$. In the previous equation, τ is the ion-ion collision time and $G(x) = [(x^2 - 1/2) \times \mathrm{erf}(x) + x\exp(-x^2)/\sqrt{\pi}]/x^5$. The Langevin equation corresponding to the collision operator (5) is $\dot{\lambda} = -\nu\lambda + \sqrt{\nu(1-\lambda^2)}\,\Xi(t)$, with a Gaussian random noise $\Xi(t)$. The change in the parallel velocity of the particles can then be written $\delta v_\parallel = -v_\parallel \nu \Delta t + \gamma v_\perp \sqrt{\nu \Delta t_c}$ [so that $\delta v_\perp^2 = -(2v_\parallel + \delta v_\parallel)\delta v_\parallel$], with random numbers γ such that $\langle \gamma \rangle = 0$ and $\langle \gamma^2 \rangle = 1$. The scheme is implemented in such a way that momentum is conserved. Quantities of interest are obtained by flux surface average according to the definition

$$\frac{1}{n}\left\langle \int A \delta f \, d^3\mathbf{v} \right\rangle \simeq \frac{\int_{\Omega-\delta\Omega}^{\Omega+\delta\Omega} A \delta f \, d\Gamma}{\int_{\Omega-\delta\Omega}^{\Omega+\delta\Omega} f_0 \, d\Gamma}, \qquad (6)$$

where $d\Gamma$ is the phase-space volume element. Therefore, the plasma column is divided into cells, bounded between two neighboring flux surfaces (labeled by the helical flux Ω).

The approach described previously is applied to the study of the bootstrap current in the island region for the case of a (3,2) mode in a tokamak with ITER-like and ASDEX Upgrade (AUG)-like parameters. Typical parameters are for ITER (deuterium plasma): major radius $R = 8$ m, magnetic field on the magnetic axis $B_0 = 6$ T, central density $n_0 = 10^{20}$ cm^{-3}, central temperature $T_0 = 10$ keV; for AUG (hydrogen, deuterium plasma): $R = 1.5$ m, $B_0 = 2.5$ T, $n_0 = 6 \times 10^{19}$ cm^{-3}, $T_0 = 2$ keV. The magnetic equilibrium is specified analytically and the unperturbed flux surfaces are circular and concentric. The equilibrium density and temperature profiles decay exponentially with respect to ψ, i.e., roughly Gaussian with respect to the radius r. In some simulations (cf. Fig. 3), a flat density profile has also been considered in order to show that the effect under investigation takes place also in the absence of density gradients. The parameters are chosen such that the bounce time $\tau_B = qR/v_T\sqrt{\varepsilon}$ is much shorter than the trapped-to-passing scattering time $\tau_S = \varepsilon/\nu_i$, and the plasma is hence in the banana collisionality regime $\nu_* \equiv \tau_B/\tau_S \ll 1$.

In order to investigate finite-banana-width effects on the neoclassical drive of the tearing mode, the bootstrap current in the island region has been studied varying the ratio w_b/W. As a first example, in Fig. 1 a "large" island ($w_b/W \approx 0.11$) is considered. Figure 1a shows the density profile (the similar behavior of the temperature profile is not reported here) resulting from the simulation, which exhibits a flattening in the center of the island and steeper gradients just outside, in such a way that far from the resonant surface the unperturbed profile is recovered. These features of the density profile explain the behavior shown in Fig. 1b, where a drastic drop of the (ion) bootstrap current $j_{i\parallel} = \langle env_\parallel \rangle$ inside the island can be observed, along with a small residual current near the island edge and an excess of current just outside. The ion current is compared with the theoretical value calculated analytically in the absence of the island [9]. Figure 1b also shows the helical component of the current (i.e., that part of the current which has the same helicity as the resonant surface) $j_{\mathrm{he}} = \langle env_\parallel \cos\xi \rangle$, which represents the actual driving term in the Rutherford equation (1). Inside the island (where the current itself vanishes) j_{he} is obviously zero. Just outside the island, the main contribution to j_{he} comes from the region around the X point, where $\cos\xi = -1$, and hence j_{he} is negative.

Figure 2 shows the opposite limit of a "small" island. In this case, the width of the island becomes comparable

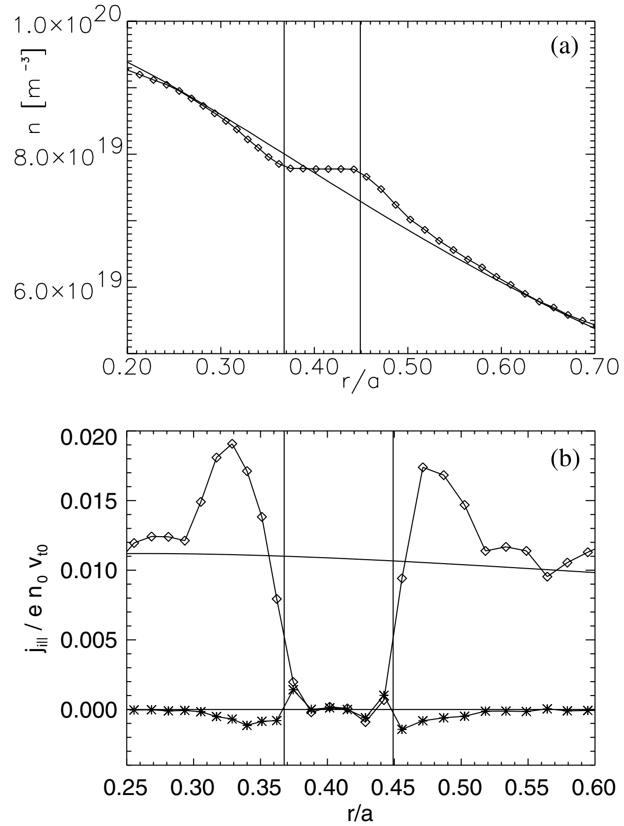

FIG. 1. Density (a) and ion bootstrap current (b) profiles in the presence of a large island $W \gg w_b$. The diamonds refer to the results of the Monte Carlo δf simulations, and the solid curves to the analytical calculations for an unperturbed magnetic equilibrium. In (b), stars show the helical component of the ion current.

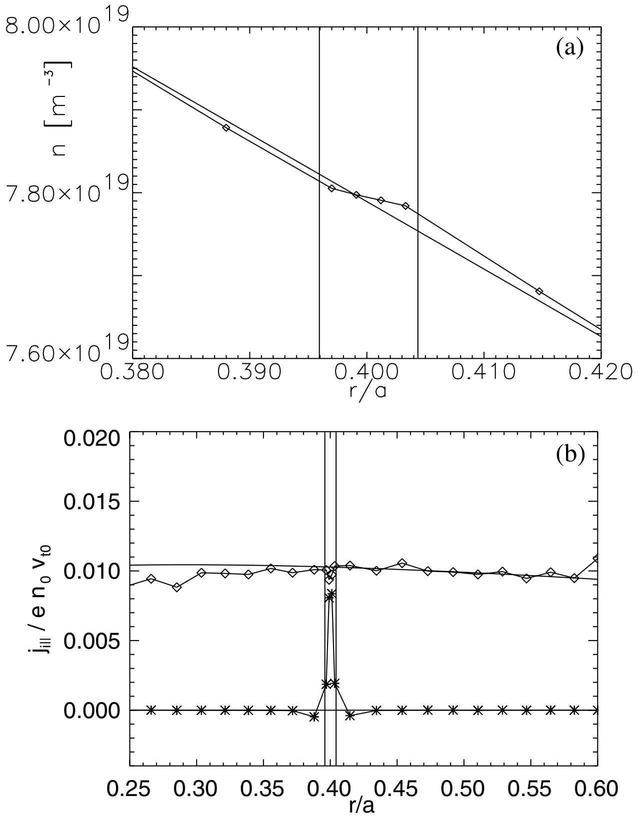

FIG. 2. Density (a) and ion bootstrap current (b) profiles in the presence of a small island $w_b/W = 1.1$. Solid lines again show the analytical calculation; diamonds and stars refer to the simulated ion bootstrap current and its helical component, respectively.

or even smaller than the width of the ion banana orbits and it can be expected that the trapped particles overlap the island and generate a nonvanishing bootstrap current also inside it. This picture is confirmed by the simulations. No drop of the ion current in the island is observed and the unperturbed profile is recovered over the whole radial range. Correspondingly, a nonzero contribution to the helical current coming from the O point (where $\cos\xi = 1$) of the island is observed. It can be seen from Fig. 2a that the overlapping process is not directly related to a recovery of the unperturbed density profile inside the island, and the density profile still significantly flattens. In other words, in this magnetic configuration the local value of the bootstrap current is not consistent with the value of the local gradients.

These features are summarized in Fig. 3. The averaged current density inside the island j_{isl} (normalized to the unperturbed current density at the resonant surface) is plotted as a function of the ratio w_b/W for ITER and ASDEX Upgrade parameters. For large values of the island width, $j_{\mathrm{isl}} \rightarrow 0$ according to the standard picture of the NTM. When the island width is reduced, j_{isl} increases until it reaches the unpertubed value for $W \approx w_b$. In this case, no perturbation of the ion bootstrap current is present in the plasma and there is no ion contribution to the drive of the mode. This has significant consequences for instance for AUG, since the typical width of the seed island which triggers the mode is between 1 and 5 cm, and the width of a banana orbit is between 7 mm and 3 cm, depending on both the plasma composition and discharge parameters. Hence, at least in its early phase, the NTM is more stable than usually assumed. Two other remarks can be made. First of all, the fact that ITER and AUG simulations lie approximately on the same curve when plotted as a function of w_b/W confirms the interpretation that this ratio is the parameter governing this effect. Moreover, the data can be fitted by the curve $j_{\mathrm{isl}}/j_{\mathrm{unpert}} \approx 7x^2/(1 + 7x^2)$, showing a quadratic dependence on $x \equiv w_b/W$. This can be connected with the simple picture that the strength of finite-banana-width effects is proportional to the area of the island overlapped by the trapped particles.

It is interesting to finally discuss the scaling of β_θ at the onset of the NTM as a function of the normalized ion poloidal gyroradius $\rho_\theta^* \equiv \rho_\theta/a$ (where a is the minor radius of the tokamak). At AUG, a linear scaling law

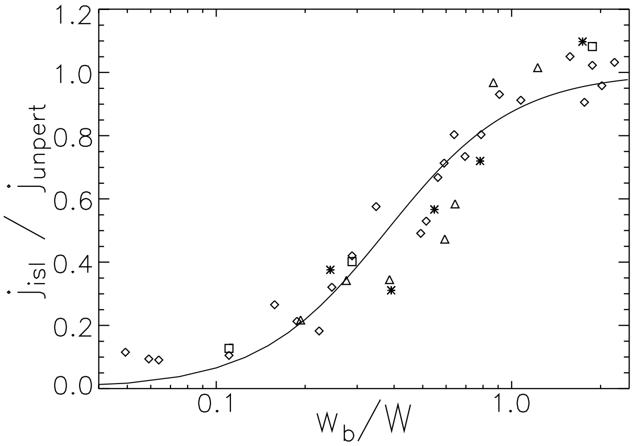

FIG. 3. Averaged current density inside the island versus the ratio w_b/W. Diamonds refer to simulations performed using ITER parameters (squares: flat density profile), triangles to AUG parameters with hydrogen plasma, and stars to AUG parameters with deuterium plasma. The solid line shows the fit $j_{\rm isl}/j_{\rm unpert} \approx 7x^2/(1 + 7x^2)$, with $x \equiv w_b/W$.

$\beta_\theta^{\rm onset} \propto \rho_\theta^{*1.02}$ has been observed [10] for islands whose width remained constant after the onset (in these cases the NTM is usually triggered by the sawtoothing activity and the seed island can be very close to the saturated island width). Supposing $W_0 < w_b$, it can be assumed that the most important stabilizing effect for the ions at small island widths is that presented in this Letter (the role of the polarization current is neglected). For the electrons, the finite perpendicular transport can be taken as the main stabilizing effect at small island widths. The Rutherford equation (2) might therefore be modified to

$$\frac{4\pi}{1.22\eta c^2}\frac{dW}{dt} = \frac{\Delta'}{2} + \frac{a_2}{2}\sqrt{\varepsilon}\,\frac{L_q}{L_p}\frac{\beta_\theta}{W} \times \left(\frac{1}{1 + (W_0/W)^2} + \frac{1}{1 + 7(w_b/W)^2}\right), \tag{7}$$

where the second term between parentheses has been taken according to the fit of Fig. 3. The value of $\beta_\theta^{\rm onset}$ corresponding to marginal stability ($dW/dt = 0$ for a given seed $W = W_{\rm seed}$) can be calculated directly from Eq. (7). In the limit $W_0 < w_b$, this yields

$$\beta_\theta^{\rm onset} \propto \frac{y^3 + 7y}{2y^2 + 7}\frac{w_b}{r_s}, \tag{8}$$

where $y \equiv W_{\rm seed}/w_b$. The scaling $W_{\rm seed}/r \propto \rho_\theta^{*3\alpha}$ has been predicted theoretically [11], where the exponent α depends on the details of the physical model. A fit to AUG data gives [12] $\alpha \approx 0.38$. Since it is clearly $w_b/r \propto \rho_\theta^*$, it results that y depends very weakly on ρ_θ^*. Equation (8) hence gives $\beta_\theta^{\rm onset} \propto w_b/r \propto \rho_\theta^*$ which is in agreement with the experimental observations of AUG.

All previous studies have neglected the effect of the overlap of the seed island by the trapped particles. It has been shown in this Letter that this is not justified. The dependence of the residual ion current inside the island on the ratio w_b/W has been derived from a large set of numerical simulations. Furthermore, it has been shown that this effect can predict the observed ρ_θ^* scaling of the value of β_θ at the mode onset. The latter point sheds an entirely new light on the scaling properties of the instability, since the only previously known explanation relied on the polarization current model.

[1] P. H. Rutherford, Phys. Fluids **16**, 1903 (1973).
[2] R. Carrera, R. D. Hazeltine, and M. Kotschenreuther, Phys. Fluids **29**, 899 (1986).
[3] See National Technical Information Service Document No. DE6008946 (W. X. Qu and J. D. Callen, University of Wisconsin Plasma Report No. UWPR 85-5, 1985). Copies may be ordered from the National Technical Information Service, Springfield, VA 22161.
[4] A. I. Smolyakov *et al.,* Phys. Plasmas **2**, 1581 (1995).
[5] H. R. Wilson *et al.,* Phys. Plasmas **3**, 248 (1996).
[6] R. Fitzpatrick, Phys. Plasmas **2**, 825 (1995).
[7] S. D. Pinches *et al.,* Comput. Phys. Commun. **111**, 133 (1998).
[8] A. Bergmann, A. G. Peeters, and S. D. Pinches, Phys. Plasmas **8**, 5192 (2001).
[9] O. Sauter, C. Angioni, and Y. R. Lin-Liu, Phys. Plasmas **6**, 2834 (1999).
[10] A. Gude, S. Günter, S. Sesnic, and the ASDEX Upgrade Team, Nucl. Fusion **39**, 127 (1999).
[11] C. C. Hegna, J. D. Callen, and J. R. La Haye, Phys. Plasmas **6**, 130 (1999).
[12] S. Günter *et al.,* Plasma Phys. Controlled Fusion **41**, B231 (1999).

INSTITUTE OF PHYSICS PUBLISHING PLASMA PHYSICS AND CONTROLLED FUSION

Plasma Phys. Control. Fusion **45** (2003) 71–87 PII: S0741-3335(03)53087-1

Monte Carlo δf simulation of the bootstrap current in the presence of a magnetic island

E Poli, A G Peeters, A Bergmann, S Günter and S D Pinches

Max-Planck-Institut für Plasmaphysik, Boltzmannstrasse 2, D-85748 Garching bei München, Germany

Received 6 September 2002, in final form 18 November 2002
Published 31 December 2002

Abstract

In the theoretical description of the neoclassical tearing mode the bootstrap current is assumed to completely vanish inside the magnetic island if finite perpendicular transport can be neglected. In this paper, the effects due to both the finite-orbit width of the trapped ions and their toroidal precession (not included in the standard analytic theory) on the island current are investigated. The evolution of the ion distribution function in toroidal geometry in the presence of a perturbed magnetic equilibrium is computed numerically employing the δf method, collisions being implemented by means of a Monte Carlo procedure. It is shown that a significant fraction of the (ion) bootstrap current survives inside the island when the ion banana width w_b approaches the island width W, and no loss is observed for $w_b/W \geqslant 1$. This effect is reduced when the collision time becomes longer than the toroidal drift time. The value of the current is found to be inconsistent with the local gradients in the island region. The finite-banana-width effect leads to a linear scaling of the value of the poloidal β at the mode onset with the normalized ion poloidal gyroradius ρ_p^*, in agreement with the experimental results of ASDEX Upgrade.

1. Introduction

Neoclassical tearing modes (NTMs) have often been found to determine the achievable β (the ratio of plasma to magnetic pressure) in long-pulse discharges in tokamak devices and are predicted to be the most significant β-limiting phenomenon for ITER. The NTM occurs when a sufficiently large initial magnetic perturbation, the so-called 'seed' island, is produced by the background magnetohydrodynamic activity. The perturbed magnetic configuration leads to a flattening of the pressure profile inside the island and, consequently, to a loss of the bootstrap current. For conventional scenarios with monotonic safety factor profiles, this loss leads to a further growth of the perturbation field and is the origin of the instability. This neoclassical drive of the tearing mode was first identified at TFTR [1] and subsequently in several experiments[1]. A fully-developed NTM usually produces a degradation in the plasma confinement and sometimes a disruptive end of the discharge.

---

[1] See [8] for a complete list.

0741-3335/03/020071+17$30.00

The thoretical description of the temporal evolution of the neoclassical tearing mode relies on the generalized Rutherford equation which allows for the different mechanisms that drive or damp the mode [2–8]. It can be obtained from the integration of the (toroidal component of) Ampère's law for current and field perturbations across the island region:

$$\frac{4\pi}{1.22\eta c^2}\frac{\mathrm{d}W}{\mathrm{d}t} = \frac{\Delta'}{2} + \frac{4\sqrt{2}}{c}\frac{qR}{sBW}\int_{-1}^{\infty}\mathrm{d}\Omega\oint\frac{\mathrm{d}\xi\cos\xi}{\sqrt{\cos\xi+\Omega}}\,j_{\|}^{\text{n.i.}}. \tag{1}$$

In equation (1), W is the island half-width, η is the neoclassical resistivity, Δ' is the usual stability parameter of the current profile [3], q is the safety factor, R the major radius, $s = (r/q)\mathrm{d}q/\mathrm{d}r$ the magnetic shear (r being the minor radius) and B the modulus of the magnetic field. Two coordinates have been introduced in equation (1). The first one is the helical angle $\xi \equiv m\theta - n\varphi$, where m and n are the poloidal and toroidal number of the resonant surface and θ and φ are the poloidal and toroidal angles. Along an unperturbed field line at the resonant surface $\xi = \text{const}$. The second coordinate is the helical flux $\Omega \equiv (q_s'/2q_s)(\psi - \psi_s)^2/\tilde{\psi} - \cos\xi$, where ψ is the (unperturbed) poloidal flux, the prime denotes the derivative with respect to ψ, $\tilde{\psi}$ is the strength of the flux perturbation and the subscript s means that a quantity is evaluted at the resonant surface. In a perturbed equilibrium, Ω must be used instead of ψ to label the perturbed magnetic surfaces (it can be shown that $\boldsymbol{B}\cdot\nabla\Omega = 0$). With this definition, $\Omega = -1$ corresponds to the O-point of the island and $\Omega = 1$ to the separatrix. The only contribution to the non-inductive current $j_{\|}^{\text{n.i.}}$ considered here is the bootstrap current since the focus is on the behaviour of this current in the presence of the island and not on the evolution of the NTM. In the analytic theory, approximate expressions for the bootstrap current are calculated and substituted into equation (1). They rely on the assumption that the orbit width of the trapped ions $w_b = \sqrt{\varepsilon_s}v_T/\omega_{\text{cp}}$ (where $\varepsilon = r/R$, v_T is the thermal velocity and ω_{cp} is the cyclotron frequency evaluated using the poloidal field) is much smaller than the island size, $w_b \ll W$. However, the opposite limit $w_b \gtrsim W$ also deserves attention, since this turns out to be the experimental situation at least at the onset of a NTM in today's fusion devices. In ASDEX Upgrade, for instance, the typical size of a seed island is about 1–5 cm, whereas the usual size of a (thermal) ion banana orbit is about 7 mm–3 cm, depending upon the isotope and the plasma temperature. Moreover, the theoretical description of the NTM in its early phase is still under debate, and an explanation of the observed behaviour is still to be achieved.

It is useful to briefly recall here the kinetic description of the bootstrap current generation for the standard case of an unperturbed magnetic configuration. The driving mechanism of the current at a certain point is given by the trapped particles that describe an orbit passing through that point. Depending on the sign of their parallel velocity, these particles will drift inward or outward with respect to that point. In the presence of a density (temperature) gradient, there will be then more (faster) particles on the inner orbits than on the outer orbits. The difference between the flows related to the inner and outer orbits gives the so-called 'banana' current [9] at the point under consideration for each particle species (this flow can be considered the parallel analog of the diamagnetic flow). The banana flow is then transferred by collisions to the passing particles, which carry the largest part of the (bootstrap) current. More precisely, the aforementioned flows can be ordered as follows. Banana current: total ion and electron flow (separately): bootstrap current (difference between ion and electron flows) $= \varepsilon^{3/2} : 1 : \varepsilon^{1/2}$. Returning to the case of a magnetic island, in the analytic theory of the NTM it is usually assumed that inside an island the pressure profile is flat, so that there is no net banana flow due to the trapped particles drifting in opposite directions and hence no bootstrap current. However, this description neglects those orbits that lie partly inside and partly outside the island. Since the particle population of these orbits is still influenced by the gradients outside the island, the aforementioned flux difference leading to the banana current could still take place also inside the island. It can be assumed that this (partly) restored banana flow is then again transferred to the passing particles by collisions, giving rise to a (partly) restored bootstrap current. When w_b and W are comparable, this overlap of an island by the trapped particles coming form outside can be thought to be the standard situation.

An additional mechanism which may modify the standard picture of the bootstrap current in the island is the drift of the trapped particles in the toroidal direction. It is known that the (vertical) drift of the particles due to both the gradient of the confinement field and its curvature is responsible for a finite radial excursion of the particle orbits with respect to the flux surface which leads not only to the finite orbit (banana) width but also to a precession of the trapped particles in toroidal direction, as the orbits do not close on themselves. Such a process could partly restore the toroidal symmetry of the perturbed system and change the fraction of the bootstrap current that survive inside the island.

Both aforementioned effects are expected to be more important for ions than for electrons, which have a much smaller banana width and a much faster trapped-to-passing scattering time. Therefore, only the behaviour of the ions is considered in the paper. The parallel current in the island is to be expressed in terms of a distribution function which is the solution of the drift kinetic equation. This solution is obtained by means of Monte Carlo δf simulations; this approach is described in section 2. The numerical simulations are presented in section 3, where the main results are discussed. The conclusions are summarized in section 4.

2. The numerical scheme

2.1. The Monte Carlo δf approach

An accurate description of the bootstrap current in the presence of an island structure requires the solution of the drift kinetic equation

$$\frac{\partial f}{\partial t} + (\boldsymbol{v}_{\parallel} + \boldsymbol{v}_d) \cdot \nabla f = C(f). \tag{2}$$

In equation (2), $\boldsymbol{v}_{\parallel}$ is the velocity parallel to the magnetic field, $\boldsymbol{v}_d$ is the magnetic-drift velocity and C is the (pitch-angle) scattering operator (see equation (4)). The function f describes the distribution in the phase space of the guiding centres of the ions. As it has already been mentioned, approximate analytic solutions to equation (2) can be found [5, 7] by employing a double expansion in $W/r_s \ll 1$, $w_b/W \ll 1$. In the limit we are interested in, $w_b \approx W$, this approach cannot be used and a numerical solution is needed. A useful scheme is the so-called δf method. The solution f of equation (2) is supposed to be a deviation δf from a bulk distribution function f_0 which is supposed to be analytically known and will be assumed in the following to be a Maxwellian, $f_0 = f_M$. In principle, $f = f_0 + \delta f$ is nothing but a way of re-writing the distribution function. However, since δf is to be represented numerically by an ensemble of 'markers', a significant reduction of the computational effort can be achieved if $\delta f \ll f_M$. Indeed, this is expected to be the case, since the drift velocity is usually much smaller than the parallel velocity. The resulting equation for δf is then

$$\frac{\partial \delta f}{\partial t} + (\boldsymbol{v}_{\parallel} + \boldsymbol{v}_d) \cdot \nabla \delta f = C(\delta f) - \boldsymbol{v}_d \cdot \nabla f_M. \tag{3}$$

In the numerical approach employed here, δf is represented by a distribution of marker particles. Equation (3) is solved in two steps. In the first one, the markers evolve collisionless according to the system's Hamiltonian equations of motion which are integrated in the full tokamak geometry in the presence of the magnetic perturbation (NTM) using the HAGIS code [10] (HAmiltonian GuIding centre System). In HAGIS, the equations are formulated using the Boozer magnetic coordinates ψ, θ, φ. In the second step, the velocities of the particles are changed according to the pitch-angle part of the collision operator,

$$C(f) = \frac{3\sqrt{2\pi}}{4\tau_i} G\left(\frac{v}{v_T}\right) \frac{1}{2} \frac{\partial}{\partial\lambda}(1-\lambda^2)\frac{\partial f}{\partial\lambda}, \tag{4}$$

where τ_i is the Braginskii ion collision time, $\lambda \equiv v_\parallel / v$ is the cosine of the pitch-angle and

$$G(x) = \frac{1}{x^5}\left[\left(x^2 - \frac{1}{2}\right)\operatorname{erf}(x) + \frac{x\exp(-x^2)}{\sqrt{\pi}}\right].$$

The Langevin equation corresponding to equation (4) is $\dot{\lambda} = -\nu\lambda + \sqrt{\nu(1-\lambda^2)}\,\Xi(t)$ (with a Gaussian random noise, Ξ). It can be solved using random numbers γ such that $\langle\gamma\rangle = 0$ and $\langle\gamma^2\rangle = 1$: the change of the particle velocity in a time step Δt_c is then

$$\delta v_\parallel = -v_\parallel \nu \Delta t + \gamma v_\perp \sqrt{\nu \Delta t_c},$$
$$\delta v_\perp^2 = -(2v_\parallel + \delta v_\parallel)\delta v_\parallel.$$

It should finally be remarked that the collision operator (equation (4)) does not conserve the parallel momentum, i.e. $\int v_\parallel C(f)\,\mathrm{d}\Gamma = \Delta p_\parallel \neq 0$ ($\mathrm{d}\Gamma$ is the phase-space element). The momentum is conserved in this scheme by modifying the weights δf of the markers $\delta f \to \delta f + \Delta\delta f$ such that

$$\int v_\parallel \Delta\delta f\,\mathrm{d}\Gamma = -\Delta p_\parallel = -\int v_\parallel C(f)\,\mathrm{d}\Gamma.$$

This Monte Carlo approach has recently been implemented into the HAGIS code and has been applied to the study of wide-orbit neoclassical transport in an unperturbed magnetic configuration [11].

2.2. *The magnetic configuration*

In the numerical simulations presented in this paper, the magnetic equilibrium is specified analytically and the unperturbed flux surfaces are circular and concentric, i.e. the toroidal and poloidal components of the magnetic field and the safety factor can be expressed in the usual polar coordinates r, χ as

$$B_t = \frac{B_{\mathrm{tc}}}{1+\varepsilon\cos\chi}, \qquad B_p = \frac{B_{\mathrm{pc}}(r)}{1+\varepsilon\cos\chi}, \qquad q(r) = q_0(1+br^2). \tag{5}$$

In the previous equations, the subscript c means evaluation at $\chi = \pi/2$. B_{tc} (the toroidal field on the magnetic axis) is assumed to be constant and $B_{\mathrm{pc}}(r)$ can be expressed as a function of B_{tc} and $q(r)$ as

$$B_{\mathrm{pc}}(r) = \frac{\varepsilon B_{\mathrm{tc}}}{q(r)\sqrt{1-\varepsilon^2}}. \tag{6}$$

A useful feature of equation (5) is that the polar coordinates r, χ can be linked analytically to the Boozer coordinates ψ, θ:

$$r = R_c\sqrt{1 - \frac{1+b}{b}\tanh^2\left[\sqrt{b(1+b)}(a_0 - q_0\psi)\right]}, \tag{7}$$

$$\chi = 2\arctan\left[\sqrt{\frac{1+r}{1-r}}\tan\left(\frac{\theta}{2}\right)\right], \tag{8}$$

with $a_0 \equiv \operatorname{arctanh}\left[\sqrt{b/(b+1)}\right]/\sqrt{b(b+1)}$. Equations (6)–(8) allow a considerable saving in the amount of computing time necessary for the numerical inversion. The detailed derivation is reported in the appendix.

In the presence of an island, the poloidal flux ψ can no longer be used to label the magnetic surfaces. To this aim, a suitable coordinate (the helical flux Ω) has been already introduced in section 1 (cf equation (1)). In the code, the more accurate helical flux function $\bar{\Psi}$ defined as

$$\bar{\Psi} \equiv \bar{\Psi}_{\text{helical}}(\psi, \xi) \equiv \psi - \frac{\psi_t(\psi)}{q_s} + \tilde{\psi}\cos\xi,$$

where $\psi_t = \int_0^{\psi} q(\psi')\,\mathrm{d}\psi'$ is the toroidal magnetic flux, is employed to describe the magnetic surfaces. On expanding $\bar{\Psi}$ to the second order around the resonant surface $\psi = \psi_s$ and using $q = \mathrm{d}\psi_t/\mathrm{d}\psi$, it can be seen that $\Omega \simeq -[\bar{\Psi} - \bar{\Psi}_s(\tilde{\psi} = 0)]/\tilde{\psi}$. Flux-surface averages are then evaluted according to the definition

$$\langle A\rangle = \lim_{\delta\bar{\Psi}\to 0}\frac{\int A\,\mathrm{d}^3\boldsymbol{r}}{\int \mathrm{d}^3\boldsymbol{r}} \Rightarrow \frac{1}{n}\left\langle\int A\delta f\,\mathrm{d}^3\boldsymbol{v}\right\rangle \simeq \frac{\int_{\bar{\Psi}-\delta\bar{\Psi}}^{\bar{\Psi}+\delta\bar{\Psi}} A\delta f\,\mathrm{d}\Gamma}{\int_{\bar{\Psi}-\delta\bar{\Psi}}^{\bar{\Psi}+\delta\bar{\Psi}} f_0\,\mathrm{d}\Gamma}. \tag{9}$$

In the perturbed magnetic configuration, the boundary surfaces between neighbouring cells are then functions of the three Boozer coordinates ψ, θ, φ and not of the poloidal flux ψ alone. Consistently with the definition of Ω in section 1, the island half-width can be expressed in terms of ψ as

$$\Delta\psi \simeq 2\sqrt{\frac{\tilde{\psi}q_s}{q_s'}}. \tag{10}$$

In the simulations, the island width can be controlled by changing the perturbation parameter $\tilde{\psi}$. The motion of the particles is calculated along the perturbed field lines, i.e. including the effect of the axisymmetry-breaking due to the presence of the helical island.

3. The bootstrap current in the island region

In the simulations, a $m = 3, n = 2$ mode in a tokamak with the magnetic equilibrium described in section 2.2 has been studied. Two sets of parameters have been taken into consideration: ITER-like (major radius $R = 8$ m, magnetic field on the magnetic axis $B_0 = 6$ T, central density $n_0 = 10^{20}\,\mathrm{m}^{-3}$, central temperature $T_0 = 10$ keV) and ASDEX Upgrade (AUG)-like ($R = 1.5$ m, $B_0 = 2.5$ T, $n_0 = 6\times 10^{19}\,\mathrm{m}^{-3}$, $T_0 = 2$ keV). For the case of AUG, simulations with both hydrogen and deuterium have been carried out in order to vary the width of the banana orbit at a given temperature. The density and temperature profile were exponentially decaying with respect to the poloidal flux ψ (i.e. approximately Gaussian with respect to r): $n = n_0\exp(-\psi/\psi_a)$, $T = T_0\exp(-2\psi/\psi_a)$. The case of flat density $n = n_0$ is discussed in section 3.2. During each simulation, the position and the width of the island are kept constant.

In the process under consideration there are three different timescales of interest, i.e. the bounce time $\tau_B = qR/v_T\sqrt{\varepsilon}$, the trapped-to-passing scattering time $\tau_S = \varepsilon/\nu_i$ and the toroidal drift time of trapped particles $\tau_D = 4\pi\varepsilon\omega_c R^2/qv_T^2$. Here, only the case of banana regime $\nu_* \equiv \tau_B/\tau_S \ll 1$ is considered.

3.1. Finite-banana-width effects

First of all, the change of bootstrap current profile in the island region for different values of the ratio w_b/W has been considered [12]. In the simulations, this has been investigated by

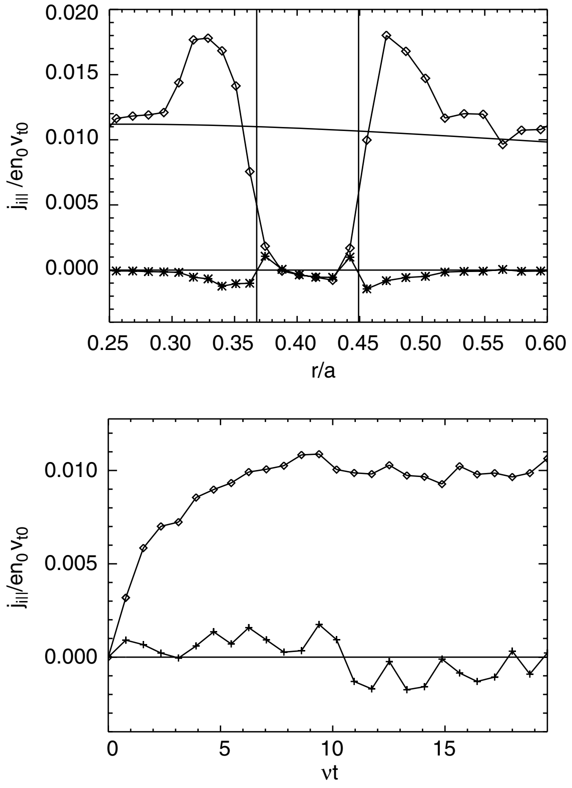

Figure 1. (*a*) Ion bootstrap current in the presence of a large ($w_b/W \approx 0.1$) island. The radial position chosen for the cells is a cut through the O-point of the island. Diamonds represent the bootstrap ion flow obtained from the simulations and the stars its helical component. The solid line gives the analytic calculation for the case of an unperturbed equilibrium. (*b*) Time evolution of the current inside the island ($\times$) and far from it ($\Diamond$). On the x-axis, the time is normalized to the (ion–ion) collision time.

varying the island width W (acting on the flux perturbation $\tilde{\psi}$, see equation (10)) and leaving the other parameters unchanged. The case $\tau_D \gg \tau_S$ is considered in order to exclude any possible contribution from the toroidal drift of the trapped particles.

Figure 1(*a*) shows the case of a large island for which $w_b/W \approx 0.1$. The island is represented by a radial cut through the O-point. It should be pointed out that the simulation points are actually flux-surface averages calculated inside cells bounded by surfaces with $\bar{\Psi} =$ const. according to equation (9), so that not all the points inside a given cell have the same radial position. The bootstrap current (or more precisely the parallel ion flow) obtained from the simulation as $j_{i\parallel} = \langle \mathrm{env}_{i\parallel} B \rangle$ is compared with the analytic prediction in the absence of any magnetic perturbation [13]. Inside the island, the expected drop of the current is observed, while far from the island the current converges to the unperturbed value. As can be seen in figure 1(*b*), the bootstrap current requires a few collisional times to build up (outside the island). Inside the island, the current oscillates about zero (the poorer statistics is essentially due to the smaller number of simulation particles in the island). Also reported in figure 1(*a*) is the so-called helical component of the current $j_{\mathrm{he}} = \langle \mathrm{env}_{i\parallel} B \cos\xi \rangle$, which according to equation (1) gives the actual drive of the mode. The helical current vanishes in the island, where the total current itself is zero, and has mainly a $\cos\xi = -1$ contribution from the

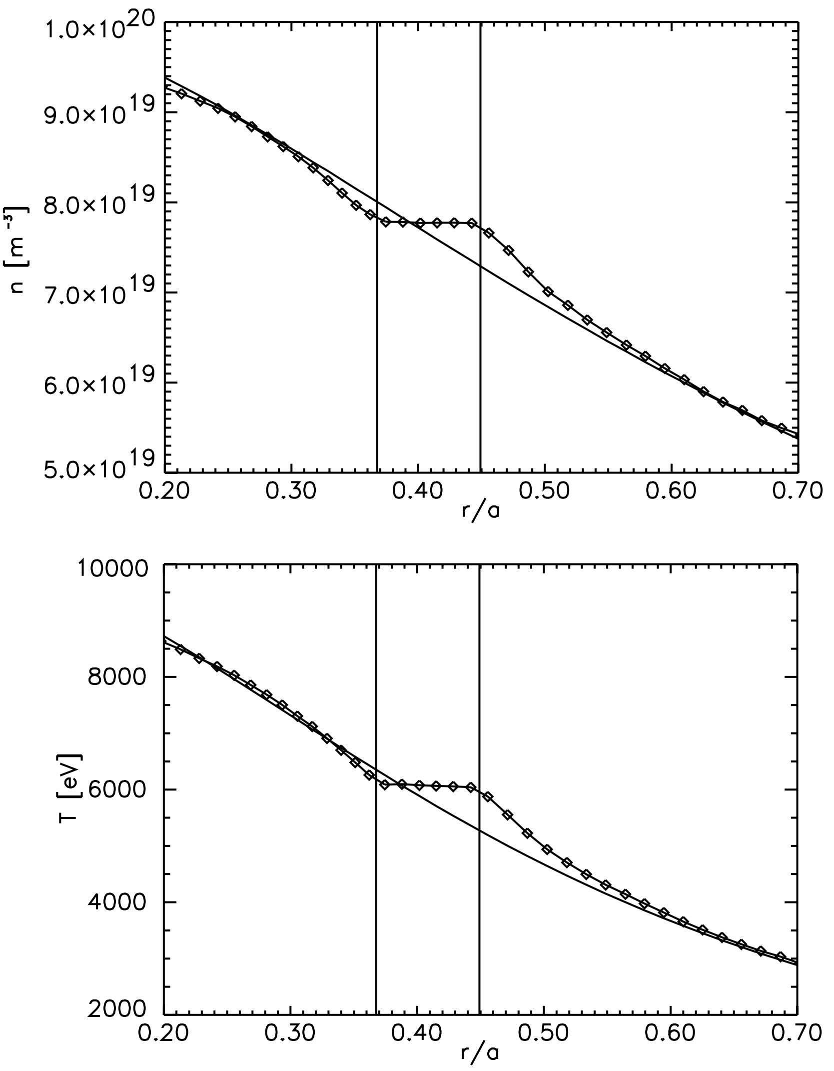

Figure 2. Density (*a*) and temperature (*b*) profiles for $w_b/W \approx 0.1$. Diamonds refer to the results of the simulations, the solid curves to the unperturbed profiles.

region outside the island around the X-point. The behaviour of the current shown in figure 1 is consistent with the density and temperature profiles presented in figure 2. The current excess just outside the island of figure 1(*a*) can be explained by the steeper profiles which tend to recover the unperturbed shape far from the island (this is not expected to be the experimental case, at least for the temperature profile in the presence of a critical gradient).

Figure 3 shows the transition to smaller island widths, i.e. to larger values of the ratio w_b/W. As the overlap of the island by the trapped particles (cf section 1) increases, the bootstrap current inside the island grows, starting from the edge. When w_b/W approaches unity, no drop in the current is observed. A positive contribution to the helical current can now be noticed inside the island, in particular close to the O-point, where $\cos\xi = +1$. Unlike the case of a large island presented in figures 1 and 2, in the presence of a large overlap between the particles and the perturbed region, the behaviour of the current is not consistent with the local

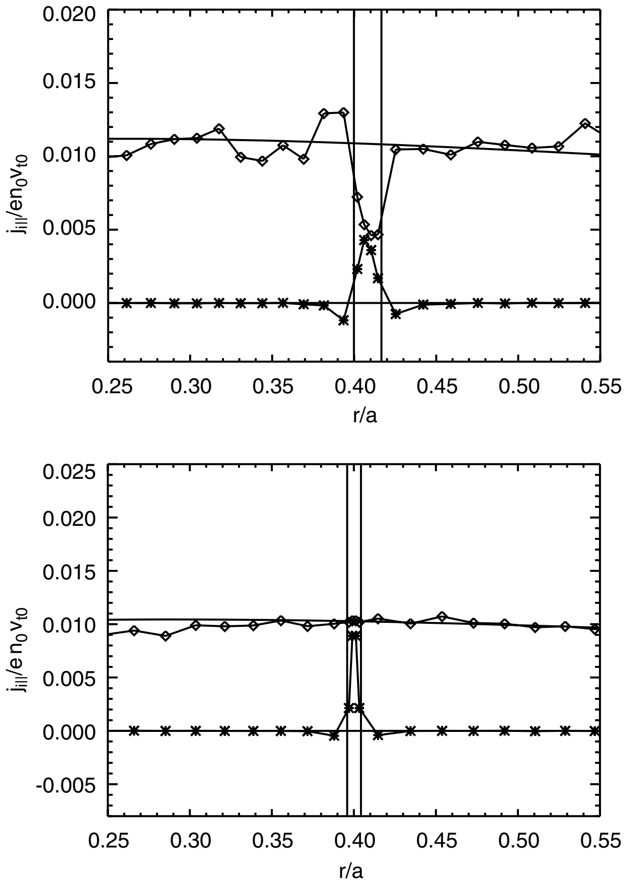

Figure 3. Bootstrap current profiles for (*a*) an intermediate ($w_b/W \approx 0.5$) and (*b*) a small ($w_b/W \approx 1.1$) island width. Solid lines again represent the analytic calculation, while diamonds and stars refer to the simulated ion bootstrap current and its helical component, respectively.

gradients. Even when the unperturbed current profile is completely recovered, the pressure exhibits a significant residual flattening inside the island, as shown in figure 4. This is consistent with the simple physical picture that the trapped ions which contribute to the banana current ‘feel’ the gradients that are outside the island and spend most of their time there. Hence, they contribute little to the pressure inside the island. ITER parameters have been employed in figures 1–4.

The averaged value of the bootstrap current inside the island from several simulations is plotted in figure 5(*a*) as a function of w_b/W. For large islands, the island current vanishes according to the usual NTM description. In the opposite limit $W \rightarrow w_b$, the island current has the same value as in the unperturbed case, which corresponds to the situation of no drive. In figure 5(*b*), the ‘radial’ integral (i.e. the sum over the cells) of the helical current j_{he} across the island region, which is proportional to the neoclassical drive of the NTM (see again equation (1)), as a function of w_b/W is plotted. It can be seen that in the limit of small islands the positive contribution to j_{he} coming from inside the island cancels the negative contribution coming from the region around the X-point outside the island (cf figure 3(*b*)), confirming that in this case the ion drive vanishes. This means that in the limit $w_b/W \approx 1$ the NTM is driven only by the electrons.

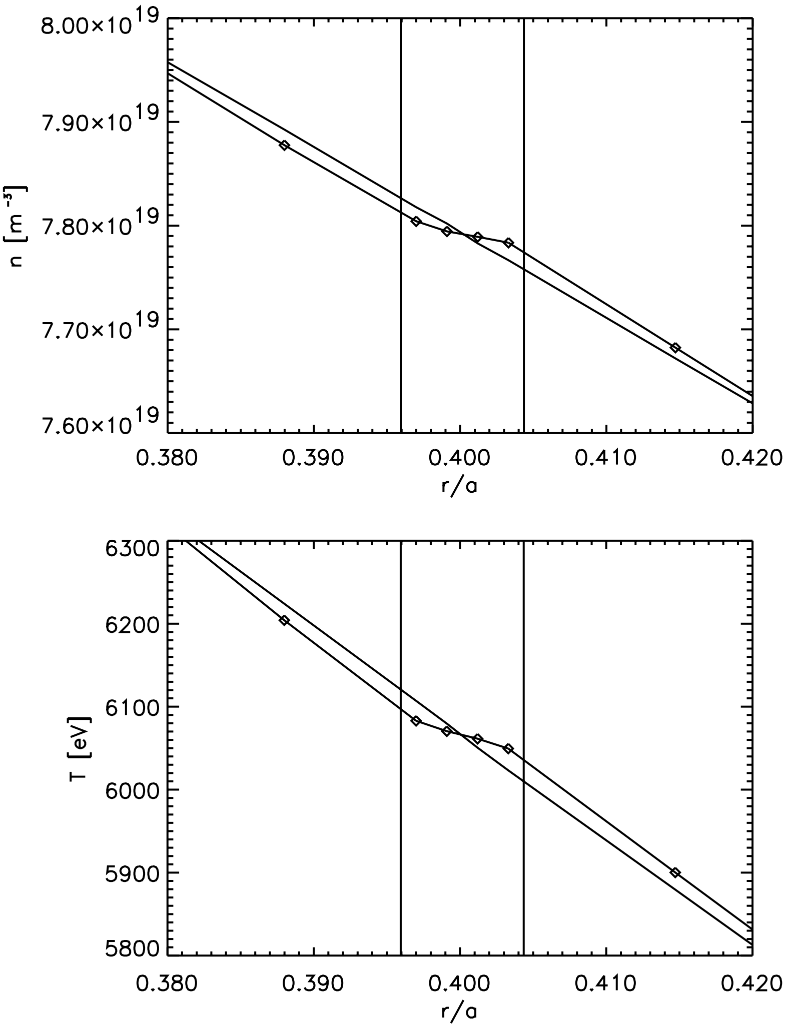

Figure 4. The same as figure 2 for $w_b/W \approx 1.1$.

With regard to this last point, the reaction of the electrons to the ion flow in the island is briefly discussed here. It is recalled that in the standard picture (i.e. in an unperturbed equilibrium) the total ion flow originating from the 'banana' flow can be written in the steady state as

$$\mathrm{en}u_{\parallel i} = \frac{c}{B_p}\frac{\mathrm{d}p_i}{\mathrm{d}r},$$

(where for simplicity only the contribution of the pressure gradient has been considered and the contribution of the second thermodynamic force, i.e. the temperature gradient, has been neglected). The previous equation arises in the fluid picture from the condition that in steady state the viscous force is zero[2]. On the other hand, the electron flow is determined by both the friction between electron and ions, which forces the electrons to flow in the same direction

---

[2] Cf [9], p B234, and references therein.

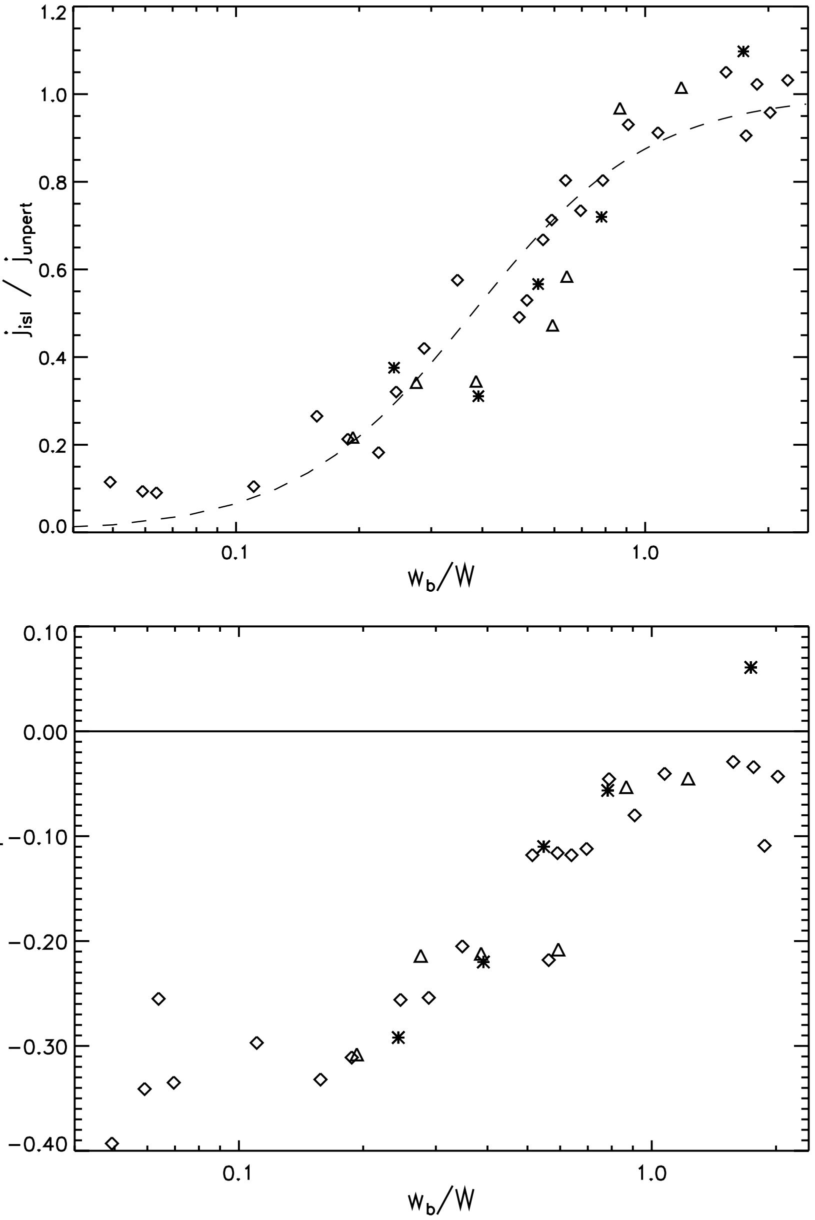

Figure 5. Averaged current density inside the island (a) and radial average of the helical current across the island region (b) versus the ratio w_b/W. Diamonds refer to simulations performed using ITER parameters, triangles to AUG parameters with hydrogen plasma, stars to AUG parameters with deuterium plasma. In (a), the fitting curve $j_{\rm isl}/j_{\rm unpert} = 7x^2/(1 + 7x^2)$, with $x = w_b/W$, is shown.

as the ions, and the flow originating from the electron banana flow (which is in the opposite direction and is smaller than the former term by a factor $\sqrt{\varepsilon}$):

$$\mathrm{enu}_{\|e} = \frac{l_{\rm ei}}{l_{\rm ei} + \mu_e}\mathrm{enu}_{\|i} - \frac{\mu_e}{l_{\rm ei} + \mu_e}\frac{c}{B_p}\frac{\mathrm{d}p_e}{\mathrm{d}r},$$

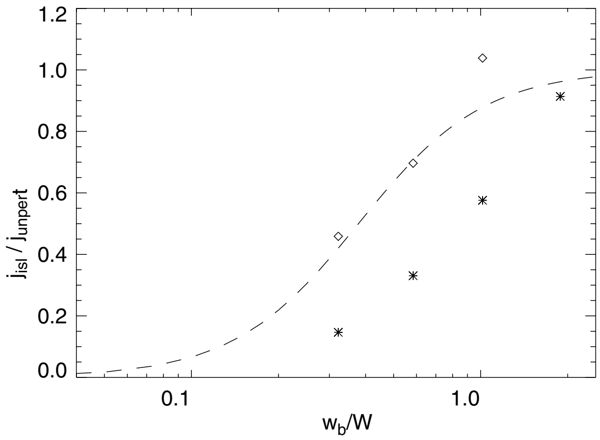

Figure 6. The same as figure 5(*a*), where the diamond refer to simulations where $\tau_S \ll \tau_D$ and stars to simulations where $\tau_S > \tau_D$. The parameters of the simulations are given in the text. The dashed line is the same as in figure 5(*a*).

where $l_{\rm ei} = m_e n \nu_{\rm ei}$ is the electron–ion friction coefficient and $\mu_e = m_e n \nu_{\rm ei}\sqrt{\varepsilon}$ is the electron viscosity coefficient (the electron–electron collisions have been neglected for simplicity). The bootstrap current arises as the difference between the ion and electron flows, i.e.

$$j_{\rm bs} = \frac{\mu_e}{l_{\rm ei} + \mu_e}\left({\rm enu}_{\parallel i} + \frac{c}{B_p}\frac{{\rm d}p_e}{{\rm d}r}\right).$$

In the frame of the finite-banana-width effect discussed above, it can be assumed that the ion contribution is restored by the overlap between trapped particles and island. However, if the electron pressure is supposed to remain substantially flat inside the island, the second term in the previous equation vanishes (and the bootstrap current is proportional to the parallel ion velocity $u_{\parallel i}$, which is calculated in the numerical simulations). It is then this 'hole' in the bootstrap current that drives the NTM when $w_b \approx W$.

The role of the toroidal precession of the trapped particles has been investigated comparing simulations with $\tau_D \ll \tau_S$ (this can be obtained for instance by lowering the collision frequency in the code) with simulations where $\tau_D \gg \tau_S$ (as those presented above). A new parameter set has been considered in order to approach a reasonable CPU time in the simulations: $R = 4$ m, $B_0 = 8$ T, $n_0 = 10^{20}$ m^{-3}, $T_0 = 20$ keV. These values yield at the resonant surface $\tau_S/\tau_D = 2.4$ for $\nu_* = 0.001$ (i.e. a trapped particle can drift approximately twice around the torus before experiencing a collision) and $\tau_S/\tau_D = 0.024$ for $\nu_* = 0.1$. The averaged island current obtained from these simulations is shown in figure 6. It is seen that for $\tau_D \gg \tau_S$ the island current follows the curve shown in figure 5(*a*). Rather surprisingly, when the toroidal precession time of the trapped ions becomes shorter than the collision time, the simulations show a reduction of the bootstrap current inside the island, i.e. the limit $j_{\rm isl} \approx j_{\rm unpert}$ is reached at higher values of the ratio w_b/W.

3.2. *The case of a flat density profile*

The behaviour of the ion flow for the case of a flat equilibrium density has also been studied. Indeed, in a tokamak H-mode discharge the density profile is often almost flat at the resonant surface. In this case, for a certain range of island widths the value of the bootstrap current inside the island could be expected to even slightly exceed the unperturbed value. This can be understood remembering that only those trapped particles which significantly overlap the island (i.e. have a part of their orbits outside the island and a part inside) lead to a non-vanishing banana current in the island. In other words, the island acts as a filter on the banana particles contributing to the current. For large islands no particle significantly overlaps the island (except for the region close to the separatrix), whilst for small islands nearly every trapped particle contribute to the overlap and hence to the current inside the island. In the intermediate region, only particles with large orbits (high velocity), can contribute, while particles with thin orbits (small velocity) can only produce a current near the separatrix. A simple picture is the following: only particles whose velocity exceeds some threshold (depending on w_b/W) contribute to the current, while the slow particles (the shaded region marked 'cut' in figure 7(*a*)) do not contribute. It can be seen that on the outer side of the island, where the temperature is lower, the number of particles having a small orbit width is larger than on the inner side, so that

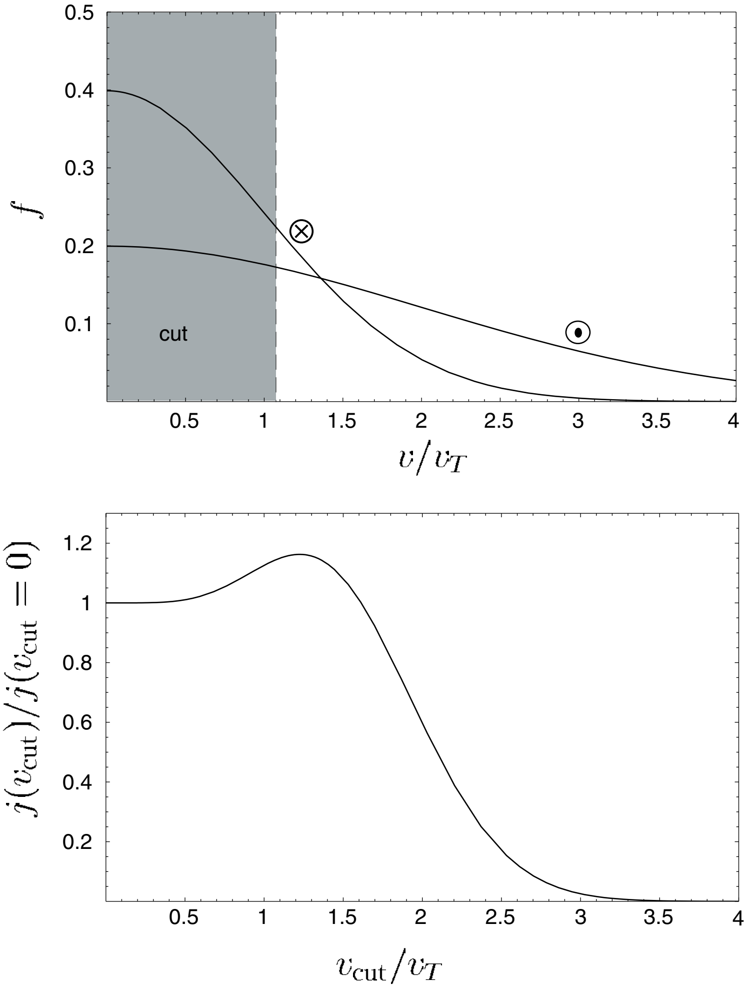

Figure 7. (*a*) Distribution functions on the inner (——) and outer (- - - -) side of the island in the presence of a temperature gradient and their contributions to the current (the total current is flowing out of the page). (*b*) Banana current as a function of a cut in the velocity space.

the ‘small-v’ region of the velocity space would give a contribution in the opposite direction with respect to the total current. If this region of the phase space is supposed to be cut off by the island, the current can exceed the standard value.

This effect can first be estimated analytically for the trapped particles, which provide the seed for the bootstrap current. In order to get an analytic estimate of this effect, a distribution function f_0 which is a function of the constants of motion, i.e. satisfying $\mathrm{d}f_0/\mathrm{d}t = 0$, with $\mathrm{d}/\mathrm{d}t = \partial/\partial t + (\boldsymbol{v}_\parallel + \boldsymbol{v}_d)\cdot\nabla$, can be considered

$$f_0 = n(P_t)\sqrt{\left(\frac{m}{2\pi T(P_t)}\right)^3}\,\mathrm{e}^{-\mathcal{E}/T(P_t)},$$

where the conserved toroidal momentum P_t is

$$P_t = mRv_t + \frac{e}{c}RA_t = mR\frac{B_t}{B}v_\parallel - \frac{e}{c}\psi$$

and $\mathcal{E} = mv^2/2$. In the standard neoclassical ordering, the first term on the right-hand side of the previous expression is small compared with the second one by a factor w_b/r (as can be seen taking $\psi \sim rRB_p$), and the distribution function is close to a local Maxwellian

$$f_0 \simeq f_M(\psi) - \frac{mcR}{e}\frac{B_t}{B}v_\parallel\frac{\partial f_M}{\partial\psi}, \tag{11}$$

where

$$\frac{\partial f_M}{\partial\psi} = f_M\left[\frac{1}{n}\frac{\partial n}{\partial\psi} + \left(\frac{\mathcal{E}}{T} - \frac{3}{2}\right)\frac{1}{T}\frac{\partial T}{\partial\psi}\right].$$

The case $\mathrm{d}n/\mathrm{d}\psi = 0$ is discussed. The contribution of the trapped particles to the current $e\int v_\parallel f_0\,\mathrm{d}^3\boldsymbol{v}$ inside the island can be then written

$$j_b = 2\pi e\int_{v_\perp^{\mathrm{cut}}}^{\infty} v_\perp\,\mathrm{d}v_\perp\int_{-\sqrt{2\varepsilon}v_\perp}^{\sqrt{2\varepsilon}v_\perp} v_\parallel f_0\,\mathrm{d}v_\parallel, \tag{12}$$

where $\mathrm{d}^3\boldsymbol{v} = 2\pi v_\perp\,\mathrm{d}v_\perp\,\mathrm{d}v_\parallel$ and the cut $v_\perp^{\mathrm{cut}}$ expresses the integration over the region of ‘large’ banana orbits. The term $\mathcal{O}(0)$ in equation (11) (which corresponds to the approximation of no drift) is even in $v_\parallel$ and does not contribute to the previous integral. The integration of equation (12) can be carried out using the formulae

$$\int_{-\bar{v}_\parallel}^{\bar{v}_\parallel} v_\parallel^2\left(\frac{mv_\parallel^2}{2T} - \frac{3}{2}\right)\mathrm{e}^{-mv_\parallel^2/2T}\,\mathrm{d}v_\parallel = -\bar{v}_\parallel^3\,\mathrm{e}^{-m\bar{v}_\parallel^2/2T} \simeq -2\sqrt{2}\varepsilon^{3/2}v_\perp^3,$$

$$\begin{aligned}\int_{-\bar{v}_\parallel}^{\bar{v}_\parallel} v_\parallel^2\frac{mv_\perp^2}{2T}\,\mathrm{e}^{-mv_\parallel^2/2T}\,\mathrm{d}v_\parallel &= v_\perp^2\left[-\bar{v}_\parallel\,\mathrm{e}^{-m\bar{v}_\parallel^2/2T} + \sqrt{\frac{\pi T}{2m}}\,\mathrm{erf}\left(\sqrt{\frac{m\bar{v}_\parallel^2}{2T}}\right)\right]\\ &\simeq -\sqrt{2}\varepsilon^{1/2}v_\perp^3\left(1 - \varepsilon\frac{mv_\perp^2}{T} - 1 + \frac{\varepsilon}{3}\frac{mv_\perp^2}{T}\right),\end{aligned}$$

where in the second step $\bar{v}_\parallel = \sqrt{2\varepsilon} v_\perp$ has been used and terms up to $\mathcal{O}(\varepsilon^{3/2})$ have been retained; it is noted that the contributions $\mathcal{O}(\sqrt{\varepsilon})$ cancel. One has then

$$
\begin{aligned}
j_b &= -2\pi \frac{cmRB_t}{B} \frac{\mathrm{d}T/\mathrm{d}\psi}{T} n \left(\frac{m}{2\pi T}\right)^{3/2} \sqrt{2}\varepsilon^{3/2} \int_{v_\perp^{\mathrm{cut}}}^{\infty} v_\perp^4 \left(\frac{2m}{3T} v_\perp^2 - 2\right) \mathrm{e}^{-mv_\perp^2/2T}\, \mathrm{d}v_\perp \\
&= -\frac{(2\varepsilon)^{3/2}}{3\sqrt{2\pi}} \frac{cn}{B_p} \frac{\mathrm{d}T}{\mathrm{d}r} \left\{ \mathrm{e}^{-m(v_\perp^{\mathrm{cut}})^2/2T} \left[6v_\perp^{\mathrm{cut}} \sqrt{\frac{m}{T}} + 2\left(v_\perp^{\mathrm{cut}} \sqrt{\frac{m}{T}}\right)^3 + \left(v_\perp^{\mathrm{cut}} \sqrt{\frac{m}{T}}\right)^5 \right] \right. \\
&\quad \left. + 3\sqrt{2\pi} \left[1 - \mathrm{erf}\left(\sqrt{\frac{m(v_\perp^{\mathrm{cut}})^2}{2T}} \right) \right] \right\}. \qquad (13)
\end{aligned}
$$

It is noted in passing that for $v_\perp^{\mathrm{cut}} \to 0$, i.e. for integration over the whole trapping cone, the previous formula yields the expression for the banana current [9] in the presence of a temperature gradient

$$
j_b = -(2\varepsilon)^{3/2} \frac{cn}{B_p} \frac{\mathrm{d}T}{\mathrm{d}r}.
$$

The banana current in the presence of a cut $v_\perp^{\mathrm{cut}}$ in the velocity space, equation (13), exhibits a maximum for $\bar{v}_\perp^{\mathrm{cut}} = \sqrt{3/2} v_T$, where $j_b(v_\perp^{\mathrm{cut}} = \bar{v}_\perp^{\mathrm{cut}})/j_b(v_\perp^{\mathrm{cut}} = 0) = 1.16$ (see figure 7(*b*)). It can be assumed that only those particles having a banana width larger than the island width W significantly overlap the island. In this case, the banana current inside the island has a maximum for $W = \sqrt{3/2} w_b$ (it is recalled that w_b is the ion banana width calculated with the thermal velocity), i.e. for

$$
\left.\frac{w_b}{W}\right|_{\max} = \sqrt{\frac{2}{3}} \approx 0.8.
$$

This condition for the banana current to be maximum can be assumed to hold for the total bootstrap current as well. In the case of a flat density profile, there is then a competition between this effect and the usual drop of the bootstrap current due to the pressure flattening in the island. The result is a widening of the 'plateau' $j_{\mathrm{isl}}/j_{\mathrm{unpert}} \approx 1$ towards smaller values of the ratio w_b/W, as shown in figure 8.

3.3. Scaling of β_p at the onset of the NTM

An interesting consequence of the reduction of the ion drive of the NTM due to finite-orbit-width effects is the scaling law for the value of $\beta_p \equiv 8\pi p/B_p^2$ at the onset of the mode (p is the plasma pressure). This parameter plays a significant role both theoretically and experimentally. In the standard analytic theory of the NTM, the bootstrap current can be calculated (in the aforementioned limits w_b/W, $W/r_s \ll 1$) and substituted into the right-hand side of equation (1). This yields

$$
\frac{4\pi}{1.22\eta c^2} \frac{\mathrm{d}W}{\mathrm{d}t} = \frac{\Delta'}{2} + a_2\sqrt{\varepsilon} \frac{L_q}{L_p} \frac{\beta_p}{W} \frac{1}{1 + (W_0/W)^2}, \qquad (14)
$$

where a_2 is of order unity, $1/L_q = \mathrm{d}\ln q/\mathrm{d}r$ and $1/L_p = -\mathrm{d}\ln p/\mathrm{d}r$. In the previous equation, the reduction of the neoclassical drive due to the finite radial transport across the island (which can partly restore the pressure gradient inside the island [14]) has been taken into account through the 'threshold' term $W_0 = 2.55 r_s(\chi_\perp/\chi_\parallel)^{1/4}(q/ms\varepsilon)^{1/2}$. For $\Delta' < 0$, equation (14) predicts that (for given p and q profiles) the mode can become unstable ($\mathrm{d}W/\mathrm{d}t > 0$) only for sufficiently high values of β_p. Moreover, since the second term on the right-hand side of equation (1) becomes smaller as W increases, a saturation of the island growth is predicted.

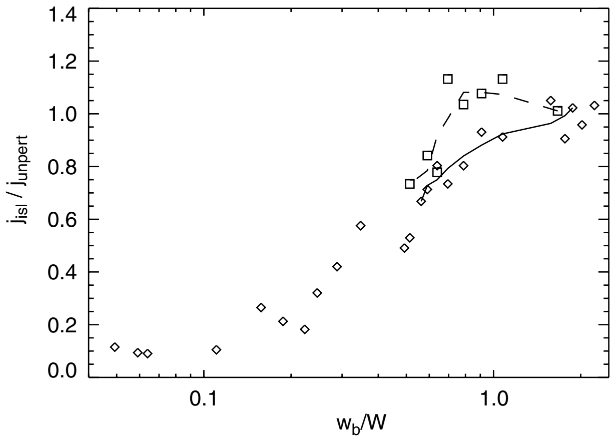

Figure 8. Diamonds represent the averaged island current as in figure 5(*a*); squares represent simulations with flat equilibrium density. ITER parameters are considered. The fitting curves in the region around $w_b/W \approx 1$ are shown to guide the eye.

From the experimental point of view, a linear scaling of $\beta_p^{\rm onset}$ with the normalized poloidal ion gyroradius ρ_p^* has been observed at AUG in those NTM events for which the seed island was as large as the saturated island width. This can happen when the NTM is caused by the sawtooth activity [15].

It has been shown in section 3.1 that the ion drive vanishes when $w_b \approx W$. A way to incorporate this effect in equation (1), neglecting the role of the polarization current (which is still under debate), and assuming that the electron drive is limited by finite-$\chi_\perp$ effects, is to re-write it as

$$\frac{4\pi}{1.22\eta c^2}\frac{{\rm d}W}{{\rm d}t} = \frac{\Delta'}{2} + \frac{a_2}{2}\sqrt{\varepsilon}\frac{L_q}{L_p}\frac{\beta_p}{W}\left(\frac{1}{1+(W_0/W)^2} + \frac{1}{1+7(w_b/W)^2}\right). \qquad (15)$$

The second term between parentheses on the right-hand side has been taken from the fit to the simulations shown in figure 5, assuming that for the ions $W_0^2 \ll 7w_b^2$. The scaling for β_p at the onset of a nearly-saturated (${\rm d}W/{\rm d}t \approx 0$) NTM can be obtained directly inverting equation (15) evaluated for $W = W_{\rm seed}$:

$$\beta_p^{\rm onset} \propto \frac{w_b}{r_s}\frac{y^4 + (7 + W_0^2/w_b^2)y^2 + 7W_0^2/w_b^2}{2y^3 + (7 + W_0^2/w_b^2)y}, \qquad (16)$$

where $y \equiv W_{\rm seed}/w_b$. Theoretical predictions for the scaling of the seed island [16] give $W_{\rm seed}/r_s \propto \rho_p^{*3\alpha}$, with α in the range between 0.25 and 0.66 depending on the physical model. Fitting the AUG experimental data [17] yields $\alpha \approx 0.38$. This means that the dependence of y on ρ_p^* is very weak. The scaling (and the size) of W_0 is also controversial. Evaluating W_0 using the Spitzer formula for $\chi_\parallel$ yields $W_0 < w_b$ and equation (16) gives a scaling $\beta_p^{\rm onset} \propto w_b/r_s \propto \rho_p^*$, in agreement the AUG experimental results. It has already been stressed (see for instance [18]) that such small values of W_0 can hardly be the only explanation for the NTM treshold in the experiments. Recently it has been pointed out [19] that the so-called heat flux limit gives much larger values of W_0, and $W_0 \approx w_b$ can hold. In this case, the last term in the numerator of equation (16) could play a role. However, in this limit it has also been found that W_0/r_s scales linearly with ρ_p^*. It is then possible that two effects leading to a linear scaling $\beta_p^{\rm onset} \propto \rho_p^*$ take place simultaneously.

Generally speaking, equation (15) predicts larger threshold widths and smaller saturation widths than a model where only finite-$\chi_\perp$ effects are considered.

4. Conclusions

The details of the behaviour of a NTM in its early phase is still a challenge for both theory and experiment. A numerical description of the bootstrap current in the presence of a magnetic island based on a numerical solution of the drift kinetic equation has been presented in this paper. It has been shown that the effects due to the finite ion banana width (compared to the island size) cannot be neglected. The numerical tool developed in order to study these effects is also a promising candidate for the investigation of kinetic effects in the presence of a potential connected with the island motion with respect to the surrounding plasma.

The persistence of the bootstrap current in an island for which $w_b \approx W$ has been traced back to the overlap of the trapped particles with the island. This is consistent with the residual flattening of the pressure profile observed in the simulations even when the unperturbed current profile is completely recovered and gives also an explanation for the behaviour of the current in the presence of a flat density profile. In present-day experiments, the situation $w_b \approx W$ is very common at least at the beginning of a NTM. The relevance of finite-banana-width effects in connection with the experimental observations, such as the scaling of β_p at the mode onset has been stressed. A detailed investigation, however, is still to be performed and has to cope with several theoretical uncertainties, such as the role of the polarization current, the transport model to be used for W_0 and the value of the coefficients for the various terms contributing to the Rutherford equation. The reduction of the ion drive discussed in this paper is also potentially important for ITER. In which range the ratio w_b/W_{seed} will be in ITER is still under discussion, as the scaling law for the seed island is still unknown.

Appendix. The circular equilibrium

In the numerical simulations, an analytic equilibrium with (unperturbed) circular concentric magnetic surfaces is adopted. The magnetic field and the safety factor are given by equation (5), i.e.

$$B_t = \frac{B_{\text{tc}}}{1+\varepsilon\cos\chi}, \qquad B_p = \frac{B_{\text{pc}}(r)}{1+\varepsilon\cos\chi}, \qquad q(r) = q_0\left(1+br^2\right),$$

with $B_{\text{tc}} = \text{const}$. The factor $B_{\text{pc}}(r)$ can be obtained by expressing the safety factor according to its definition and recalling that for a circular equilibrium it is $B_t/B_p = \mathrm{d}\ell_t/\mathrm{d}\ell_p = (R\,\mathrm{d}\phi)/(r\,\mathrm{d}\chi)$:

$$q(r) \equiv \oint \frac{\mathrm{d}\chi}{2\pi}\left.\frac{\mathrm{d}\phi}{\mathrm{d}\chi}\right|_{\text{field line}} = \oint \frac{\mathrm{d}\chi}{2\pi}\frac{rB_t}{RB_p} = \frac{rB_{\text{tc}}}{R_cB_{\text{pc}}(r)}\oint\frac{\mathrm{d}\chi}{2\pi}\frac{1}{1+\varepsilon\cos\chi},$$

where $R = R_c(1+\varepsilon\cos\chi)$ and ϕ is the usual toroidal angle. From the evaluation of the integral $\oint \mathrm{d}\chi/(1+\varepsilon\cos\chi) = 2\pi/\sqrt{1-\varepsilon^2}$, equation (6) follows.

Integration of $\mathrm{d}\psi/\mathrm{d}r = RB_p = R_cB_{\text{pc}}$, which follows from the expression for the poloidal magnetic field $B_p = \nabla\phi\times\nabla\psi$ and $|\nabla\phi| = 1/R$, yields

$$\psi(\varepsilon) = R_c^2B_{\text{tc}}\int_0^{\varepsilon}\frac{\epsilon\,\mathrm{d}\epsilon}{q(\epsilon)\sqrt{1-\epsilon^2}} = \frac{R_c^2B_{\text{tc}}}{q_0}\left[a_0 - \frac{1}{\sqrt{b(1+b)}}\,\text{arctanh}\left(\sqrt{\frac{b(1-\varepsilon^2)}{1+b}}\right)\right],$$

where $a_0 \equiv \text{arctanh}\left[\sqrt{b/(b+1)}\right]/\sqrt{b(b+1)}$ and $\psi(0) = 0$ has been chosen. The last equation can be inverted to give equation (7).

The covariant θ-component of the magnetic field in Boozer coordinates is related with the total toroidal current flowing inside a flux surface by the formula $2\pi B_\theta = \int \mathrm{d}\boldsymbol{S}_t \cdot (\nabla \times \boldsymbol{B})$, where $\mathrm{d}\boldsymbol{S}_t$ is the surface element in the poloidal plane. It follows

$$B_\theta = \frac{1}{2\pi}\int_0^r \mathrm{d}r' \int_0^{2\pi} r'\,\mathrm{d}\chi \frac{1}{r'}\frac{\partial(r'B_p)}{\partial r'} = \frac{rB_{\mathrm{pc}}}{\sqrt{1-\varepsilon^2}},$$

where equation (6) has been used. On the other hand, by definition it is

$$B_\theta = \boldsymbol{B}\cdot\frac{\partial \boldsymbol{r}}{\partial\theta} = \boldsymbol{B}\cdot\frac{\partial \boldsymbol{r}}{\partial\chi}\frac{\partial\chi}{\partial\theta} = rB_p\frac{\partial\chi}{\partial\theta}$$

and hence

$$\frac{\mathrm{d}\theta}{\mathrm{d}\chi} = \frac{rB_p}{B_\theta} = \frac{\sqrt{1-\varepsilon^2}}{1+\varepsilon\cos\chi}.$$

Integration of the last equation yields

$$\theta = 2\arctan\left[\sqrt{\frac{1-\varepsilon}{1+\varepsilon}}\tan\left(\frac{\chi}{2}\right)\right]$$

which can be inverted to give equation (8).

References

[1] Chang Z *et al* 1995 *Phys. Rev. Lett.* **74** 4663
[2] Qu W X and Callen J D 1985 University of Wisconsin, Plasma Report No. UWPR 85-5
[3] Rutherford P H 1973 *Phys. Fluids* **16** 1903
[4] Glasser A H, Greene J M and Johnson J L 1975 *Phys. Fluids* **18** 875
[5] Carrera R, Hazeltine R D and Kotschenreuther M 1986 *Phys. Fluids* **29** 899
[6] Smolyakov A I, Hirose A, Lazzaro E, Re G B and Callen J D 1995 *Phys. Plasmas* **2** 1581
[7] Wilson H R, Connor J W, Hastie R J and Hegna C C 1996 *Phys. Plasmas* **3** 248
[8] Sauter O *et al* 1997 *Phys. Plasmas* **4** 1654
[9] Peeters A G 2000 *Plasma Phys. Control. Fusion* **42** B231
[10] Pinches S D *et al* 1998 *Comp. Phys. Commun.* **111** 133
[11] Bergmann A, Peeters A G and Pinches S D 2001 *Phys. Plasmas* **8** 5192
[12] Poli E, Peeters A G, Bergmann A, Günter S and Pinches S D 2002 *Phys. Rev. Lett.* **88** 075001
[13] Sauter O, Angioni C and Lin-Liu Y R 1999 *Phys. Plasmas* **6** 2834
[14] Fitzpatrick R 1995 *Phys. Plasmas* **2** 825
[15] Gude A, Günter S, Sesnic S and the ASDEX Upgrade Team 1999 *Nucl. Fusion* **39** 127
[16] Hegna C C, Callen J D and La Haye J R 1999 *Phys. Plasmas* **6** 130
[17] Günter S *et al* 1999 *Plasma Phys. Control. Fusion* **41** B231
[18] Buttery R *et al* 2000 *Plasma Phys. Control. Fusion* **42** B61
[19] Zohm H *et al* 2001 *Nucl. Fusion* **41** 197

Role of Kinetic Effects on the Polarization Current around a Magnetic Island

E. Poli, A. Bergmann, and A. G. Peeters
Max-Planck-Institut für Plasmaphysik, Boltzmannstrasse 2, D-85748 Garching bei München, Germany

(Received 21 May 2004; published 23 May 2005)

The polarization current due to a magnetic island rotating in a tokamak plasma is believed to play a central role in the initial evolution of the neoclassical tearing mode. Monte Carlo δf simulations are performed which also cover a parameter range that is not amenable to analytic treatment but is relevant to experiments. It is shown that the polarization current can change sign when the island rotation frequency is of the order of the ion parallel streaming around the island. Moreover, the current is reduced when the island width is of the order of the ion banana width. Finally, the transition to the enhanced high-collisionality regime is shown to occur for collision frequencies higher than those typical of today's experiments.

DOI: 10.1103/PhysRevLett.94.205001 PACS numbers: 52.55.Fa, 52.25.Dg, 52.30.Cv, 52.65.−y

The magnetic-field lines of a toroidal fusion device usually lie on nested toroidal surfaces, called magnetic surfaces. This situation implies good radial confinement, since the particle transport along the field lines exceeds by several orders of magnitude the transport perpendicular to them. This favorable configuration, however, can be broken by the appearance of radially extended magnetic islands. As in this case the confinement becomes poorer, the control of this kind of plasma instabilities constitutes a major issue for present fusion machines and the future experimental International Thermonuclear Experimental Reactor (ITER). In more detail, a magnetic island can be driven unstable by the drop of a part of the plasma current (the so-called bootstrap current) inside the island itself [1,2]. This instability is called the neoclassical tearing mode (NTM). Several other ingredients play a role in the evolution of a NTM. In particular, many investigations on the role of the polarization current associated with the motion of the island relative to the bulk plasma [3,4] have been carried out. In the time-varying electric field of the island, the plasma ions move perpendicularly to the magnetic field. A parallel flow of the mobile electrons ensures charge neutrality and contributes through Ampère's law to the evolution of the magnetic field of the island. Under the assumption that the polarization current is stabilizing, it has been invoked as a possible explanation for the threshold observed in the experiments for the minimum island size which leads to an unstable NTM and for the scaling with the normalized ion gyroradius of the plasma pressure at the onset of the instability. It is shown in this Letter that a proper calculation of the polarization current requires a full kinetic treatment of the orbit of the particles in toroidal geometry in the presence of a rotating island and the related electric field.

The evolution of the island half-width W is usually studied in terms of the generalized Rutherford equation [5,6]. Its final form is obtained by substituting the noninductive part of the parallel current density $j_\parallel^{\text{n.i.}}$ into

$$\frac{dW}{dt} = c_1\Delta' + \frac{c_2}{W}\int_{-1}^{\infty} \mathrm{d}\Omega \oint \frac{d\xi \cos\xi}{\sqrt{\cos\xi + \Omega}}\, j_\parallel^{\text{n.i.}}, \qquad (1)$$

where Δ' is the stability parameter of the equilibrium current profile, Ω is a magnetic-surface label ($\mathbf{B}\cdot\nabla\Omega = 0$) defined as $\Omega \equiv (q_s'/2q_s)(\psi - \psi_s)^2/\tilde{\psi} - \cos\xi$, where q is the safety factor, ψ is the (unperturbed) poloidal flux, the prime denotes the derivative with respect to ψ, $\tilde{\psi}$ is the strength of the flux perturbation, the subscript s means that a quantity is evaluated at the resonant surface, and $\xi = m\theta - n\varphi - \omega t$ is the helical angle (m and n are and poloidal and toroidal mode numbers, θ and φ the poloidal and toroidal angles, and ω the mode rotation frequency). With this definition, $\Omega = -1$ denotes the O point of the island, $\Omega = 1$ the separatrix. The electrostatic potential associated with the island rotation through the plasma is assumed to be a flux-surface function, $\Phi = \Phi(\Omega)$, in the island's rest frame [3,4]. Finite-Larmor-radius corrections, which could lead to deviations from this assumption, are of higher order and are not included here. As shown in Fig. 1, in this reference system the electric field of the island

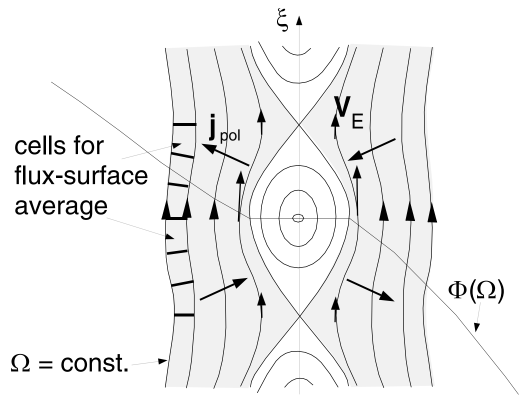

FIG. 1. Polarization current j_{pol} in the presence of a magnetic island.

generates an $E \times B$ flow along the flux surfaces with a velocity v_E which is larger around the island O point than around the X point, since $\nabla\Omega$ is larger in the first case and smaller in the second one. This acceleration and deceleration is balanced by a Lorentz force $\mathbf{j}_{\mathrm{pol}} \times \mathbf{B}$, where $\mathbf{j}_{\mathrm{pol}} = en_i/\omega_c(dv_E/dt)$ must be directed perpendicularly to the flux surfaces as shown in the figure (e is the particle charge, n_i the density, and ω_c the cyclotron frequency). This is the classical polarization current. Since the cyclotron frequency is much smaller for the ions than for the electrons, it results that the polarization current is mainly carried by the former ones. In a toroidal device, the poloidal $E \times B$ flow is damped due to the neoclassical viscosity and a parallel flow $u_{\|} = cE/B_p$ (B_p is the poloidal component of the magnetic field) develops in such a way that its poloidal component compensates the poloidal component of the $E \times B$ flow. This corresponds in the fluid picture to an enhancement of the polarization current by a factor $B^2/B_p^2 = q^2/\varepsilon^2$ (where $\varepsilon = r/R$ is the inverse aspect ratio), since the accelerated and decelerated parallel flow is a factor B/B_p larger than the poloidal flow, and this acceleration is to be provided now by the poloidal component of the magnetic field in the Lorentz force. This enhancement is lower by a factor $\varepsilon^{3/2}$ if the collision frequency ν is much smaller than ω, since in this case only the trapped-particle component of $u_{\|}$ varies along the island, as discussed later.

In order to calculate from $\nabla \cdot \mathbf{j} = 0$ the contribution to $j_{\|}^{\mathrm{n.i.}}$ due to the polarization current, some assumptions are made in the standard toroidal theory of NTMs. First of all, it is assumed that $\omega > k_{\|}v_{\|}$, where $k_{\|} = -m(r - r_s)/RqL_q$ is the parallel wave vector [$1/L_q = (1/q)dq/dr$] and $v_{\|}$ is the velocity component parallel to the magnetic field. This means that the advection which causes a particle to "feel" different electric fields is due to the $E \times B$ motion around the island rather than the streaming of the particles around the island along the field lines. For ω of the order of the diamagnetic frequency, the previous condition approximately corresponds to $\rho_p > W$; i.e., the island width should be smaller than the poloidal ion gyroradius (cf. also the discussion below). A second assumption is made on the island width, namely, that it has to be larger than the ion banana width $w_b = \sqrt{\varepsilon}\rho_p$, so that the distribution function can be analytically expanded in powers of w_b/W. This means that the standard theory of the polarization current in a toroidal configuration is valid only in the range [4] $w_b < W < \rho_p$. Finally, the value of the collision frequency at which the transition (referred to above) from the low-collisionality to the high-collisionality regimes takes place is under debate.

An investigation of the behavior of the polarization current in the parameter range not covered by the existing theory is of prime importance to understand its contribution to the NTM evolution under experimental conditions. In this Letter, this issue is addressed making use of a Monte Carlo δf approach. The drift kinetic equation is solved numerically by following the distribution in the phase space of a number of markers (which represent the plasma ions and evolve according to the equations of motion) in a tokamak geometry in the presence of a perturbed magnetic field [7]. More exactly, the markers describe the time dependent deviation δf from the stationary background distribution function, supposed to be a Maxwellian. The integration of the equations of motion is performed using the HAGIS code [8]. Collisions are implemented by a Monte Carlo procedure [9]. In this numerical scheme, no assumption on the island size, the island rotation frequency, or the collision frequency is required. In the simulations presented below, no mode evolution is considered, i.e., W and ω remain constant during each run. The electric potential associated with the island is prescribed such as to ensure an asymptotically vanishing electric field [3,4]:

$$\Phi = \frac{\omega q}{mc}[(\psi - \psi_s) - h(\Omega)], \qquad (2)$$

where $h(\Omega) = (WRB_p/\sqrt{2})(\sqrt{\Omega} - 1)\Theta(\Omega - 1)$ and c is the speed of light [$\Theta(x)$ is the Heaviside function]. The first term on the right-hand side of Eq. (2) leads to the $E \times B$ rotation of the whole plasma, and the second term describes the modification of this potential outside the island (where $\Omega > 1$). The boundary condition of vanishing electric field far from the island is satisfied by the profile function $h(\Omega)$, i.e., $h(\Omega \gg 1) = \psi - \psi_s$. The results presented in the following do not depend critically on the exact functional form of $h(\Omega)$ close to the separatrix, as the electric drift remains of the same magnitude compared to the magnetic drift, and local effects are smeared out by the finite width of the trapped-particle orbits when $W \approx w_b$. In the island's rest frame, the first term on the right-hand side of Eq. (2), proportional to ψ, drops and in $d/dt = \partial/\partial t + \mathbf{v} \cdot \nabla$ the explicit time derivative does not contribute. The perpendicular current (mainly carried by the ions) can be directly found as

$$\mathbf{j}_{\perp}^{\mathrm{upper,lower}} = e\left\langle \int \dot{\Omega}\frac{dr}{d\Omega}\delta f d^3\mathbf{v} \right\rangle^{\mathrm{upper,lower}},$$

where angular brackets denote a flux-surface average along the perturbed magnetic surfaces and the superscripts refer to the lower (from the X point to the O point) and upper (O point to X point) part of the island, cf. Figure 1. A magnetic island with $m = 3$, $n = 2$ is considered.

The first set of simulations (Fig. 2) shows a scan over ω of the perpendicular current $j_{\perp} \equiv (j_{\perp}^{\mathrm{upper}} - j_{\perp}^{\mathrm{lower}})/2$, averaged on the island inside and over a region lying within a distance of $3W$ from the island separatrix. In these simulations, the following parameters have been employed: major radius $R = 8$ m, magnetic field $B_0 = 8$ T, deuterium plasma with density $n_i = 10^{20}$ m^{-3}, and temperature $T_i = 5$ keV. For these parameters, the polarization current is in the "low-collisionality" regime and the dominant contribution to it comes from the trapped particles. The background pressure profile is chosen to be flat. Since the diamagnetic frequency is zero in this case, the polarization

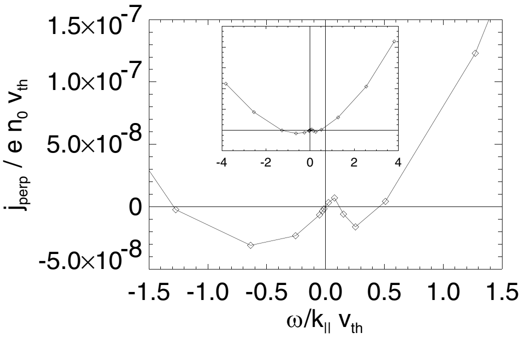

FIG. 2. Perpendicular current around the island as a function of the island rotation frequency normalized to $k_\parallel v_{\rm th}$.

current is predicted to be proportional to ω^2, such that it has two coincident zeros for the case of a nonrotating mode. The perpendicular ion current found in the simulations, however, shows a more complicated behavior. Around $\omega = 0$, the perpendicular current scales nearly linearly with the rotation frequency. This can be understood recalling the fact that in this range the toroidal precession of the trapped particles related with the magnetic-field inhomogeneity dominates over the electric drift. In this case, $j_\perp \propto \mathbf{v}_{td} \cdot \nabla u_\parallel \propto \omega$, where $\mathbf{v}_{td}$ is the toroidal precession velocity. This mechanism explains also the sign reversal which is found for positive ω at about $\omega/k_\parallel v_{\rm th} \approx 0.1$, i.e., for $\omega \approx n\omega_{td}$, where ω_{td} is the precession frequency of trapped thermal ions. In the island's rest frame, this value of ω corresponds to the inversion of the precession direction. Another sign reversal is found in the region $\omega \approx k_\parallel v_{\rm th}$, i.e., for ω of the order of few thousand rad/s. It is seen in the simulations that only if ω reaches this order of magnitude the $E \times B$ drift dominates the motion of the trapped particles around the island so that the particles follow approximately the perturbed flux surfaces. For lower values of the frequency, they show a larger excursion away from the magnetic surfaces due to a competition between electric drift and toroidal precession, and this motion dominates over the polarization drift. This effect is not captured by a fluid treatment or within a slab-geometry description. This second sign reversal, which reflects through the quasineutrality equation on the parallel current entering Eq. (1), is particularly important for the NTM theory, as it occurs in the range where the island rotation frequency is likely to lie. In fact, in different sets of simulations this transition occurs always in the range $\omega \approx k_\parallel v_{\rm th}$, which in the experiment is close to the diamagnetic frequency ω_*, since $\omega_*/k_\parallel v_\parallel = (\rho_p/W) \times (L_q/L_n)$, where L_n is the gradient scale length. This shows that the contribution of the polarization current to the NTM evolution depends critically on the exact value of the rotation frequency even for flat pressure gradients. The interplay between these toroidicity-induced kinetic effects in this frequency range and the physics connected with the interaction with the drift wave described by the sheared-slab gyrokinetic model by Waelbroeck *et al.* [10] still remain an issue for further investigation. At large frequencies, the quadratic scaling of the perpendicular current is found, due to the fact that the advection occurs through the $E \times B$ velocity, so that $j_\perp \propto \mathbf{v}_E \cdot \nabla u_\parallel \propto \omega^2$ as in the standard theory (Fig. 2, small picture). It is interesting to note that in this regime the effect of the polarization current on the island evolution through $j_\parallel$, inferred from $\nabla \cdot \mathbf{j} = 0$ and an estimate of $\nabla_\perp \cdot \mathbf{j}_\perp$ obtained from the simulations, gives a stabilizing influence if the region across the separatrix is neglected, and destabilizing if it is included in the radial integration, according to previous results[11,12].

The second point dealt with in this Letter is the behavior of the polarization current when the island width is comparable to the ion banana width. In this limit, the standard neoclassical approximation that w_b is smaller than any gradient length breaks down. The condition $W \approx w_b$ is experimentally relevant, as it is satisfied in present-day machines at least in the initial phase of a NTM. Since the plasma parameters (in this case the electrostatic potential) are different inside and outside the island, one can suppose that a trapped particle near the island separatrix moves according to a banana-width-averaged potential. It has been shown recently that the bootstrap-current drive of the NTM is significantly reduced with respect to the standard theory if $W \approx w_b$ [13]. In order to isolate the contribution of the "standard" polarization current, simulations at relatively high frequency ($\omega = 10^4$ rad/s, which corresponds to $\omega/k_\parallel v_{\rm th} = 2.5$) have been performed. Moreover, a lower magnetic field ($B_0 = 2$ T) has been taken in order to have $W/w_b \approx 1$ without reducing the island size too much with respect to the minor plasma radius (since this would require a larger number of simulation particles). The other parameters are the same as discussed above. The behavior of $u_\parallel$ at $W \approx w_b$ around the island region is found to be very similar to that of the parallel ion flow due to the pressure gradient in the same limit [13]; i.e., the motion of the trapped particles depends on the variation of the plasma properties across the island separatrix, as expected. For the polarization current, the standard theory ($W \gg w_b$) predicts no dependence on the island width [and hence $j_\parallel^{\rm pol} \propto 1/W^2$ from $\nabla_\parallel j_\parallel = -\nabla \cdot \mathbf{j}_\perp$

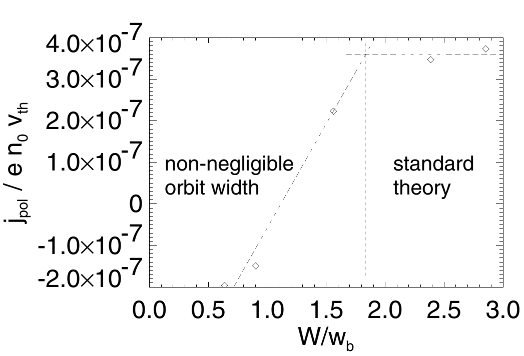

FIG. 3. Polarization current reduction for island widths W comparable to the ion banana width w_b.

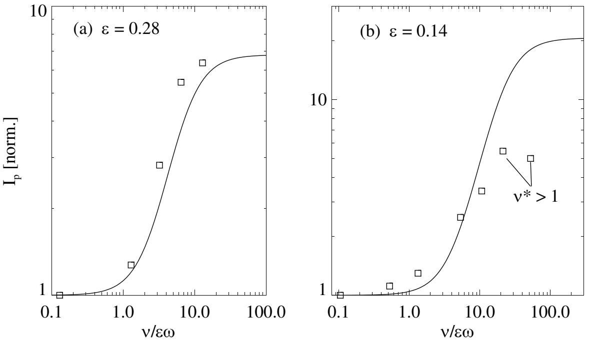

FIG. 4. Dependence of the polarization current on the effective collision frequency $\nu/\varepsilon\omega$. The local inverse aspect ratio ε has been varied by changing the ratio of minor to major radius from 2/3 (a) to 1/3 (b). Analytic predictions [14] are shown for comparison.

and $\nabla_\parallel \propto W$, $\nabla_\perp \propto 1/W$, yielding the known $1/W^3$ scaling of the polarization-current term in the Rutherford equation, cf. Equation (1)]. This can be seen in Fig. 3 to hold only if $W \gtrsim 2w_b$ for the parameters discussed here. The polarization current then decays nearly linearly as a function of W/w_b. The sign reversal shown in the figure for very small island widths comes from the current generated inside the island. Analyzing again the radial profile, it turns out that the parallel current follows a similar trend, due on one hand to the reduction of the gradients outside the island, and on the other hand because of the stabilizing influence of the current inside the island found in the simulations. For too small values of W/w_b, the island width becomes of the order of the ion gyroradius and the drift kinetic approach employed here becomes invalid.

As the last topic, the behavior of the polarization current as a function of the collision frequency is investigated. This collisionality dependence is related to the rate at which the collisional momentum transfer from the trapped particles to the passing particles in the parallel flow $u_\parallel$ occurs. The trapped particles (which undergo a toroidal precession to compensate the poloidal component of $\mathbf{v}_E$) transfer their momentum to the passing particles at a rate ν/ε. If this rate is much smaller than ω (or $k_\parallel v_\parallel$, whichever is the larger), a passing particle can orbit the island many times between two successive collisions, and receives from the trapped particles a momentum input averaged along the island, i.e., flux-surface averaged. The passing-particle component of the parallel flow $u_\parallel$ is therefore constant along the flux surface and does not contribute to $\mathbf{v} \cdot \nabla u_\parallel$ and hence to the polarization current. The only contribution comes from the trapped-particle parallel flow (smaller by a factor $\varepsilon^{3/2}$), which is always connected with the local electric field and hence does vary along the flux surface. On the other side, if $\nu/\varepsilon \gg \omega$ the trapped particles transfer their momentum to the passing particles locally, and the whole $E \times B$ flow varies along the flux surface and contributes to the polarization current, according to the fluid picture mentioned at the beginning. In the simulations shown in Fig. 4, the parameters are the same as given above, except for $B = 6$ T. The high-collisionality regime is reached for rather high values of the collisionality, the normalized collision frequency ν_* being close to unity. The transition can even fall into the plateau regime, then the theoretical upper limit is not reached [Fig. 4(b)]. The simulations are in good agreement with the theoretical curve proposed by Mikhailovskii *et al.* [14]. These results indicate that the transition to the high-collisionality regime can hardly occur in high-temperature plasmas.

The three issues investigated here and connected with the polarization current in the presence of a rotating island show that a complete kinetic description of the particle dynamics in toroidal geometry is indispensable in order to obtain a reliable theory of the NTM. A change of sign, not predicted by the fluid theory, is found for frequencies of the order of $k_\parallel v_{\mathrm{th}}$ even in the absence of a pressure gradient. This shows the importance of kinetic effects in this frequency range. Moreover, the size of the current is usually overestimated in the analysis of the mode evolution. It is demonstrated that it is reduced when the island width is comparable to the ion banana width. The transition to the high-collisionality regime, sometimes invoked to explain the experimental results [15], can hardly be reached in mid-scale and large-scale tokamak experiments. These results point towards a reduction of the role the polarization current in the evolution of the NTM. A contribution to the determination of the NTM threshold can, however, not be excluded.

[1] See National Technical Information Service Document No. DE6008946 (W. X. Qu and J. D. Callen, University of Wisconsin Plasma Report No. UWPR 85-5, 1985). Copies may be ordered from the National Technical Information Service, Springfield, VA 22161.
[2] R. Carrera *et al.*, Phys. Fluids **29**, 899 (1986).
[3] A. I. Smolyakov *et al.*, Phys. Plasmas **2**, 1581 (1995).
[4] H. R. Wilson *et al.*, Phys. Plasmas **3**, 248 (1996).
[5] P. H. Rutherford, Phys. Fluids **16**, 1903 (1973).
[6] O. Sauter *et al.*, Phys. Plasmas **4**, 1654 (1997).
[7] E. Poli *et al.*, Plasma Phys. Controlled Fusion **45**, 71 (2003).
[8] S. D. Pinches *et al.*, Comput. Phys. Commun. **111**, 133 (1998).
[9] A. Bergmann *et al.*, Phys. Plasmas **8**, 5192 (2001).
[10] F. L. Waelbroeck *et al.*, Phys. Rev. Lett. **87**, 215003 (2001).
[11] F. L. Waelbroeck and R. Fitzpatrick, Phys. Rev. Lett. **78**, 1703 (1997).
[12] J. W. Connor *et al.*, Phys. Plasmas **8**, 2835 (2001).
[13] E. Poli *et al.*, Phys. Rev. Lett. **88**, 075001 (2002).
[14] A. B. Mikhailovskii *et al.*, Plasma Phys. Controlled Fusion **42**, 309 (2000).
[15] M. Maraschek *et al.*, Plasma Phys. Controlled Fusion **41**, L1 (1999).

INSTITUTE OF PHYSICS PUBLISHING and INTERNATIONAL ATOMIC ENERGY AGENCY NUCLEAR FUSION

Nucl. Fusion **45** (2005) 384–390 doi:10.1088/0029-5515/45/5/009

Kinetic calculation of the polarization current in the presence of a neoclassical tearing mode

E. Poli, A. Bergmann, A.G. Peeters, L.C. Appel[1] and S.D. Pinches

Max-Planck-Institut für Plasmaphysik, Boltzmannstrasse 2, D-85748 Garching bei München, Germany

[1] EURATOM/UKAEA Fusion Association, Culham Science Centre, Abingdon, Oxon, OX14 3DB, UK

Received 17 December 2004, accepted for publication 18 March 2005
Published 27 April 2005
Online at stacks.iop.org/NF/45/384

Abstract

The polarization current associated with a neoclassical tearing mode (NTM) is studied by means of drift kinetic δf simulations. This current has been invoked as a possible explanation for both the observed threshold for the minimum island size that can grow unstable and the scaling of the plasma pressure at the mode onset with the normalized gyroradius, even though the theory is not able to predict the island rotation direction and hence the role (whether stabilizing or destabilizing) of the polarization current for the island evolution. In the numerical approach presented in this paper, the island rotation frequency can be assigned as an input parameter and the corresponding behaviour of the current can be studied. The calculations are performed in toroidal geometry in the presence of a helical perturbation. It is found that kinetic effects lead to a sign reversal of the polarization current for rotation frequencies close to the diamagnetic frequency even for flat pressure profiles, thus influencing both the sign and size of the polarization-current contribution to the NTM evolution.

PACS numbers: 52.25.Dg, 52.30.Cv, 52.65.Pp, 52.65.Cc

1. Introduction

The tearing mode [1, 2] can be neoclassically destabilized in an otherwise tearing-stable plasma, as it has long been shown both theoretically [3[2], 4] and experimentally [5, 6]. In this case, the mode is driven unstable by the loss of bootstrap current inside an initial ('seed') magnetic island. The magnetic perturbation associated with this drop in the bootstrap current leads to a further growth of the island. A saturated neoclassical tearing mode (NTM) causes a confinement degradation in today's fusion devices, and would significantly reduce the performance of ITER. At present, predictions of the conditions under which the NTM will appear in ITER, and calculations about its possible stabilization, are made difficult mainly by the uncertainties about the physics determining the stability of 'small' islands, i.e. islands with a size comparable to the seed-island size, as is the case in the early phase of the mode, or when the island width is reduced, e.g. through localized current drive [7]. In particular, it is often seen experimentally that the seed island must exceed a given threshold in order for the mode to become unstable. This is an indication that, in these cases, there must be some stabilizing mechanism, acting at small island widths, that balances the neoclassical drive. Among the possible candidates discussed in the literature, the one that has probably received the most attention is the polarization current related to the time-dependent electric field associated with the rotation of the island with respect to the plasma [8, 9]. Actually, whether this contribution to the evolution of the NTM is stabilizing or destabilizing is far from being clear (see [10] for a comprehensive summary). This is basically due to the fact that an accurate description of the physics determining the island rotation frequency is missing, so that the magnitude and even the sign of this frequency are still under debate. Actually, this is not the only uncertainty in the theory of the island polarization current. First of all, its contribution to the NTM evolution has been discussed extensively in the 'low' [9] and 'high' [8] collisionality regimes. It is found that in the low-collisionality regime the polarization current is neoclassically enhanced by a factor $q^2/\sqrt{\varepsilon}$ with respect to the classical value (q is the safety factor and ε the inverse aspect ratio of the resonant rational surface), whereas in the high-collisionality regime the enhancement factor is q^2/ε^2. The value of the collisionality (or, better, of the ratio between

---

[2] See National Technical Information Service Document No DE6008946. Copies may be ordered from the National Technical Information Service, Springfield VA 22161.

the collision frequency and the island rotation frequency) at which the transition between the two regimes takes place is under discussion both experimentally and theoretically. This point is briefly touched upon in the next section. Moreover, in order to isolate the polarization current from the contribution of the parallel ion streaming in the analytic solution of the drift kinetic equation [9], it is to be assumed that

$$\omega \gg k_\parallel v_\parallel, \tag{1}$$

where ω is the island rotation frequency in the plasma rest frame, $v_\parallel$ is the particle velocity parallel to the magnetic field and $k_\parallel \approx (m/Rq)W/L_q$ is the parallel wave vector (m is the poloidal mode number of the perturbation, R is the major radius, W is the island half-width and $1/L_q = (1/q)(\mathrm{d}q/\mathrm{d}r)$ is the inverse scale length of the safety-factor profile q). An investigation of the polarization current for frequencies that do not satisfy the condition expressed by equation (1) is necessary, since the actual value of ω is unknown, and the relevant physics in a full three-dimensional geometry has not been considered so far. This is the aim of this paper.

An accurate determination of the conditions under which an unstable NTM appears in a plasma is a very complicated task, requiring a full understanding of both the seeding process (and hence coupling of perturbations of different helicities [11] and the inclusion of electromagnetic turbulence [12]) and the dynamics of small islands, where the standard neoclassical ordering breaks down [13] and several other effects are believed to play a role (anomalous transport across the island [14,15], interaction with the drift wave [16], pressure variation within the perturbed magnetic surfaces [17], etc). In progressing towards the goal of a self-consistent description of the NTM, it is therefore important to determine which physics ingredients must be taken into account. In this sense, a numerical solution of the drift kinetic equation (as presented in this paper) allows one to explore physical processes that are experimentally relevant but cannot be addressed through a fluid description, a sheared-slab analysis or an analytic approach. It is shown here that a detailed calculation of the ion motion modifies the accepted picture of the NTM polarization current.

This paper is structured as follows. In section 2, a physical picture of the polarization current associated with a rotating magnetic island is given and the basic features of the Rutherford [2] equation used in the NTM theory are recalled. The distribution of the ions (which carry the polarization current) in phase space is calculated by means of a Monte Carlo δf scheme, as outlined in section 3. The results of the numerical simulations are discussed in section 4, while conclusions are drawn in section 5.

2. Physical picture of the polarization current in the presence of a rotating island

Under experimental conditions, a magnetic island, in general, rotates with respect to the surrounding plasma. As mentioned above, there still exists no reliable prediction for the value of the island rotation frequency ω. This issue will not be addressed in this paper. The rotation frequency will be taken as a free parameter in the numerical simulations. The electrostatic potential associated with the island rotation, which determines the island polarization current, is proportional to ω, cf equation (2). In this section, the potential that is used in the simulations is briefly derived and the resulting polarization current is discussed.

In the presence of an island, the magnetic field $\boldsymbol{B}$ can be written as $\boldsymbol{B} = RB_t\nabla\varphi + \nabla\varphi \times \nabla(\psi + \tilde{\psi})$, where B_t is the equilibrium toroidal magnetic field, φ the toroidal angle, ψ the unperturbed poloidal flux and $\tilde{\psi} = \alpha\cos\xi = -RA_\parallel$ is the helical flux perturbation that describes the island, α representing the strength of the perturbation (which can again be treated as an input parameter in the simulations presented in section 4). The helical angle $\xi \equiv m\theta - n\varphi - \omega t$ has been introduced, where m and n are the poloidal and toroidal numbers of the mode and θ is the poloidal angle. The quantity Ω defined as $\Omega \equiv 2(\psi - \psi_s)^2/W_\psi^2 - \cos\xi$ (the subscript s denotes evaluation at the resonant surface and $W_\psi^2 = 4\alpha q_s/q_s'$, the prime indicating differentiation with respect to ψ) can then be used as a flux-surface label, since $\boldsymbol{B}\cdot\nabla\Omega = 0$. With this definition, $\Omega = -1$ corresponds to the O-point of the island, $\Omega = 1$ to the separatrix. It can be shown that the (poloidally averaged) gradient operator along $\boldsymbol{B}$ can be introduced as $\nabla_\parallel = k_\parallel\,\partial/\partial\xi|_\Omega$. The electrostatic potential can be obtained by supposing that the mobile electrons short-circuit the parallel electric field $E_\parallel = -\nabla_\parallel\Phi - (1/c)\partial A_\parallel/\partial t$. Using the identity $\partial A_\parallel/\partial\xi = (qk_\parallel/m)\partial\psi/\partial\xi|_\Omega$, the condition $E_\parallel = 0$ yields

$$\Phi = \frac{\omega q}{mc}[(\psi - \psi_s) - h(\Omega)], \tag{2}$$

where $h(\Omega)$ is a flux-surface function to be determined from the boundary conditions. It can be assumed that the electric field vanishes far away from the island,

$$h(\Omega) \to (\psi - \psi_s) \qquad \text{if } |\psi - \psi_s| \gg W_\psi. \tag{3}$$

A simple choice for $h(\Omega)$ is then [8]

$$h(\Omega) = \frac{W_\psi}{\sqrt{2}}(\sqrt{\Omega} - 1)\Theta(\Omega - 1). \tag{4}$$

Here, W_ψ is defined to have the same sign as $\psi - \psi_s$ and $\Theta(x)$ is the Heaviside step function ($\Theta(x) = 1$ for $x \geqslant 0$ and $\Theta(x) = 0$ otherwise). It can be shown that $n = n_s + n_s' h(\Omega)$, so that equation (4) is consistent with the assumption that the density is flat inside the island [8,9] (in the limit of vanishing perpendicular transport).

The electric field $\boldsymbol{E} = -\nabla\Phi$ can be regarded as composed of two terms, cf equation (2). The first one is proportional to the unperturbed flux ψ and leads to an $E \times B$ rotation of the whole plasma, mainly in the poloidal direction. The term proportional to $h(\Omega)$ vanishes inside the island and damps the electric field far away from it. In other words, the second term in equation (2) represents the potential in the island's rest frame. In this reference frame, the polarization current can be understood more easily. A sheared-slab geometry, in which toroidicity effects are ignored, is considered first. The $E \times B$ flow is faster around the island O-point than around the X-point, cf figure 1. The corresponding acceleration and deceleration of the plasma along the flux surfaces, $\rho\,\mathrm{d}\boldsymbol{v}/\mathrm{d}t$ (ρ is the mass density here), must be balanced by a Lorentz force $\boldsymbol{j} \times \boldsymbol{B}$, where the current is flowing perpendicular to

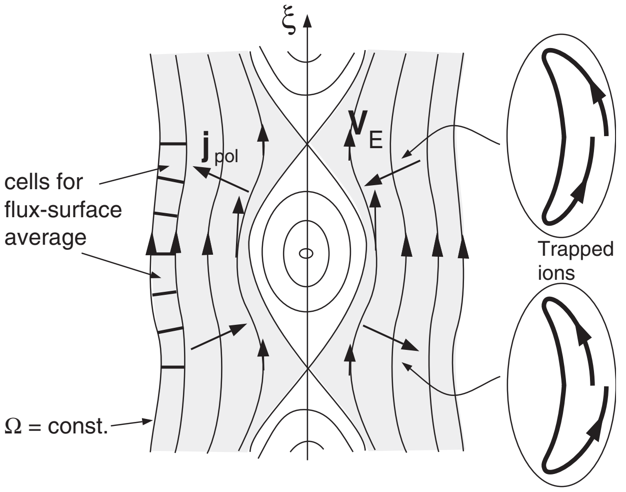

Figure 1. Polarization current j_{pol} in the presence of a magnetic island.

the flux surfaces. This current is the classical polarization current [18],

$$j_{\mathrm{pol}}^{\mathrm{class}} = \frac{en}{\omega_c}\frac{\mathrm{d}v_E}{\mathrm{d}t} = \frac{en}{\omega_c}(\boldsymbol{v}_E \cdot \nabla)v_E. \qquad (5)$$

The picture is slightly more complicated in a toroidal device, where the poloidal rotation is neoclassically damped and a parallel flux $u_\parallel = cE/B_p$ develops in such a way that its poloidal component compensates the poloidal component of the $E \times B$ flow. The neoclassical polarization current, is then [19],

$$j_{\mathrm{pol}}^{\mathrm{nc}} = \frac{en}{\omega_{cp}}(\boldsymbol{v}_E \cdot \nabla)u_\parallel, \qquad (6)$$

which is a factor $B^2/B_p^2 = q^2/\varepsilon^2$ higher than the classical one, because in the latter case the flow that varies along the flux surface is a factor B/B_p larger than in the former case, and the corresponding acceleration in the Lorentz force must be provided by the poloidal component of the magnetic field. As is apparent from equation (6), the polarization current is mainly carried by the ions, which have a larger inertia. If the collision frequency is smaller than the island rotation frequency, only the trapped-particles component of $u_\parallel$ actually varies along the flux surfaces, leading to a reduced neoclassical enhancement [9] $j_{\mathrm{pol}}^{\mathrm{nc}}/j_{\mathrm{pol}}^{\mathrm{class}} = q^2/\sqrt{\varepsilon}$. The transition between the low- and the high-collisionality regime can also be investigated using a Monte Carlo δf approach [20].

The motion of the particles carrying the neoclassical polarization current has been investigated by Hinton and Robertson [19] in connection with the radial field generated by neutral-beam injection. Their results can be applied to the electric field related to the island rotation. A time-varying electric field modifies the orbits of the trapped particles in such a way that a net radial drift (much larger for the ions) is obtained. In the island's rest frame, the trapped particles drifting along the island under the influence of the $E \times B$ flow experience, say, an increasing electric field when moving from the region around the X-point to the region around the O-point, and a decreasing electric field in the opposite case. The corresponding radial drift is schematically depicted on the right-hand side of figure 1. This drift is transferred collisionally to the untrapped particles, yielding the neoclassical polarization current as given by equation (6). However, if the collision frequency is smaller than the island rotation frequency, a trapped particle can drift radially back and forth several times before a collision occurs, so that the collisional momentum transfer to the passing particles flux-averages to zero and the polarization current is carried by the trapped ions alone. In this case, the neoclassical enhancement factor is $q^2/\sqrt{\varepsilon}$, as discussed above. This will be the situation considered in the simulations presented in section 4.

The polarization current (perpendicular to $\boldsymbol{B}$) is closed by a parallel electron current to ensure charge neutrality, $\nabla \cdot \boldsymbol{j} = 0$. This parallel current contributes to the NTM evolution as described by the Rutherford equation, which is obtained by substituting $j_\parallel^{n.i.}$ into [4, 9]

$$\frac{4\pi}{1.22\eta c^2}\frac{\mathrm{d}W}{\mathrm{d}t} = \frac{\Delta'}{2} + \frac{4\sqrt{2}}{c}\frac{qR}{sBW}\int_{-1}^{\infty}\mathrm{d}\Omega \oint \frac{\mathrm{d}\xi\cos\xi}{\sqrt{\cos\xi+\Omega}}\, j_\parallel^{n.i.}. \qquad (7)$$

In equation (7), η is the neoclassical resistivity, Δ' is the usual tearing stability parameter [2] and $s = (r/q)\mathrm{d}q/\mathrm{d}r$ is the magnetic shear (r being the minor radius). The contribution to $j_\parallel^{n.i.}$ due to the polarization current is found to scale proportional to $1/W^2$, leading to a term proportional to $1/W^3$ in equation (7). This explains why the polarization current is particularly important in the initial phase of the NTM, when the island width is small. The scaling $j_\parallel^{\mathrm{pol}} \propto 1/W^2$ is due to the fact that in $\nabla_\parallel j_\parallel = -\nabla_\perp \cdot \boldsymbol{j}_\perp$ one has $\nabla_\parallel \propto k_\parallel \propto W$ and $\nabla_\perp \propto 1/W$. The (perpendicular) polarization current itself is independent of the island size because $\boldsymbol{v}_E$ and its derivative along the $\boldsymbol{v}_E$ direction do not depend on W; cf equation (5) or equation (6). The limits of validity of the picture outlined in this section are discussed below on the basis of Monte Carlo δf solutions of the ion drift-kinetic equation.

3. The Monte Carlo δf approach

The calculation of the polarization current in a three-dimensional geometry relies on the solution of the drift kinetic equation,

$$\frac{\mathrm{d}f}{\mathrm{d}t} = \frac{\partial f}{\partial t} + (v_\parallel\hat{\boldsymbol{b}} + \boldsymbol{v}_d + \boldsymbol{v}_E)\cdot\frac{\partial f}{\partial \boldsymbol{r}} - \frac{e}{m_i}\frac{\boldsymbol{v}_d\cdot\nabla\Phi}{v}\frac{\partial f}{\partial v} = C(f) \qquad (8)$$

in a toroidal geometry, including the presence of the island in the magnetic configuration. In equation (8), f is the ion distribution function, $\boldsymbol{v}_d$ and $\boldsymbol{v}_E$ are the magnetic and electric drift velocities, e and m_i are the charge and the mass of the ions and C is the pitch-angle scattering operator. The parallel electric field $E_\parallel$ has been set to zero in equation (8), since it is assumed to be immediately short-circuited by the electrons (cf [9]). In this paper, the δf method is employed. The distribution function is written as the sum of a time-independent analytically known bulk term f_0 and a deviation δf to be evaluated numerically. The equation for δf is, then,

$$\frac{\mathrm{d}(\delta f)}{\mathrm{d}t} = C(\delta f) - \boldsymbol{v}_d\cdot\nabla f_M - \frac{ef_M}{T}\boldsymbol{v}_d\cdot\nabla\Phi, \qquad (9)$$

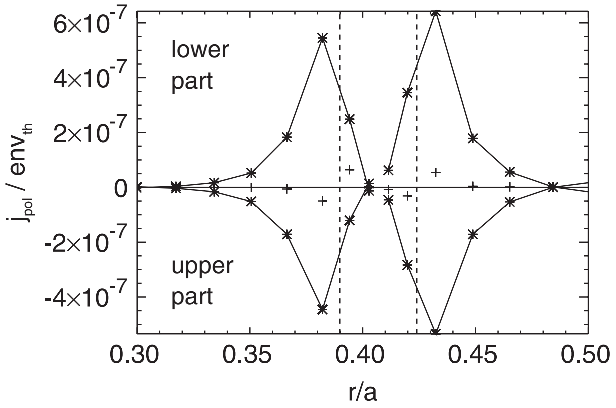

Figure 2. A typical radial profile of the polarization current j_{pol} (normalized to $en_e v_{\mathrm{th}}$) as obtained from the Monte Carlo δf simulations. The current flows in the lower and in the upper part of the island in opposite directions, cf figure 1.

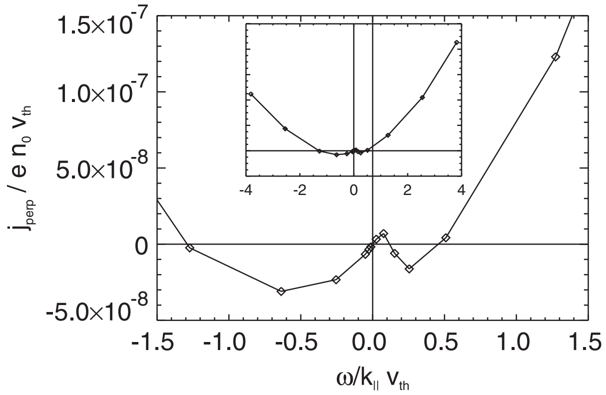

Figure 3. The perpendicular current $j_\perp$ as a function of the island rotation frequency ω (normalized to the parallel streaming frequency $k_\parallel v_{\mathrm{th}}$).

where the right-hand side of equation (9) represents the ‘source’ that leads to a deviation from f_0, supposed here to be a Maxwellian f_M. No assumption is made here about the magnitude of δf as compared to f_0, so that equation (9) is completely equivalent to equation (8). However, computational time is saved with respect to a full-f solution if $|\delta f| \ll |f_0|$, as is usually the case since $|\boldsymbol{v}_d, \boldsymbol{v}_E| \ll v_{\mathrm{th}}$. This numerical scheme is pretty similar to that already described in detail in previous papers, where it was used to study near-axis neoclassical transport [21] and bootstrap current in the presence of an island [22]. The evolution of the system is represented by means of ‘markers’, which span the whole phase space and represent the ions. They evolve according to the equations of motion, which are integrated by means of the code HAGIS [23]. Collisions are implemented by means of a momentum-conserving Monte Carlo procedure [21].

The magnetic equilibrium is specified analytically to save computational time. The unperturbed magnetic surfaces are circular and concentric. A magnetic perturbation of given helicity can be assigned by choosing the mode amplitude $\alpha \propto W^2$ and the mode rotation frequency ω (contained in ξ), as explained in section 2. No evolution of W and ω is considered. Flux-surface averages are obtained by integrating in space between neighbouring surfaces. For quantities which flux-surface average to zero, a further refinement in the spatial integration is obtained by introducing smaller cells in the ξ-direction (figure 1). A typical polarization-current profile is shown in figure 2, where a cut through the O-point in the radial direction has been taken to highlight the presence of the island. It can be seen that the contributions originating from the upper and lower parts of the island average to zero within the numerical accuracy. A knowledge of the profile is important in order to deduce the behaviour of the parallel closure current, as discussed at the end of the next section.

4. Numerical results

In the numerical simulations, the following parameters have been employed: major radius $R = 8\,\mathrm{m}$, magnetic field $B_0 = 8\,\mathrm{T}$, deuterium plasma with density $n_i = 10^{20}\,\mathrm{m}^{-3}$, temperature $T_i = 5\,\mathrm{keV}$. A flat background pressure profile is taken and no bootstrap current is generated. The only contribution to the parallel flow is then due to the island electric field. An island width $W = 6.8\,\mathrm{cm}$ has been taken, which corresponds to $W/w_b = 9.6$ and $W/a = 0.017$, where w_b is the (thermal) ion banana width and a is the minor radius. A discussion of the behaviour of the polarization current in the limit $W \approx w_b$ (for which the neoclassical ordering breaks down) will be performed in a separate paper. Since the perpendicular current is zero when flux-surface averaged, it is calculated here as $j_\perp \equiv (j_\perp^{\mathrm{lower}} - j_\perp^{\mathrm{upper}})/2$, where the superscripts refer to the lower (from the X-point to the O-point) and upper (O-point to X-point) parts of the island, see figure 1. The poloidal and toroidal mode numbers in the simulations are $m = 3$, $n = 2$. The behaviour of $j_\perp$ as a function of ω is discussed, beyond the limitation expressed by equation (1). The results of the simulations are shown in figure 3, where $j_\perp$ is radially averaged over a region lying within a distance of $4W$ from the resonant surface. Since the pressure gradient is zero in these simulations, the polarization current could be expected to scale as $j_\perp \propto \omega^2$, consistently with equation (5) and the fact that $\Phi \propto \omega$, equation (2). The actual behaviour of $j_\perp$ is much more complicated, indicating that other physical processes are involved.

An analysis of the particle motion in the island potential helps us understand the features of figure 3. It turns out that for frequencies in the range $-1 \lesssim \omega/k_\parallel v_{\mathrm{th}} \lesssim 1$ (where in these simulations $k_\parallel v_{\mathrm{th}} = 3.9 \times 10^3\,\mathrm{s}^{-1}$), the toroidal drift of the trapped particles cannot remain out of consideration. The motion of a trapped particle for $\omega/k_\parallel v_{\mathrm{th}} \simeq 0.15$ and $\omega/k_\parallel v_{\mathrm{th}} \simeq 0.77$ is shown in figure 4. In figure 4(a), the island rotation frequency and the toroidal precession frequency ω_{tp} are comparable. This modifies the fluid picture of figure 1, where only the $E \times B$ drift in the island’s electric field is considered. The result of this combination of electric and magnetic drifts is a deviation from the perturbed flux surface under the influence of the radial component of the $E \times B$ velocity, which dominates over the polarization drift. The direction of this radial drift depends on whether the toroidal precession is slower or faster than the island rotation, as can be seen in figure 5(a), where particles having $v/v_{\mathrm{th}} \approx 2.3$ precess at the same speed at which the island is rotating, $\omega_{\mathrm{tp}} \approx \omega/2$ (the toroidal mode number is here $n = 2$). This

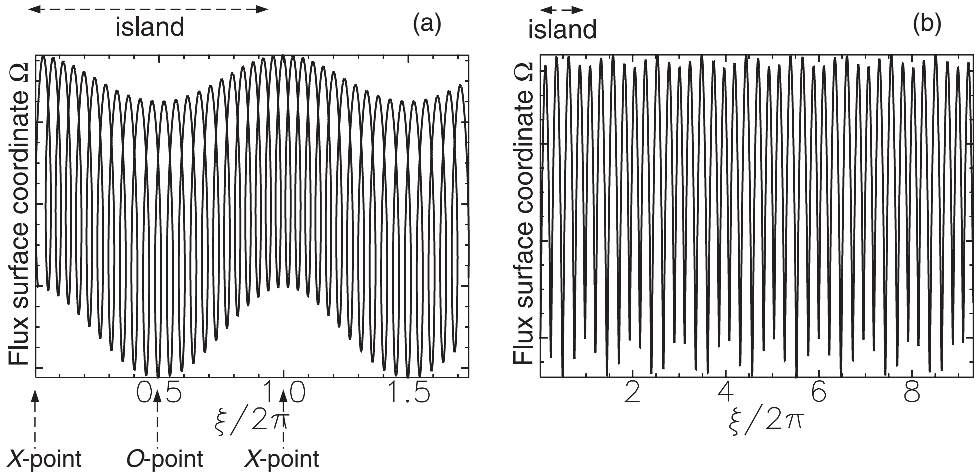

Figure 4. Motion (with respect to the perturbed-surface label Ω) of a 3 keV trapped ion drifting beside a magnetic island. The island rotation frequencies are $\omega = 600\,\mathrm{rad\,s^{-1}}$ (*a*) and $\omega = 3000\,\mathrm{rad\,s^{-1}}$ (*b*). Motion along the whole island corresponds to $\Delta\xi/2\pi = 1$.

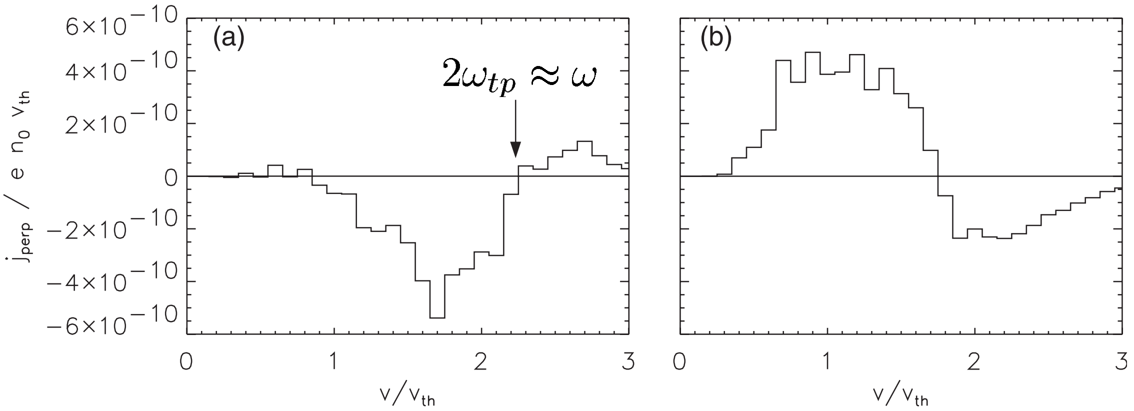

Figure 5. Velocity distribution of the perpendicular current $j_\perp$ in the first outer cell after the island separatrix for $\omega/k_\parallel v_{\mathrm{th}} = 0.15$ (*a*) and $\omega/k_\parallel v_{\mathrm{th}} = 0.51$ (*b*).

explains the sign reversal in $j_\perp$ (see figure 3) for $\omega/k_\parallel v_{\mathrm{th}} \simeq 0.1$. When the island rotation frequency becomes larger and larger, the toroidal precession becomes less and less important so that the trapped particles bounce following, on average, the perturbed flux surface as in the fluid picture (cf figure 4(*b*), where the perturbed flux surfaces are represented by horizontal lines) and the polarization drift becomes comparable with the combination of electric and magnetic drift described above. This happens first for low-energy particles, which have a correspondingly small precession frequency ($\omega_{\mathrm{tp}} \propto v^2$), as can be observed in figure 5(*b*), where the motion of thermal particles is dominated by the polarization drift, whereas for suprathermal particles the toroidal precession is still not negligible. Moreover, it can be seen from figure 5(*b*) that the polarization drift and this precession-induced drift are in opposite directions, leading to the second sign reversal seen in figure 3 for ω of the order of the parallel streaming $k_\parallel v_{\mathrm{th}}$. This sign reversal is particularly important, because it occurs for values of ω that lie in the range where it is expected to be experimentally, i.e. close to the diamagnetic frequency. It is noted that $\omega_*/k_\parallel v_\parallel \simeq (\rho_p/W)(L_q/L_n)$, which is close to unity, at least when the island is not fully developed. This transition is not captured by a fluid approach, or by a kinetic treatment in a slab geometry. It is also interesting to note that in the range where the 'standard' polarization current is found, ω starts to be comparable to the bounce frequency of the ions ω_b and the ion motion is the result of the superposition of the two periodic motions (figure 6(*a*)). This is confirmed by a Fourier analysis of the trapped-particle trajectory (figure 6(*b*)). It is found in the simulations that slow particles with $\omega_b \lesssim \omega$ do not contribute to (or even reduce the value of) $j_\perp$.

It is recalled that the polarization current contributes to the island evolution through its parallel closure, which can be obtained by integrating the continuity equation $\nabla_\parallel j_\parallel = -\nabla_\perp \cdot \boldsymbol{j}_\perp$. One could wonder whether the sign reversal found for $j_\perp$ also holds for $j_\parallel$. If one evaluates the contribution of the parallel current to the island stability using the simulated radial profiles and the current continuity equation, it turns out that the polarization current is stabilizing if the region across the island separatrix is excluded from the radial integration, while it is destabilizing if it is included, according to the present theoretical understanding [24]. This clearly shows that a major role is played by the current profile across the island separatrix. Analysing the simulated $j_\perp$-profiles, one can deduce that the different sign of $j_\perp$ around $\omega = \mathcal{O}(k_\parallel v_{\mathrm{th}})$ corresponds to a different sign of $j_\parallel$, implying a different contribution of the polarization current to equation (7).

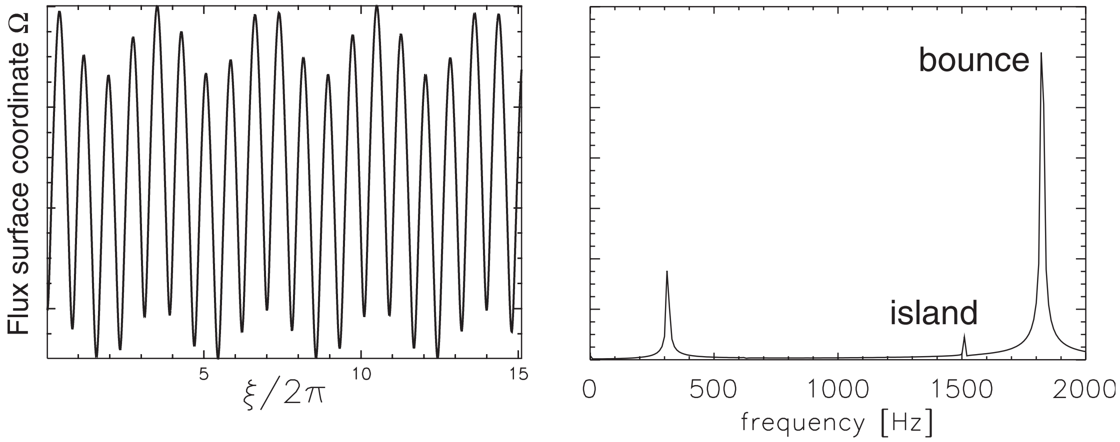

Figure 6. Trajectory of a 3 keV trapped particle with respect to the perturbed flux surfaces (*a*) and its Fourier transform (*b*) for an island rotation frequency $\omega/2\pi = 1.53$ kHz. The bounce frequency is $\omega_b/2\pi = 1.83$ kHz. The peak on the left corresponds to a frequency $(\omega_b - \omega)/2\pi$.

5. Summary and conclusions

The polarization current due to a rotating magnetic island has been studied in this paper employing drift kinetic δf simulations. A drift kinetic approach was employed by Carrera *et al* [4] to describe the neoclassical drive due to the drop of the bootstrap current inside the island and by Wilson *et al* [9] to investigate the role of the polarization current in a low-collisionality tokamak. The numerical approach enables one to investigate a broader parameter range than allowed by the analytic three-dimensional theory. In the calculations presented in this paper, the island width is supposed to be much larger than the ion banana width, i.e. the drift kinetic equation can be employed for the solution of the problem as usually done in neoclassical theory. It is interesting to note that the numerical method explained in section 3 allows one to explore the limit where the neoclassical ordering breaks down and $w_b \approx W$, as long as the island width remains much larger than the gyroradius (which seems to be usually the case in the experiment; for instance, the initial island width measured in ASDEX Upgrade is usually above 1 cm). The limit $w_b \approx W$, however, is not addressed here. Only the ions are described by the simulation markers, and the potential is prescribed. The electrons just short-circuit the parallel electric field. An extension of the analysis to include self-consistent potentials and the electron dynamics would be very interesting and is planned for the future. Anyway, the results presented in the paper are rather insensitive to the details of the electric potential around the separatrix, if the boundary condition expressed in equation (3) is assumed. Substituting the function $h(\Omega)$ given by equation (4), which corresponds to equation (42) of [25], with a different profile function, like equation (43) proposed in the same paper, $h(\Omega) = (W_\psi/\sqrt{2})(\sqrt{\Omega+1}/\sqrt{2} - 1)\Theta(\Omega - 1)$, merely leads to some shifts of the values of $j_\perp$. The general picture, however, remains the same as described in the preceding sections.

Kinetic effects have a strong impact on the simple fluid picture of the polarization current. In particular, the toroidal precession modifies the motion of the trapped particles along the island. The resulting combination of electric and magnetic drifts leads to a (mainly radial) motion, which dominates over the polarization drift when $\omega \approx \omega_{\mathrm{tp}}$. For frequencies of the order of $k_\parallel v_{\mathrm{th}}$ (which is used as a measure of the diamagnetic frequency), the drift kinetic analysis presented here shows that the polarization current goes through zero even in the absence of any pressure gradients both for positive and negative ω. A semianalytic evaluation of the sign of the parallel closure current based on the simulated $j_\perp$-profiles yields a similar behaviour as found for the perpendicular current. This demonstrates that a full toroidal treatment of kinetic effects is necessary in order to have reliable predictions of the behaviour of the neoclassical polarization current and of its role for NTM stability.

References

[1] Furth H.P., Killeen J. and Rosenbluth M.N. 1963 *Phys. Fluids* **6** 459

[2] Rutherford P.H. 1973 *Phys. Fluids* **16** 1903

[3] Qu W.X. and Callen J.D. 1985 *University of Wisconsin Plasma Report* No UWPR 85-5

[4] Carrera R., Hazeltine R.D. and Kotschenreuther M. 1986 *Phys. Fluids* **29** 899

[5] Chang Z. *et al* 1995 *Phys. Rev. Lett.* **74** 4663

[6] Sauter O. *et al* 1997 *Phys. Plasmas* **4** 1654

[7] Zohm H. 1997 *Phys. Plasmas* **4** 3433

[8] Smolyakov A.I., Hirose A., Lazzaro E., Re G.B. and Callen J.D. 1995 *Phys. Plasmas* **2** 1581

[9] Wilson H.R., Connor J.W., Hastie R.J. and Hegna C.C. 1996 *Phys. Plasmas* **3** 248

[10] Mikhailovskii A.B. 2003 *Contrib. Plasma Phys.* **43** 125

[11] Hegna C.C. and Callen J.D. 1992 *Phys. Fluids* B **4** 1855

[12] Itoh S.I., Itoh K. and Yagi M. 2004 *Plasma Phys. Control. Fusion* **46** 123

[13] Poli E., Peeters A.G., Bergmann A., Günter S. and Pinches S.D. 2002 *Phys. Rev. Lett.* **88** 075001

[14] Fitzpatrick R. 1995 *Phys. Plasmas* **2** 825

[15] Konovalov S.V., Mikhailovskii A.B., Ozeki T., Takizuka T., Shirokov M.S. and Hayashi N. 2004 *Proc. 20th Int. Conf. on IAEA Fusion Energy 2004 (Vilamoura, 2004)* (Vienna: IAEA) CD-ROM file TH/P4-43 and http://www-naweb.iaea.org/napc/physics/fec/fec2004/datasets/index.html

[16] Waelbroeck F.L., Connor J.W. and Wilson H.R. 2001 *Phys. Rev. Lett.* **87** 215003

[17] Smolyakov A.I. and Lazzaro E. 2004 *Phys. Plasmas* **11** 4353
[18] Wesson J.A. 1997 *Tokamaks* 2nd edn (Oxford: Oxford University Press) p 84
[19] Hinton F.L. and Robertson J.A. 1984 *Phys. Fluids* **27** 1243
[20] Bergmann A., Peeters A.G. and Poli E. Collisionality dependence of the polarization current caused by a rotating magnetic island *Phys. Plasmas* submitted
[21] Bergmann A., Peeters A.G. and Pinches S.D. 2001 *Phys. Plasmas* **8** 5192
[22] Poli E., Peeters A.G., Bergmann A., Günter S. and Pinches S.D. 2003 *Plasma Phys. Control. Fusion* **45** 71
[23] Pinches S.D. *et al* 1998 *Comput. Phys. Commun.* **111** 133
[24] Waelbroeck F.L. and Fitzpatrick R. 1997 *Phys. Rev. Lett.* **78** 1703
[25] Connor J.W., Waelbroeck F.L. and Wilson H.R. 2001 *Phys. Plasmas* **8** 2835

IOP Publishing and International Atomic Energy Agency Nuclear Fusion
Nucl. Fusion **48** (2008) 054012 (11pp) doi:10.1088/0029-5515/48/5/054012

Physics analysis of the ITER ECW system for optimized performance

G. Ramponi[1], D. Farina[1], M.A. Henderson[2], E. Poli[3], O. Sauter[2], G. Saibene[4], H. Zohm[3] and C. Zucca[2]

[1] Istituto di Fisica del Plasma, EURATOM-ENEA-CNR Association, Milano, Italy
[2] CRPP, EURATOM–Confédération Suisse, EPFL, CH-1015, Lausanne, Switzerland
[3] IPP-Garching, Max-Planck-Institut für Plasmaphysik, D-85748 Garching, Germany
[4] EFDA Close Support Unit, Boltzmannstrasse 2, D-85748 Garching, Germany

Received 23 July 2007, accepted for publication 2 November 2007
Published 8 April 2008
Online at stacks.iop.org/NF/48/054012

Abstract

A predictive analysis of the capabilities of the ITER electron cyclotron wave system is presented in this work. Modifications of both the upper launcher and the equatorial launcher aimed at increasing the potentialities of the system are identified and discussed. A modification of the upper launcher has already been incorporated in the updated front steering design called the extended physics launcher. By adopting different deposition ranges for the upper and lower steering mirrors, this design offers the flexibility to drive current from the radial region required for the stabilization of neoclassical tearing modes (NTM) up to that required for sawtooth control, allowing a synergy with the equatorial launcher. Here a comparison of the performance of the new design of the upper launcher with those of a dropped upper launcher is performed, showing that better performance for both NTM stabilization and sawtooth control may be obtained by lowering the upper port location. An analysis of the EC current driven by the equatorial launcher is also presented, showing that adding to the present design the possibility to drive counter-current in addition to the existing co-current capability would increase the flexibility of the system. The behaviour of all launchers at reduced magnetic fields is also discussed.

PACS numbers: 52.35.Hr, 52.50.Sw, 52.55.Fa

(Some figures in this article are in colour only in the electronic version)

1. Introduction

The ITER electron cyclotron wave (ECW) system consists of up to 24, 170 GHz gyrotrons, 1–2 MW each, connected to one launcher situated in one equatorial port (EL) or four launchers situated in the upper ports (UL), for a nominal injected power of 20 MW. Both the UL and the EL will launch wave beams polarized as ordinary mode (O-mode) in the case of magnetic fields close to the nominal one ($B_T = 5.3$ T) or such that the EC wave resonates as first harmonic inside the plasma, polarized as extraordinary mode (X-mode) in the case of B_T in the range of second harmonic. Key objectives of the whole system are central heating, q profile control and stabilization of magnetohydrodynamic (MHD) instabilities, mainly neoclassical tearing modes (NTM) and sawteeth. The two launchers systems have different current drive characteristics: the EL, where the beams are steered in the toroidal direction, gives broad driven current density (j_{CD}) profiles and high driven current (I_{cd}), good for central deposition and current profile control, while the UL, where the beams are steered in the poloidal direction, may allow narrow j_{CD} profiles, good for controlling MHD activity such as NTM and sawteeth. However, to fulfil all the above-mentioned goals, both systems should be optimized such as to adequately cover the largest operational domain possible.

We recall that up to the end of 2005 the exclusive goal assigned to the UL (based on three upper ports) was NTM stabilization, while all other functions were ascribed to the EL. Detailed beam tracing calculations have been carried out by means of two beam tracing codes, GRAY [1] and TORBEAM [2], with the goal of evaluating the performance of the UL for NTM stabilization considering a number of different mm-wave designs proposed for the remote steering (RS) and the front steering (FS) launcher options, as part of EFDA technology tasks [3]. The analysis of all launcher design options has been based on three selected H-mode scenarios (scenarios 2, 3 and 5) having considerably different q, T, n and bootstrap current profiles at one time slice (end of burn or EOB) [4] (see also table 1). To account for the uncertainties in the detailed predictions of the ITER plasma profiles, both the equilibrium database and the analysis have been extended to include variations of the poloidal beta β_p and of the internal

Table 1. Parameters of the ITER H-mode reference scenarios.

Scenario	I_p (MA)	β_N	n_{e0} (10^{20} m^{-3})	T_{e0} (keV)	$\rho_{tor2/1}$	J_{bs} ($\rho_{2/1}$) (MA m^{-2})	$\rho_{tor3/2}$	J_{bs} ($\rho_{3/2}$) (MA m^{-2})
EOB2	15	1.8	1.02	24.8	0.75	0.073	0.62	0.094
EOB3	12	2.2	0.86	31.8	0.67	0.120	0.56	0.147
EOB5	17	2.1	1.24	29.5	0.78	0.096	0.67	0.111

inductance l_i representative of typical variations observed in JET and ASDEX Upgrade H-modes with q_{95} between 3 and 4. Only the two modes having the most severe effects on plasma confinement, namely (2,1) and (3,2), have been included in the analysis. The radial range of interest, representative of likely locations of the 3/2 and 2/1 q surfaces in most NTM-prone ITER plasmas, turned out to be from $\rho_{tor} \sim 0.55$ to $\rho_{tor} \sim 0.85$ (ρ_{tor} being the square root of the normalized toroidal flux). This set of conditions established the access requirements for the UL, and provided the basis for the definition of the steering range. Considering that the main effect of ECCD in stabilizing the NTM is to drive a helical current within the island to compensate the missing bootstrap current j_{bs}, $\eta_{NTM} = j_{ECCD}/j_{bs}$ has been defined as the NTM stabilization efficiency. Further, we adopted a criterion to evaluate the launcher performance based on a fit to experimental data [5], i.e. η_{NTM} has to be above 1.2 at $q = 2$ and $q = 3/2$ flux surfaces of all the H-mode reference scenarios considered. The analysis showed that, provided an 'optimal' fixed toroidal injection angle and well collimated beams are used, the FS launcher exceeds the requirements by a large margin, bringing the power requirement down to 2/3 of the installed 20 MW [6].

Since the FS design offers appreciable reserve in η_{NTM}, a new variant of the UL has been designed that, by adopting different deposition ranges for upper and lower mirrors, offers the flexibility to increase the access range beyond that required by the NTM stabilization, thus allowing a synergy between UL and EL [7]. Besides providing good values of η_{NTM}, this new variant, called extended physics launcher (EPL), allows to drive well-localized current density up to the $q = 1$ location. This makes it attractive for additional applications besides active NTM stabilization, as, for instance, plasma current tailoring, control of a (4,3) mode in order to achieve a 'frequently interrupted regime' (FIR) and sawtooth control. In the FIR regime the growth of (3,2) NTM is often interrupted by ergodization due to its nonlinear coupling to an ideal (4,3) mode. On ASDEX Upgrade it has been shown that lowering the magnetic shear with co-ECCD just outside the radius of the $q = 4/3$ flux surface triggers the transition to this regime [8]. Sawtooth activity is of primary importance for ITER where the energetic alpha particles are expected to transiently stabilize the internal kink modes, allowing the radius of the $q = 1$ surface to expand and periods between crashes to become long [9]. The crashes events terminating long sawtooth free periods can provide 'seed islands' for the NTMs [10]. Therefore sawteeth destabilization, i.e. shortening the sawtooth period, may prevent destabilization of the NTMs. It has also been shown, both theoretically and experimentally, that localized co-CD just inside (or counter-CD just outside) the $q = 1$ surface may shorten the sawtooth period [11, 12]. The effectiveness in controlling the sawtooth period depends on the capability of ECCD to modify the evolution of the magnetic shear at the $q = 1$ surface, i.e. on the radial derivative of the driven current profile [13].

All this leads to the conclusion that the efficiency for all the objectives of the EPL increases with more localized, higher current density profiles. A larger efficiency means that less power is required to fulfil the objective. Minimizing the EC power is in itself an important issue for ITER since this will limit the deterioration of the fusion gain Q [14]. The optimization of the EC current driven by the EPL has been carried out with respect to the injection angles and the beam parameters, by considering the present upper port location. However, additional optimization of the driven current density profiles may be obtained by lowering the upper port location, due to a greater localization occurring when the EC beam travels tangentially to the flux surface in the neighbourhood of the absorption region [15, 16]. Here a variant of the EPL is considered. We refer to this variant in terms of dropped upper launcher (DUL), which is similar to the EPL except for the fact that it is lowered by approximately 65 cm (one blanket shield module).

As far as the equatorial launcher is concerned, we point out two possible modifications of the present design. Note that one of the main applications foreseen for the EL is central heating, that might be required, for example, to go above the L–H threshold or to control the density peaking during the early stage of the scenario, as currently done in experiments [17]. Presently central heating can only be provided with co-current drive (co-CD), which might lead to excessive peaking of the current density profile in the standard scenario 2, to early onset of $q = 1$ surface in the hybrid scenario 3 or even to prevent the development of steady state scenario 4. Recent experimental results demonstrated the advantages of using counter-ECCD for q profile control in advanced scenarios or balanced co- and counter-ECCD to achieve 'pure' heating [18, 19]. Extending the present design of the EL to have at least one of the three rows of beams providing counter-ECCD would allow to nearly cancel out the current drive effects on the plasma current profile whenever 'pure' heating is required. Moreover, this would improve the flexibility of the system for central q control, since three actuators, i.e. central co-ECCD, counter-ECCD and heating, would be made available. An additional useful modification is the possibility of launching poloidally tilted beams from the top and low steering mirrors in order to improve their capability of accessing the core plasma region.

The paper is organized as follows. In section 2 a comparison of the efficiencies for NTM stabilization and sawteeth control of the EPL and the DUL is presented. In section 3 the capabilities of the EL are shown and the potential effects of central co- and counter-ECCD on the q profile of the inductive scenario 2, the hybrid scenario 3 and the reverse shear scenario 4 are discussed. In section 4 an overview of the capabilities of all launchers at reduced magnetic fields is

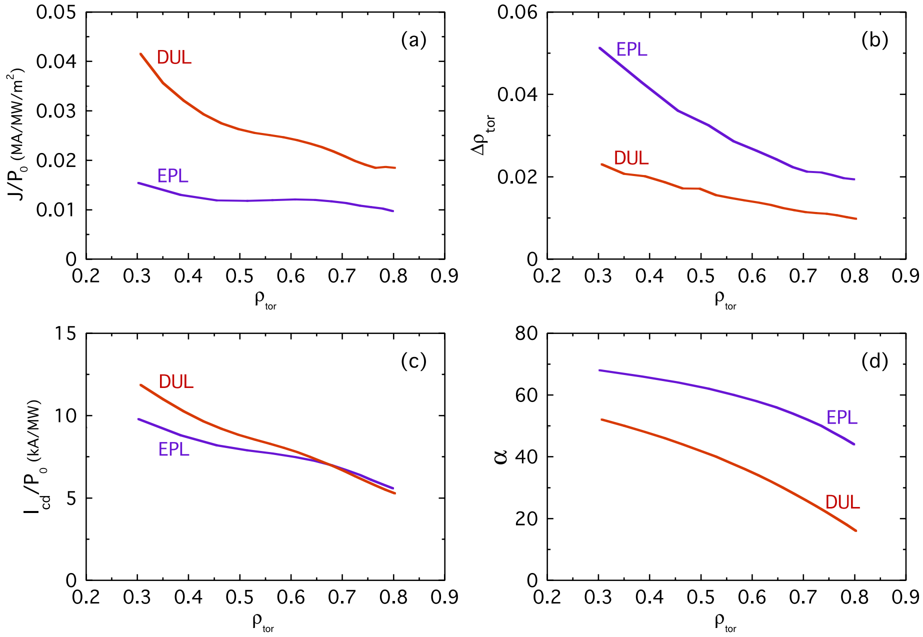

Figure 1. Peak of the driven current density (*a*), normalized width at $1/e\Delta\rho_{\rm tor}$ (*b*), total driven current (*c*) and poloidal steering angle (*d*) as a function of the radial location $\rho_{\rm tor}$ for 1 MW of injected power into the plasma of scenario 2 (EOB2) from the USM of the DUL and of the EPL with toroidal injection angle $\beta = 20°$.

presented. The last section is devoted to some concluding remarks.

2. Comparison of the EPL and DUL performances

The EPL consists of four launchers, each housing eight beams, and two steering mechanisms, positioned at different heights in the present upper port plug. The two steering mirrors are identified as upper steering mirror (USM) and lower steering mirror (LSM). A switching system prior to the port entrance can deviate the beams coming from the 24 gyrotrons to either the 16 entrances associated with the USM or the 16 entrances with the LSM; therefore the maximum power that can be injected from each set of steering mirrors is ∼13.3 MW. The lower set is dedicated to covering the outer region of the plasma, i.e. $0.55 \leqslant \rho_{\rm tor} \leqslant 0.85$, and the upper set to accessing radial range $0.3 \leqslant \rho_{\rm tor} \leqslant 0.8$. In the region of overlap, the injected power may reach 20 MW. The main physics objectives of this launcher are NTM stabilization and sawtooth control.

As already mentioned, the optimization study for the EPL has been carried out with respect to the toroidal injection angles to find the 'optimal' compromise between the driven current and the Doppler shift broadening and with respect to the beam parameters to find the 'optimal' beam size. Using well-collimated beams with focus inside the plasma and 'optimal' toroidal injection angles, values in excess of the requirements in the figures of merit for both NTM stabilization and sawteeth control have been achieved [20]. Here, considering that additional optimization of the driven current density profiles is obtainable lowering the launching location, namely using the 'DUL', we shall compare the performances of the two launchers in terms of the figures of merit for their main physics objectives.

The ECCD calculations by the GRAY code have been carried out for both steering mirrors of the EPL and the DUL having the following locations: EPL_LSM: (R, Z)=(6.90 m, 4.18 m); DUL_LSM = (R, Z)=(7.70 m, 3.55 m); EPL_USM: (R, Z)=(6.85 m, 4.39 m); DUL_USM = (R, Z)= (7.56 m, 3.73 m). The same circular, well-collimated beams, proved to be 'optimal' for EPL, have been used to compare the two launchers: the beam launched from the LSM locations has its waist $w_0 = 2.1$ cm at a distance +1.62 m from the steering mirror (+ means towards the plasma) while that launched from the USM has its waist $w_0 = 2.9$ cm at a larger distance from the mirror (+2.13 m). The beams are launched with fixed toroidal angle β, where β is the angle between the vertical plane containing the beam line and the vertical plane containing a major radius, and are steered by varying the poloidal angle α, i.e. the angle between the horizontal and the projection of the beam line on the plasma cross section. The comparison is performed for $\beta = 20°$ (except for EPL_LSM where $\beta = 18°$ in the range of radial locations that has been chosen for the EPL.

Figures 1 and 2 show the peak values of the current density profiles, their normalized full widths at $1/e$ ($\Delta\rho_{\rm tor}$), the driven currents and the poloidal steering ranges for USM and LSM injection into the plasma of scenario 2 (EOB2). The better performance of the DUL is evident mainly at the innermost surfaces. This is mainly due to the better relation between the launcher location and the geometry of flux surfaces providing narrower current density profiles. In addition, larger values of the driven current are obtained due to the larger local values of $n_{||}$. In the case of USM (figure 1), an increase in the driven current density by a factor of up to 2.6 (at $\rho_{\rm tor} = 0.3$) and a substantial reduction in the profile width (up to a factor 0.5) are obtained. We note, however, that a larger steering range is required for the DUL to cover the same radial region as covered by the EPL. For instance, while with the DUL_USM the steering range required to drive current from $\rho_{\rm tor} = 0.8$ to

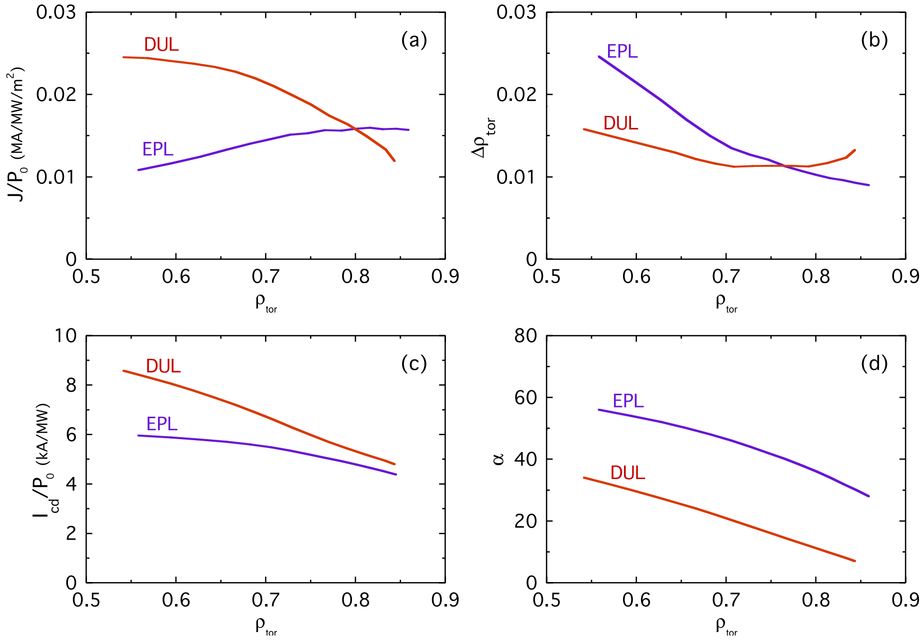

Figure 2. Same as figure 1, for injection from the LSM of the DUL at $\beta = 20°$ and from the LSM of the EPL at $\beta = 18°$.

$\rho_{\rm tor} = 0.3$ is $\Delta\alpha = 36°$, with the EPL_USM $\Delta\alpha = 24°$ is sufficient.

In the case of the LSM (figure 2), an exception to the favourable behaviour of the DUL is observed for $\rho_{\rm tor} \geqslant 0.8$. This is mainly due to the fact that the power absorption in that radial region occurs at larger distances from the DUL_LSM with respect to EPL_LSM, so that the 'local' spot size of the beam launched from DUL_LSM is larger than the 'local' spot size of the same beam when launched from EPL_LSM. This may be deduced by looking at beam trajectories from the LSM of both DUL and EPL shown in figure 3. By taking this into account, a different beam, with focus at a larger distance from the LSM, should be used for a better performance of DUL at the outermost flux surfaces. We further note that, if the EC power is injected from the DUL_LSM, low α, 'quasi horizontal' beam trajectories are needed to get ECCD at the outermost surfaces. These trajectories are affected by high refraction that, in its turn, affects the local beam size making the beam astigmatic. These observations indicate that a specific optimization study would be required for the DUL to assess its performances at the outermost surfaces, by also taking into account the possibility of exchanging the roles of the two steering mechanisms.

In order to compare the efficiencies of the two launchers for NTM stabilization with localized ECCD, the three H-mode reference scenarios, i.e. the inductive scenario 2 (EOB2), the hybrid scenario 3 (EOB3) and the low q scenario 5 (EOB5) have been considered. The main parameters of the scenarios are summarized in table 1.

The values of the figure of merit for (2, 1) and (3, 2) NTM stabilization are shown in table 2 and in table 3, for 13.3 MW of EC power injected, respectively, from the EPL_LSM and from the DUL_LSM. Besides $\eta_{\rm NTM}$, the full widths, $w_{\rm cd}$, of the EC current profiles (with $w_{\rm cd} = a\Delta\rho_{\rm tor}$ and $a = 200$ cm the plasma minor radius), and the products $\eta_{\rm NTM}w_{\rm cd}$ reflecting the effective total driven current are quoted in the tables.

Looking at tables 1 and 2, the following observations can be made: (i) all $\eta_{\rm NTM}$ values are above 1.2 by injecting 13.3 MW from either launcher; (ii) in the case of the DUL, larger $\eta_{\rm NTM}$ values (by a factor from 1.2 at $q = 2$ of scenario 2 up to 2.3 at the $q = 3/2$ of scenario 3) and smaller $w_{\rm cd}$ are obtained at the resonant surfaces of all scenarios (apart from at the $q = 2$ surface of the low q scenario 5 due to the above-mentioned beam size effect); (iii) still in the case of DUL, for all relevant surfaces the product $\eta_{\rm NTM}w_{\rm cd}$ is larger by a factor from 13% ($q = 2$ of scenario 2) up to 39% ($q = 3/2$ of scenario 3).

Since the power required for full stabilization, which also depends on the width at which the mode is stabilized, decreases for smaller $w_{\rm cd}$ and for larger values of the products $\eta_{\rm NTM}w_{\rm cd}$, we may argue that, by injecting the EC power from the DUL, a reduction of ~20% (on average) of the power needed to stabilize the NTMs may be achieved. We also stress, however, that accurate evaluations should also take into account the marginal island width below which the modes self-stabilize [21].

Concerning the capabilities of the two launchers for sawtooth control, it is clear that accurate predictions require transport modelling including a sawtooth period model that takes into account the stabilizing effect of alpha particles. However, a criterion to alter the shear at $q = 1$ for a significant change in the sawtooth period has been provided in the form $I_{\rm ECCD}/\Delta\rho^2 \geqslant I_{\rm p}(\rho_{q=1})/2(\rho_{q=1})^2$, $I_{\rm ECCD}$ being the total driven current, $\Delta\rho$ the (normalized) full width at $1/e$ of the driven current profile, and $I_{\rm p}(\rho_{q=1})$ the plasma current inside the $q = 1$ surface [22]. Although this criterion does not take into account the stabilizing effect of alpha particles, so that it will not apply quantitatively to ITER, $\eta_{\rm s} = I_{\rm ECCD}/\Delta\rho^2$ is taken as a figure of merit and used here to compare the EPL and DUL efficiencies for local shear modification. The values of $\eta_{\rm s}$ for $P_{\rm EC} = 1$ MW injected from the DUL_USM and EPL_USM are shown in figure 4. According to these results, the DUL

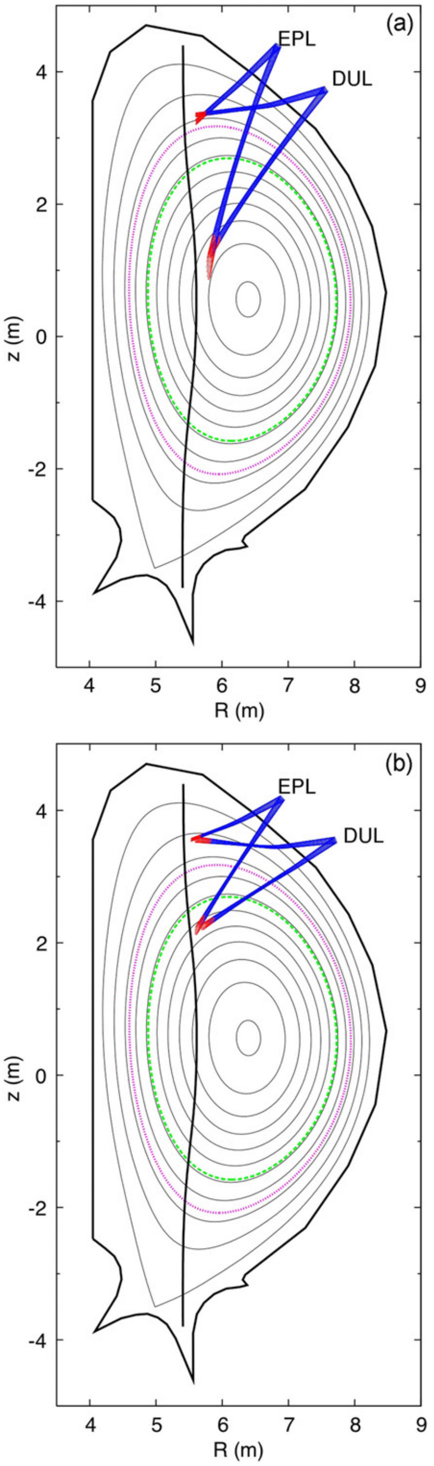

Figure 3. Trajectories of the wave beams injected into the plasma of scenario 2 from USM (*a*) and from LSM (*b*), aiming to drive current at the extrema of the corresponding radial range, for both EPL and DUL. The dotted and dashed lines denote the $q = 2$ and $q = 3/2$ flux surfaces, respectively.

efficiency to alter the magnetic shear close to $q = 1$ appears to be a factor ~4 superior to the EPL efficiency. However, to confirm that the DUL can increase the shear at $q = 1$ at a faster rate and to a larger value compared with the EPL requires a full simulation.

Table 2. NTM figures of merit for EPL_LSM.

Scenario	q	η_{NTM}	w_{cd} (cm)	$\eta_{\mathrm{NTM}}\ w_{\mathrm{cd}}$
EOB2	2	2.8	2.4	6.7
	3/2	1.8	3.8	6.8
EOB3	2	2.0	3.0	6.0
	3/2	1.3	4.7	6.1
EOB5	2	1.7	2.0	3.4
	3/2	1.4	2.8	3.9

Table 3. NTM figures of merit for DUL_LSM.

Scenario	q	η_{NTM}	w_{cd} (cm)	$\eta_{\mathrm{NTM}}\ w_{\mathrm{cd}}$
EOB2	2	3.4	2.3	7.6
	3/2	3.4	2.7	9.0
EOB3	2	3.2	2.2	7.1
	3/2	3.0	2.9	8.5
EOB5	2	1.5	2.7	4.0
	3/2	2.0	2.5	5.0

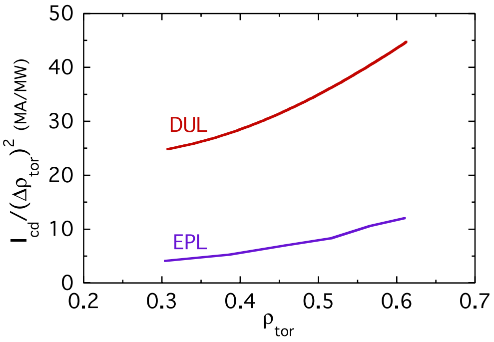

Figure 4. Figure of merit for sawtooth control for 1 MW injected into the plasma of scenario 2 from the DUL_USM and the EPL_USM.

3. Analysis and performances of the equatorial launcher

The current design of the EL foresees 1 equatorial port, 24 beams injected from 3 steering mirrors (8 beams/mirror) located at $R = 9.2$ m and $z = 0.02, 0.62$ and 1.22 m, which we shall call low, mid- and top mirrors, respectively. The launch is horizontal, with a toroidal steering capability between 20° and 46°, and provides only co-current drive [23]. As already pointed out by several authors, see e.g. references [24, 25], only the mid-mirror can deposit the power close to the plasma centre, while central deposition may be improved by adding a fixed poloidal angle to the top and low front mirrors. In reference [20] it has been shown that a tilt angle $\alpha \sim \pm 10^0$ allows driving current very close to the centre of the plasma of scenario 2. To account for possible vertical shifts of the plasma centre, we performed the calculations assuming a tilt angle of ±5° for the top and low front mirrors, respectively. To simulate the eight beams, a single wide astigmatic beam has been considered. In a local reference frame where the z-axis is along the beam line and the x- and y-axes are in a plane orthogonal to it (with x in the horizontal plane) the beam is characterized by the waists $w_x = 4.04$ cm and $w_y = 1.02$ cm at distances $d_x = -678.1$ cm and $d_y = 69$ cm from the front mirrors along the z-axis (where negative d values mean behind the mirror). The driven co-current, the peak current density,

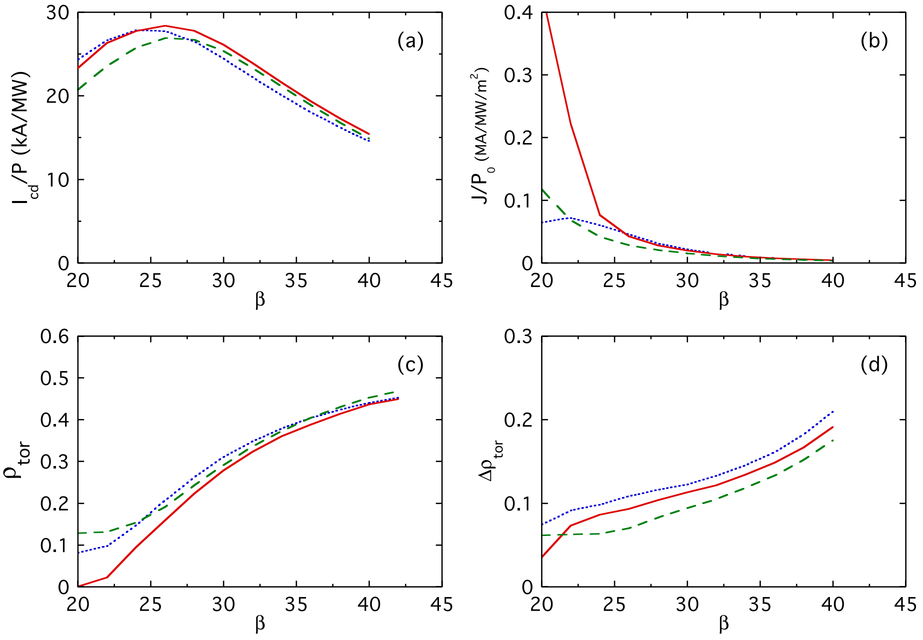

Figure 5. Driven co-current per unit power (*a*), peak current density (*b*) normalized radius of the peak current density (*c*) and normalized width at $1/e$ of the current density profile (*d*) as a function of the toroidal steering angle for the three rows of the EL with a tilt angle of 5° of the top and low front mirrors. The solid curves refer to the mid-mirror, the dotted ones to the low-mirror and the dashed ones to the top-mirror. The equilibrium and plasma parameters are those of scenario 2 at EOB. The curves are plotted up to β values that allow full power absorption.

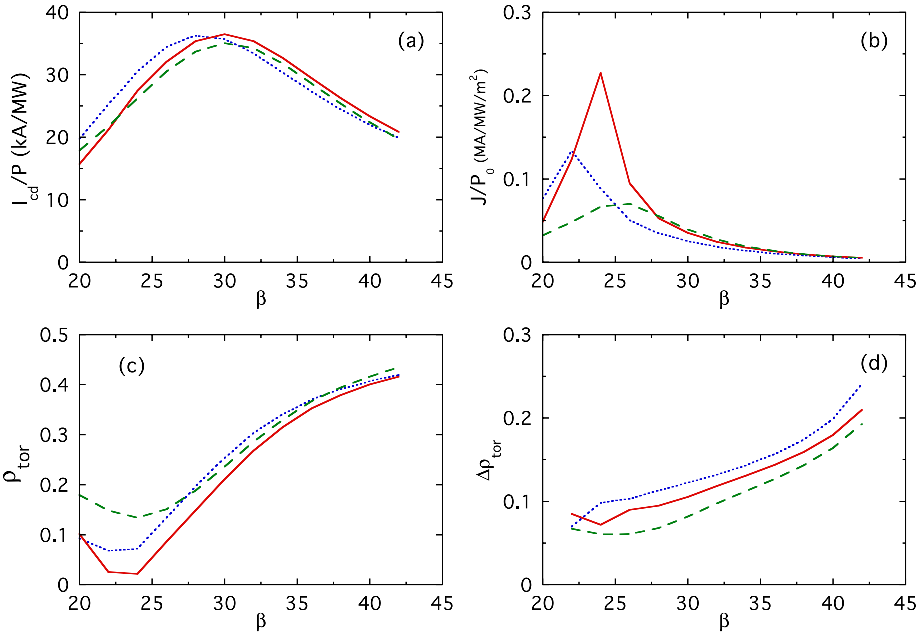

Figure 6. Same as figure 5, for scenario 3.

the normalized radius of the peak current density and the normalized width of the current density profiles as a function of the toroidal injection angle are shown in figure 5 for scenario 2 and in figure 6 for the case of the hybrid scenario 3. It may be observed that a large amount of co-current close to the plasma centre is driven for $\beta = 20°$, in the case of scenario 2, and for $\beta \sim 23°$ in the case of scenario 3, while the current density profiles are much broader than those obtained with the upper launchers. For instance, in the radial region where $q = 1$ is likely to occur ($\rho_{\mathrm{tor}} \sim 0.4$), the width of the current density profiles driven by the EL appears to be up to 4 (8) times larger than the width of the profiles driven by the EPL (DUL). Both the beam size and the Doppler shift are seen to contribute to the current density profiles broadening up to $\beta = 30°$ in scenario 2 and up to $\beta = 28°$ in scenario 3. For larger β values, the Doppler shift prevails. Therefore, a beam with a smaller size would not improve the poor localization of the EC current driven at radii $\rho_{\mathrm{tor}} > 0.3$ in scenario 2 and $\rho_{\mathrm{tor}} > 0.2$

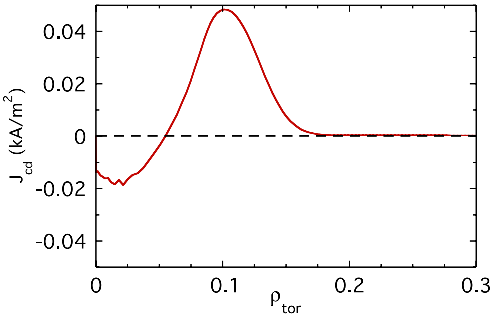

Figure 7. Current density profile for 1 MW of EC power injected from the mid-row at $\beta = 20°$ into the plasma of scenario 3.

in scenario 3. Also to be noticed is that for high β values ($\beta > 40°$), high $n_\parallel$ effects lead to incomplete absorption of the O-mode EC power. As a consequence, the access range for each mirror is limited up to $\rho_{tor} < 0.5$, depending on the scenario. Moreover, for the low β values for which the interaction with the O-mode first harmonic occurs on the high field side (this happens for scenario 3 at β values below 22°), a fraction of the power may be absorbed at downshifted second harmonic, leading to ECCD profiles with a counter-current in addition to the driven co-current. An example of such a profile is shown in figure 7, in the case of the high temperature scenario 3 for injection at $\beta = 20°$. In the case shown in the figure, 40% of the power injected from the mid-row is absorbed as second harmonic close to the plasma centre.

In order to fulfil its physics objectives as core heating (without peaking the plasma current), sawtooth control, to assist a reversed shear formation, the EL design should allow also for counter-current drive. Therefore, in addition to the inductive scenario 2 and the hybrid scenario 3, here we shall also consider the advanced scenario 4. The latter is a steady state 9 MA strong reverse shear scenario producing about 300 MW of fusion power with $Q = 5$. Its main parameters are listed in table 4.

Profiles of co- and counter-ECCD computed for the three scenarios by taking into account the full available power $P_{EC} = 20$ MW are shown in figure 8. The toroidal angles β have been chosen to get the ECCD profiles closest to the plasma centre in each scenario. The total driven current values are +0.45 MA and −0.47 MA for scenario 2, +0.51 MA and −0.54 MA for scenario 3 and, +0.66 MA and −0.67 MA for scenario 4, where + refers to co-ECCD and − to counter-ECCD.

The potential effects of the driven current on the q profiles have been estimated by the equilibrium code CHEASE [26] and are shown in figure 9. Although the resistive evolution of the plasma current profile is not taken into account in this analysis, results show that, with an improved design, the EL could provide a large range of variation of central q for all scenarios, particularly if counter-ECCD is included in the EL capabilities. It is also important to note that, whenever central heating is required, the driven co-current might peak the plasma current density profile and lead to early appearance of the $q = 1$ surface for the hybrid scenario or to a monotonic profile for scenario 4. The only possibility of avoiding unwanted low central q values is to compensate with a counter-current to allow either central heating (co- + counter-CD) or central counter-CD. Even a single row of counter ECCD beams in the EL would significantly increase the potentialities of the system, providing a larger flexibility in controlling q_0 in the advanced scenario 4.

4. Analysis at reduced magnetic field

The analysis presented so far has been carried out at the nominal value of the ITER magnetic field. However, at initial operation ITER will work at magnetic fields $B_T < 5.3$ T. Actually it is foreseen that the full field operation will occur about two years after the 'first plasma' [27]. The question therefore arises on determining the accessibility of the present system at reduced magnetic fields. The problem for the UL (based on three upper ports) was analysed in [25,28]. Although the magnetic topology of the equilibrium of scenario 2 was not identical and a different scaling of kinetic parameters was used, similar conclusions were drawn for the UL in the two papers. The analysis we present here has been performed for scenario 2 (EOB2), scaling the plasma current and kinetic profiles in order to keep fixed the edge safety factor q_{95}, the plasma β and the Greenwald number n/n_G.

It is worth recalling that neither upper nor equatorial launchers can work in the magnetic field range 3.4–4.2 T since the EC resonances for $f = 170$ GHz are located outside the plasma or quite close to the boundary. For the UL, where the toroidal angle β is fixed, when the magnetic field is reduced below 5.3 T for the case of the O-mode, first harmonic (OM1), and below 2.65 T, for the case of the X-mode second harmonic (XM2), it is generally observed that the access to the innermost flux surfaces is strongly reduced whenever the EC resonance is too far to the high field side. In the case of XM2, for magnetic fields higher than 2.65 T low and broad current density profiles are obtained when the EC resonance falls close to the radial location of the launcher. This is due to both trapping effects and to the 'quasi' vertical trajectories (with high α values) required to drive current at the relevant flux surfaces.

In the case of the EL, where the toroidal angle β is used to steer the radial location of the driven current, when B_T decreases with respect to 5.3 T the OM1 power absorption and ECCD occurs in the high field side with respect to the plasma centre. On these long trajectories, a fraction of the EC power may be absorbed at downshifted second harmonic, leading to ECCD profiles with a counter-current in addition to the driven co-current. For magnetic fields around 2.65 T (XM2 case), finally, third harmonic absorption (XM3) may considerably reduce the EC power available close to the second harmonic resonance.

Let us then investigate whether, using the DUL instead of the EPL, advantages can be found in terms of accessibility and performances in plasmas at reduced magnetic fields. The OM1 case is represented in figures 10 and 11, where the driven current density as a function of its radial location is shown for magnetic fields reduced by 10%, 15% and 20 % with respect to the nominal field. As may be observed, ECCD down to $\rho_{tor} < 0.5$ is no more allowed for both the DUL_USM and the EPL_USM, already for a 10% reduction of the nominal magnetic field. The possibility of using the USM for sawtooth control is therefore lost in both cases. In order to determine the allowed B_T range, we therefore use the criterion that co-current has to be driven in the entire radial range of NTMs, i.e. from

Table 4. Main parameters of scenario 4.

I_p (MA)	β_N	n_{e0} (10^{19} m^{-3})	T_{e0} (keV)	q_0	q_{min}	ρ_{qmin}	R_{axis} (m)	Z_{axis} (m)
9	2.5	7.3	23.9	4.3	2.7	0.7	6.67	0.52

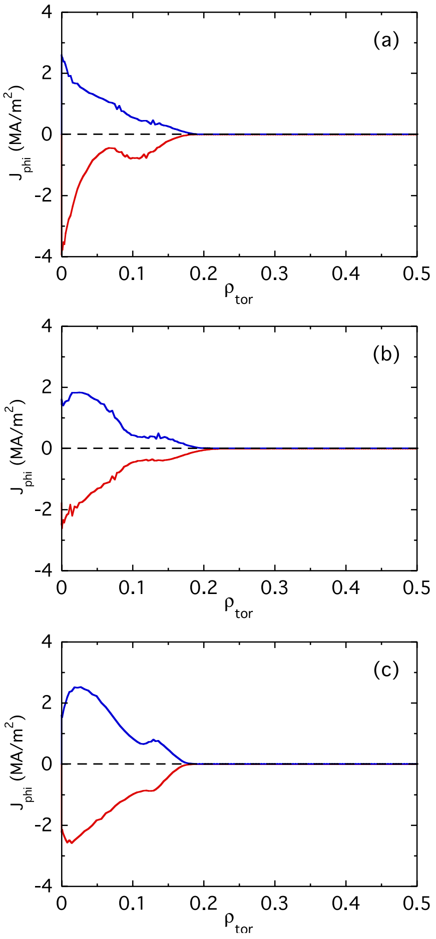

Figure 8. Co- and counter-ECCD profiles for 20 MW injected from the EL with a tilt angle of 5° of the top and low front mirrors, and with a toroidal angle $\beta = \pm 20°$ for scenario 2 (*a*), $\beta = \pm 23°$ for scenario 3 (*b*), $\beta = \pm 25°$ for scenario 4 (*c*).

$\rho_{tor} = 0.55$ up to $\rho_{tor} \leqslant 0.85$, at least by launching from the LSM. As easily argued from figure 11, the minimum field for which the above criterion is satisfied is $B_T \sim 4.5$ T for the DUL, and $B_T \sim 4.7$ T for the EPL. Therefore the B_T range where OM1 current drive is efficient for stabilization of all NTMs is larger for DUL. Furthermore, recalling that the bootstrap current density is scaled as the magnetic field, we also find that at resonant surfaces of scenario EOB2 the values of the NTM figure of merit, for a power of 13.3 MW, exceed the threshold value 1.2 in the whole range of magnetic field available for each launcher.

The same analysis has been performed for XM2 around half the nominal magnetic field, $B = 2.65$ T. The range of magnetic fields where the two launchers efficiently drive current is from 2.3 to 2.8 T for the EPL, and from 2.3 T up to 3 T for the DUL. Therefore the magnetic field gap between OM1 and XM2 is reduced by 20% if the EC power is launched from the DUL.

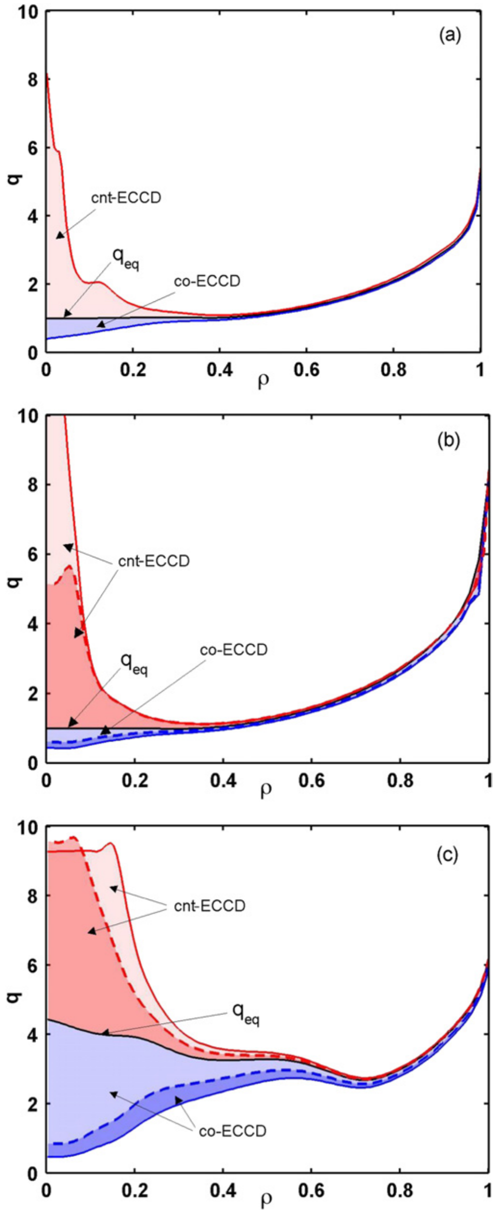

Figure 9. Potential effects of co- and counter-ECCD on the q profiles of scenario 2 (*a*), scenario 3 (*b*) and scenario 4 (*c*), estimated by the CHEASE code. The equilibrium q profile q_{eq} is shown for each scenario. The upper and lower solid lines represent the q profiles in the case of counter- and co-ECCD with $P_{EC} = 20$ MW. The dashed upper lines refer to the case of counter-ECCD obtained with 6.7 MW in the case of scenario 3, and with only 3 MW in the case of scenario 4. The dashed lower lines refer to the case of co-ECCD with 10 MW in both scenarios 3 and 4.

The capabilities of the EL at reduced B_T have been investigated by considering the mid-row only. The results obtained for the OM1 case are shown in figure 12, for values of B_T reduced by 10%, 15% and 20%. It is worth pointing

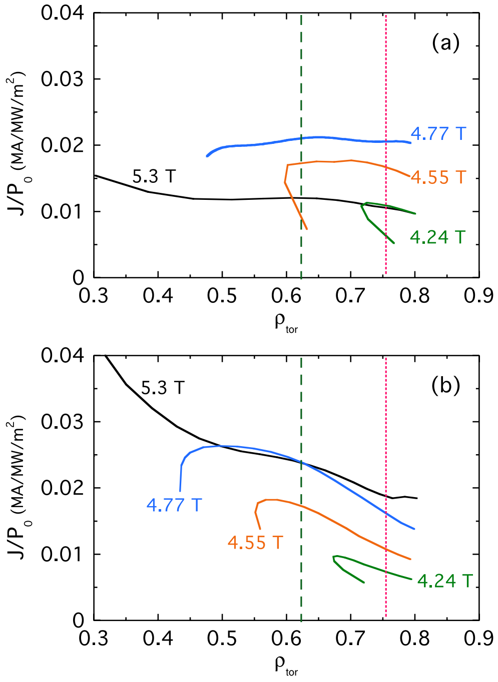

Figure 10. Driven current density per unit EC power, for magnetic fields reduced by 10%, 15% and 20%, for injection from the USM of the EPL (*a*), for injection from the USM of the DUL (*b*). The nominal field case is included as a reference. The vertical dashed lines indicate the radial location of the $q = 3/2$ surface and the $q = 2$ surface for scenario EOB2.

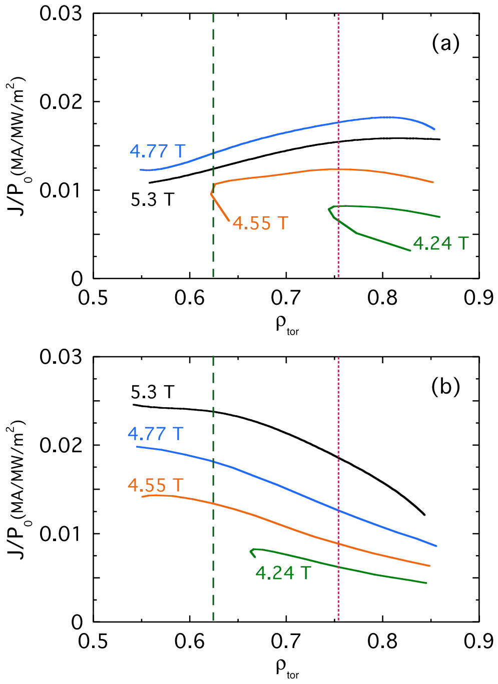

Figure 11. Same as figure 10, for injection from the EPL_LSM, (*a*), for injection from the DUL_LSM (*b*).

out that, as $B_T < 5.3$ T, the effective β range decreases due to incomplete power absorption. As already mentioned, at the low β values for which co-current is driven in the high field side with respect to the plasma centre, a counter-current affects the driven current profiles. This occurs at $\beta < 25°$ for

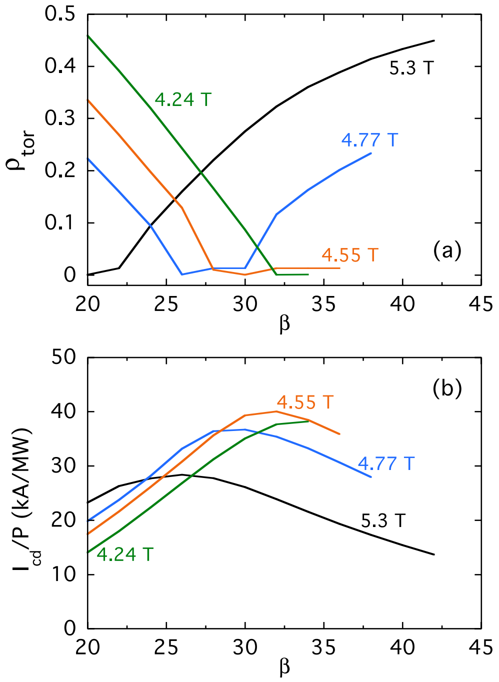

Figure 12. Radial location (*a*) and total driven current (*b*) as a function of β, by injecting 1 MW of EC power as OM1 from the mid-row of the EL at nominal field and three values of B_T reduced by 10%, 15% and 20%. The curves are shown up to values of the toroidal angle β for which the EC power is fully absorbed.

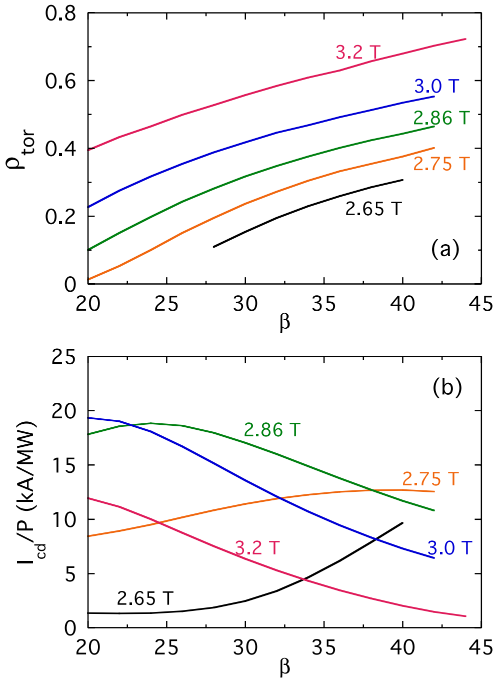

Figure 13. Same as figure 12, for XM2 and for values of B_T in the range 2.65–3.2 T.

$B_T = 4.77$ T, at $\beta < 27°$ for $B_T = 4.55$ T and at $\beta < 32°$ for $B_T = 4.24$ T. Moreover, we note that the access range is limited up to $\rho_{tor} \leqslant 0.2$ for $B_T = 4.77$ T, and up to $\rho_{tor} \leqslant 0.3$ for $B_T = 4.55$ T.

The performances of the EL for injection of the second harmonic X-mode (XM2) are shown in figure 13. As already mentioned, we observe that, for $B_T \leqslant 2.75$ T, third harmonic effects are dominant. A large fraction of the injected power is absorbed as XM3 in the low field side region, even preventing the interaction in the XM2 region, and the values of the driven current become quite low. This result, however, is strongly dependent on the assumption one makes for the temperature at scaled magnetic field. We also observe that a significant amount of current may be driven in the central region only for B_T in the range 2.75–3 T. For B_T increasing from 3 to 3.2 T, the radial range where a significant amount of current may be driven is shifted towards large radii, therefore the main goals of the EL, i.e. heating and CD close to the centre, can no more be fulfilled. We finally observe that for $B_T > 3.2$ T, negligible current is driven at the outermost surfaces since ECCD is dominated by trapped particle effects.

5. Summary and conclusions

The analysis performed in this work compared the performance of the present EC upper launcher design, the EPL launcher, with that of the same launcher moved vertically down in the ITER machine by approximately one blanket shield module, labelled the DUL launcher. The comparison showed that the DUL, by providing higher and narrower current density profiles, would increase the performance for both NTM stabilization and sawtooth control. The better performance for the DUL occurs mainly at the innermost surfaces, leading to an increment of the figure of merit for sawtooth control up to a factor 4. An exception to the favourable behaviour is found for the EC current driven at the outermost surfaces, and is mainly due to the fact that the beam used for the LSM in the present simulation is not 'optimized' for the DUL. Another advantage of lowering the upper port plug is that, at low B_T operation, the range of magnetic field where EC current may be driven in the whole radial range of NTMs would increase both in the OM1 case and in the XM2 case. Therefore the magnetic field range where the NTM region is not accessible would be reduced by 20% with respect to the present location. The main disadvantage of the DUL is that it requires a larger steering range to drive current in the same plasma region compared with the EPL. This would result in a larger rotation of the steering mirror and, as a consequence, in higher levels of induced stress in the critical component of the steering mechanism.

The main results provided by the analysis performed for the equatorial launcher are that, with a tilt angle of 5° added to the top and low front mirrors, better access to the plasma core can be provided. However the access range is limited to $\rho_{tor} < 0.5$, due to incomplete power absorption for the O-mode at large $n_\parallel$ values. Quite broad current density profiles ($\Delta\rho_t > 0.1$) are observed in the radial region where the $q = 1$ surface is likely to occur, i.e. $\rho_{tor} \sim 0.3$–0.4, the broadening being dominated by the Doppler shift. This makes the EL less efficient than the UL for sawtooth control. Moreover it has been shown that, adding to the present design the possibility to drive counter-current in addition to the existing co-current capability would largely increase the flexibility of the system, by decoupling heating and current drive, whenever only heating is necessary, or providing the possibility of controlling the central q in the advanced scenario 4.

Finally, it has been shown that the EL has a very limited access range (up to $\rho_{tor} \leqslant 0.2$) when the magnetic field is reduced by only 10%. Recalling that, for the same magnetic field, the UL cannot drive current inside $\rho_{tor} = 0.5$, sawtooth control is not possible anymore at this field. For a magnetic field reduced by 15% or by 20%, the access range of the EL increases up to $\rho_{tor} \sim 0.3$ or up to $\rho_{tor} \sim 0.45$, respectively; however, the current density profiles also show a counter-current due to power absorption at the downshifted second harmonic. Moreover, in the range of the second harmonic X-mode, a significant amount of current may be driven in the central region only for B_T in the range 2.75–3 T. Therefore the capabilities of the EL are strongly reduced by reducing the magnetic field.

Acknowledgments

This work, supported by the European Community, was carried out within the framework of the European Fusion Development Agreement (TASK TW6-TPHE). The views and opinions expressed herein do not necessarily reflect those of the European Commission. Some of the authors are supported in part by the Swiss National Science Foundation.

References

[1] Farina D. 2007 *Fusion Sci. Technol.* **52** 154

[2] Poli E. Peeters A.G. and Pereverzev G.V. 2001 *Comput. Phys. Commun.* **136** 90

[3] Zohm H. *et al* 2005 *J. Phys.: Conf. Ser.* **25** 234

[4] Gribov Y. *et al* 2000 *Proc. 18th Int. Conf. on Fusion Energy 2000 (Sorrento, Italy, 2000)* (Vienna: IAEA) CD-ROM file ITERP/02 and http://www-pub.iaea.org/MTCD/publications/PDF/csp_008c/Start.htm

[5] La Haye R.J. *et al* 2006 *Nucl. Fusion* **46** 451

[6] Saibene G. *et al* 2006 *Proc. 21st Int. Conf. on Fusion Energy 2006 (Chengdu, China, 2006)* (Vienna: IAEA) CD-ROM file IT//P2-14, and http://www-naweb.iaea.org/napc/physics/FEC/FEC2006/html/index.htm

[7] Henderson M. *et al* 2006 *Proc. 21st Int. Conf. on Fusion Energy 2006 (Chengdu, China, 2006)* (Vienna: IAEA) CD-ROM file IT/P2-15, and http://www-naweb.iaea.org/napc/physics/FEC/FEC2006/html/index.htm

[8] Marasheck M. *et al* 2004 *Proc. 20th Int. Conf. on Fusion Energy 2004 (Vilamoura, Portugal, 2004)* (Vienna: IAEA) CD-ROM file EX-7/2 and http://www-naweb.iaea.org/napc/physics/fec/fec2004/datasets/index.html

[9] Porcelli F., Boucher D. and Rosenbluth M.N. 1996 *Plasma Phys. Control. Fusion* **38** 2163

[10] Sauter O. *et al* 2002 *Phys. Rev. Lett.* **88** 105001

[11] Angioni C. *et al* 2003 *Nucl. Fusion* **43** 455

[12] Eriksson L.G. 2004 *Phys. Rev. Lett.* **92** 235004

[13] Graves J.P. *et al* 2005 *Plasma Phys. Control. Fusion* **47** B121–3

[14] Sauter O. and Zohm H. 2005 *Proc. 26th EPS Conf. on Plasma Physics and Controlled Fusion (Tarragona, Spain, 2005)* vol 29C P-2.059 and http://epsppd.epfl.ch/Tarragona/pdf/P2_059.pdf

[15] Harvey R.W. and Perkins F.W 2001 *Nucl. Fusion* **41** 1847

[16] Ramponi G. *et al* 2003 Optimisation of the ITER ECRH Top Launcher *2nd IAEA Technical Meeting on ECRH for ITER (Kloster Seeon, Germany, 2003)* available at http://www.ipp.mpg.de/eng/for/veranstaltungen/tmseeon/

[17] Weisen H. *et al* 2006 *Plasma Phys. Control. Fusion* **48** A457

[18] Henderson M.A. *et al* 2004 *Plasma Phys. Control. Fusion* **46** A275

[19] Manini A. *et al* 2006 *Proc. 14th Joint Workshop on Electron Cyclotron Emission and Electron Cyclotron Resonance Heating (Santorini, Greece)* p 44

[20] Ramponi G. *et al* 2007 *Fusion Sci. Technol.* **52** 193

[21] Sauter O. *et al* 2006 *Proc. 21st Int. Conf. on Fusion Energy 2006 (Chengdu, China 2006)* (Vienna: IAEA) CD-ROM file TH/P3-10, and http://www-naweb.iaea.org/napc/physics/FEC/FEC2006/html/index.htm

[22] Merkulov A. *et al* 2004 *Proc. Joint Varenna–Lausanne Int. Workshop on Theory of Fusion Plasmas (Varenna, Italy, 2004)* p 279

[23] Takahashi K. *et al* 2007 *Fusion Sci. Technol.* **52** 266

[24] Volpe F. 2005 *J. Phys.: Conf. Ser.* **25** 283

[25] Prater R. 2005 *J. Phys.: Conf. Ser.* **25** 257

[26] Lutiens H., Bondeson A. and Sauter O. 1996 *Comput. Phys. Comm.* **98** 219

[27] Shimomura Y. *et al* 2000 *Proc. 18th Int. Conf. on Fusion Energy 2000 (Sorrento, Italy, 2000)* (Vienna: IAEA) CD-ROM file ITER/1 and http://www-pub.iaea.org/MTCD/publications/PDF/csp_008c/Start.htm

[28] Ramponi G., Farina D. and Nowak S. 2005 *J. Phys.: Conf. Ser.* **25** 243

IOP Publishing Plasma Physics and Controlled Fusion

Plasma Phys. Control. Fusion **51** (2009) 075005 (21pp) doi:10.1088/0741-3335/51/7/075005

Kinetic effects on slowly rotating magnetic islands in tokamaks

Mattia Siccinio and Emanuele Poli

Max-Planck-Institut für Plasmaphysik, EURATOM Association, Boltzmannstrasse 2, D-85748, Garching bei München, Germany

Received 25 September 2008, in final form 23 April 2009
Published 19 May 2009
Online at stacks.iop.org/PPCF/51/075005

Abstract

The current flowing around a magnetic island and connected to its rotation with respect to the plasma is studied by means of a drift-kinetic approach. It is shown that the current due to a change in the precession frequency of the trapped particles in the island potential can compete with the standard polarization current for island rotation frequencies close to or below the diamagnetic frequency. The passing particles are found, on the contrary, to have little impact on the standard picture. The analytical results are shown to explain the features of the island current seen in numerical simulations.

(Some figures in this article are in colour only in the electronic version)

1. Introduction

The tearing mode is a non-ideal MHD instability which changes the topology of the magnetic field by reconnecting separate field lines, thus causing the appearance of magnetic islands. In a toroidal fusion device, this severely deteriorates the radial confinement of particles and energy. These modes are localized on the so-called *resonant surfaces*, where the safety factor q is a rational number. First studies [1, 2] described the tearing mode as a dissipative phenomenon for the magnetic energy stored in the plasma, so that the growth rate of the mode was basically determined by the equilibrium magnetic configuration through the parameter Δ'. Later, it was shown both theoretically [3, 4] and experimentally [5, 6] that the tearing mode can also be destabilized in a tokamak by the loss of bootstrap current caused by the appearance of a 'seed' island, and this neoclassical drive characterizes the so-called neoclassical tearing modes (NTMs). While the neoclassical drive and the stabilizing effect of the equilibrium current profile can describe the non-linear saturation of the mode under experimental conditions, to compute the stability and the growth of a seed island, one needs to take into account other effects which are still to be fully explained. Among these, the rotation of the island with respect to the plasma turns out to potentially play a major role. For 'fast' rotating islands (i.e. ω sufficiently larger than $k_{\parallel} v_{\mathrm{th}}$, where ω is the island rotation frequency with respect to the

0741-3335/09/075005+21$30.00

plasma, i.e. in the local equilibrium $\boldsymbol{E} \times \boldsymbol{B}$ frame, $k_\parallel$ is the parallel wave vector defined in equation (6) below and $v_{\rm th}$ is the ion thermal velocity) sufficiently larger than the ion banana width [7], a well-known contribution comes from the polarization current [8, 9], which arises because particles experience a time-dependent electric field during their streaming around the island. This phenomenon has different physical features depending on collisionality [10–13] and frequency [14]. Moreover, other effects have been shown to be relevant, for example finite ion banana width effects [7, 15] or even finite Larmor radius effects [16]. As a matter of fact, for small islands the gyroradius scale starts to be relevant, and a gyro-kinetic approach can be necessary to get a satisfactory physical picture [17–19].

As a general theory for the determination of the mode rotation frequency ω is currently not available, we perform a parametric study in ω focusing on a frequency range which has not been explored yet, even though it can be physically meaningful for a NTM. A common assumption in the theory of the polarization current consists of the ordering $\omega \sim \omega_*$, where ω_* is the electron diamagnetic frequency. According to the scaling criteria discussed in detail in section 4, this ordering leads to $\omega \sim k_\parallel v_{\rm th}$. Physically, this means that the island rotation occurs on the same timescale as the transit time of the particles around it, potentially leading to resonant interactions between the mode and the particles, as already pointed out previously [14]. To investigate these processes, a kinetic approach is necessary. In a previous study [11], focusing on the contribution of the polarization current, terms in $k_\parallel v_{\rm th}$ have been disregarded. In this paper, we retain these terms and investigate their contribution to the currents generated by a rotating magnetic island. We neglect the mode evolution due to the plasma response, so that the island width and its rotation frequency are constant with time. Moreover, we assume for simplicity a flat pressure gradient for the background plasma. Although fundamental for a self-consistent determination of the island dynamics, the inclusion of a finite gradient in the background pressure is not strictly necessary to understand the phenomena related to the resonances between island and particle motion, which are the subject of this paper.

We show that, at low frequencies, the contribution of the polarization current can be overcome by other electric and magnetic effects. In particular, we demonstrate in this work that a crucial contribution comes from the mutual interaction between the island propagation and the electric and magnetic precession of the trapped particles in the toroidal direction. The corresponding perturbed parallel current is shown to stabilize the NTM for $\omega > 0$, or for $|\omega|$ sufficiently larger than $\omega_{\rm tp}$ if $\omega < 0$, where $\omega_{\rm tp}$ is the precession frequency of trapped particles defined in equation (29) below. Passing particles are, on the contrary, shown to give a negligible current contribution. The analytical results are shown to explain the behaviour of the island current as calculated by means of the Hamiltonian drift-kinetic code HAGIS [20].

This paper is structured as follows. In section 2, the chosen magnetic geometry is outlined. In section 3 we describe the analytical and numerical techniques adopted to solve the drift-kinetic equation. In sections 4 and 5 we solve the drift-kinetic equation in the $\omega \sim k_\parallel v_{\rm th}$ and in the $\omega \ll k_\parallel v_{\rm th}$ regime. This allows us to highlight the role of passing and trapped particles, respectively. Analytic solutions are compared with numerical simulations. The results are further discussed and summarized in section 6.

2. Magnetic geometry

In the calculations which follow, we assume an axisymmetric, large-aspect-ratio toroidal geometry, with circular cross section. We define ϵ as the inverse aspect ratio. For convenience we use here the same notation as in [11]. The coordinate system is represented by a poloidal flux χ, which can be used as a radial coordinate, a toroidal angle ζ and a poloidal angle θ.

This choice is such that

$$\nabla\zeta \times \nabla\chi = rB_\theta \nabla\theta,$$

where r is the minor radius coordinate and B_θ the poloidal component of the magnetic field. The equilibrium magnetic field is expressed by

$$\boldsymbol{B} = I(\chi)\nabla\zeta + \nabla\zeta \times \nabla\chi, \tag{1}$$

having defined $I(\chi) = RB_\zeta$, where R is the major radius and B_ζ the toroidal component of the magnetic field. Thus, the equilibrium magnetic field is such that $\boldsymbol{B} \cdot \nabla\chi = 0$. We suppose that the magnitude of the magnetic field B varies over the poloidal cross section as $B = B_0\,(1 - \epsilon\cos\theta)$. The helical angle ξ is introduced as

$$\xi = m\theta - n\zeta - \omega t,$$

where m, n are the poloidal and toroidal mode numbers, respectively and ω is the island rotation frequency, supposed to be a constant in time for simplicity. We can include the magnetic island as a perturbation in the magnetic field writing

$$\boldsymbol{B} = I(\chi)\nabla\zeta + \nabla\zeta \times \nabla\left(\chi + \psi\right), \tag{2}$$

where

$$\psi = \tilde{\psi}\cos\xi, \tag{3}$$

where $\tilde{\psi}$ is supposed to be a constant according to the well-known constant-ψ approximation [2]. We can define a new coordinate system, using χ, ξ and θ, and this is the system which will be used in this paper from here on. It is possible to build a perturbed flux surface label Ω, such that in the presence of the magnetic island $\boldsymbol{B} \cdot \nabla\Omega = 0$. Writing with a subscript s quantities which are calculated on the resonant surface, we obtain

$$\Omega = \frac{2\left(\chi - \chi_{\mathrm{s}}\right)^2}{W_\chi^2} - \cos\xi, \tag{4}$$

where $W_\chi^2 = 4\tilde{\psi}q_{\mathrm{s}}/q_s'$, is connected to the island half-width w by the relation $W_\chi = RB_\theta w$, q is the safety factor and the apex $'$ refers to the derivative with respect to χ. With the help of the function Ω, one arrives at the following expression for the parallel gradient:

$$\nabla_\parallel = \frac{1}{Rq}\frac{\partial}{\partial\theta} + k_\parallel \left.\frac{\partial}{\partial\xi}\right|_\Omega, \tag{5}$$

where

$$k_\parallel = -m\frac{\left(\chi - \chi_{\mathrm{s}}\right)}{Rq}\frac{q_{\mathrm{s}}'}{q_{\mathrm{s}}}. \tag{6}$$

It can be seen that ψ can be thought of as a perturbation of the parallel component of the magnetic vector potential $\boldsymbol{A}$. As we suppose that every parallel electric field $E_\parallel$ is immediately shorted out by the very fast electron streaming along the field lines, we obtain an analytical expression for the (θ-independent) scalar potential using the Faraday's law:

$$\nabla_\parallel\Phi = -\frac{1}{c}\frac{\partial A_\parallel}{\partial t} \Rightarrow \Phi = \frac{\omega q}{mc}\left[\chi - \chi_{\mathrm{s}} - h(\Omega)\right], \tag{7}$$

where use has been made of equation (26) below. Here, $h(\Omega)$ is a function which plays the role of an integration constant, and can be determined from boundary conditions. A simple choice for $h(\Omega)$ can be found in [10]:

$$h(\Omega) = \frac{W_\chi}{\sqrt{2}}\left(\sqrt{\Omega} - 1\right)\Theta\left(\Omega - 1\right),$$

where W_χ is defined to have the same sign as $(\chi - \chi_{\mathrm{s}})$ and $\Theta(x)$ is the Heaviside step function. This choice allows the scalar potential to vanish far away from the magnetic island. Moreover, this fixes $h(\Omega)$ to the value of zero inside the island ($\Omega = -1$ corresponds to the O-point, while $\Omega = 1$ to the island separatrix).

3. The Drift-kinetic equation

3.1. Analytic approach

The drift-kinetic equation describes the time evolution of the distribution of the particles' guiding centres in a magnetized plasma. This means that particles are treated like streaming along magnetic field lines through their parallel velocity, and drifting across the field lines through their electric and magnetic drifts. Gyration motion is implicitly present in the mirror force and in defining the magnetic moment μ (supposed to be a constant), but spatial variation of physical quantities on the Larmor radius scale is neglected:

$$\frac{\partial f_j}{\partial t} + v_{\parallel j} \nabla_\parallel f_j + \boldsymbol{v}_{\boldsymbol{E}\times\boldsymbol{B}} \cdot \nabla f_j + \boldsymbol{v}_{\mathrm{D}j} \cdot \nabla f_j - \frac{q_j}{m_j} \frac{\boldsymbol{v}_{\mathrm{D}j} \cdot \nabla \Phi}{v} \frac{\partial f_j}{\partial v} = C_j(f_j). \quad (8)$$

The subscript j labels the different species that are present in the plasma. Spatial derivatives have to be taken at constant kinetic energy. This form of the drift-kinetic equation is explained in detail in [21].

The magnetic drift velocity can be written in the form

$$\boldsymbol{v}_{\mathrm{D}j} = -v_{\parallel j} \boldsymbol{b} \times \nabla \left(\frac{v_{\parallel j}}{\omega_{\mathrm{c}j}} \right), \quad (9)$$

where $\boldsymbol{b}$ is the unit vector parallel to the magnetic field and $\omega_{\mathrm{c}j}$ is the cyclotron frequency for the jth particle species. In this work we focus on ions, supposing that the only contribution of electrons is shorting out the parallel electric field $E_\parallel$. As every physical quantity such as temperature (T) or the distribution itself is referred to ions, we can from here on drop the subscript j without ambiguity. We keep the index i only for the ion mass m_{i} and for the ion charge q_{i} in order to avoid confusion with the poloidal mode number m and the safety factor q, respectively. Equation (8) is solved splitting the distribution function into an analytically known part F_0, assumed here to be an isotropic Maxwellian

$$F_{\mathrm{M}}(v) = n_0 \left(\frac{m_{\mathrm{i}}}{2\pi T} \right)^{3/2} \mathrm{e}^{m_{\mathrm{i}} v^2 / 2T}$$

(where the density n_0 and the temperature T are assumed to be uniform, cf section 1), and a part g do be determined perturbatively. Specifically, in the coordinate system discussed in section 2, writing the full expression for drifts, equation (8) takes the form

$$\begin{aligned} &-\omega \frac{\partial g}{\partial \xi} + \frac{v_\parallel}{Rq} \frac{\partial g}{\partial \theta} + k_\parallel v_\parallel \left.\frac{\partial g}{\partial \xi}\right|_{\Omega} + m \frac{c}{B} \frac{I}{Rq} \frac{\partial \Phi}{\partial \chi} \frac{\partial g}{\partial \xi} - m \frac{c}{B} \frac{I}{Rq} \frac{\partial \Phi}{\partial \xi} \frac{\partial g}{\partial \chi} + \frac{I v_\parallel}{Rq} \frac{\partial}{\partial \theta} \left(\frac{v_\parallel}{\omega_{\mathrm{c}}} \right) \frac{\partial g}{\partial \chi} \\ &\quad -m \frac{I v_\parallel}{Rq} \frac{\partial}{\partial \chi} \left(\frac{v_\parallel}{\omega_{\mathrm{c}}} \right) \frac{\partial g}{\partial \xi} - \frac{q_{\mathrm{i}}}{m_{\mathrm{i}}} \left[\frac{I v_\parallel}{Rq} \frac{\partial}{\partial \theta} \left(\frac{v_\parallel}{\omega_{\mathrm{c}}} \right) \frac{\partial \Phi}{\partial \chi} - m \frac{I v_\parallel}{Rq} \frac{\partial}{\partial \chi} \left(\frac{v_\parallel}{\omega_{\mathrm{c}}} \right) \frac{\partial \Phi}{\partial \xi} \right] \frac{\partial g}{\partial v} \\ &= -\frac{q_{\mathrm{i}} F_{\mathrm{M}}}{T} \left[\frac{I v_\parallel}{Rq} \frac{\partial}{\partial \theta} \left(\frac{v_\parallel}{\omega_{\mathrm{c}}} \right) \frac{\partial \Phi}{\partial \chi} - m \frac{I v_\parallel}{Rq} \frac{\partial}{\partial \chi} \left(\frac{v_\parallel}{\omega_{\mathrm{c}}} \right) \frac{\partial \Phi}{\partial \xi} \right], \quad (10) \end{aligned}$$

where we have neglected the collision operator (the role of collisions will be discussed later on). The parallel velocity $v_\parallel$ is written in the so-called pitch-angle variables [21]:

$$v_\parallel = \sigma v \sqrt{1 - \lambda B}.$$

Here $\lambda = 2\mu / m_{\mathrm{i}} v^2$, where μ is the magnetic moment and σ is the sign of the parallel velocity. A trapped particle has $1/B > \lambda > 1/B_{\mathrm{M}}$, where B_{M} is the maximum value of the magnetic field on a given flux surface. With these variables, the integration operator over velocity space becomes

$$\int_{-\infty}^{\infty} \ldots \mathrm{d}^3 v = \pi B \sum_{\sigma = \pm 1} \int_0^{\infty} v^2 \, \mathrm{d}v \int_0^{1/B} \ldots \frac{\mathrm{d}\lambda}{\sqrt{1 - \lambda B}}. \quad (11)$$

Equation (10) is solved performing a double parameter expansion of the perturbed distribution g, i.e.

$$g = \sum_{m,n}^{\infty} g^{(m,n)} \delta^m \Delta^n, \tag{12}$$

where

$$\delta = \frac{\rho_b}{w}, \qquad \Delta = \frac{w}{a} \tag{13}$$

are supposed to be two small parameters (here, ρ_b is the ion banana width and a the tokamak minor radius). The ordering of the various terms in equation (10) with respect to δ and Δ will be discussed in sections 4 and 5. The only 'free' parameter is the island propagation frequency ω. In section 4 we maintain the ordering assumptions for ω used in [11], which leads to $\omega \sim k_\parallel v_{\mathrm{th}}$. In section 5, we order $\omega \sim \omega_{\mathrm{D}}$, where

$$\omega_{\mathrm{D}} = \frac{q}{Rr\omega_c} \frac{1}{2\theta_b} \int_{-\theta_b}^{\theta_b} \left[\frac{\mu B}{m_{\ \mathrm{i}}} + v_\parallel^2 \right] \cos\theta \, \mathrm{d}\theta \tag{14}$$

is the (bounce averaged) toroidal precession frequency of the trapped particles [22], as defined θ_b the bounce angle.

The aim of these ordering assumptions is to study which physical phenomena can take place when the island propagation frequency ω starts to be comparable with the particles' transit frequencies around the island itself, which are basically linked to $k_\parallel v_\parallel$ (with $v_\parallel \sim v_{\mathrm{th}}$) for passing particles, and to ω_{D} for trapped particles. This second case can also be thought of as ordering the island propagation frequency like the parallel streaming of the trapped particle, as $\omega \sim \omega_{\mathrm{D}}$ means $\omega \sim \sqrt{\epsilon} k_\parallel v_{\mathrm{th}}$. This point will be developed in section 5.

3.2. Numerical approach

The HAGIS code (HAmiltonian GuIding centre System) [20] solves the drift-kinetic equation for ions by means of a Hamiltonan approach and with the δf technique. This method consists of writing the distribution f as $f = F_0 + \delta f$, where F_0 is known and arbitrary. This approach is completely general, but can be convenient from the numerical point of view only if f is not expected to be so different from the chosen F_0, which means

$$\frac{\delta f}{F_0} \ll 1,$$

which is what we expect to find. The HAGIS code calculates the evolution in time of the distribution function by means of 'markers' which span the whole phase space and represent the ions. These 'markers' evolve according to the Hamiltonian equations of motion, which are integrated by the code. As in section 3.1, we choose F_0 as a space-independent isotropic Maxwellian. In the simulations presented in the next sections, we consider a tokamak with circular concentric flux surfaces and major radius $R = 8$ m, aspect ratio $a/R = 0.5$, magnetic field $B_0 = 8$ T, deuterium plasma with density $n_{\mathrm{i}} = 10^{20}\,\mathrm{m}^{-3}$ and temperature $T = 5$ keV. Collisions are described by a Monte Carlo algorithm which models pitch-angle scattering [23]. A ($m = 3$, $n = 2$) magnetic island with a fixed half-width $w = 6.8$ cm is included in the simulations, and the island frequency ω is treated as an input parameter. With these values, the ratio between the island width and the thermal ion banana width corresponds to $w/\rho_b \approx 9.6$ and the ratio between the island width and the tokamak minor radius a corresponds to $w/a \approx 0.017$. The space domain is divided into 'radial' cells (between two neighbouring perturbed flux surfaces) and into helical cells, in such a way that the volume between two

X-points of a magnetic island consists of six helical cells (for further details see [24]). All numerical results presented below refer to the 'upper' half of the magnetic island (i.e. from O-point to X-point travelling in the positive-θ direction). In the 'lower' half, results can be shown to simply change their sign.

4. The $\omega \sim k_\parallel v_\parallel$ regime

4.1. Solution of the drift-kinetic equation

The solution of the drift-kinetic equation presented in this paper closely follows the analytic treatment presented in [11]. In that paper, F_0 is chosen so that an adiabatic response of the ions to the electrostatic potential is included, and equilibrium gradients are retained. Under these circumstances, the lowest order perturbation $g^{(0,0)}$ has the double role of cancelling the adiabatic response and of introducing the perturbations due to the island in the density and temperature profiles. The next-order term in the expansion of the distribution function with respect to δ, i.e. $g^{(1,0)}$, is shown to be linked to the neoclassical parallel fluxes, including that due to radial electric fields. The frequency ω_E, corresponding to the latter, is defined as in [25]:

$$\omega_\mathrm{E} = c\frac{E_\mathrm{r}}{RB_\theta}, \tag{15}$$

where in this case the radial electric field we are interested in is generated by the island itself. By means of the charge continuity equation, Wilson *et al* showed that this electric drift is the physical trigger of the polarization current, because it allows trapped particles to experience a time-varying electric field.

Let us now turn to equation (10). In this section, we follow the ordering assumptions adopted in [11]. This, in particular, consists of

$$\frac{\partial}{\partial\theta} \sim \frac{\partial}{\partial\xi} \sim 1, \qquad \frac{q_\mathrm{i}\Phi}{T} \sim \frac{g}{F_\mathrm{M}} \sim \Delta \qquad \rho_\theta \sim w$$

(ρ_θ being the poloidal ion Larmor radius). As for the island propagation frequency, if the pressure profile possesses a finite gradient characterized by the length L_p, a natural choice is to assume ω to be of the same order as the diamagnetic frequency ($\omega_* = mcTn_\mathrm{e}'/q_\mathrm{i}qn_\mathrm{e}$, with $n_\mathrm{e}' = \partial n_\mathrm{e}/\partial\chi$, n_e being the electron density). Supposing $n_\mathrm{e}' \sim n_\mathrm{e}/RB_\theta a$ (i.e. making the choice $L_p \sim a$), this implies (cf equation (13)):

$$\frac{Rq}{v_\parallel}\omega \sim \frac{Rq}{v_\parallel}\omega_* \sim \frac{Rq}{v_\mathrm{th}}\frac{mcTn_\mathrm{e}'}{q_\mathrm{i}qn_\mathrm{e}} \sim \frac{\rho_\theta}{a} \sim \Delta.$$

The term describing the parallel streaming turns out to be of the same order, since (see equation (6))

$$\frac{Rq}{v_\parallel}k_\parallel v_\parallel \sim (\chi - \chi_\mathrm{s})\frac{q_s'}{q_\mathrm{s}} \sim \frac{w}{r} \sim \Delta,$$

having assumed $(\chi - \chi_\mathrm{s}) \sim W_\chi$, as we focus our calculations on the vicinity of the island, and $L_p \sim L_q \sim \epsilon L_s$, L_q and L_s being the radial scale length of the safety factor and of the magnetic shear, respectively.

As already mentioned, to point out the effects linked to the mutual rotation of particles and island, in our analysis we take a flat pressure profile, $\omega_* = 0$, and treat ω as a free parameter. In this section, we retain the ordering $\omega Rq/v_\parallel \sim \Delta$, which implies $\omega \sim k_\parallel v_\mathrm{th}$. The resulting ordering of the terms in equation (10) is

$$\Delta : 1 : \Delta : \Delta : \Delta : \delta : \Delta\delta : \Delta\delta : \Delta^2\delta = \delta : \Delta\delta.$$

It is worthwile to stress the fact that the term $\boldsymbol{v}_D \cdot \nabla$ in equation (8) consists of two different components which, under our assumptions, are not of the same order.

We now turn to the order-by-order solution of equation (10). As we do not include an adiabatic split in F_0, and as we do not consider density and temperature equilibrium gradients, according to the meaning of $g^{(0,0)}$ elucidated above, we assume

$$g^{(0,0)} = 0. \tag{16}$$

The $\mathcal{O}(\delta)$ equation reads

$$\frac{v_\parallel}{Rq}\frac{\partial}{\partial\theta}g^{(1,0)} = -\frac{q_\mathrm{i}F_\mathrm{M}}{T}\frac{Iv_\parallel}{Rq}\frac{\partial}{\partial\theta}\left(\frac{v_\parallel}{\omega_\mathrm{c}}\right)\frac{\partial\Phi}{\partial\chi}, \tag{17}$$

which can be directly integrated to give

$$g^{(1,0)} = -I\frac{v_\parallel}{\omega_\mathrm{c}}\frac{\partial\Phi}{\partial\chi}\frac{q_\mathrm{i}F_\mathrm{M}}{T} + \bar{h}_\mathrm{P}^{(1,0)} + \bar{h}_\mathrm{T}^{(1,0)} \tag{18}$$

(in the first term on the right-hand side of this expression, it is easy to identify the first-order expansion of a Maxwellian shifted by a velocity cE_r/B_θ in the parallel direction). The bar over a function indicates that it is θ-independent, so, $\bar{h}$-functions represent the integration constants. We have divided them, separating the passing region of phase space (subscript P) from the trapped one (subscript T).

As $g^{(0,0)} = 0$, the $\mathcal{O}(\Delta)$ equation simply amounts to

$$\frac{v_\parallel}{Rq}\frac{\partial}{\partial\theta}g^{(0,1)} = 0. \tag{19}$$

The $g^{(0,1)} = \bar{g}^{(0,1)}$ is θ-independent. This information allows us to eliminate the contribution of $g^{(0,1)}$ when performing the θ averages in equation (21) below.

To calculate the $\bar{h}$-functions, we move to the $\mathcal{O}(\Delta\delta)$ equation. Using the identity

$$\frac{\partial}{\partial t} + c\frac{\boldsymbol{B}\times\nabla\Phi}{B^2}\cdot\nabla = \frac{\mathrm{d}_0}{\mathrm{d}t} = \frac{\mathrm{d}h}{\mathrm{d}\Omega}\frac{\omega}{m\tilde{\psi}}Rqk_\parallel\left.\frac{\partial}{\partial\xi}\right|_\Omega + \frac{\omega}{m}\left(1 - \frac{\partial h}{\partial\chi}\right)\frac{\partial}{\partial\theta}, \tag{20}$$

we obtain

$$\begin{aligned}\frac{\mathrm{d}h}{\mathrm{d}\Omega}\frac{\omega}{m\tilde{\psi}}Rqk_\parallel\left.\frac{\partial g^{(1,0)}}{\partial\xi}\right|_\Omega + \frac{\omega}{m}\left(1 - \frac{\partial h}{\partial\chi}\right)\frac{\partial g^{(1,0)}}{\partial\theta} + \frac{v_\parallel}{Rq}\frac{\partial g^{(1,1)}}{\partial\theta}\\ + k_\parallel v_\parallel\left.\frac{\partial g^{(1,0)}}{\partial\xi}\right|_\Omega + \frac{Iv_\parallel}{Rq}\frac{\partial}{\partial\theta}\left(\frac{v_\parallel}{\omega_\mathrm{c}}\right)\frac{\partial g^{(0,1)}}{\partial\chi} = m\frac{Iv_\parallel}{Rq}\frac{\partial}{\partial\chi}\left(\frac{v_\parallel}{\omega_\mathrm{c}}\right)\frac{\partial\Phi}{\partial\xi}\frac{q_\mathrm{i}F_\mathrm{M}}{T}.\end{aligned} \tag{21}$$

In order to calculate the $\bar{h}$-functions, it is convenient to use the bounce average operator, which has two different definitions in the trapped and in the passing region of phase space. We consider the passing region first. Starting from the average operator

$$\langle\ldots\rangle_\theta = \frac{1}{2\pi}\oint\ldots\mathrm{d}\theta,$$

the bounce average operator is defined as [21]

$$\left\langle\frac{Rq}{v_\parallel}\ldots\right\rangle_\theta = \frac{1}{2\pi}\oint\frac{Rq}{v_\parallel}\ldots\mathrm{d}\theta.$$

So we find

$$\begin{aligned}\left\langle\frac{\mathrm{d}h}{\mathrm{d}\Omega}\frac{\omega}{m\tilde{\psi}}\frac{Rqk_\parallel}{v_\parallel} + k_\parallel\right\rangle_\theta\left.\frac{\partial\bar{h}_\mathrm{P}^{(1,0)}}{\partial\xi}\right|_\Omega = I\left\langle\left(\frac{\mathrm{d}h}{\mathrm{d}\Omega}\frac{\omega}{m\tilde{\psi}}\frac{Rqk_\parallel}{v_\parallel} + k_\parallel\right)\frac{v_\parallel}{\omega_\mathrm{c}}\right\rangle_\theta\left.\frac{\partial}{\partial\xi}\right|_\Omega\left(\frac{\partial\Phi}{\partial\chi}\right)\frac{q_\mathrm{i}F_\mathrm{M}}{T}\\ + I\left\langle\frac{m}{Rq}\frac{\partial}{\partial\chi}\left(\frac{v_\parallel}{\omega_\mathrm{c}}\right)\right\rangle_\theta\frac{\partial\Phi}{\partial\xi}\frac{q_\mathrm{i}F_\mathrm{M}}{T}.\end{aligned} \tag{22}$$

As we focus on the contributions which vanish on the flux-surface average, $\bar{h}$-functions are supposed here to vanish when averaged over Ω, where the average on Ω is defined as

$$\langle \ldots \rangle_\Omega = \frac{\oint \cdots \mathrm{d}\xi/\sqrt{\Omega + \cos\xi}}{\oint \mathrm{d}\xi/\sqrt{\Omega + \cos\xi}}.$$

This is because all the contributions which do not vanish by using this operator are related to the bootstrap current. So we obtain

$$\bar{h}_{\mathrm{P}}^{(1,0)} = -\frac{4I}{W_\chi^2}\frac{\omega q}{mc}\frac{\mathrm{d}h}{\mathrm{d}\Omega}\frac{q_{\mathrm{i}}F_{\mathrm{M}}}{T}\left\langle\left(\frac{\mathrm{d}h}{\mathrm{d}\Omega}\frac{\omega}{m\tilde{\psi}}\frac{Rq}{v_\|}+1\right)\frac{v_\|}{\omega_{\mathrm{c}}}+\frac{q_{\mathrm{s}}}{q_{\mathrm{s}}'}\frac{\partial}{\partial\chi}\left(\frac{v_\|}{\omega_{\mathrm{c}}}\right)\right\rangle_\theta \cdot \left[\left\langle\frac{\mathrm{d}h}{\mathrm{d}\Omega}\frac{\omega}{m\tilde{\psi}}\frac{Rq}{v_\|}+1\right\rangle_\theta\right]^{-1}\left[\chi-\langle\chi\rangle_\Omega\right]. \tag{23}$$

The physical features related to this solution will be discussed in the next section.

We now solve equation (21) in the trapped region of velocity space. The corresponding bounce average operator becomes [21]

$$\left\langle\frac{Rq}{|v_\||}\ldots\right\rangle_\theta^{\mathrm{T}} = \sum_{\sigma=\pm1}\frac{1}{2\theta_{\mathrm{b}}}\int_{-\theta_{\mathrm{b}}}^{\theta_{\mathrm{b}}}\frac{Rq}{|v_\||}\ldots\mathrm{d}\theta,$$

yielding

$$\left.\frac{\partial\bar{h}_{\mathrm{T}}^{(1,0)}}{\partial\xi}\right|_\Omega = I\left\langle k_\|\frac{|v_\||}{\omega_{\mathrm{c}}}\left.\frac{\partial}{\partial\xi}\right|_\Omega\left(\frac{\partial\Phi}{\partial\chi}\right)+m\frac{\partial}{\partial\chi}\left(\frac{|v_\||}{\omega_{\mathrm{c}}}\right)\frac{\partial\Phi}{\partial\xi}\right\rangle_\theta^{\mathrm{T}} \times\left(\left\langle\frac{\mathrm{d}h}{\mathrm{d}\Omega}\frac{\omega}{m\tilde{\psi}}\frac{Rqk_\|}{|v_\||}\right\rangle_\theta^{\mathrm{T}}\right)^{-1}\frac{q_{\mathrm{i}}F_{\mathrm{M}}}{T}. \tag{24}$$

We can approximate the right-hand side of this equation noting that

$$\left\langle\frac{1}{v_\|}\right\rangle_\theta^{-1}\left\langle\nabla v_\|\right\rangle_\theta = \left\langle v_\|\nabla v_\|\right\rangle_\theta + \mathcal{O}\left(\epsilon^2\right). \tag{25}$$

Equation (25) and the identity

$$k_\|\left.\frac{\partial\chi}{\partial\xi}\right|_\Omega = \frac{m}{q}\frac{\partial A_\|}{\partial\xi} = \frac{m}{q}\frac{\tilde{\psi}}{R}\sin\xi \tag{26}$$

allow us to write equation (24) in the more perspicuous form

$$\bar{h}_{\mathrm{T}}^{(1,0)} = -\frac{q_{\mathrm{i}}F_{\mathrm{M}}}{T}\left[\omega_{\mathrm{D}}+\omega_{\hat{s}}\right]\frac{\left[\chi-\langle\chi\rangle_\Omega\right]}{c}. \tag{27}$$

Here, ω_{D} is defined as in equation (14) and $\omega_{\hat{s}}$ is related to the toroidal precession of a trapped particle due to the magnetic shear [22],

$$\omega_{\hat{s}} = \left\langle\frac{q\hat{s}v_\|^2}{r^2\omega_{\mathrm{c}}}\right\rangle_\theta^{\mathrm{T}}, \tag{28}$$

where $\hat{s}$ is the magnetic shear (the correlation of the ω_{D} and $\omega_{\hat{s}}$-terms with the poloidal component of magnetic drifts and the terms in $k_\| v_\|$, respectively, is discussed in the appendix). As both ω_{D} and $\omega_{\hat{s}}$ are related to magnetic effects, from here on we define the magnetic toroidal precession frequency [22]:

$$\omega_{\mathrm{tp}} = \omega_{\mathrm{D}} + \omega_{\hat{s}}. \tag{29}$$

Note that, within this ordering, $\bar{h}_{\mathrm{T}}^{(1,0)}$ does not depend on any quantity related to the island, apart from the average radial position $\langle\chi\rangle_\Omega$.

4.2. The perturbed current

The quasi-neutrality condition $\nabla \cdot \boldsymbol{J} = 0$ is now used to derive an expression for the θ-independent parallel current which closes the polarization drift. In [11], this equation reads

$$k_\parallel \left.\frac{\partial J_\parallel^{\mathrm{Pol}}}{\partial \xi}\right|_\Omega = -\frac{q_\mathrm{i} I}{\omega_\mathrm{c}}\frac{\omega}{m\tilde{\psi}}\int \mathrm{d}^3 v\, v_\parallel \frac{\partial}{\partial \chi}\left[\frac{\mathrm{d}h}{\mathrm{d}\Omega}\left\langle R q k_\parallel \left.\frac{\partial g^{(1,0)}}{\partial \xi}\right|_\Omega\right\rangle_\theta\right], \qquad (30)$$

where the superscript Pol refers to the polarization current. Considering the physical relation previously discussed between $g^{(1,0)}$ and ω_E, the integral on the right-hand side can be connected to the total time derivative of the electric precession (i.e. the acceleration along the island surface which allows the particle to experience a time-dependent electric field, see equation (20)). This is the physical mechanism of the neoclassical polarization. In the limit $\omega \gg k_\parallel v_\parallel$ adopted in [11] (which is an assumption that goes beyond the chosen scaling, and was adopted to isolate the polarization current), $\bar{h}_\mathrm{T}^{(1,0)}$ is zero, while a leading order annihilation takes place because the θ-dependent part of $g^{(1,0)}$ and $\bar{h}_\mathrm{P}^{(1,0)}$ differ only for higher order terms in ϵ. As a result, the polarization current contributing to the island dynamics is carried only by the trapped particles and is therefore $\mathcal{O}\left(\epsilon^{3/2}\right)$.

In our case, the quasi-neutrality condition includes the terms in $k_\parallel v_\parallel$ and has the following expression:

$$k_\parallel \left.\frac{\partial J_\parallel}{\partial \xi}\right|_\Omega = -\frac{q_\mathrm{i} I}{\omega_\mathrm{c}}\frac{\partial}{\partial \chi}\int \mathrm{d}^3 v\, v_\parallel \left\langle\left[\frac{\mathrm{d}h}{\mathrm{d}\Omega}\frac{\omega}{m\tilde{\psi}} R q k_\parallel + k_\parallel v_\parallel\right]\left.\frac{\partial g^{(1,0)}}{\partial \xi}\right|_\Omega\right\rangle_\theta . \qquad (31)$$

The terms in square brackets represent the advection along the magnetic surface, which includes now, in addition to that due to the island rotation and to the electric drift $\mathrm{d}_0/\mathrm{d}t$ (see equation (20)), also the parallel streaming of the ions through the term in $k_\parallel v_\parallel$. According to equations (18) and (23), we obtain

$$\begin{aligned}\left.\frac{\partial J_\parallel}{\partial \xi}\right|_\Omega = &-\frac{q_\mathrm{i} I}{\omega_\mathrm{c}}\frac{\partial}{\partial \chi}\int \mathrm{d}^3 v\, v_\parallel \Lambda F_\mathrm{M}\left\langle\left(\bar{u} + v_\parallel\right)\cdot\left[\left(\frac{v_\parallel}{\omega_\mathrm{c}}\right)\right.\right. \\ &\left.\left.-\left\langle\left(\frac{\bar{u}}{v_\parallel}+1\right)\frac{v_\parallel}{\omega_\mathrm{c}} + \frac{q_\mathrm{s}}{q_\mathrm{s}'}\frac{\partial}{\partial \chi}\left(\frac{v_\parallel}{\omega_\mathrm{c}}\right)\right\rangle_\theta \cdot \left\langle\frac{\bar{u}}{v_\parallel}+1\right\rangle_\theta^{-1}\right]\right\rangle_\theta ,\end{aligned} \qquad (32)$$

with

$$\Lambda = \frac{4I}{W_\chi^2}\frac{\omega q}{mc}\frac{\mathrm{d}h}{\mathrm{d}\Omega}\frac{q_\mathrm{i}}{T}\left.\frac{\partial \chi}{\partial \xi}\right|_\Omega$$

and

$$\bar{u} = \frac{\mathrm{d}h}{\mathrm{d}\Omega}\frac{\omega}{m\tilde{\psi}} R q .$$

Equation (32) exhibits an important feature: the resonant denominator that appears in the distribution function (23) is almost cancelled by a similar numerator which arises from including the parallel streaming in the advection, as discussed above (this cancellation can be shown to occur up to $\mathcal{O}\left(\epsilon^2\right)$). This is a consequence of the motion of the particles, which have (at least in this ordering) vanishing θ-averaged drifts across the flux surfaces when they approach the resonance.

Numerically, a resonant behaviour of the perturbed distribution function in velocity space can be clearly observed in figure 1(*a*), which shows δf in the vicinity of the inner island separatrix as a function of $v_\parallel/v$ and of v/v_th. The resonance is visible in the part of the velocity space with $v_\parallel < 0$. Passing particles with $v_\parallel > 0$ resonate on the other (outer) side

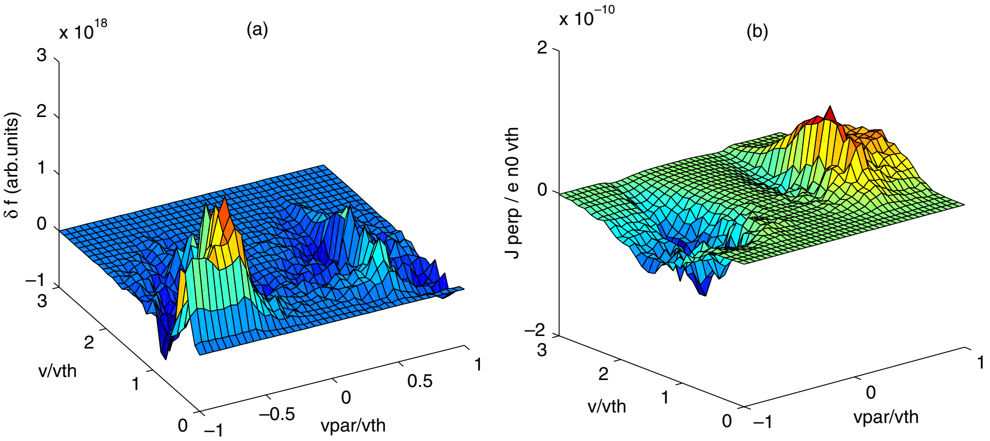

Figure 1. Perturbed distribution (*a*) and perpendicular current (*b*) in velocity space for the parameters described in section 3.2 and $\omega = -4000\,\mathrm{rad\,s^{-1}}$, calculated at the fourth radial cells outside the magnetic island towards the centre (cf figure 2).

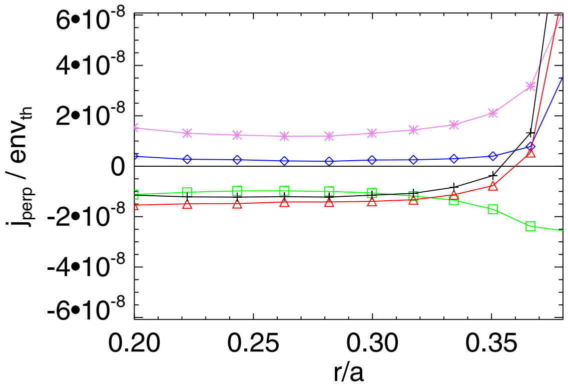

Figure 2. Radial profile of the perpendicular current (the inner island separatrix is located at $r/a = 0.38$) for $\omega = -4000\,\mathrm{rad\,s^{-1}}$. Magenta stars represent the contribution of the passing particles with $v_\parallel > 0$, green squares passing particles with $v_\parallel < 0$, blue diamonds the total current due to passing particles, red triangles the trapped particles and the crossed black line the total perpendicular current. The sudden rise of the current close to the island separatrix is due to the onset of the standard polarization current [14].

of the island, since $k_\parallel$ reverses its sign across the resonant surface. The corresponding current (figure 1(*b*)), however, does not present such a resonant behaviour. Moreover, it shows an odd symmetry with respect to $v_\parallel/v$, so that the passing particles do not contribute to the total current, i.e. their contribution vanishes after integration over velocity space because of the sum over σ, as can be seen in figure 2.

Formally, the contribution of the resonance to higher order corrections (not retained in our calculations) should be treated employing an approach similar to that of e.g. [17, 26–29]. However, we stress the fact that the Landau resonance contributes only to the 'out of phase' part of the current, determining the island rotation. These effects are not included in the analysis presented in this paper, where the rotation frequency ω is treated as a parameter and not determined self-consistently.

We conclude this section with a remark concerning the behaviour of the trapped particles. According to equation (27), the perturbed distribution $\bar{h}_{\mathrm{T}}^{(1,0)}$ introduces in the solution the magnetic toroidal precession of the trapped particles. In the next section, we will discuss in more detail how this precession can interact with the magnetic island. We anticipate that the $\bar{h}_{\mathrm{T}}^{(1,0)}$ found above represents an asymptotic limit for the solution we will find in section 5 if one supposes $\omega \gg \omega_{\mathrm{tp}}$.

5. The $\omega \sim \omega_{\mathrm{D}}$ regime

5.1. Solution of the drift-kinetic equation

We now order the terms of equation (10) supposing $\omega \sim \omega_{\mathrm{D}}$ (cf equation (14)). As previously stated, our goal is to study the physical mechanisms linked to the mutual interaction between the island propagation and the precession of trapped particles around it. The ordering of the terms in equation (10) becomes

$$\Delta\delta : 1 : \Delta : \Delta\delta : \Delta\delta : \delta : \Delta\delta : \Delta\delta^2 : \Delta^2\delta^2 = \delta^2 : \Delta\delta^2.$$

Again, as we did not include an adiabatic split of the Maxwellian, and as we are neglecting equilibrium gradients, we can set (see section 4):

$$g^{(0,0)} = 0. \tag{33}$$

Let us then move to the $\mathcal{O}(\delta)$ equation. We have

$$\frac{v_\parallel}{Rq}\frac{\partial}{\partial\theta}g^{(1,0)} = 0, \tag{34}$$

and this means

$$g^{(1,0)} = \bar{h}_{\mathrm{P}}^{(1,0)} + \bar{h}_{\mathrm{T}}^{(1,0)}. \tag{35}$$

The bar over a function again indicates that it is θ-independent. We have again divided the solution into two parts, each describing a different region of the velocity space.

Next we write the $\mathcal{O}(\Delta)$ equation. This is simply

$$\frac{v_\parallel}{Rq}\frac{\partial}{\partial\theta}g^{(0,1)} = 0. \tag{36}$$

So also $g^{(0,1)} = \bar{g}^{(0,1)}$ is θ-independent.

The following step is to calculate the $\mathcal{O}\left(\delta^2\right)$ equation,

$$\frac{v_\parallel}{Rq}\frac{\partial}{\partial\theta}g^{(2,0)} + \frac{Iv_\parallel}{Rq}\frac{\partial}{\partial\theta}\left(\frac{v_\parallel}{\omega_{\mathrm{c}}}\right)\frac{\partial}{\partial\chi}\bar{g}^{(1,0)} = -\frac{Iv_\parallel}{Rq}\frac{\partial}{\partial\theta}\left(\frac{v_\parallel}{\omega_{\mathrm{c}}}\right)\frac{\partial\Phi}{\partial\chi}\frac{q_{\mathrm{i}}F_{\mathrm{M}}}{T} \tag{37}$$

which can be integrated over θ, so we have

$$g^{(2,0)} = -I\frac{v_\parallel}{\omega_{\mathrm{c}}}\frac{\partial}{\partial\chi}\left[\frac{q_{\mathrm{i}}\Phi}{T}F_{\mathrm{M}} + \bar{g}^{(1,0)}\right] + \bar{h}_{\mathrm{P}}^{(2,0)} + \bar{h}_{\mathrm{T}}^{(2,0)}, \tag{38}$$

where again we separate the trapped and passing contributions in defining the functions $\bar{h}_{\mathrm{P}}^{(2,0)}$ and $\bar{h}_{\mathrm{T}}^{(2,0)}$, which result as constants of integration.

To evaluate the lowest order contribution due to the island, i.e. the $\bar{g}^{(1,0)}$, we now turn to the $\mathcal{O}\left(\Delta\delta^2\right)$ equation, which has the form

$$\begin{aligned} &-\omega\frac{\partial}{\partial\xi}\bar{g}^{(1,0)} + \frac{v_\parallel}{Rq}\frac{\partial}{\partial\theta}g^{(2,1)} + k_\parallel v_\parallel\left.\frac{\partial}{\partial\xi}\bar{g}^{(2,0)}\right|_{\Omega} + c\frac{\boldsymbol{B}\times\nabla\Phi}{B^2}\cdot\nabla\bar{g}^{(1,0)} + \frac{Iv_\parallel}{Rq}\frac{\partial}{\partial\theta}\left(\frac{v_\parallel}{\omega_{\mathrm{c}}}\right)\frac{\partial}{\partial\chi}\bar{g}^{(1,1)} \\ &\quad -m\frac{Iv_\parallel}{Rq}\frac{\partial}{\partial\chi}\left(\frac{v_\parallel}{\omega_{\mathrm{c}}}\right)\frac{\partial}{\partial\xi}\bar{g}^{(1,0)} = m\frac{Iv_\parallel}{Rq}\frac{\partial}{\partial\chi}\left(\frac{v_\parallel}{\omega_{\mathrm{c}}}\right)\frac{\partial\Phi}{\partial\xi}\frac{q_{\mathrm{i}}F_{\mathrm{M}}}{T}. \end{aligned} \tag{39}$$

Let us solve this equation first in the trapped region of phase space. We use the bounce average operator defined for the trapped region (see section 4). Recalling equation (38), this yields

$$\begin{aligned}
-\omega\left\langle\frac{Rq}{|v_\parallel|}\right\rangle_\theta^{\mathrm{T}}\frac{\partial}{\partial\xi}\bar{h}_{\mathrm{T}}^{(1,0)} &- I\left\langle Rqk_\parallel\frac{\partial}{\partial\xi}\left(\frac{|v|_\parallel}{\omega_{\mathrm{c}}}\frac{\partial}{\partial\chi}\bar{h}_{\mathrm{T}}^{(1,0)}\right)\Big|_\Omega\right\rangle_\theta^{\mathrm{T}}\\
&+c\left\langle\frac{Rq}{|v_\parallel|}\frac{\boldsymbol{B}\times\nabla\Phi}{B^2}\right\rangle_\theta^{\mathrm{T}}\cdot\nabla\bar{h}_{\mathrm{T}}^{(1,0)} - mI\left\langle\frac{\partial}{\partial\chi}\frac{|v|_\parallel}{\omega_{\mathrm{c}}}\right\rangle_\theta^{\mathrm{T}}\frac{\partial}{\partial\xi}\bar{h}_{\mathrm{T}}^{(1,0)}\\
&= mI\left\langle\frac{\partial}{\partial\chi}\frac{|v|_\parallel}{\omega_{\mathrm{c}}}\right\rangle_\theta^{\mathrm{T}}\frac{\partial\Phi}{\partial\xi}\frac{q_{\mathrm{i}}F_{\mathrm{M}}}{\mathrm{T}} + I\left\langle Rqk_\parallel\frac{\partial}{\partial\xi}\left[\frac{|v|_\parallel}{\omega_{\mathrm{c}}}\frac{\partial}{\partial\chi}\left(\frac{q_{\mathrm{i}}\Phi}{T}F_{\mathrm{M}}\right)\right]\Big|_\Omega\right\rangle_\theta^{\mathrm{T}}. \qquad (40)
\end{aligned}$$

We note that

$$\left\langle\frac{\partial}{\partial\theta}\left(\frac{|v_\parallel|}{\omega_{\mathrm{c}}}\right)\frac{\partial g^{(1,1)}}{\partial\chi}\right\rangle_\theta^{\mathrm{T}} = 0$$

because, for symmetry reasons, we can suppose $g^{(1,1)}$ to be an even function in θ . We also suppose that $\bar{h}_{\mathrm{T}}^{(2,0)}$ is independent of σ, which is consistent with the bounce point continuity condition.

An analytic solution of equation (40) is extremely difficult. However, we can greatly simplify this equation by employing the same approximation as in equation (25) (for the details of the calculation see the appendix). If we focus on the dynamics along the island (the radial component of the $\boldsymbol{E}\times\boldsymbol{B}$ drift, which goes to zero faster with χ than the other terms, will be shown later to be important only to unlock resonating particles), it is possible to write equation (40) as:

$$\left[-\omega-\frac{m}{q}\omega_{\mathrm{E}}-\frac{m}{q}\omega_{\mathrm{tp}}\right]\frac{\partial\bar{h}_{\mathrm{T}}^{(1,0)}}{\partial\xi} = \frac{m}{q}\omega_{\mathrm{tp}}\frac{q_{\mathrm{i}}F_{\mathrm{M}}}{T}\frac{\partial\Phi}{\partial\xi}. \qquad (41)$$

Equation (41) can be integrated with the condition $\bar{h}_{\mathrm{T}}^{(1,0)}\to 0$ for $\chi\to\infty$. For the sake of simplicity, we neglect the dependence of ω_{E} on ξ, so that the only quantity depending on ξ is the electrostatic potential.

$$\bar{h}_{\mathrm{T}}^{(1,0)} = -\frac{m}{q}\frac{\omega_{\mathrm{tp}}}{\omega+(m/q)\omega_{\mathrm{E}}+(m/q)\omega_{\mathrm{tp}}}\frac{q_{\mathrm{i}}\Phi}{T}F_{\mathrm{M}}. \qquad (42)$$

Note that in this case the χ part of the potential plays the role of an integration constant. The physical implications of equation (42) will be discussed in the following section.

We now turn back to equation (39) and we solve it in the passing region of phase space. Again we suppose that the bounce average operator (see section 4) cancels the $g^{(1,1)}$ contribution. The fundamental difference with respect to the trapped particles is that for passing particles

$$\left\langle\frac{\partial}{\partial\chi}\left(\frac{v_\parallel}{\omega_{\mathrm{c}}}\right)\right\rangle_\theta = \mathcal{O}\left(\epsilon^2\right),$$

so the term on the right-hand side of equation (39) is negligible. This equation then becomes

$$-\omega\frac{\partial}{\partial\xi}\bar{h}_{\mathrm{P}}^{(1,0)} - \left\langle Rqk_\parallel\frac{\partial}{\partial\xi}g^{(2,0)}\Big|_\Omega\right\rangle_\theta + c\frac{\boldsymbol{B}\times\nabla\Phi}{B^2}\cdot\nabla\bar{h}_{\mathrm{P}}^{(1,0)} = 0. \qquad (43)$$

We can choose

$$\bar{h}_{\mathrm{P}}^{(1,0)} = 0.$$

This solution is consistent with the fact that, in this regime, the contribution of the passing particles to the perpendicular current is negligible. So we obtain

$$\left\langle Rqk_{\|}\,\frac{\partial}{\partial\xi}g^{(2,0)}\Big|_{\Omega}\right\rangle_{\theta} = 0 \tag{44}$$

which in view of equation (38) leads to

$$\bar{h}_{\mathrm{P}}^{(2,0)} = \left\langle I\,\frac{v_{\|}}{\omega_{\mathrm{c}}}\frac{\partial}{\partial\chi}\frac{q_{\mathrm{i}}\Phi}{T}F_{\mathrm{M}}\right\rangle_{\theta}. \tag{45}$$

Inserting equation (45) into equation (38), we see that these equations are linked to the annihilation in the passing region of the phase space discussed in section 4. Within the ordering employed in this section, this contribution still exists, but it pertains to a higher order because of the island propagation frequency ordering, and by consequence all the purely electric effects (see equation (7)) become less important.

5.2. *The perturbed current*

The velocity perpendicular to perturbed magnetic surface can be thought as the variation of the Ω coordinate with respect to time, i.e. $\mathrm{d}\Omega/\mathrm{d}t$. We are interested in the lowest order, θ-averaged perturbed current.

By the definition of the total derivative, and noticing that $\nabla_{\|}\Omega = 0$, we can write

$$\frac{\mathrm{d}\Omega}{\mathrm{d}t} = \frac{\partial\Omega}{\partial t} + \boldsymbol{v}\cdot\nabla\Omega = \frac{\partial\Omega}{\partial t} + (\boldsymbol{v}_{\boldsymbol{E}\times\boldsymbol{B}} + \boldsymbol{v}_{\mathrm{D}})\cdot\nabla\Omega. \tag{46}$$

Considering equation (7), and recalling that

$$\frac{\partial}{\partial t} = -\omega\frac{\partial}{\partial\xi},$$

we note that

$$\frac{\partial\Omega}{\partial t} + \boldsymbol{v}_{\boldsymbol{E}\times\boldsymbol{B}}\cdot\nabla\Omega = 0$$

and this means, for trapped particles

$$\frac{\mathrm{d}\Omega}{\mathrm{d}t} = -\frac{m}{q}\omega_{\mathrm{D}}\sin\xi. \tag{47}$$

The radial component of the magnetic drift does not contribute to the current we are interested in because it θ-averages to zero even in the trapped region of phase space. So the toroidal precession in this island propagation frequency regime is the main mechanism which allows a particle to explore different magnetic surfaces. This is a fundamental difference with the previous section, because for passing particles this contribution averages to $\mathcal{O}\left(\epsilon^2\right)$, so that what forces particles to explore different magnetic surface is not an equilibrium velocity contribution.

Equation (47) allows us to write an approximate expression for the θ-averaged current crossing the perturbed magnetic surface in the presence of a slowly rotating NTM as a function of v:

$$J_{\perp}(v) = q_{\mathrm{i}}\left\langle g^{(1,0)}\frac{\mathrm{d}\Omega}{\mathrm{d}t}\frac{1}{|\nabla\Omega|}\right\rangle_{\theta} = \frac{m^2}{q^2}\frac{q_{\mathrm{i}}^2\Phi}{T}\frac{\omega_{\mathrm{D}}\omega_{\mathrm{tp}}}{\omega + (m/q)\omega_{\mathrm{tp}} + (m/q)\omega_{\mathrm{E}}}\frac{1}{|\nabla\Omega|}F_{\mathrm{M}}\sin\xi, \tag{48}$$

estimating with $\mathrm{d}\Omega/\mathrm{d}t\cdot 1/|\nabla\Omega|$ the velocity component perpendicular to the perturbed magnetic surface. We recall that $g^{(1,0)}$ is non-zero only for trapped particles. This expression

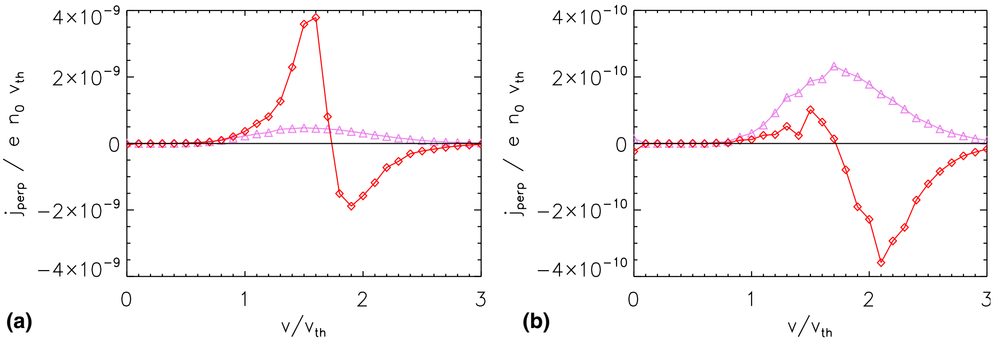

Figure 3. Perpendicular current as a function of velocity, calculated at the fourth radial cells outside the magnetic island towards the plasma centre, for $\omega = 300\,\mathrm{rad\,s^{-1}}$ (triangles) and for $\omega = -300\,\mathrm{rad\,s^{-1}}$ (diamonds) in the collisionless regime (*a*) and in a standard banana collisional regime (*b*). Note the different scale on the y-axis.

for the perpendicular current at low rotation frequencies is confirmed by our numerical simulations.

We see in figure 3 that for positive frequencies no particle can be resonant with the NTM, since the island drift and the precession of the trapped particles are in opposite directions, so the distribution is quite smooth. On the other hand, if the frequency is negative, the distribution starts to be very peaked around that region of phase space where $\omega \approx n\omega_{\mathrm{tp}}$ (we recall that ω_{tp} depends on v), and changes sign around this critical value of velocity.

Another important information which can be gained from figure 3 is that, for the trapped-particle resonance under consideration, the physical effect that resolves the singularity in equation (48) is represented by collisions, even for the low-collisionality regime discussed in this paper. This is consistent with the fact that, in our simulations, the frequency on which trapped particles can be scattered into the passing domain is comparable to or higher than the toroidal precession of thermal ions $\omega_{\mathrm{tp}} \sim \omega$. Figure 3(*b*) is obtained in the standard banana regime ($\nu_{\mathrm{coll}}/\epsilon \sim 10^2$ Hz, and $\omega_{\mathrm{b}}/2\pi \sim 10^4$ Hz, where ν_{coll} is the collision frequency and ω_{b} the banana bounce frequency), whereas in figure 3(*a*), where the collision frequency is reduced by five orders of magnitude (we call this a 'collisionless' regime). Collisions drastically reduce the peaks of $J_{\perp}(v)$ around the resonance, this effect being more pronounced for slower particles, as can be expected. As a consequence of this last fact, in particular, the sign of the total perpendicular current density (i.e. of the integral of $J_{\perp}(v)$ over v) can change depending on the collision frequency, as shown in figure 4(*a*). The sign of the perpendicular current is of course crucial for the determination of the stabilizing or destabilizing nature of the perturbed parallel current.

To evaluate explicitly the influence of this current on the NTM stabilization, we need to compute the closure parallel current. However, the integration over the velocity space cannot be performed because of the resonant denominator in $\bar{h}_{\mathrm{T}}^{(1,0)}$ (see equation (42)). To account of the effect of collisions, we go back to equation (41) and we add a simple Krook collision operator $(\partial f/\partial t|_{\mathrm{coll}} = -\nu(f - F_{\mathrm{M}})$, where $(f - F_{\mathrm{M}}) = \bar{h}_{\mathrm{T}}^{(1,0)}$ and $\nu = \nu_0 {v_{\mathrm{th}}}^3/v^3)$. We obtain

$$\left[-\omega - \frac{m}{q}\omega_{\mathrm{tp}} - \frac{m}{q}\omega_{\mathrm{E}}\right]\frac{\partial \bar{h}_{\mathrm{T}}^{(1,0)}}{\partial \xi} = \frac{m}{q}\omega_{\mathrm{tp}}\frac{q_{\mathrm{i}}F_{\mathrm{M}}}{T}\frac{\partial \Phi}{\partial \xi} - \nu \bar{h}_{\mathrm{T}}^{(1,0)}. \tag{49}$$

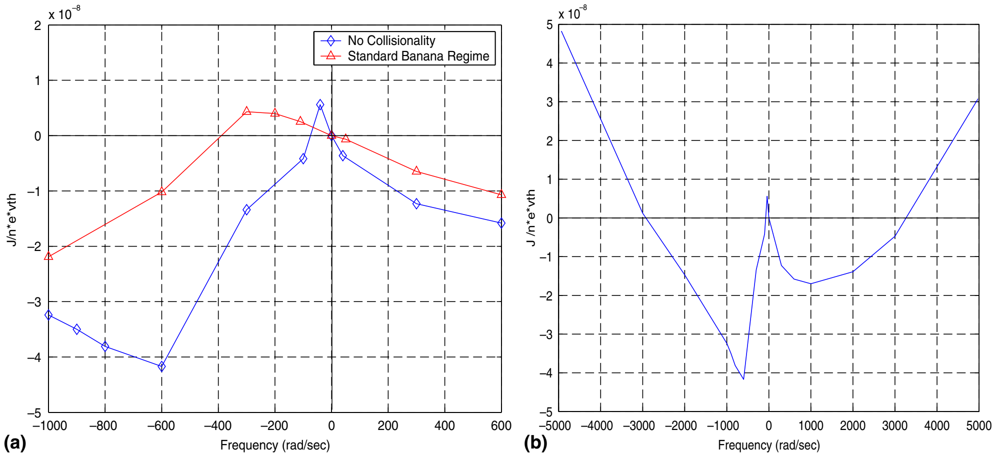

Figure 4. (*a*) Comparison between the perpendicular current integrated in the velocity space versus island propagation frequency in non-collisional regime (diamonds) and in standard banana regime (triangles). (*b*) Perpendicular current integrated in the velocity space versus island propagation frequency in the non-collisional regime showing the transition to the standard polarization current (proportional to ω^2) at high frequencies.

Again, we neglect the ξ dependence of ω_{E} for the sake of simplicity. Indicating

$$\bar{\omega} = \omega + \frac{m}{q}\omega_{\mathrm{tp}} + \frac{m}{q}\omega_{\mathrm{E}}, \qquad \bar{F} = \frac{m}{q}\omega_{\mathrm{tp}}\frac{q_{\mathrm{i}}F_{\mathrm{M}}}{T}$$

and expanding the island potential into its Fourier components

$$\Phi = \sum_{k=0}^{\infty} \hat{\Phi}_k(\chi)\cos(k\xi)$$

a solution to equation (49) is found in the form

$$\bar{h}_{\mathrm{T}}^{(1,0)} = -\bar{\omega}\bar{F}\sum_{k=0}^{\infty}\frac{k^2\hat{\Phi}_k(\chi)}{\bar{\omega}^2k^2+\nu^2}\mathrm{e}^{\nu/\bar{\omega}\cdot\xi} - \mathrm{e}^{\nu/\bar{\omega}\cdot\xi}\frac{\bar{F}}{\bar{\omega}}\int_0^{\xi}\mathrm{d}\xi'\mathrm{e}^{-\nu/\bar{\omega}\cdot\xi'}\frac{\partial\Phi}{\partial\xi'}, \tag{50}$$

using as a boundary condition the fact that the solution must be finite for $\bar{\omega}\to 0$.

Now we use the quasi-neutrality condition $\nabla\cdot\boldsymbol{J} = 0$, multiplying the ion and electron drift-kinetic equations times the respective charge, and then summing them, neglecting the magnetic drifts of the electrons (cf [11]). The θ-averaged parallel current is then

$$k_{\|}\left.\frac{\partial J_{\|}}{\partial\xi}\right|_{\Omega} = mq_{\mathrm{i}}\left\langle\int\mathrm{d}^3v\frac{Iv_{\|}}{Rq}\frac{\partial}{\partial\chi}\left(\frac{v_{\|}}{\omega_{\mathrm{c}}}\right)\frac{\partial\bar{h}_{\mathrm{T}}^{(1,0)}}{\partial\xi}\right\rangle_{\theta} \approx nq_{\mathrm{i}}\int\mathrm{d}^3v\;\omega_{\mathrm{D}}\frac{\partial\bar{h}_{\mathrm{T}}^{(1,0)}}{\partial\xi}. \tag{51}$$

The approximations leading to the appearance of ω_{D} in the last step have been discussed previously (see again the appendix for details). Exploiting equation (50), one obtains after some algebra

$$\frac{\partial\bar{h}_{\mathrm{T}}^{(1,0)}}{\partial\xi} = \bar{F}\sum_{k=0}^{\infty}k^2\hat{\Phi}_k\frac{\bar{\omega}k\,\sin(k\xi) - \nu\,\cos(k\xi)}{\bar{\omega}^2k^2+\nu^2}. \tag{52}$$

We neglect the cosine terms in equation (52), because they are related to out-of-phase current contributions which are not involved in the island stabilization [2] (they contribute to determining the island rotation frequency; a detailed analysis of these effects, however, is beyond the scope of this paper). With this approximation

$$\frac{\partial \bar{h}_{\mathrm{T}}^{(1,0)}}{\partial \xi} = \bar{F} \sum_{k=0}^{\infty} \hat{\Phi}_k \frac{\bar{\omega} k \, \sin(k\xi)}{\bar{\omega}^2 + \nu^2/k^2} = -\frac{\bar{\omega}\bar{F}}{\bar{\omega}^2 + \nu_{\mathrm{eff}}^2} \frac{\partial \Phi}{\partial \xi}, \tag{53}$$

where the effective collision frequency ν_{eff} is implicitly defined by this equation.

Going back to equation (51), with the help of the pitch-angle variables (v, λ) and supposing $\omega_{\mathrm{tp}} = \omega_{\mathrm{tp}}(v)$ (which relies on the fact that in the trapped region of phase space $v \approx v_\perp \gg v_\parallel$), one obtains

$$J_\parallel = -n_0 \frac{4}{\sqrt{\pi} k_\parallel} \sqrt{\epsilon} n^2 \frac{q_{\mathrm{i}}^2}{T} \omega_{\mathrm{tp}}^0 \omega_{\mathrm{D}}^0 \frac{q}{mc} \frac{\mathrm{d}h}{\mathrm{d}\Omega} K_1(\omega) \left[\cos(\xi) - \langle \cos(\xi) \rangle_\Omega \right], \tag{54}$$

where

$$K_1(\omega) = \int_0^\infty \mathrm{d}y\, y^{12} \frac{\omega e^{-y^2} \left(\omega + n\omega_{\mathrm{E}} + n\omega_{\mathrm{tp}} y^2\right)}{\left(\omega + n\omega_{\mathrm{E}} + n\omega_{\mathrm{tp}} y^2\right)^2 y^6 + \left(\nu_{\mathrm{eff}}^0\right)^2},$$

having defined $y = v/v_{\mathrm{th}}$ and $\omega_{\mathrm{tp}} = \omega_{\mathrm{tp}}^0 y^2$, $\nu_{\mathrm{eff}} = \nu_{\mathrm{eff}}^0/y^3$. The parameter $K_1(\omega)$ can be computed if all the plasma parameters are known, and it is important to note that it is the only factor in equation (54) which depends on the island rotation frequency. The integration has been performed within the condition that this parallel current vanishes when flux-surface averaged. From here on, we call this perturbed current the *precessional current*, and we indicate it as $J_\parallel^{\mathrm{Pr}}$. Its contribution to the island stability can be found with the help of the Ampère equation [2]:

$$\sum_{\pm} \int_{-1}^{\infty} \mathrm{d}\Omega \oint \mathrm{d}\xi \frac{J_\parallel^{\mathrm{Pr}} \cos(\xi)}{\sqrt{\Omega + \cos(\xi)}} = \frac{c}{8\sqrt{2}} \Delta'_{\mathrm{Pr}} \frac{wB}{Rq}. \tag{55}$$

Here, the sum is defined over the $\chi > \chi_{\mathrm{s}}$ and $\chi < \chi_{\mathrm{s}}$ regions. It yields, after some algebra

$$\Delta'_{\mathrm{Pr}} = \frac{32 n_0}{\sqrt{2\pi} wB} \sqrt{\epsilon} n^2 \frac{q_{\mathrm{i}}^2}{T} \omega_{\mathrm{tp}}^0 \omega_{\mathrm{D}}^0 \frac{q}{m^2 c^2} \frac{q_{\mathrm{s}}}{q'_{\mathrm{s}}} R^2 q^2 K_1(\omega) K_2, \tag{56}$$

where K_2 is a negative constant defined as

$$K_2 = \int_1^\infty \frac{\mathrm{d}\Omega}{\sqrt{\Omega}} \oint \mathrm{d}\xi \frac{\cos^2(\xi) - \cos(\xi) \langle \cos(\xi) \rangle_\Omega}{\Omega + \cos(\xi)} \simeq -6.65.$$

The sign of Δ'_{Pr} depends only on the sign of $K_1(\omega)$. We recall that positive values of Δ' correspond to destabilizing effects [2]. Thus, we have a stabilizing current for $\omega > 0$ and, if $\omega < 0$, for $|\omega|$ sufficiently larger than ω_{tp}.

We now compare the contribution we just found and that of the polarization current, in order to understand under what circumstances one prevails over the other. For the parallel current which closes the polarization current, equation (30), we refer to the $\omega \gg k_\parallel v_\parallel$ case, so that $\bar{h}_{\mathrm{T}}$ is zero, while for this comparison we refer to the parallel precessional current as expressed in equation (51). As we are comparing the two contributions in trapped space, we do not consider $\bar{h}_{\mathrm{P}}$ functions. Using the identity equation (62), see the appendix, we can write

$$k_\parallel \left. \frac{\partial J_\parallel^{\mathrm{Pol}}}{\partial \xi} \right|_\Omega = -\frac{q_{\mathrm{i}} I^2}{\omega_{\mathrm{c}}^2} \frac{\omega^2 q}{mc} \frac{\mathrm{d}h}{\mathrm{d}\Omega} \frac{8}{W_\chi^2} \int \mathrm{d}^3 v \, v_\parallel^2 \frac{\partial}{\partial \chi} \left(\frac{\mathrm{d}h}{\mathrm{d}\Omega} \right) \frac{q_{\mathrm{i}} F_{\mathrm{M}}}{T} \sin \xi. \tag{57}$$

We can compare $J_\parallel^{\mathrm{Pr}}$ and $J_\parallel^{\mathrm{Pol}}$ by comparing the two functions under the integration operator. So, the two contributions are comparable if

$$\frac{I}{\omega_{\mathrm{c}}^2} \omega \frac{1}{W_\chi^2} \frac{\partial}{\partial \chi} \frac{\mathrm{d}h}{\mathrm{d}\Omega} \sim \frac{m}{Rq} \frac{\partial}{\partial \chi} \left(\frac{v_\parallel}{\omega_{\mathrm{c}}} \right) \frac{n\omega_{\mathrm{tp}}}{\omega + n\omega_{\mathrm{tp}}}, \tag{58}$$

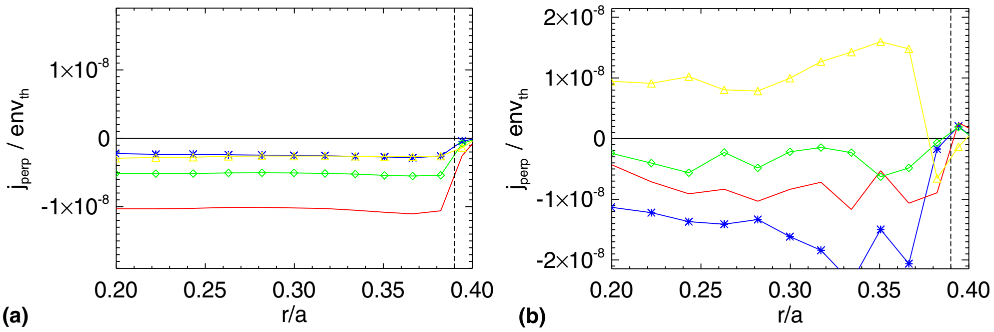

Figure 5. Current on the X-point helical cell (triangles), on the O-point cell (stars), on the intermediate cell (diamonds) and their sum (solid) for (*a*) $\omega = 300\,\mathrm{rad\,s^{-1}}$ and (*b*) $\omega = -300\,\mathrm{rad\,s^{-1}}$.

where ω_E in equation (51) has been discarded for the sake of simplicity. If we are not so far away from the island (i.e. $(\chi - \chi_s) \sim W_\chi$) the derivative in χ of $\mathrm{d}h/\mathrm{d}\Omega$ is $\mathcal{O}(1)$. According to the estimate (see the appendix)

$$\frac{\partial}{\partial\chi}\left(\frac{v_\parallel}{\omega_c}\right) \approx \frac{Rq\omega_{tp}}{Iv_\parallel}, \tag{59}$$

equation (58) becomes

$$\frac{I^2}{\omega_c^2}\omega\frac{v_\parallel^2}{W_\chi^2} \sim n\omega_{tp}\frac{n\omega_{tp}}{\omega}. \tag{60}$$

We estimate $v_\parallel \sim \sqrt{\epsilon}v_{th}$. Recalling that the ion banana width ρ_b can be calculated as $\rho_b = \sqrt{\epsilon}\rho_\theta$, we can conclude that the polarization current is comparable with the precessional current if

$$\frac{n\omega_{tp}}{\omega} \sim \frac{\rho_b}{w}. \tag{61}$$

The ratio on the right-hand side of equation (61) is assumed to be small in our calculations, cf equation (13), so that the assumption that the ratio on the left-hand side of equation (61) is of the same order of magnitude is absolutely realistic.

6. Discussion and conclusions

We have studied the plasma current due to a rotating magnetic island when the island propagation frequency is comparable to the parallel streaming of the passing particles ($k_\parallel v_\parallel$) or to the toroidal precession frequency the trapped particles (ω_{tp}) in a low-collisional plasma. When the absolute value of ω is large ($\omega \gg k_\parallel v_\parallel$, assuming for passing particles $v_\parallel \sim v_{th}$), the polarization current, which scales like ω^2 in the absence of equilibrium gradients, is the dominant contribution. In section 4, we showed that even if $\omega \sim k_\parallel v_\parallel$ the polarization current remains the most important perturbed current linked to the presence of the island rotation, since the contribution of the resonating (passing) particles, significant for the distribution function, is almost cancelled when the corresponding current is calculated. In section 5, we showed that for decreasing values of ω other electric and magnetic effects dominate over the polarization current. In particular, the toroidal electric field generated by a magnetic island can modify the magnetic toroidal precession a trapped particle experiences in an equilibrium configuration, braking or accelerating the particle itself. This leads to the appearance of a *precessional* current competing with the polarization current. For a more detailed physical explanation of this effect, we distinguish between positive and negative frequencies. For positive frequencies, the magnetic island is moving towards the $-\nabla\zeta$-direction, while both electric and magnetic toroidal drifts point in the $\nabla\zeta$-direction. If we suppose to build a frame of reference which moves in the toroidal direction together with the island (from here on: IFR, island frame of reference), we will see all the trapped particles travelling in the $\nabla\zeta$-direction. The toroidal component of the electric field E_ζ varies sinusoidally along the island, see equation (7). So in regions where it points in the $\nabla\zeta$-direction, all particles tend to increase their kinetic energy and finally their magnetic precession frequency (recall $\omega_{\mathrm{tp}} \propto v^2$), while they slow down in the opposite case. This means that between O and X and between X and O, all trapped particles either accelerate or decelerate, depending on the sign of E_ζ (they accelerate for $E_\zeta > 0$ and decelerate for $E_\zeta < 0$, respectively). Where they decelerate, they tend to accumulate, so that the local density increases. On the contrary, they tend to disperse as they accelerate, so that the local density decreases. Figure 5(*a*) shows this situation in the 'upper' half of the island (as stated before, the situation is opposite in the 'lower' half).

This picture is different when $\omega < 0$. In this case the island is propagating in the same direction as the particles ($\nabla\zeta$-direction), so *in the IFR* there are particles moving in the $\nabla\zeta$ direction (if $|\omega| < \omega_{\mathrm{tp}}$, high-energy particles) and in the $-\nabla\zeta$ direction (if $|\omega| > \omega_{\mathrm{tp}}$, low-energy particles). Now, when, for example, E_ζ points in the $-\nabla\zeta$-direction, again all particles decrease their magnetic precession frequency. The behaviour of more energetic particles is the same as the one described before. But slower particles, if decelerated in the laboratory frame, *actually increase their relative speed with respect to the island, so the effect is an acceleration in the* IFR. In other words, where slower particles accumulate, faster particles disperse and vice versa, and this explains why the perturbation on the distribution function changes sign around $w_{\mathrm{tp}} \sim |w|$. Moreover, another mechanism complicates the overall picture in the case $\omega < 0$. In this case, the electric toroidal precession ω_{E} acts in the opposite direction with respect to the magnetic drifts. So, moving from the O-point (where the radial electric field is maximum, in absolute value) to the X-point (where the radial electric field is the lowest in absolute value) *the number of particles which overtake the island or are overtaken by it in* IFR *can change* (cf equation (42)). The variation of ω_{E} with ξ is such that the integral of $J_\perp$ over velocity space can change its sign depending on where, with respect to the island, we are performing the integration. This especially happens if $|\omega| \sim \omega_{\mathrm{tp}}\,(v_{\mathrm{th}})$, because in that region of phase space lies a large number of particles, so even a small shift of the resonant point means turning a large number of faster particles into slower or vice versa (cf figure 3(*a*)). This physical picture is confirmed in figure 5(*b*)). In this case, we are able to identify the change of sign of the current going from O-point to X-point, as indeed $|\omega| \approx \omega_{\mathrm{tp}}\,(v_{\mathrm{th}})$. It is important to stress that resonance conditions are highly local, so after a while a resonant particle will be able to unlock from the island, for example through the radial component of the $\boldsymbol{E} \times \boldsymbol{B}$ drift.

There are some strong analogies between the behaviour of the trapped and passing particles as their motion along the island start to be comparable with the rotation of the island itself (i.e. the case $\omega \sim \omega_{\mathrm{D}}$ and $\omega \sim k_\parallel v_\parallel$, respectively). In both cases, the lowest order perturbed distribution function exhibits a resonant denominator (equations (23) and (42)), which underlines the fact that the interaction between the particles and the mode (and the subsequent modification of the distribution function) is stronger if the particle and the island have a small relative motion. Indeed, this result is not surprising for most wave–particle interactions. Nevertheless, significant differences occur as we focus on the corresponding perturbed current. Trapped particles cross the perturbed magnetic surfaces just because of their equilibrium drift velocity (see equation (47)), so that every perturbation on the distribution immediately leads to a current such that

$$\delta J_\perp \propto q_\mathrm{i} \left\langle \delta f \boldsymbol{v}_\mathrm{D} \cdot \nabla\Omega \right\rangle_\theta .$$

This is not the case for passing particles, as their θ-averaged equilibrium drift across the perturbed flux surface is much smaller. For resonating particles, in particular, the advection is such that it nearly cancels the contribution of the perturbed distribution function to the current, as shown in section 4.

Referring to figure 4(*b*), we can now discuss all the changes of sign of $J_\perp$ as a function of ω, going from right to left. For positive island frequencies, we experience a change of sign when the precessional current starts to exceed the standard polarization current. The sign reversal at ω=0 is due to the fact that the electric potential goes through zero and changes sign across that value (cf equations (7) and (42)). As a matter of fact, for extremely small negative values of ω, the situation more or less corresponds to the one which occurs for small positive values of ω, as almost all particles are faster than the island. So the sign reversal is due to a sign reversal in the electric field. As ω grows, the fraction of slower particles gets larger, and this leads to the third change of sign. Collisions contribute to determine the position of this third reversal, since they determine how the singularity in equation (48) is resolved. Finally, for large negative values of ω the polarization current prevails again. The qualitative agreement between the analytical and numerical results is remarkable.

The change of sign determines the stabilizing or destabilizing effect of these currents. The precessional current is found to be stabilizing for $\omega > 0$ and, if $\omega < 0$, for $|\omega|$ sufficiently larger than ω_tp. It is known that polarization current is globally *destabilizing*, neglecting equilibrium gradients effects, because of the 'current spike' at the island separatrix [30], without which it would be stabilizing. This precessional current acts against the polarization current (which is in our case always destabilizing, according to the analysis of [30]). We emphasize that in this paper we neglected effects connected to equilibrium pressure gradients, as our aim was not a complete determination of the island dynamics, but rather the discussion of the contributions linked to the island rotation and to possible resonances with the motion of the particles. Our finding that precessional effects can compete with the neoclassical polarization and that trapped-particle resonances have a major impact on this effect highlights once again that a kinetic description is mandatory in view of an exhaustive theory of NTMs in toroidal plasmas.

Appendix

In this appendix the relation between the toroidal magnetic precession frequencies of trapped particles ω_D and $\omega_{\hat{s}}$ and the corresponding terms in equation (41) is briefly discussed. We start with ω_D, which deals with the poloidal component of the equilibrium magnetic drift $\boldsymbol{v}_D$. As the spatial derivatives have to be taken at constant kinetic energy, one can write [21]

$$\nabla v_\parallel = -\frac{1}{m_\mathrm{i} v_\parallel}\mu\nabla B.$$

Using this relation, recalling that the parallel velocity and the cyclotron frequency depend on space only through the magnitude of the magnetic field, one can write

$$\frac{\partial}{\partial\chi}\left(\frac{v_\parallel}{\omega_\mathrm{c}}\right) = -\frac{1}{\omega_\mathrm{c}}\left[\frac{\mu}{m_\mathrm{i} v_\parallel} + \frac{v_\parallel}{B}\right]\frac{\partial B}{\partial\chi}.$$

In the large-aspect-ratio approximation $B = B_0\,(1 - \epsilon\, \cos\theta)$, so

$$\frac{\partial B}{\partial\chi} = -\frac{q}{rR}\cos\theta$$

neglecting higher order terms in ϵ. This implies

$$\frac{\partial}{\partial\chi}\left(\frac{v_\parallel}{\omega_\mathrm{c}}\right) = \frac{q}{rR\omega_\mathrm{c}}\left[\frac{\mu}{mv_\parallel} + \frac{v_\parallel}{B}\right]\cos\theta .$$

The poloidal component of the magnetic drift can, for this reason, be written as

$$m\frac{Iv_\parallel}{Rq}\frac{\partial}{\partial\chi}\left(\frac{v_\parallel}{\omega_\mathrm{c}}\right) = \frac{m}{q}\frac{q}{rR\omega_\mathrm{c}}\left[\frac{\mu B}{m}_{\mathrm{i}} + v_\parallel^2\right]\cos\theta .$$

This result, after being bounce averaged, corresponds exactly to $(m/q)\,\omega_\mathrm{D}$ (see equation (14)).

We now focus on the relation between the terms in $k_\parallel v_\parallel$ in equation (40) and the magnetic shear frequency $\omega_{\hat{s}}$. We concentrate on

$$I\frac{v_\parallel}{\omega_\mathrm{c}}k_\parallel v_\parallel \left.\frac{\partial}{\partial\xi}\right|_\Omega \left(\frac{\partial}{\partial\chi}\Phi\right)$$

because all terms related to $\omega_{\hat{s}}$ have this form in our equations. It is easy to see that

$$I\frac{v_\parallel}{\omega_\mathrm{c}}k_\parallel v_\parallel \left.\frac{\partial}{\partial\xi}\right|_\Omega \left(\frac{\partial\Phi}{\partial\chi}\right) = -I\frac{v_\parallel}{\omega_\mathrm{c}}k_\parallel v_\parallel \frac{4}{W_\chi^2}\frac{\omega q}{mc}\frac{\mathrm{d}h}{\mathrm{d}\Omega}\left.\frac{\partial\chi}{\partial\xi}\right|_\Omega .$$

Recalling that

$$k_\parallel \left.\frac{\partial\chi}{\partial\xi}\right|_\Omega = \frac{m}{q}\frac{\partial A_\parallel}{\partial\xi} = \frac{m}{q}\frac{\tilde{\psi}}{R}\sin\xi \tag{62}$$

and

$$\tilde{\psi} = \frac{W_\chi^2}{4}\frac{q_\mathrm{s}'}{q_\mathrm{s}}$$

one can find with a little algebra

$$I\frac{v_\parallel}{\omega_\mathrm{c}}k_\parallel v_\parallel \left.\frac{\partial}{\partial\xi}\right|_\Omega \frac{\partial\Phi}{\partial\chi} = \frac{m}{q}\frac{q\hat{s}v_\parallel^2}{r^2\omega_\mathrm{c}}\frac{\partial\Phi}{\partial\xi},$$

where $\hat{s}$ is the magnetic shear ($\hat{s} = r/q\,\mathrm{d}q/\mathrm{d}r$) and the shear precession frequency [22] can be easily identified after θ-averaging this expression.

References

[1] Furth H P, Killeen J and Rosenbluth M N 1963 *Phys. Fluids* **6** 459
[2] Rutherford P H 1973 *Phys. Fluids* **16** 1903
[3] Carrera R, Hazeltine R D and Kotschenreuther M 1986 *Phys. Fluids* **29** 899
[4] Qu W X and Callen J D 1985 *University of Wisconsin Plasma Report* No UWPR 85-5
[5] Chang Z *et al* 1995 *Phys. Rev. Lett.* **74** 4663
[6] Sauter O *et al* 1997 *Phys. Plasmas* **4** 1654
[7] Poli E *et al* 2005 *Phys. Rev. Lett.* **94** 205001
[8] Smolyakov A I 1989 *Sov. J. Plasma Phys.* **15** 667
[9] Mikhailovskii A B 2003 *Contrib. Plasma Phys.* **43** 125
[10] Smolyakov A I *et al* 1995 *Phys. Plasmas* **2** 1581
[11] Wilson H R *et al* 1996 *Phys. Plasmas* **3** 248
[12] Mikhailovskii A B, Pustovitov V D and Smolyakov A I 2000 *Plasma Phys. Control. Fusion* **42** 309
[13] Bergmann A, Poli E and Peeters A G 2005 *Phys. Plasmas* **12** 072501
[14] Poli E *et al* 2005 *Nucl. Fusion* **45** 384
[15] Konovalov S V *et al* 2002 *Dok. Phys.* **47** 488
[16] Smolyakov A I 1993 *Plasma Phys. Control. Fusion* **35** 657
[17] Connor J W and Wilson H R 1995 *Phys. Plasmas* **2** 4575
[18] Waelbroeck F L Connor J W and Wilson H R 2001 *Phys. Rev. Lett.* **87** 215003

[19] James M and Wilson H R 2006 *Plasma Phys. Control. Fusion* **48** 1647
[20] Pinches S D *et al* 1998 *Comput. Phys. Commun.* **111** 133
[21] Hazeltine R D and Meiss J D 1992 *Plasma Confinement* (New York: Addison-Wesley)
[22] Peeters A G 1994 *PhD Thesis* Technische Universiteit Eindhoven
[23] Bergmann A, Peeters A G and Pinches S D 2001 *Phys. Plasmas* **8** 5192
[24] Poli E *et al* 2003 *Plasma Phys. Control. Fusion* **45** 71
[25] Hinton F L and Robertson J A 1984 *Phys. Fluids* **27** 1243
[26] Berk H L and Breizman B N 1990 *Phys. Fluids* B **2** 2226
[27] Berk H L and Breizman B N 1990 *Phys. Fluids* B **2** 2235
[28] Berk H L and Breizman B N 1990 *Phys. Fluids* B **2** 2246
[29] Marchenko V S 1999 *Nucl. Fusion* **39** 1541
[30] Waelbroeck F L and Fitzpatrick R 1997 *Phys. Rev. Lett.* **78** 1703

IOP Publishing and International Atomic Energy Agency Nuclear Fusion

Nucl. Fusion **49** (2009) 075010 (8pp) doi:10.1088/0029-5515/49/7/075010

Behaviour of turbulent transport in the vicinity of a magnetic island

E. Poli[1], **A. Bottino**[1] **and A.G. Peeters**[2]

[1] Max-Planck-Institut für Plasmaphysik, Boltzmannstrasse 2, D-85748 Garching bei München, Germany
[2] Centre for Fusion, Space and Astrophysics, Department of Physics, University of Warwick, CV4 7AL Coventry, UK

Received 28 January 2009, accepted for publication 6 May 2009
Published 28 May 2009
Online at stacks.iop.org/NF/49/075010

Abstract

The influence of a static magnetic island on the behaviour of the electrostatic turbulence in a tokamak is investigated numerically employing global nonlinear gyrokinetic particle-in-cell simulations. The excitation of turbulence is modified by the magnetic topology of the island. Low mode numbers in the energy spectrum of the potential disturbances, corresponding to the island perturbation, are amplified by nonlinear coupling with the microinstabilities, particularly in the presence of strong turbulence. The associated large-scale flows affect the transport directly and through strain of small-scale eddies. The temperature profile determined numerically in the island region agrees qualitatively with analytic estimates; however, quantitative discrepancies are found.

PACS numbers: 52.35.Py, 52.65.Rr, 52.65.Tt

(Some figures in this article are in colour only in the electronic version)

1. Introduction

In the calculation of turbulent transport due to electrostatic or electromagnetic microinstabilities in tokamaks, the equilibrium configuration is usually supposed to be axisymmetric. However, large-scale magnetohydrodynamic instabilities like the tearing mode [1, 2], leading to the formation of helical structures (called magnetic islands) that destroy the toroidal symmetry of a tokamak, are often observed in fusion experiments. A saturated tearing mode can lead to a significant degradation of the energy confined in the plasma or even cause disruptive termination of a discharge. For these reasons, tearing modes are an area of very active research. In many tokamak reactors, the tearing mode is found to be driven unstable by the decrease in the bootstrap current due to the flattening of the pressure profile inside the island [3–5] (in this case, the mode is called neoclassical tearing mode, NTM).

It is easy to imagine that the change in the magnetic topology due to the presence of a large helical perturbation influences the dynamics of transport. First of all, since a magnetic island reconnects the magnetic field on both sides of the rational surface where it develops, it provides a radial magnetic-field component, thus leading to the appearance of a huge radial *parallel* transport, which is otherwise absent in a tokamak. This is the origin of the flattening of the pressure profile within the reconnected region mentioned above. As the microinstabilities that lead to turbulence are driven by density and temperature gradients, this flattening drastically reduces the turbulence level in the island. Finally, the development and the shape of the turbulent structures can be modified by the helical magnetic field of the mode and by the interaction with the sheared flows connected to the large-scale (island) components of the electric field. On the other hand, the turbulence itself affects the dynamics of magnetic islands. First of all, small-scale electromagnetic fluctuations modify the seeding and growth processes [6–8]. Moreover, the competition between perpendicular and parallel transport contributes to determining the pressure profile around the island separatrix [9, 10], in a region which can be as large as the island itself in the early stage of the island evolution. The shape of the pressure profile has a strong impact on the island stability, first of all because it determines the level of the bootstrap current (and hence its neoclasical stability [9]), but also because the island rotation due to diamagnetic effects gives rise to a polarization current [11–13] which is found to be potentially important for the dynamics of small islands. The behaviour of the island propagation velocity in the presence of turbulence has been investigated recently employing a Hasegawa–Wakatani model in a slab configuration [14].

A complete kinetic self-consistent solution of the problem of the island evolution in the presence of turbulence in a realistic tokamak geometry, which involves the resolution of

0029-5515/09/075010+08$30.00

time scales ranging from those typical of the particle orbits to those characterizing the island growth, is computationally prohibitive. The size of the problem can be reduced, e.g. by choosing a fluid approach to the computation of the turbulent fields, by simplifying the magnetic geometry (slab or cylindrical instead of toroidal), or by considering only short (turbulence-related) or long (island-related) time scales. A 'minimal model' for a self-consistent description of turbulence and island dynamics has been put forward in [15], which also includes a detailed discussion of the basic features of the mutual interaction between small-scale and large-scale instabilities typical of this problem.

In this paper, full toroidal geometry and a gyrokinetic description of the ions are retained. Toroidicity and kinetic effects are known to play a fundamental role in the dynamics of both the turbulence and the tearing mode. On the other hand, in the model adopted here, the magnetic island is treated as a prescribed static perturbation of the background axisymmetric configuration, and its time evolution is disregarded. A particle-in-cell (PIC) approach is well suited for a direct numerical implementation of this model, since PIC codes are based on the integration of the trajectories of an ensemble of markers evolving according to a set of Hamiltonian equations of motion, where the magnetic-field perturbation due to the island can be included in a quite straightforward way. The self-consistent electric field is calculated by solving the Poisson equation on a fixed spatial grid. In the simulations presented here, performed employing the global gyrokinetic PIC code ORB5 [16, 17], only electrostatic microinstabilities are considered. With respect to the considerations made above, the model adopted here is used to describe the influence of the island on the development of the turbulence (spectrum, coupling to long-wavelengths modes, shape of the eddies, etc), to determine self-consistently the heat transport and its dependence on the island size and geometry and (related to this) to check the assumptions of previous studies on the transport properties in the island region.

It is noted in passing that a gyrokinetic approach is needed not only to properly treat the dynamics of the microinstabilities but also because finite-orbit effects can become essential for small islands and in any case around the separatrix [18, 19].

In this paper, section 2 is devoted to a description of the approach used to include an island structure in numerical simulations based on the PIC method. Some earlier results on the determination of the balance between perpendicular and parallel transport across a magnetic island are summarized in section 3. The numerical results of the ORB5 simulations are presented in section 4. Some concluding remarks follow in section 5.

2. Numerical scheme

2.1. The PIC code ORB5

The PIC method is based on the introduction of an ensemble of 'super-particles', or markers, each one describing a piece of the phase space associated with a given particle species. The evolution of the markers is determined by the corresponding equations of motion, which are coupled to Maxwell's equations. The self-consistent fields are calculated projecting the charge and current associated with each marker onto a fixed spatial grid. This approach is implemented in the global gyrokinetic PIC code ORB5, which provides a numerical solution to the electrostatic approximation of the gyrokinetic equations in the formulation of Hahm [20]. The distribution function is split into an analytically known time-independent part f_0 and a perturbation δf which is represented numerically. The gyrokinetic equations of motion for the markers are

$$\frac{\mathrm{d}\boldsymbol{R}}{\mathrm{d}t} = v_\parallel \boldsymbol{b} + \frac{1}{B_\parallel^*}\left[\frac{\mu B + {v_\parallel}^2}{\Omega_{\mathrm{ci}}}\boldsymbol{b}\times\nabla B \right.$$
$$\left. - \frac{{v_\parallel}^2}{\Omega_{\mathrm{ci}}}\boldsymbol{b}\times(\boldsymbol{b}\times\nabla\times\boldsymbol{B}) - \nabla\langle\phi\rangle_g \times \boldsymbol{b}\ \right], \tag{1}$$

$$\frac{\mathrm{d}v_\parallel}{\mathrm{d}t} = -\mu\left[\boldsymbol{b} - \frac{v_\parallel}{B_\parallel^*\Omega_{\mathrm{ci}}}\boldsymbol{b}\times(\boldsymbol{b}\times\nabla\times\boldsymbol{B})\right]\cdot\nabla B \tag{2}$$
$$-\frac{q_i}{m_i}\left\{\boldsymbol{b} + \frac{v_\parallel}{B_\parallel^*\Omega_{\mathrm{ci}}}\left[\boldsymbol{b}\times\nabla B - \boldsymbol{b}\times(\boldsymbol{b}\times\nabla\times\boldsymbol{B})\right]\right\}\cdot\nabla\langle\phi\rangle_g,$$

$$\frac{\mathrm{d}\mu}{\mathrm{d}t} = 0, \tag{3}$$

where $\boldsymbol{R}$ is the position of the gyrocentre, $v_\parallel$ is the velocity component along the magnetic field, $\boldsymbol{b}$ is the unit vector along the magnetic field $\boldsymbol{B}$, μ is the magnetic moment, Ω_{ci} is the cyclotron frequency, $\langle\phi\rangle_g$ is the perturbed potential (solution of the Poisson equation) averaged over the gyroperiod, q_i and m_i are the particle's charge and mass, respectively, and $B_\parallel^* = B + (m_i/q_i)v_\parallel \boldsymbol{b}\cdot\nabla\times\boldsymbol{b}$. Since along the orbits $\mathrm{d}f/\mathrm{d}t = 0$, δf must obey the equation

$$\frac{\mathrm{d}(\delta f)}{\mathrm{d}t} = -\frac{\mathrm{d}f_0}{\mathrm{d}t} = -\boldsymbol{v}\cdot\nabla f_0 - \dot{v}_\parallel\frac{\partial f_0}{\partial v_\parallel}. \tag{4}$$

The δf method described above can be successfully applied to represent the deviation of the moments of the distribution function from the 'unperturbed' state (when no island is present), as has been shown previously for the case of drift kinetic simulations [21, 22].

The perturbed potential is obtained as the solution of the Poisson equation

$$\nabla^2\phi = 4\pi q_i\left\{n_e - \int\left[f + \frac{q_i}{m_i B}(\phi - \langle\phi\rangle)\frac{\partial f}{\partial\mu}\right]\right.$$
$$\left. \times\,\delta(\boldsymbol{R} + \rho - \boldsymbol{r})\mathrm{d}^6\boldsymbol{Z}\right\}, \tag{5}$$

where ρ is a vector directed from the gyrocentre to the position of the particle and $\langle\phi\rangle$ is the flux-surface-averaged potential. The charge connected to each marker is assigned pointwise to a spatial mesh in order to provide the source term. The computation of the gyroaveraged density follows an adaptive procedure, in order to have the same number of sampling points per arclength along the gyro-ring. Once the perturbed gyroaveraged charge density associated with each marker has been projected onto the (B-spline) basis, the equation for the components of the potential on this basis reduces to an algebraic matrix equation. The same B-spline basis can be used to interpolate the radial magnetic-field perturbation associated with the magnetic island, which is initially assigned on a grid.

2.2. Including a magnetic island

In the presence of a (static) magnetic island, the tokamak magnetic field can be represented as

$$\boldsymbol{B} = \nabla\psi_{\rm t} \times \nabla\xi/m + \nabla\varphi \times \nabla\Psi_{\rm he}, \qquad (6)$$

where $\psi_{\rm t}$ is the toroidal flux, $\xi = m\theta - n\varphi$ is the helical angle (θ and φ being the poloidal and toroidal angles, respectively, and m and n the poloidal and toroidal mode numbers associated with the island) and

$$\Psi_{\rm he} = \psi - \frac{\psi_{\rm t}}{q_{\rm s}} + \alpha\cos\xi \qquad (7)$$

is the helical flux (ψ is the poloidal flux and the subscript s denotes that a quantity is calculated at the resonant (m, n) surface), which can be used to label the perturbed magnetic surfaces, since $\boldsymbol{B}\cdot\nabla\Psi_{\rm he} = 0$. In the limit of vanishing magnetic perturbation, $\alpha \to 0$, it is easy to show that equations (6) and (7) reduce to the usual representation of the axisymmetric tokamak field. The last term of equation (7) describes the island magnetic field, which is therefore

$$\tilde{\boldsymbol{B}} = \alpha\nabla\varphi \times \nabla\cos\xi = m\alpha\sin\xi\nabla\theta \times \nabla\varphi,$$

where the perturbation strength α is approximated to be a constant. With this assumption, the island field is directed along $\nabla\psi$. This radial component accounts for the most important modification of particle orbits [23] and has been included in ORB5 by operating the substitution $\boldsymbol{b} \to \boldsymbol{b} + \tilde{\boldsymbol{b}}$ (where $\tilde{\boldsymbol{b}} = \tilde{\boldsymbol{B}}/B$) in the first term of both equations (1) and (2).

Figure 1(*a*) is a Poincaré puncture plot produced by following the orbits of 23 particles along the torus, the electrostatic potential being switched off. The dots obtained as the intersection of the trajectories with the plane $\varphi = 0$ show the pattern of the perturbed field lines, which coincides with the contour levels of $\Psi_{\rm he}$ (for this plot, particles with low energy and $v_\parallel/v \simeq 1$ have been employed to reduce their drift with respect to the flux surfaces). The density profile, obtained again in the absence of the electrostatic potential, is reported in figure 1(*b*). Here and in the following, the flux-surface averages are performed in helical cells delimited by neighbouring surfaces of constant $\Psi_{\rm he}$, according to the definition

$$\langle A\rangle = \lim_{\delta\Psi_{\rm he}\to 0} \frac{\int_{\Psi_{\rm he}-\delta\Psi_{\rm he}}^{\Psi_{\rm he}+\delta\Psi_{\rm he}} A\, d^3\boldsymbol{r}}{\int_{\Psi_{\rm he}-\delta\Psi_{\rm he}}^{\Psi_{\rm he}+\delta\Psi_{\rm he}} d^3\boldsymbol{r}}. \qquad (8)$$

The density profile shown in figure 1(*b*) exhibits a clear flattening within the island. The contribution of the simulation markers, namely $\delta n = \int {\rm d}\Omega_{\rm p}\delta f/V$ (where ${\rm d}\Omega_{\rm p}$ is the phase-space element and V is the volume of the cell) is shown by the dashed line reversing its sign across the island centre.

In the determination of the balance between parallel and perpendicular transport in the island region, an important role is played by the (θ-averaged) parallel gradient operator $\nabla_\parallel = \boldsymbol{b}\cdot\nabla = k_\parallel\, \partial/\partial\xi|_{\Psi_{\rm he}}$. The parallel wavevector $k_\parallel$ defined through this expression for $\nabla_\parallel$ is proportional to the distance from the rational surface and to the magnetic shear:

$$k_\parallel = -\frac{m}{qR}\frac{\psi - \psi_{\rm s}}{q_{\rm s}}\frac{{\rm d}q}{{\rm d}\psi} = \frac{\epsilon_{\rm s} s_{\rm s} n}{r_{\rm s}^2}(r - r_{\rm s}), \qquad (9)$$

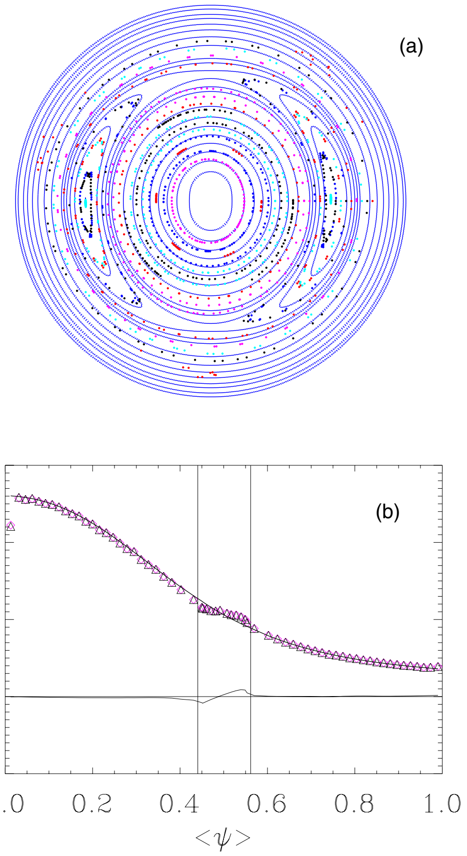

Figure 1. ORB5 simulation performed excluding the self-consistent electric fields to highlight the motion of the ions along the perturbed field lines in the presence of a magnetic island: Poincaré puncture plot (*a*) and radial density profile (*b*). The island region is denoted by the two vertical lines.

where the first expression refers to a full toroidal geometry and the second to a slab or cylindrical geometry. In equation (9), ϵ is the inverse aspect ratio and $s = (r/q)\,{\rm d}q/{\rm d}r$ the magnetic shear.

3. Parallel and perpendicular transport close to the island separatrix

In the presence of a magnetic island, since the transport along the field lines is much larger than across the field, the pressure profile can be thought to be a function of the perturbed magnetic-flux label $\Psi_{\rm he}$ introduced above. Under this assumption, the pressure gradient jumps from a finite value to zero when the island separatrix is crossed. However, the ratio between, say, the parallel and perpendicular heat conductivity in a tokamak is indeed very large (up to $\chi_\parallel/\chi_\perp \approx 10^9$–$10^{10}$) but finite. As a consequence, a boundary layer appears around the island separatrix, along which the heat is transported from one side of the rational surface to the other [9, 10]. The features of this process have been investigated solving the steady-state heat diffusion equation [9]:

$$\chi_\parallel\nabla_\parallel^2 T + \chi_\perp\nabla_\perp^2 T = 0, \qquad (10)$$

or, alternatively[3], the kinetic equation [10]

$$v_\parallel \nabla_\parallel f = D_\perp \nabla^2 f. \qquad (11)$$

The critical width w_c in which parallel and perendicular transport compete is obtained by equating the two terms of the previous equations. Thus in equation (10) one can estimate $\chi_\parallel k_\parallel{}^2 \sim \chi_\perp / w_c^2$, and assuming $r - r_s \sim w_c$ in equation (9), the scaling for w_c turns out to be $w_c/r \sim (\chi_\perp/\chi_\parallel)^{1/4}(1/\epsilon_s s_s n)^{1/2}$. The corresponding estimate derived from equation (11), namely $w_c \sim (D_\perp/k_\parallel v_{th})^{1/2}$, is reduced to the above if a parallel diffusivity $D_\parallel \sim v_{th}/k_\parallel$ is introduced (see footnote) and again taking $r - r_s \sim w_c$ in equation (9). In the transition layer, the temperature is not a flux-surface function. The heat is found to be transported along the layer and to flow across the rational surface near the X-point [9]. The analysis of Hazeltine *et al* [10], moreover, predicts that the jump Δf of the distribution function on both sides of the island should be proportional to the gradient $\mathrm{d}f/\mathrm{d}r$ at the island separatrix, the proportionality factor being approximately given by the width of the critical layer $w_c \simeq \sqrt{\chi_\perp/k_\parallel v_{th}}$. It has to be stressed that, in both approaches, the dependence of the perpendicular (heat) diffusion coefficient on the radial coordinate ψ and on the helical angle along the island ξ has been neglected, in order to obtain an analytic solution of the starting equation. In the next section, this picture is compared with the results of direct numerical simulations of turbulent transport.

4. Numerical results

The numerical simulations presented in this section have been performed for a tokamak with circular concentric flux surfaces, major radius $R_0 = 3.3$ m and minor radius $a = 0.47$ m. A flat density profile is considered, the turbulent transport being caused by an electrostatic ion-temperature-gradient (ITG) instability. As explained in section 2.2, flux-surface ('zonal') averages have to be performed between surfaces of constant Ψ_{he}, which are not axisymmetric ($n = 0$) if a magnetic island is present. However, the assumption that the zonal potential coincides with an $n = 0$ mode is hard-wired in ORB5 when adiabatic electrons are considered. Therefore, within the adiabatic approximation, a proper computation of the zonal flows turns out to be extremely difficult and is excluded from the simulations presented here (i.e. $n = 0$ modes are set to zero). No source terms have been used, so that the temperature profile relaxes according to the level of the heat flux. In simulations of this kind, if the normalized gyroradius $\rho_* \equiv \rho_s/a$ is sufficiently small, the time evolution of both the temperature and the heat flux profiles is slow, so that a 'quasi-steady' state can be identified [24]. This approach has been used in most of global turbulence analysis and has been chosen as a standard benchmark case for European global codes [25]. For simulations without zonal flows such as those described in this paper, a quasi-steady state can be reached for $\rho_* < 1/200$ (see e.g. [17]). In the ORB5 runs analysed here, $\rho_* = 1/320$. As this corresponds to a pretty low value for the ion temperature, the ion streaming along the island is not very fast. Typical values of $\chi_\parallel/\chi_\perp$ are therefore[4] in the range 10^6–10^7.

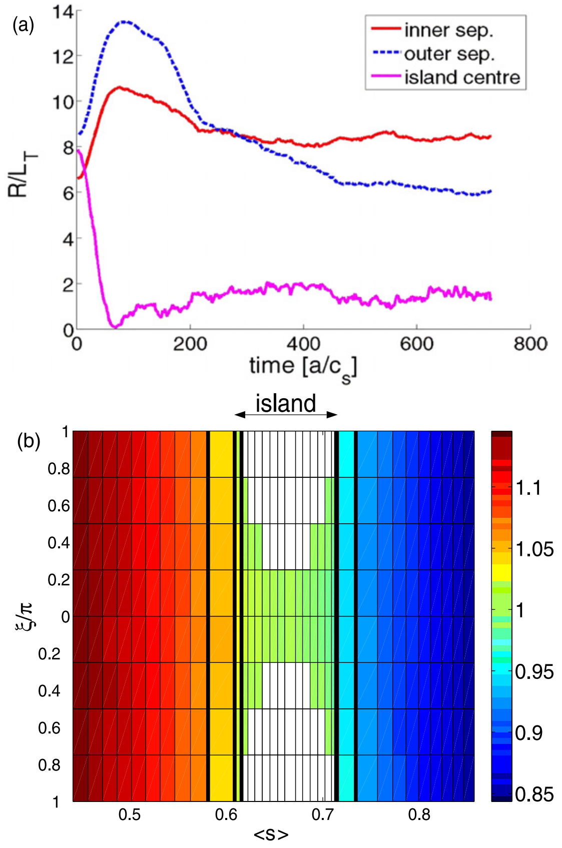

Figure 2. Time evolution of the temperature gradient in the island region in a typical ORB5 simulation (*a*). In the turbulence-free phase, the profile flattens in the centre of the island and peaks just outside because of the 'compression' of the magnetic surfaces. In the turbulent phase, the profile relaxes to a lower value of the gradient. The time is expressed in units of a/c_s (where c_s is the sound speed). Temperature profile at the end of the turbulence-free phase (*b*) as a function of the radial coordinate $\langle\sqrt{\psi}\rangle$ and of the helical angle ξ (where $\xi = \mp\pi$ corresponds to the X-point, $\xi = 0$ to the O-point) for a large island ($W/a \simeq 0.1$).

An example of the evolution of the ion temperature profile in a typical ORB5 simulation is shown in figure 2(*a*). Since the temperature is initialized as a function of the unperturbed flux coordinate ψ, each run is started with a turbulence-free phase, in which only potential perturbations with low mode numbers are allowed. During this time, the ion temperature becomes constant on the perturbed (constant-Ψ_{he}) flux surfaces and flattens inside the island. Outside the island, the temperature gradient increases because the flux surfaces are on average 'compressed' with respect to the unperturbed magnetic equilibrium. After this phase, turbulent modes are switched on. Under the influence of the turbulent transport, the temperature gradient outside the island decreases, at a particularly fast rate at the end of the linear phase (overshoot). At the end of the run, a phase with almost constant temperature gradients in the island region is observed. It is noted that the gradients are computed in this figure as the variation of the

---

[3] It is noted that replacing conduction by convection, i.e. replacing in equation (10) the term $\chi_\parallel \nabla_\parallel^2 T$ with $v_\parallel \nabla_\parallel T$ (which is in turn equivalent to estimating [9] $\chi_\parallel \sim v_{th}/k_\parallel$) one obtains an equation of the same form as equation (11).

[4] Here, according to [9], we estimate $\chi_\parallel \sim v_{th}/k_\parallel$, see section 3.

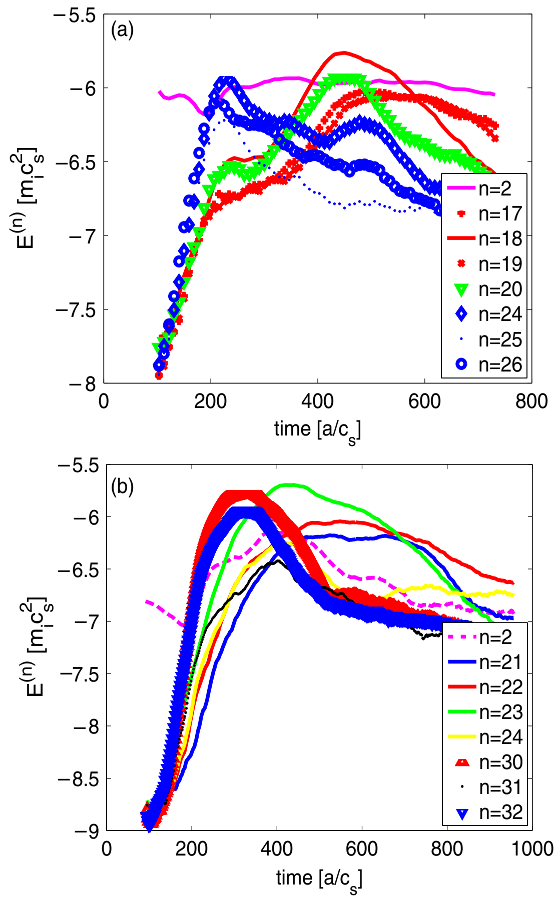

Figure 3. Time evolution of the energy spectrum of the turbulence for a large ($W/a \simeq 0.1$, (*a*)) and small ($W/a \simeq 0.04$, (*b*)) island, showing the coupling between large-scale and small-scale fields. The y-axis reports the logarithm of the toroidal-mode energy normalized to $m_i c_s^2$.

temperature with respect to the flux-surface averaged value of the radial coordinate, i.e. with respect to $\langle\psi\rangle$. In the calculation of heat conductivity (defined as ratio of heat fluxes and temperature gradients) presented below, the gradients are evaluated taking into account that the distance between neighbouring flux surfaces is a function of the helical angle ξ. Figure 2(*b*) shows the flattened temperature profile at the end of the turbulence-free phase as a function of the radial (x-axis) and helical (y-axis) coordinates (the inner and outer separatrices are represented by the two vertical thick solid lines). For plotting reasons, the island is 'stretched' along the x-axis at the X-points ($\xi = \mp\pi$). The resulting unphysical cells are displayed in white.

The first set of results presented here concerns the development of the turbulence in the presence of a magnetic island. In figure 3, the time evolution of the toroidal energy spectrum (averaged over the minor radius) is shown for two different values of the island width. Moving from the linear to the nonlinear phase the spectrum exhibits an inverse cascade to smaller mode numbers, as usually seen also when the island is absent. The nonlinear coupling between the 'turbulent' modes (high n) and the 'island' modes (low n) deserves particular attention. In these simulations with a (3,2) island, a coupling between mode numbers n_1 and n_2 in the turbulence spectrum

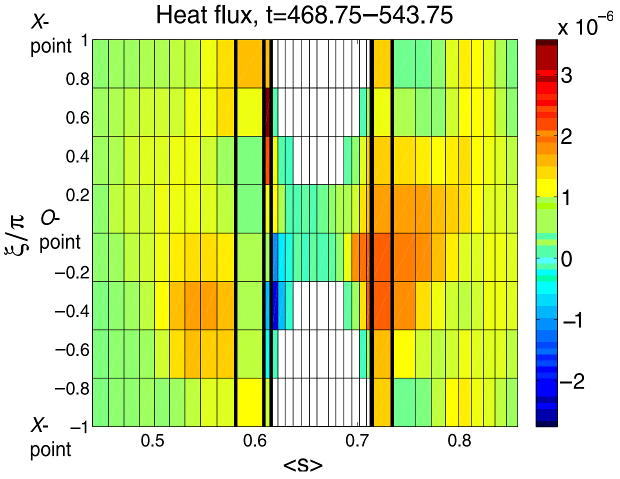

Figure 4. $\boldsymbol{E} \times \boldsymbol{B}$ heat flux defined in equation (12) as a function of $\langle\sqrt{\psi}\rangle$ and of the helical angle ξ for a large island ($W/a \simeq 0.1$). The transport due to the large-scale field components (with different directions) is clearly visible inside the island.

satisfying the relation $n_1 = n_2+2$ is found in both the linear and the nonlinear phase. The low-n modes amplification through this coupling with the small-scale turbulence is more evident when the island and the background temperature are larger. Moreover, the whole spectrum shifts to lower n for larger islands. In the simulations presented here, 'seed' $n = 2$ and $n = 4$ harmonics arise during the turbulence-free phase of the run described above; under realistic conditions, in general, the low-n potential associated with the island rotation with respect to the plasma can play a similar role and interact nonlinearly with the fluctuating field of the microinstabilities. These low-n field components affect the transport in the island region in a twofold way . First of all, they yield a direct transport signal, in particular where high-n modes have smaller amplitude, for instance inside the island (an example is shown in figure 4). While the direct contribution of the large-scale modes to the transport *across* the separatrix is negligible, they are essential for the residual transport level *inside* the island and finally for the shape of the temperature profile close to the resonant surface. As they are generated through nonlinear coupling with the background turbulence, their importance is directly related to the strength of the small-scale modes, cf the discussion after equations (12) and (13) below. The second effect of low-n modes on the transport is that they generate sheared flows which strain the turbulent eddies, thus reducing the transport level. This process, which is closely analogous to the familiar effect of zonal flows on drift-wave turbulence, is predicted theoretically (see e.g. [15]) and is nicely confirmed in our simulations.

We now turn to the analysis of the transport in the island region. In the simulations, the formation of elongated eddies across the X-point region is often observed. These eddies split when they drift inside the island, where the temperature gradient is much smaller (it is recalled that the island has a fixed position in these runs). In the region of the plasma corresponding to the island's O-point ($\xi \simeq 0$), a breaking of the eddies close to the (in particular inner) separatrix is observed. In this regard, an interesting observation is that low-n components in the local energy spectrum are usually

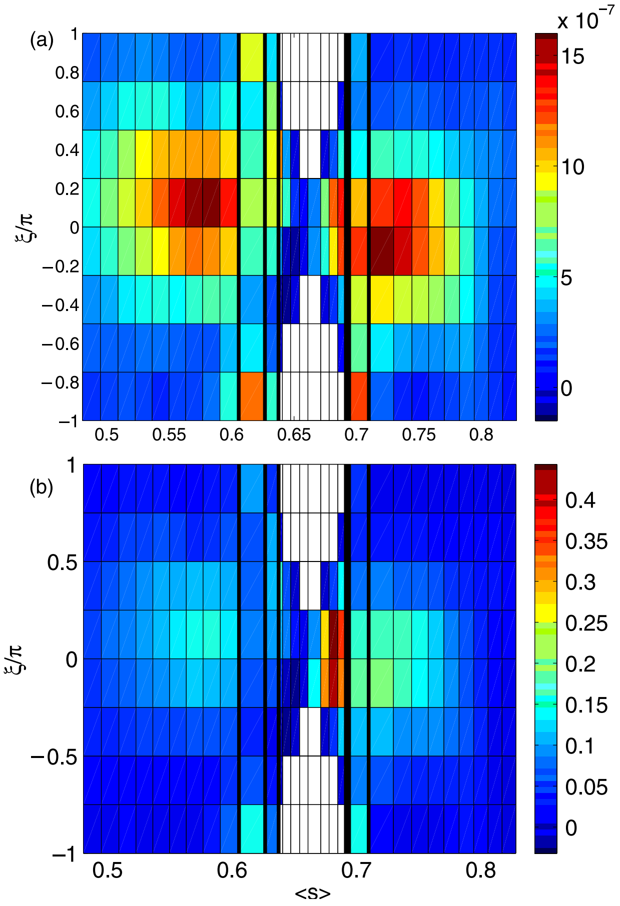

Figure 5. Heat flux (*a*) and heat conductivity (*b*) in the nonlinear phase, for a mid-size island ($W/a \simeq 0.06$).

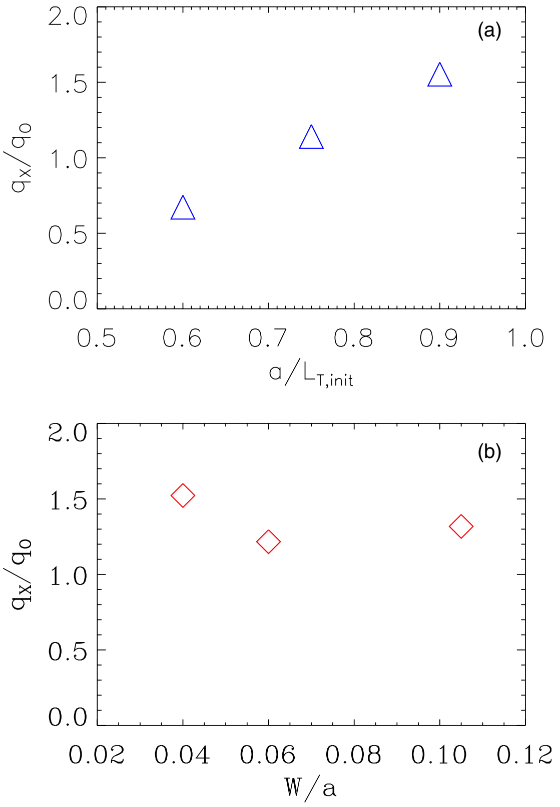

Figure 6. Dependence of the ratio between the heat flux across the inner island separatrix at $\xi = \pi$ (X-point region) and at $\xi = 0$ (O-point region) on the initial temperature gradient at constant island width (*a*) and on the island width at constant temperature gradient (calculated at the beginning of the turbulence phase) (*b*).

observed to prevail on the inner side of the island, whereas they are less strong on the outer side. Correspondingly, the turbulent eddies are seen to be more pronounced on the outer side. This is a strong indication that the amplitude of the turbulent modes is regulated by the sheared flows associated with low-n fields. These qualitative observations are confirmed by the transport levels measured numerically. An example is shown in figure 5(*a*). Outside the island, in the O-point region, the $\boldsymbol{E} \times \boldsymbol{B}$ transport is strong, consistently with the fact that the flux surfaces are closer to each other and the temperature gradient is therefore higher. However, close to the island separatrix, the largest heat fluxes are often found in the X-point region, whereas the transport around the O-point is reduced. These features are found in both the linear and nonlinear phases. The turbulent transport is of course very low in the island core. The behaviour of the heat flux as a function of the helical angle ξ cannot be explained simply in terms of the different 'distance' of the flux surfaces at the O-point as compared with the X-point (i.e. in terms of different local gradients). This can be seen in figure 5(*b*), which reports the values of the heat conductivity. It is noted, in addition, that the penetration (spreading) of the turbulent structures into the outer side of the island leads to high values of the conductivity (relatively high transport in a region of low gradient). The ratio of the heat flux at the separatrix through the X-point (q_X) and through the O-point (q_O) is reported in figure 6 as a function of the initial inverse gradient length and of the island width. The behaviour of q_X/q_O shown in figure 6(*a*) is due to the fact that, below a given value of the ∇T at the island, the formation of elongated eddies through the X-point mentioned above is reduced. Moreover, at higher gradients, i.e. when the turbulence is stronger, the large-scale sheared flows become stronger as well. The connected straining of the eddies close to the island separatrix seems to be more effective in the O-point region than in the X-point region (this result could change in the presence of strong zonal flows). The dependence of the ratio q_X/q_O on the island width reported in figure 6(*b*) has been computed for very similar values of the temperature gradient outside the island. Correspondingly, the ratio between the energy of small-scale and large-scale modes is comparable. The assumption that the transport level is determined by the interaction between low-n and turbulent flows would then explain the weak dependence of q_X/q_O on the island width and be consistent with the results shown in figure 6(*a*).

The analytic predictions on the shape of the temperature profile across the island mentioned in section 3 [9, 10] are finally checked against direct numerical simulations of turbulent transport. The basic picture, according to which the temperature profile must exhibit a transition layer across the island separatrix, where it is not a flux-surface function, is qualitatively confirmed. It is recalled that, in addition to the finite perpendicular transport, finite-orbit effects also play a role in smoothing the pressure profile across the separatrix [21, 22]. In the simulations, the ratio between the radial $\boldsymbol{E} \times \boldsymbol{B}$

flux

$$q_E = \int \frac{mv^2}{2}\, v_E\, \delta f\, \mathrm{d}^3\boldsymbol{v} \qquad (12)$$

and the radial component of the parallel flux along the perturbed field lines

$$q_{\parallel,r} = \int \frac{mv^2}{2}\, v_\parallel \tilde{b}\, \delta f\, \mathrm{d}^3\boldsymbol{v} \qquad (13)$$

is calculated. As expected, inside the island separatrix there is a layer where these fluxes are of the same order. Depending on the strength of the turbulence, the ratio $q_E/q_{\parallel,r}$ can be above or below one (as mentioned at the beginning of this section, the parallel streaming is not very fast in these simulations). In the very centre of the island, this ratio can be one or two orders of magnitude higher than at the separatrix, depending on the temperature gradients set in the simulations. In the island centre, the parallel transport becomes less and less effective, since $k_\parallel$ is proportional to the distance from the rational surface, whereas turbulent structures can in some cases reach the O-point or be transported there by the diamagnetic rotation of the instability. Moreover, the excitation of low-n modes inside the island is much stronger if the level of the background turbulence is increased, as discussed above. A consequence of the fact that large eddies can develop across the X-point is that heat can be transported across the resonant rational surface without undergoing the process of crossing the separatrix at the O-point and being transported to the X-point, which is usually considered the standard process for the transport of heat from one side of the rational surface to the other [9]. The suggested proportionality between the jump ΔT of the temperature profile on both sides of the island and the gradient $\mathrm{d}T/\mathrm{d}r$ at the island separatrix [10] has been investigated through a scan in the background temperature gradient for two different sets of simulation parameters. The result of this scan, reported in figure 7, is that the product $w_\mathrm{c}\ \mathrm{d}T/\mathrm{d}r$ increases faster than ΔT if the temperature gradient is increased, whereas their ratio is predicted to be constant, cf section 3. One possible explanation for this result is that the assumption of uniform (both across and along the island) heat conductivity is too crude (it is in fact never verified in the simulations). Close to the island separatrix, $\chi_\perp$ displays a strong variation as a function of the radius and in particular of the helical angle, see figure 5(*b*). Moreover, $\chi_{\perp,X}$ and $\chi_{\perp,O}$ vary differently depending on plasma parameters, particularly on the temperature gradient, as shown above. Whether a diffusive ansatz can be used at all to describe the transport across the island separatrix is an interesting issue which will be addressed in the future.

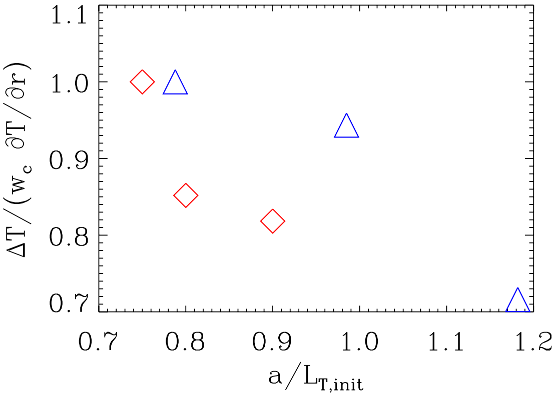

Figure 7. Ratio between the 'jump' of the ion temperature at the island separatrix and the product of the critical layer w_c times the temperature gradient as a function of the initial temperature gradient.

5. Discussion and conclusions

The investigation of the interaction between magnetic island and electrostatic drift-wave turbulence in a tokamak plasma presented in this paper is based on the solution of the gyrokinetic equation in a toroidal geometry. Emphasis has been placed on the modelling of the turbulent processes in the presence of a static island. Global electrostatic simulations have been performed employing the PIC code ORB5. PIC codes allow an—at least conceptually—straightforward implementation of a magnetic island through a modification of the equations of motion which take into account the presence of a small radial component of the magnetic field. The development of the turbulence is modified by the MHD mode through the associated flattening of the temperature gradient and through the interaction between large-scale (island) flows and small-case (turbulence) flows. These low-n flows act both radially, providing an own transport signal, and azimuthally, straining the small-scale eddies. Using the terminology of [15], the feedback of large scales on small scales occurs both in position space and in $\boldsymbol{k}$ space. The numerical results obtained in this paper confirm the importance of the complex dynamics outlined above. In particular, the inhomogeneous behaviour of the transport both across and along the island has been stressed. The validity of a transport model for the island based on the assumption of uniform heat conductivity has been questioned. More basic questions concerning the diffusive nature of the transport in the island region remain to be explored.

As discussed in the introduction, in this paper we aim rather at an accurate description of small-scale instabilities (through a global toroidal gyrokinetic approach) than at the resolution of the time scales connected with the island evolution. In this sense, the choice of a nonrotating island is linked to the fact that the present numerical scheme does not include the physics required for a self-consistent determination of the island rotation, which is connected to the dissipative phenomena leading to an 'out-of-phase' current in the island region [26]. Correspondingly, the electrostatic potential associated with the island rotation cannot be determined self-consistently, whereas it is determined from the Poisson equation for the turbulent fluctuations. Anyway, since the island rotation is supposed to occur in the range of the diamagnetic frequency, its interaction with the drift waves [18] is potentially an important element for the island stability; moreover, the rotation frequency itself is expected to by influenced by the radial profiles [14], as already noted in section 1. Similarly, an important role in the seeding and in the first phase of the island growth is played by small-scale electromagnetic fluctuations, which are not retained in the electrostatic version of ORB5 employed here. However, as far as the transport properties of the plasma in the island region are concerned, an electrostatic approach is sufficient to address the relevant features of the process studied here (energy transport generated by small-scale disturbances, nonlinear mode coupling, interaction between large and small scales, inhomogeneity of the transport properties in the island region, etc).

It is recalled that, in the simulations presented here, the electrons were assumed to be adiabatic. In ORB5, the adiabatic approximation is implemented under the assumption of unperturbed flux surfaces. For this reason, zonal flows were excluded from the computation, and the calculation of low-n fields was not exact, in particular for large islands. A way to overcome this problem, thus obtaining a more realistic prediction of the transport level in the island region, is to employ kinetic electrons, which have the correct response to the island topology. It is important to recall, however, that the physics of self-regulation of turbulent transport through sheared flows connected to large-scale components of the electrostatic potential is not entirely excluded from our simulations, since the low-n fields due to the presence of the island provide an effect similar to that of zonal flows, as mentioned above. In this respect, on the contrary, the neglect of zonal flows in our simulations allows us to discuss the role of low-n modes on their own. The investigation of the zonal-flows-physics in the presence of a magnetic island is planned for the near future. The accurate calculation of the transport levels is crucial to make more realistic predictions on the stability of small islands in the presence of significant perpendicular transport and will allow a more quantitative analysis of threshold models [9] based on the 'critical width' $w_c \propto (\chi_\perp/\chi_\parallel)^{1/4}$ mentioned in section 3.

References

[1] Furth H.P. *et al* 1963 *Phys. Fluids* **6** 459
[2] Rutherford P.H. 1973 *Phys. Fluids* **16** 1903
[3] QU W.X. *et al* 1985 University of Wisconsin *Plasma Report* **UWPR 85-5**
[4] Carrera R. *et al* 1986 *Phys. Fluids* **29** 899
[5] Chang Z. *et al* 1995 *Phys. Rev. Lett.* **74** 4663
[6] Itoh S.-I. *et al* 2004 *Plasma Phys. Control. Fusion* **46** 123
[7] Yagi M. *et al* 2005 *Nucl. Fusion* **45** 900
[8] Ishizawa A. *et al* 2007 *Phys. Plasmas* **14** 040702
[9] Fitzpatrick R. 1995 *Phys. Plasmas* **2** 825
[10] Hazeltine R.D. *et al* 1997 *Phys. Plasmas* **4** 2920
[11] Smolyakov A.I. *et al* 1995 *Phys. Plasmas* **2** 1581
[12] Wilson H.R. *et al* 1996 *Phys. Plasmas* **3** 248
[13] Poli E. *et al* 2005 *Phys. Rev. Lett.* **94** 205001
[14] Militello F. *et al* 2008 *Phys. Plasmas* **15** 050701
[15] Mcdevitt C.J. *et al* 2006 *Phys. Plasmas* **13** 032302
[16] Jolliet S. *et al* 2007 *Comput. Phys. Commun.* **177** 409
[17] Bottino A. *et al* 2007 *Phys. Plasmas* **14** 010701
[18] Waelbroeck F.L. *et al* 2001 *Phys. Rev. Lett.* **87** 215003
[19] James M. *et al* 2006 *Plasma Phys. Control. Fusion* **48** 1647
[20] Hahm T.S. 1988 *Phys. Fluids* **31** 2670
[21] Poli E. *et al* 2002 *Phys. Rev. Lett.* **88** 075001
[22] Poli E. *et al* 2003 *Plasma Phys. Control. Fusion* **45** 71
[23] White R.B. *et al* 1983 *Phys. Fluids* **26** 2958
[24] Scott B.D. 2005 *Phys. Plasmas* **12** 102307
[25] Falchetto G.L. *et al* 2008 *Plasma Phys. Control. Fusion* **50** 124015
[26] Smolyakov A.I. 1993 *Plasma Phys. Control. Fusion* **35** 657

The bootstrap current in small rotating magnetic islands

A. Bergmann,[1] E. Poli,[1] and A. G. Peeters[2]
[1]*Max-Planck-Institut für Plasmaphysik, IPP–EURATOM Association,*
D-85748 Garching bei München, Germany
[2]*Department of Physics, Centre for Fusion, Space and Astrophysics, University of Warwick,*
Coventry CV4 7AL, United Kingdom

(Received 6 July 2009; accepted 31 August 2009; published online 24 September 2009)

The bootstrap current in small magnetic islands of neoclassical tearing modes is studied with guiding center particle simulations including pitch angle scattering. A model for a rotating island and its electric field is used and a new approximation to the electric potential in small islands is derived. Islands with sizes of the order of the ion banana orbit width are studied by means of a two-step model, which allows to treat both ions and electrons kinetically. The bootstrap current in such small islands is found to depend strongly on the direction of rotation of the island. The bootstrap current in small islands rotating in the ion diamagnetic direction is strongly diminished, similarly to what happens in big islands. In small islands rotating in the electron diamagnetic direction, on the contrary, the bootstrap current is almost completely preserved, implying a reduced neoclassical drive of the island growth. © *2009 American Institute of Physics*.
[doi:10.1063/1.3234252]

I. INTRODUCTION

Neoclassical tearing modes (NTMs) play an important role in present large tokamak experiments, and the planned international experiment ITER, since they set a limit to the achievable pressure in long-pulse operation with high confinement.[1] A tearing mode occurs when a magnetic perturbation creates by field line reconnection a small unstable helical island structure in the plasma. In a tokamak, the flattening of the pressure profile due to the fast transport along the field lines inside a sufficiently big island causes a loss of the bootstrap current at the position of the island. This loss corresponds to a perturbed current in the opposite direction that can drive the mode unstable even when the unperturbed current profile would be stabilizing.[2,3] In this case the mode is called a NTM.

It is generally assumed that in small islands, due to the incomplete flattening of the density and temperature profiles, the bootstrap current is not entirely lost. The incomplete flattening of the pressure profile in a small island is due, on the one hand, to the fact that the parallel transport is indeed very high but finite. This implies that there exists always a layer around the island separatrix where the perpendicular transport across the separatrix competes with the parallel transport. Profile flattening is strongly reduced when the island width is of the order of the width of this layer. For the temperature profile, e.g., the critical size is about $(\chi_\perp/\chi_\parallel)^{1/4}(rR_0)^{1/2}$,[4] where $\chi_\perp$ and $\chi_\parallel$ are the perpendicular and parallel heat conductivities, respectively. A second reason for the incomplete disappearance of the bootstrap current is the effect of the finite ion banana orbit width, which is important when the island width is comparable or smaller than the typical ion orbit width. Previous kinetic investigations[5,6] of the bootstrap current in small static islands have shown that the ion component of the bootstrap current is entirely restored when the island width falls below the thermal ion banana width.

In this work, we study the effect of the finite ion orbit width on the bootstrap current in small islands. In addition to the model used in Refs. 5 and 6, we take into account the rotation of the island and the corresponding electric field. As is well known (cf. Sec. III), in the presence of a radial electric field E_r, the neoclassical damping of poloidal rotation leads to a contribution to the parallel flow of both ions and electrons proportional to the ratio between E_r and the poloidal magnetic field B_p.[7] In general, these flows do not lead to an electrical current. In the case of a small island, however, the response to the island electric field (which has large variations across the island separatrix) can be different for ions and electrons because of the different width of their orbits, so that a finite parallel current can be generated. Since the direction of the E_r/B_p flow is related to the direction of the island rotation with respect to the surrounding plasma, the contribution of such a current to the island dynamics can be stabilizing or destabilizing depending on the sign of the island rotation frequency. Here, we study the response of both ions and electrons to islands rotating in either direction, treating the island width and the rotation frequency as input parameters. The surface-averaged parallel current, the changes of the density and temperature profiles, and the plasma flow are determined by means of guiding center particle simulations. Ions and electrons are treated kinetically, including ion-ion, electron-electron, and electron-ion collisions, according to the two-step model presented in Sec. II.

II. THE SIMULATION MODEL

A. Perturbed equilibrium with rotating island

The magnetic field used in the numerical simulations consists of a simple equilibrium field with concentric circular flux surfaces and a perturbation that creates a rotating island with a single helicity. The toroidal and poloidal components of the equilibrium magnetic field are

$$B_t = \frac{B_0}{1+\varepsilon\cos\vartheta}, \quad B_p = \frac{\varepsilon B_t}{q\sqrt{1-\varepsilon^2}}. \tag{1}$$

This field is expressed in Boozer coordinates ψ, θ, ζ as

$$\boldsymbol{B} = \nabla\zeta \times \nabla\psi + q(\psi)\,\nabla\,\psi \times \nabla\,\theta, \tag{2}$$

where ψ is the poloidal flux, q is the safety factor, and θ and ζ are poloidal and toroidal angles. The Boozer angle θ is related to the angle ϑ appearing in Eq. (1) by $\tan(\theta/2) = \sqrt{(1-\varepsilon)/(1+\varepsilon)}\tan(\vartheta/2)$.[6] We assume $q=1+q'\psi$ with a constant q'. From the definition of the toroidal flux (per radian),

$$2\pi\psi_t = \int B_t R_0^2 \varepsilon\, d\varepsilon\, d\vartheta \tag{3}$$

and $\psi_t = \int q(\psi)d\psi$, we obtain the poloidal flux ψ as a function of the inverse aspect ratio ε,

$$\psi + q'\psi^2/2 = R_0^2 B_0 (1-\sqrt{1-\varepsilon^2}). \tag{4}$$

A perturbation of the vector potential

$$\delta A_\parallel = -\,\hat{\alpha}\cos(\xi)R_0 B, \quad \xi = m\theta - n\zeta - \omega t, \tag{5}$$

with mode numbers m and n, mode frequency ω, $B=\sqrt{B_t^2+B_p^2}$, and a constant $\hat{\alpha}$ is assumed. This leads to the poloidal flux perturbation

$$\delta\psi = \hat{\alpha}R_0 R B_t \cos\xi = \hat{\psi}\cos\xi \tag{6}$$

that creates, near the flux surface with $q=q_s=m/n$, a rotating helical island of size $w_\psi = \sqrt{4\hat{\psi}q_s/q_s'}$ (half of the poloidal flux difference across the island) and half-width $w_{\text{isld}} \approx (dr/d\psi)w_\psi$. The index s indicates the resonant surface, the prime denotes the derivative with respect to the poloidal flux ψ and ξ is a helical angle. The perturbed poloidal flux is not suited as a label for the perturbed flux surfaces inside and near the island. Employing both ψ and ψ_t we can define a helical flux as $\Psi_{\text{hel}} = \psi - \psi_t/q_s + \hat{\psi}\cos\xi$, which is constant on the perturbed flux surfaces. In the following we use, as an alternative to ψ, θ, ζ, a normalized helical flux obtained from a second-order expansion of ψ_t around ψ_s,

$$\Omega = 2(\psi-\psi_s)^2/w_\psi^2 - \cos\xi \tag{7}$$

together with ξ and θ. $\Omega=1$ defines the island separatrix and $\Omega=-1$ is the minimum value of Ω attained at the O point $(\xi=0, \psi=\psi_s)$ of the island. For the time-dependent electric potential of the rotating island we use two different analytic approximations. First we take the well-known expression[8,9]

$$\Phi = \frac{q\omega}{m}\left\{(\psi-\psi_s) \pm \frac{w_\psi}{\sqrt{2}}(\sqrt{\Omega}-1)\Theta(\Omega-1)\right\}, \tag{8}$$

which was derived assuming $E_\parallel = -\partial A_\parallel/\partial t - \nabla_\parallel\Phi = 0$. The positive sign holds for $\psi < \psi_s$ and Θ is defined as $\Theta(x)=1$ for $x \geq 0$ and $\Theta(x)=0$ for $x<0$. The first part of Φ is constant on the unperturbed flux surfaces and the corresponding part of the electric field is $E_r = -(q\omega/m)\nabla\psi \approx -(q\omega/m)RB_p$. It causes the plasma inside the island to corotate with the island, since $(\boldsymbol{E}\times\boldsymbol{B})_\theta/r = \omega/m$ is the poloidal rotation frequency of the island. The second part of Φ reduces the electric field $-\nabla\Phi$ outside the island, such that it vanishes far away from the island, where the plasma is assumed to be at rest. The expression for Φ in Eq. (8) is valid for big islands, but we shall show that in small islands the potential can be very different, depending on the rotation frequency. A second expression for the potential, valid in small islands, is derived in Sec. IV.

B. Two step δf model

The bootstrap current is a flux-surface averaged parallel current, which is driven by radial gradients of density or temperature. A kinetic description of the bootstrap current generation is obtained from the drift kinetic equation

$$\frac{df}{dt} = \frac{\partial f}{\partial t} + \boldsymbol{v}\cdot\nabla f + \left(\frac{e\boldsymbol{v}\cdot\boldsymbol{E}}{mv_\parallel} - \frac{\mu\nabla_\parallel B}{m}\right)\frac{\partial f}{\partial v_\parallel} = C(f) \tag{9}$$

for the distribution function $f(\boldsymbol{r}, v_\parallel, \mu)$ of the guiding centers. Here, $\boldsymbol{v} = v_\parallel\boldsymbol{b} + \boldsymbol{v}_d$ is the guiding center velocity with parallel component $v_\parallel$, $\boldsymbol{b} = \boldsymbol{B}/B$, and drift velocity $\boldsymbol{v}_d = \boldsymbol{B}(mv_\parallel^2(\boldsymbol{b}\cdot\nabla)\boldsymbol{b} + \mu\nabla B + e\nabla\Phi)/eB^2$, $\mu = mv_\perp^2/2B$ is the magnetic moment, $\boldsymbol{E} = -\boldsymbol{b}dA_\parallel/dt - \nabla\Phi$ is the electric field, and $C(f)$ is the collision operator. We have to solve the kinetic equations for ions and for electrons. Since we assume a given magnetic field with prescribed perturbation and electric field, the only coupling between the ion and electron equations is via the collision operator. For the ions we can neglect collisions with electrons because their effect on the ion momentum is very small. This makes it possible to compute the electric current in two steps. First the equations for the ions are solved with $C(f_i) = C_{ii}(f_i)$ to obtain the distribution function f_i. In the second step the equations for the electrons are solved, where the collision operator, $C(f_e) = C_{ee}(f_e) + C_{ei}(f_e, f_i)$, depends on f_i, because here it is important to include the friction between electrons and ions. With this procedure there is no need to follow the electrons for several ion collision times, but several electron collision times are sufficient. The procedure was successfully tested with a different code, but with the same collision model.[10]

We apply the δf method, i.e., the distribution function is split into two parts, $f = f_0 + \delta f$, and only the part δf is represented by marker particles, which trace the guiding center orbits. f_0 is chosen suitably with $|\delta f| \ll f_0$ in order to make efficient use of the marker particles. For the ions we choose a local Maxwellian on the unperturbed flux surfaces,

$$f_{i0} = \frac{n_{i0}(\psi)}{(2\pi T_{i0}(\psi)/m_i)^{3/2}}\exp\left\{-\frac{mv^2/2}{T_{i0}(\psi)}\right\}. \tag{10}$$

Here, m_i is the ion mass and $n_{i0}(\psi)$ and $T_{i0}(\psi)$ are the initial radial profiles of ion density and temperature. This choice reduces the collision operator to $C_{ii}(\delta f_i, f_{i0})$, since $C(f_{i0})=0$ holds. For the electrons we choose f_{e0} as a Maxwellian centered at the ion flow velocity $u_{i\parallel}$,

$$f_{e0} = \frac{n_{e0}(x)}{[2\pi T_{e0}(x)/m_e]^{3/2}}\exp\left\{-\frac{m_e[v_\parallel - u_{i\parallel}(x)]^2/2 + \mu B}{T_{e0}(x)}\right\}, \tag{11}$$

and in the coefficients of $C_{ei}(f_e, f_i)$ we approximate f_i by a similar Maxwellian (the exact form of f_i is not important, since the ion velocities are much smaller than the electron velocities),

$$f_{iM}=\frac{n_i(x)}{[2\pi T_i(x)/m_i]^{3/2}}\exp\left\{-\frac{m_i[v_\parallel-u_{i\parallel}(x)]^2/2+\mu B}{T_i(x)}\right\}. \tag{12}$$

In these expressions, $n_i(x)$ and $T_i(x)$ are the radial ion density and temperature profiles obtained from the ion distribution function determined in the first step, and we take $n_{e0}=n_i$. The variable x is either ψ or Ω depending on what choice fits better the solution of the ion equation. This choice of f_{e0} and f_i reduces the electron collision operator to

$$C(\delta f_e)=C_{ee}(\delta f_e,f_{e0})+C_{ei}(\delta f_e,f_{iM}), \tag{13}$$

which is applied in the frame of reference moving with the ion velocity. The distribution function f_{e0} in Eq. (11) gives a finite contribution to the parallel electric current that just cancels the ion current $en_iu_{i\parallel}$. Hence, the bootstrap current is obtained directly from an integral over δf_e. With these choices for f_{i0} and f_{e0} we arrive at the following equations:

$$\frac{d\delta f}{dt}=C(\delta f)-\frac{df_0}{dt}. \tag{14}$$

We use the Hamiltonian guiding center particle code HAGIS (Ref. 11), which contains a Monte Carlo procedure for pitch-angle scattering.[12] The Hamiltonian guiding center equations for the marker particles are consistently obtained from a Lagrangian. They are expressed in the Boozer coordinates ψ, θ, ζ and the velocity space coordinates $\rho_\parallel=mv_\parallel/eB$ and μ and solved by a Runge–Kutta method with adaptive time steps. Associated with each particle is a phase space element and the contribution of the particle to δf, the product of which is the particle's weight. The sources for this weight are the terms on the right-hand side in Eq. (14). The effect of collisions is included as follows. The particles move collisionless for the length of a collision of time step and then the change of their velocities and weights by collisions is determined as explained in the next subsection.

Without collisions the distribution function f would be constant along the particle orbit as expressed by Eq. (14). Hence, between collisions we can compute δf as the difference between the value f_j of the total distribution function on the particle orbit and the value of f_0 at the current position of the particle in phase space.[13] For the jth particle we get

$$\delta f_j(t)=f_j-f_0[\boldsymbol{r}_j(t),\boldsymbol{v}_j(t)], \tag{15a}$$

$$f_j(0)=f_0[\boldsymbol{r}_j(0),\boldsymbol{v}_j(0)]. \tag{15b}$$

Between collisions f_j is constant, but when collisions occur, their contributions to the particle weights have to be added to δf_j. This is achieved by changing f_j in the collision procedure.

C. Monte Carlo procedure for pitch angle scattering

The collision operator for pitch-angle Coulomb scattering is applied. For scattering of particles α by particles β with a Maxwellian distribution it reads

$$C_{\alpha\beta}(f_\alpha,f_{\beta M})=\hat{\nu}_{\alpha\beta}(v)\frac{1}{2}\frac{\partial}{\partial\lambda}(1-\lambda^2)\frac{\partial f_\alpha}{\partial\lambda}, \tag{16}$$

where $\lambda=v_\parallel/v$ is the cosine of the pitch angle and $\hat{\nu}_{\alpha\beta}(v)$ is the velocity-dependent collision frequency. It is obtained from the pitch angle part of the Landau–Fokker–Planck collision term [Eq. (6.40) in Ref. 7],

$$\hat{\nu}_{\alpha\beta}(v)=\nu_{0\alpha\beta}\left(\frac{v_{\mathrm{th}\alpha}}{v}\right)^3G\left(\frac{v}{v_{\mathrm{th}\beta}}\right), \tag{17a}$$

$$G(x)=\left(1-\frac{1}{2x^2}\right)\mathrm{erf}(x)+\frac{\exp(-x^2)}{x\sqrt{\pi}}. \tag{17b}$$

The quantity $\nu_{0\alpha\beta}=n_\beta Z_\alpha^2Z_\beta^2e^4\ln\Lambda_{\alpha\beta}/(4\pi\epsilon_0^2m_\alpha^2v_{\mathrm{th}\alpha}^3)$ is related to the usual collision frequencies $(\nu_{ii},\nu_{ee},\nu_{ei})$ by $\nu_{\alpha\beta}=4\nu_{0\alpha\beta}/3\sqrt{2\pi}$. The thermal velocities are defined as $v_{\mathrm{th}\alpha}=\sqrt{2T_\alpha/m_\alpha}$ and $v_{\mathrm{th}\beta}=\sqrt{2T_\beta/m_\beta}$. For the electron-ion collisions $G(x)$ is replaced by the asymptotic value $G=1$ for $x=v_e/v_{\mathrm{th}i}\gg1$. The changes of $v_\parallel$ and $v_\perp$ during a collision time step Δt_c are computed with (pseudo) random numbers η fulfilling $\langle\eta\rangle=0$ and $\langle\eta^2\rangle=1$ as follows:

$$\delta v_\parallel=-\hat{\nu}v_\parallel\Delta t_c+\eta v_\perp\sqrt{\hat{\nu}\Delta t_c}, \tag{18a}$$

$$\delta v_\perp^2=-(2v_\parallel+\delta v_\parallel)\delta v_\parallel. \tag{18b}$$

The pitch angle scattering does not conserve the particle momentum, but we achieve momentum conservation in a second step by adding a term proportional to $\hat{\nu}v_\parallel f_M$ [14,15] to δf, i.e., we change the values f_j in Eq. (15a) by

$$\delta f_{\mathrm{corr.}}=-\hat{\nu}(v)v_\parallel f_M\Delta p_\parallel\Big/\int\hat{\nu}(v)mv_\parallel^2f_Md^3v, \tag{19}$$

where $\Delta p_\parallel=\int m\delta v_\parallel\delta fd^3v$ is the momentum change in the Monte Carlo step. In the numerical simulation it is not possible to compute $\delta f_{\mathrm{corr.}}$ at each point in real space, since a minimum number of marker particles is needed for representing the velocity space in the integral in Eq. (19). Therefore the correction is done within volume elements of finite size that are constructed as follows. The plasma volume is divided into thin shells between helical flux surfaces with a closer spacing near the island for sufficient resolution. These volumes between flux surfaces are then subdivided further into smaller cells to avoid a possible spurious momentum transfer along the helical angle coordinate ξ. The range of ξ from $-\pi$ to π is divided into ten bins as indicated in the lower half of Fig. 1. The Monte Carlo procedure described above was successfully tested in Refs. 10, 12, and 16.

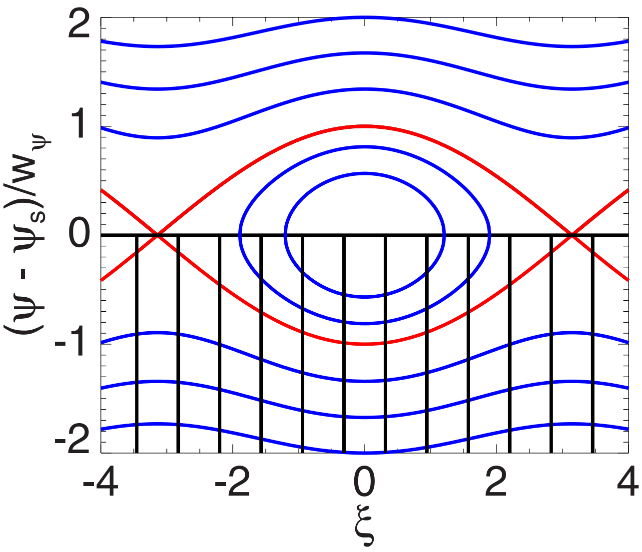

FIG. 1. (Color online) Lines of constant helical flux in the $\xi-\psi$ plane (schematic). In the lower half of the graph the grid cells for computing ξ-dependent averages and integrals for the collision operator are indicated. w_ψ is the island half width.

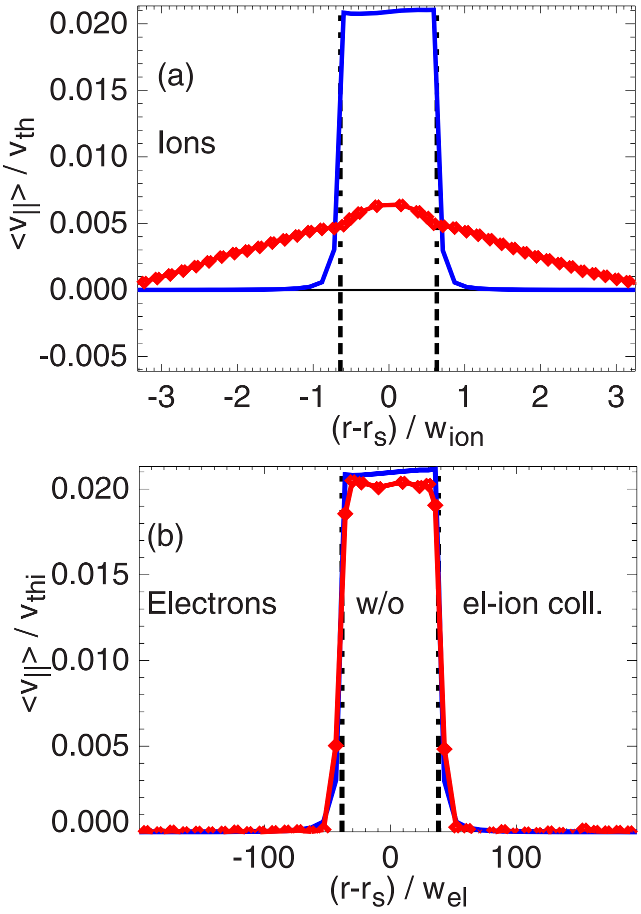

FIG. 2. (Color online) (a) Parallel ion flow velocity (red symbols) and (b) parallel electron flow velocity (red symbols) from a simulation without *e-i* collisions vs the radius through the O point of a small rotating island ($w=0.6$). Also shown by solid blue lines is $\langle E_r/B_p\rangle$.

D. Flux surface averages

The flux surface averages are approximated by volume averages within a thin shell between two helical flux surfaces,

$$\langle \int A\,\delta f d^3v \rangle \approx \int_{\Omega-\delta\Omega}^{\Omega+\delta\Omega} A\,\delta f d\Gamma \Big/ \int_{\Omega-\delta\Omega}^{\Omega+\delta\Omega} \mathcal{J} d\Omega d\xi d\theta, \qquad (20)$$

where $\mathcal{J}$ is the Jacobian and $d\Gamma = d^3v\mathcal{J}d\Omega d\xi d\theta$ is the phase space volume element. The integral in the numerator of Eq. (20) is replaced by a sum over the contributions of the marker particles,

$$\sum_{\Omega-\delta\Omega\le\Omega_j\le\Omega+\delta\Omega} A_j\delta f_j \Delta\Gamma_j, \qquad (21)$$

where $\Delta\Gamma_j$ is the phase space volume associated with the jth marker, and δf_j the marker's contribution to δf. The integral in the denominator is computed numerically directly from $\mathcal{J}$. Whenever the dependence of some variable on the helical angle ξ is to be resolved, the averages are computed for the grid cells indicated in lower half of Fig. 1.

III. THE SMALL-ISLAND EFFECT

The island of a NTM is normally rotating with respect to the surrounding plasma and a radial electric field is present inside the island that acts to force the plasma to corotate with the island. (We consider the frame of reference in which the plasma far from the island is at rest.) Since the trapped particles, on average, cannot follow the poloidal $\boldsymbol{E}\times\boldsymbol{B}$ drift and by collisions the poloidal rotation of the passing particles is also damped, a contribution $u_\parallel = \langle E_r/B_p\rangle$ to the parallel flow velocity arises,[7] where the brackets indicate the flux surface average. In a big island the parallel flow velocities of ions and electrons are equal and thus do not contribute to the electric current. When, however, the island width is of order of the ion banana orbit width, this is not the case, and a finite electric current arises. This effect can best be seen in the artificial case of a rotating island in plasma with constant background density and temperatures (equal for ions and electrons) such that no unperturbed current exists. We demonstrate the creation of this current with numerical results for a small island with $w=0.6$. Here and in the following we denote by w the ratio of the island width and the ion orbit width,

$$w = w_{\mathrm{isld}}/w_{\mathrm{ion}}, \qquad (22)$$

with $w_{\mathrm{ion}} = \sqrt{\varepsilon}\rho_{ip}$ and $\rho_{ip} = mv_{\mathrm{th}i}/eB_p$. The following parameters have been used for the calculations: $n_0 = 10^{20}\ \mathrm{m}^{-3}$, $T_0 = 1000$ eV, $\omega = 13\,000\ \mathrm{s}^{-1}$, $B_0 = 2$ T, $R_0 = 2$ m; the safety factor q varies radially between 1 and 3, and the island is located at a flux surface with $q = m/n = 3/2$ and inverse aspect ratio $\varepsilon = 0.22$; the collision frequency is set to a value corresponding to $\nu^* = \nu qR/\epsilon^{3/2}v_{\mathrm{th}} = 0.02$ at the location of the island.

The parallel ion flow velocity in steady state after eight collision times is shown in Fig. 2(a). In the island the flow velocity is much smaller than the neoclassical velocity $\langle E_r/B_p\rangle$ because the ions do not feel the strong electric field all along their orbits, but only inside the island. In addition,

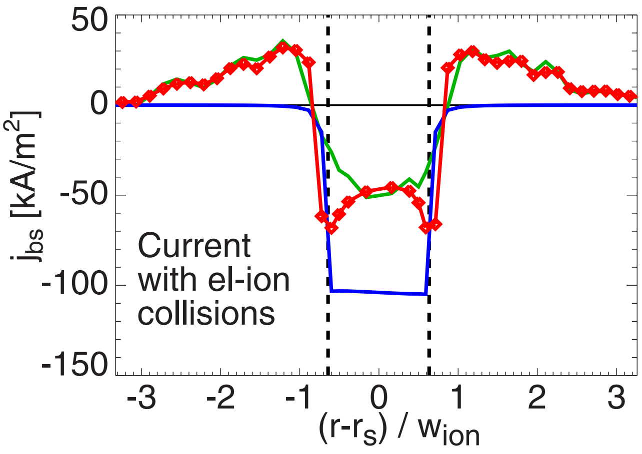

FIG. 3. (Color online) Parallel electric current (red symbols) in the island of Fig. 2. Also shown is the current $\langle -enE_r/B_p\rangle$ (solid blue line) and the bootstrap current computed with the perturbed density gradient (green/gray line).

due to the finite orbit width a finite ion flow exists outside the island, although the electric field is very small. The electron velocity, on the contrary, is close to $\langle E_r/B_p\rangle$ due to the small electron orbit width, as is shown in Fig. 2(b), when electron-ion collisions are switched off. This mismatch of the flows results in a finite electric current in the island of the order of $\langle -enE_r/B_p\rangle$, which is reduced to a smaller value, when the friction due to collisions between electrons and ions is included. This is shown in Fig. 3, where the electric current from a simulation with electron-ion collisions is depicted.

The finite electric current goes along with a small density perturbation of order $-e\Phi/T$ shown in Fig. 4, which creates a finite density gradient in the island and outside the island near the separatrix. We find that the values of the ion flow and the bootstrap current obtained from the usual neoclassical theory[7,17] with the *perturbed* density gradient match well the numerical results, except close to the separatrix. This might be surprising since the island is smaller than the ion banana orbit width, but, on the other hand, the density variation is only a percent or two over the island width, hence the gradient length $n/(dn/dr)$ is much larger than the island width. Near the separatrix the strong change of the gradient evidently has an effect. The density perturbation and the electric current have the opposite sign when the island is rotating in the opposite direction, since the potential is proportional to ω. In the normal case of negative density and temperature gradients the additional small-island current has the same direction as the unperturbed bootstrap current, when the island rotates in the direction of the electron diamagnetic drift, and it has the opposite direction in the case of rotation in the ion diamagnetic drift direction.

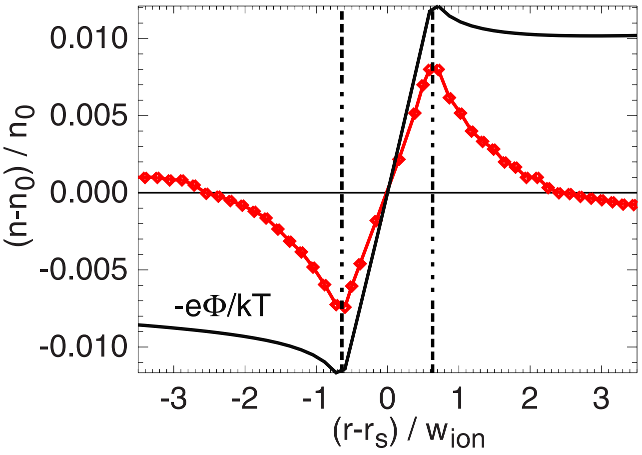

FIG. 4. (Color online) Density perturbation (symbols) in the island in Fig. 2 compared to $-e\Phi/T$ (solid line) for an island rotating in the ion diamagnetic direction.

IV. RESULTS OF THE SIMULATIONS

A. Results with electric potential like in big islands

In the simulations, the mode frequency ω is a free parameter, while in the experiment it depends on the density and temperature gradients of the unperturbed plasma. From analytic models for NTMs values $\omega=\omega_*(1+\kappa\eta)$ near either of the diamagnetic frequencies,

$$\omega_{*e}=-\frac{mT_e}{qen_0}\frac{dn_0}{d\psi},\qquad \omega_{*i}=\frac{mT_i}{qen_0}\frac{dn_0}{d\psi},\tag{23}$$

are obtained,[18] where $\eta=nT'/Tn'$ is the ratio of the logarithmic gradients and κ is a factor smaller than unity (since ω is m times the island rotation frequency, the diamagnetic frequencies are multiplied by m here). For such frequencies the current of order $\langle enE_r/B_p\rangle$ found in Sec. III is of similar size as the unperturbed bootstrap current: $\langle enE_r/B_p\rangle \approx en(q\omega_*/mB_p)d\psi/dr \approx (T/B_p)dn/dr$. Therefore, the bootstrap current in small islands can differ considerably from that in big islands. The partial preservation of the ion bootstrap current, which we found in small nonrotating islands[6] is enhanced or diminished depending on the direction of rotation.

We performed simulations for small islands with finite density and temperature gradients in the unperturbed plasma. The density profile is chosen as $n=n_0\exp\{-\gamma\psi/\psi(a)\}$ with $\gamma=1$ or $\gamma=0.5$ and $n_0=10^{20}$ m^{-3} (a is the minor radius, with $a/R_0=0.333$). The temperature has the same profile, $T=T_0\exp\{-\gamma\psi/\psi(a)\}$, where T_0 is varied (500–2000 eV) together with the magnetic field B_0 (2–6 T) and the perturbation strength $\hat{\alpha}$ (2×10^{-6}–4×10^{-5}) in order to get the desired ratio $w=w_{\mathrm{isld}}/w_{\mathrm{ion}}$ while keeping the island size small compared to the minor radius. Again, the safety factor q varies radially between 1 and 3, with $q=m/n=3/2$ and $\varepsilon=0.22$ at the location of the island. The collision frequency is scaled by a constant factor in order to obtain $\nu^*=\nu qR/\epsilon^{3/2}v_{\mathrm{th}}\approx 0.02$ at the location of the island, such that the plasma is in the banana regime.

In Fig. 5, the bootstrap current (surface averaged parallel electric current) in the island region is shown for different values of w. In the left column the results for islands rotating at the ion diamagnetic frequency are depicted, and in the right column the results for islands rotating at the electron diamagnetic frequency. In the case $\omega=\omega_{*i}$, the small-island current is opposite to the unperturbed bootstrap current and we see that only a small fraction of the unperturbed bootstrap

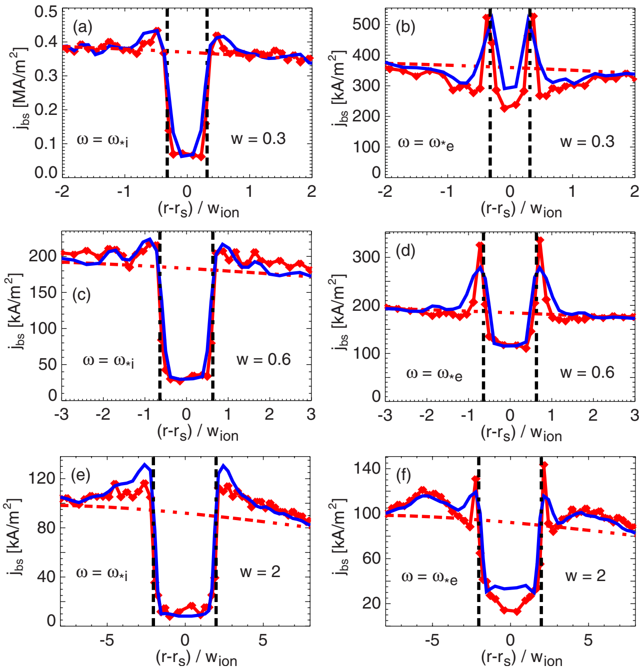

FIG. 5. (Color online) Bootstrap current from simulations (red symbols) in islands rotating at the ion diamagnetic frequency [(a), (c), and (e)] or the electron diamagnetic frequency [(b), (d), and (f)], $w=w_{\mathrm{isld}}/w_{\mathrm{ion}}$ is the normalized island width. Also shown is the neoclassical value computed with the perturbed gradients (solid blue line) and the unperturbed current (oblique dashed line). Vertical dashed lines indicate the position of the island.

current remains present in the island. That implies that almost the full bootstrap current drive for the NTM remains present in this case. With rotation at $\omega=\omega_{*e}$, however, the current due to the small-island effect is in the same direction as the bootstrap current, and a large fraction of the unperturbed bootstrap current is preserved in the island. In this case the drive of the mode due to the bootstrap current is strongly reduced in small islands.

In Fig. 5 also the bootstrap current values obtained from the neoclassical theory[17] with the perturbed density and temperature gradients are shown. They match well with the numerical results, except near the separatrix, particularly in the case $\omega=\omega_{*e}$. Looking at the perturbed density and temperature profiles in Figs. 6 and 7(a), we notice that in this case the flattening of the electron density and temperature in the island produces enhanced gradients just outside the island, but neither the ion density nor the ion temperature are flattened. The ion temperature profile is unchanged when the island width is smaller than the orbit width. (In the simulations, the finite collisional heat transport tends to flatten a little the temperature profile on a scale much larger than the island width because there is no heat source. This is not caused by the island and occurs even without the presence of an island.) In islands rotating at the electron diamagnetic frequency the ion density is even steeper than the unperturbed density. This means that quasineutrality is violated in this case, which makes it necessary to consider a modification of the electric potential which is the subject of Sec. IV B. In the case $\omega=\omega_{*i}$, the ion and electron densities are both flattened in the island and quasineutrality is preserved. In this case the residual bootstrap current in the island is due to the ion temperature gradient. The ion temperature gradient in the island starts to decrease a little at $w=2$ as shown in Fig. 7(b) and almost vanishes at $w=10$.

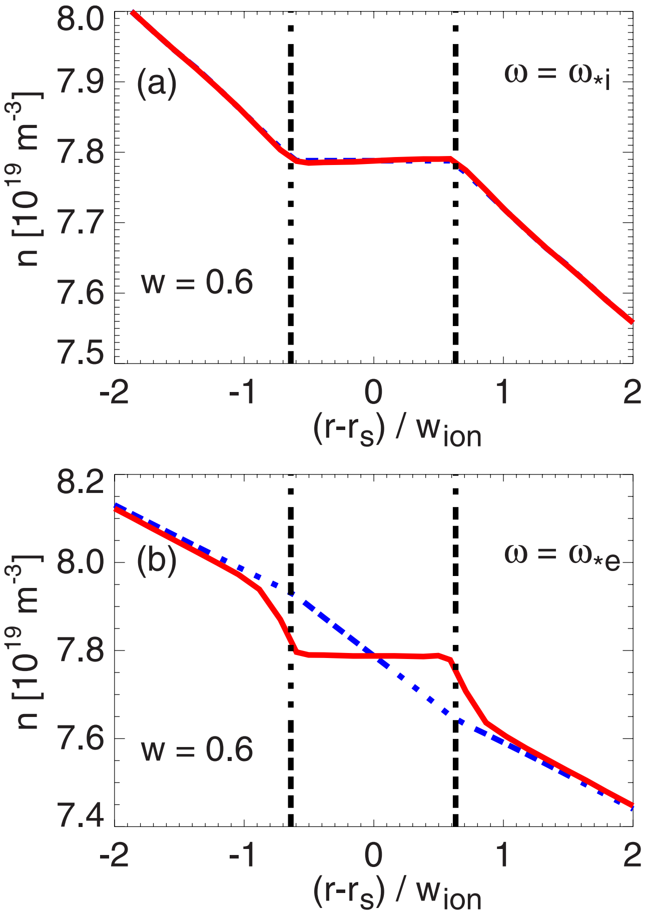

FIG. 6. (Color online) Profiles of electron density (red solid line) and ion density (blue dashed line) across small islands ($w=0.6$) rotating at ion diamagnetic frequency (a) or electron diamagnetic frequency (b). Vertical dashed lines indicate the position of the island.

Looking at the normalized ion density perturbations shown in Fig. 8, we can see how the plasma reacts differently to the rotating island and its electric field depending on the direction of rotation. In islands rotating at the ion diamagnetic frequency the ion density perturbation is always close to $-e\Phi/T_i$, which corresponds to a flattening of the ion density in Fig. 6 when the potential is given by Eq. (8). In the case $\omega=\omega_{*e}$ the ion density perturbation varies from $+e\Phi/T_i$ in big islands (not shown here, but this corresponds to flattening) to $-e\Phi/T_i$ in small islands, which corresponds to the steepening seen in Fig. 6.

The combined results of many simulations are shown in Fig. 9, where the fraction of the unperturbed bootstrap current that is preserved in small islands is plotted versus the island width. The difference between the bootstrap current values at $\omega=\omega_{*e}$ and at $\omega=\omega_{*i}$ increases with decreasing island size, but even in islands rotating at the electron diamagnetic frequency the bootstrap current is not entirely preserved. In the simulations there is a finite electron temperature gradient in the unperturbed plasma and the electron

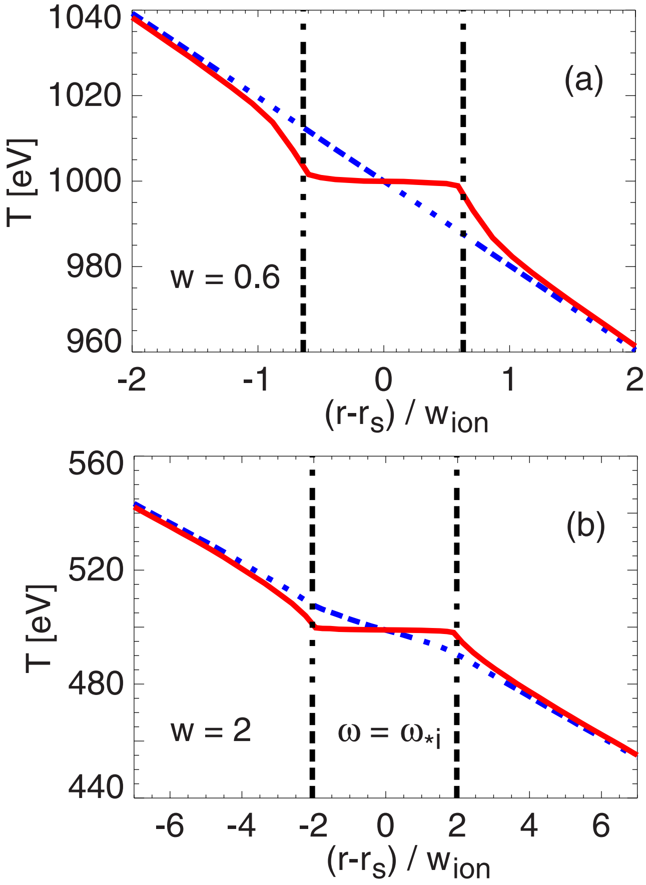

FIG. 7. (Color online) Electron (red solid line) and ion (blue dashed line) temperature profiles in a small island (a) with $w=0.6$ and a bigger island (b) with $w=2$. Vertical dashed lines indicate the position of the island.

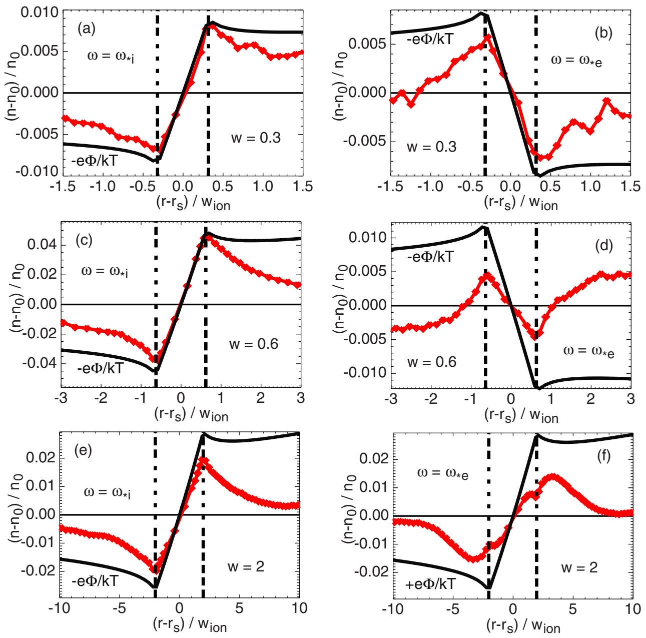

FIG. 8. (Color online) Density perturbations, $(n-n_0)/n_0$ (red symbols), in islands rotating at the ion diamagnetic frequency [(a), (c), and (e)] or at the electron diamagnetic frequency [(b), (d), and (f)]. Also shown are $-e\Phi/T_i$ or $+e\Phi/T_i$ (solid black lines), $w=w_{\mathrm{isld}}/w_{\mathrm{ion}}$.

temperature profile is flattened. The resulting loss of the contribution due to the electron temperature gradient sets an upper limit to the bootstrap current. For $\omega=\omega_{*i}$ there is a lower limit to the bootstrap current in a small island set by the current driven by the (unchanged) ion temperature gradient. The absolute values of these limits depend on the values of the density and temperature gradients in the unperturbed plasma, and on the neoclassical parameters such as collisionality and trapped particle fraction (in the simulations: $\nu^* \approx 0.02$, $f_t \approx 0.6$ at the position of the island and $\eta=1$).

B. Results with modified electric potential

The violation of quasineutrality in the case $\omega \approx \omega_{*e}$ indicates that in such islands the electric field must be different from that derived from the potential in Eq. (8), which is valid for big islands. In small islands the electric potential is a more complex function of Ω and ξ and waves can be excited by the island.[19] We can get an estimate for the potential as follows. In view of the results presented above, the ion density in small islands is approximated by $n_i \approx n_0(1-e\Phi/T_i)$. Since the small islands which we study are always big compared to the electron banana orbit width, we can take the solution for the electron distribution function for big islands. The leading terms which determine the density are[9]

$$f_e = f_{eM}\left\{1+\frac{e\Phi}{T_e}-\frac{e}{T_e}\frac{q(\omega-\omega_{*e})}{m}(\psi-\psi_s+h)\right\}, \tag{24}$$

where $h(\Omega)$ denotes the Ω-dependent part (i.e., the second term) on the right-hand side of Eq. (8). Equating the resulting density with the ion density leads to

$$\Phi_{\mathrm{small}} \approx \frac{T_i}{T_i+T_e}\frac{q(\omega-\omega_{*e})}{m}(\psi-\psi_s+h) \tag{25a}$$

$$= \frac{T_i}{T_i+T_e}\left(1-\frac{\omega_{*e}}{\omega}\right)\Phi_{\mathrm{big}} \tag{25b}$$

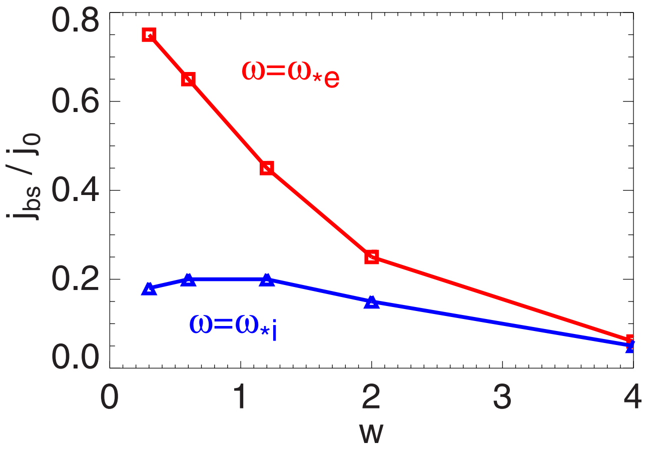

FIG. 9. (Color online) Bootstrap current in the island normalized to the unperturbed current vs normalized island width $w=w_{\mathrm{isld}}/w_{\mathrm{ion}}$ for $\omega=\omega_{*i}$ (blue triangles) and for $\omega=\omega_{*e}$ (red squares).

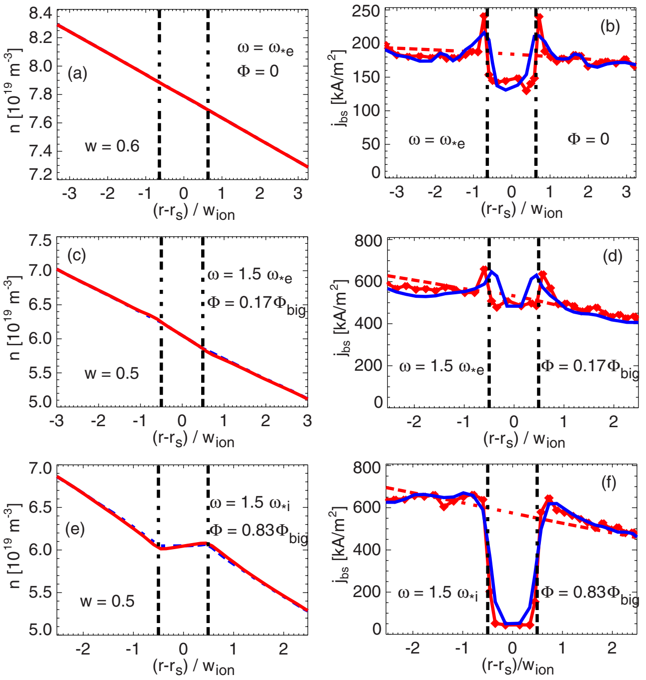

FIG. 10. (Color online) Results from simulations with the modified electric potential in Eq. (25a): [(a), (c), and (e)] electron density (red solid line) and ion density (blue dashed line) profiles, [(b), (d), and (f)] bootstrap current from simulations (red symbols), neoclassical value computed with the perturbed gradients (solid blue line), and the unperturbed current (oblique dashed line). Vertical dashed lines indicate the position of the island.

$$= \frac{T_i + T_e(\omega_{*i}/\omega)}{T_e + T_i}\Phi_{\rm big}, \qquad (25c)$$

with the potential $\Phi_{\rm big}$ given in Eq. (8). At frequencies near the ion diamagnetic frequency the potential in small islands is about the same as that in big islands, while it is very small for frequencies near the electron diamagnetic frequency. In Fig. 10 results of simulations with this modified electric potential are shown, and the dependence of the island bootstrap current on the rotation frequency is depicted in Fig. 11. In the case $\omega = \omega_{*e}$ with a vanishing electric potential the density remains unperturbed, the mismatch of the electron and ion densities is removed. The temperature profiles are not different from those in Sec. IV A, hence there is some reduction of the bootstrap current in the island caused by the flattening of the electron temperature. In spite of the flattening of the electron temperature the current in the island rotating at $\omega = 1.5\omega_{*e}$ is almost equal to the unperturbed current because the density is steepened inside the island. In the case $\omega = 1.5\omega_{*i}$ the current in the island is very small. This confirms the result from Sec. IV A that the most of the bootstrap current in the island is lost for $\omega \approx \omega_{*i}$, but that a large fraction is preserved for $\omega \approx \omega_{*e}$.

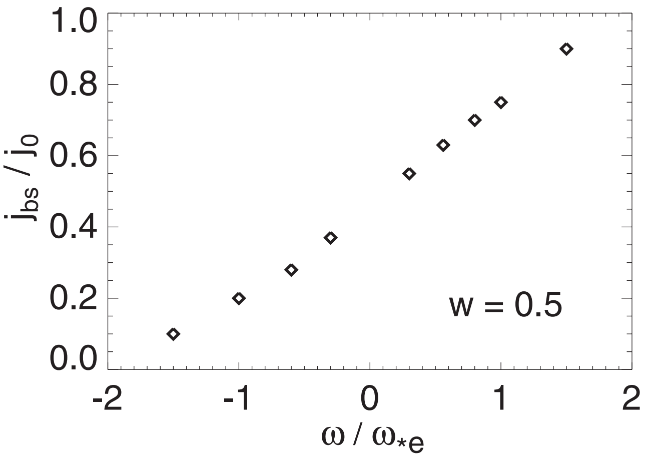

FIG. 11. Bootstrap current in a small island ($w=0.5$) normalized to the unperturbed current vs island rotation frequency. Data from simulations with modified electric potential.

V. SUMMARY

The bootstrap current in rotating islands that are of similar size or smaller than the ion banana orbit width has been computed with drift kinetic numerical simulations. A frame of reference is used in which the unperturbed electric field vanishes. When the island is rotating in this frame, there is a radial electric field E_r that leads to an additional contribution to the parallel flows of ion and electrons of magnitude $u_\parallel \sim E_r/B_p$, where B_p is the poloidal component of the magnetic field. Since the electric field varies on the scale of the island width, which is much larger than the typical electron-orbit size, but comparable to the ion orbit width, the electrons react to the local field while the ions respond rather to the orbit-averaged field. The resulting parallel electron and ion flows differ from each other, thus contributing to the parallel (bootstrap) current. The electric field also causes a density perturbation such that this current can be explained as the bootstrap current caused by this perturbation.

We have shown that when the island is rotating at a frequency near the ion diamagnetic frequency, most of the bootstrap current is lost even in small islands, only the contribution due to the ion temperature gradient remains present. In the case of rotation at a frequency near the electron diamagnetic frequency a large part of the bootstrap current is preserved in the island, and only the contribution due to the electron temperature gradient is lost. In this case the electric potential differs strongly from that in big islands. In all cases the bootstrap current is close to the value of the neoclassical theory computed with the perturbed density and temperature gradients.

Since the parallel current in the island influences the island dynamics, our results have a particular relevance for the prediction of the stability of magnetic islands. In small islands rotating in the ion diamagnetic direction, the bootstrap current drive of the island growth is strong like in big islands, since most of the bootstrap current is lost also in these small islands. However, in small islands rotating in the electron diamagnetic direction are more stable, since the bootstrap current is largely preserved by the “small-island effect” presented in this paper, hence the neoclassical drive of the island growth is strongly reduced. The competition between this effect and other (de)stabilizing effects acting on small islands (like, e.g., finite transport across the island[4] or the polarization current[8,9,18]) is likely to explain the experimental finding that magnetic islands often appear only above a given amplitude threshold, implying some stabilizing effect acting against the neoclassical drive for small islands.

[1] O. Sauter, R. J. La Haye, Z. Chang, D. A. Gates, Y. Kamada, H. Zohm, A. Bonderson, D. Boucher, J. D. Callen, M. S. Chu, T. A. Gianakon, O. Gruber, R. W. Harvey, C. C. Hegna, L. L. Lao, D. A. Monticello, F. Perkins, A. Pletzer, A. H. Reiman, M. Rosenbluth, E. J. Strait, T. S. Taylor, A. D. Turnbull, F. Waelbroeck, J. C. Wesley, H. R. Wilson, and R. Yoshino, Phys. Plasmas **4**, 1654 (1997).

[2] See National Technical Information Service Document No. DE6008946 (W. X. Qu and J. D. Callen, University of Wisconsin Plasma Report No. UWPR 85–5, 1985). Copies may be ordered from the National Technical Information Service, Springfield, VA 22161.

[3] R. Carrera, R. D. Hazeltine, and M. Kotschenreuther, Phys. Fluids **29**, 899 (1986).

[4] R. Fitzpatrick, Phys. Plasmas **2**, 825 (1995).

[5] E. Poli, A. G. Peeters, A. Bergmann, S. Günter, and S. D. Pinches, Phys. Rev. Lett. **88**, 075001 (2002).

[6] E. Poli, A. G. Peeters, A. Bergmann, S. Günter, and S. D. Pinches, Plasma Phys. Controlled Fusion **45**, 71 (2003).

[7] F. Hinton and R. Hazeltine, Rev. Mod. Phys. **48**, 239 (1976).

[8] A. I. Smolyakov, Plasma Phys. Controlled Fusion **35**, 657 (1993).

[9] H. R. Wilson, J. W. Connor, R. J. Hastie, and C. C. Hegna, Phys. Plasmas **3**, 248 (1996).

[10] A. Bergmann, E. Strumberger, and A. G. Peeters, Nucl. Fusion **45**, 1255 (2005).

[11] S. D. Pinches, L. C. Appel, J. Candy, S. E. Sharapov, H. L. Berk, D. Borba, B. N. Breizman, T. C. Hender, K. I. Hopcraft, G. T. A. Huysmans, and W. Kerner, Comput. Phys. Commun. **111**, 133 (1998).

[12] A. Bergmann, A. G. Peeters, and S. D. Pinches, Phys. Plasmas **8**, 5192 (2001).

[13] S. J. Allfrey and R. Hatzky, Comput. Phys. Commun. **154**, 98 (2003).

[14] A. M. Dimits and B. I. Cohen, Phys. Rev. E **49**, 709 (1994).

[15] Z. Lin, W. M. Tang, and W. W. Lee, Phys. Plasmas **2**, 2975 (1995).

[16] E. Poli, A. Bergmann, A. G. Peeters, L. C. Appel, and S. D. Pinches, Nucl. Fusion **45**, 384 (2005).

[17] S. P. Hirshman and D. J. Sigmar, Nucl. Fusion **21**, 1079 (1981); O. Sauter, C. Angioni, and Y. R. Lin-Liu, Phys. Plasmas **6**, 2834 (1999).

[18] A. B. Mikhailovskii, Contrib. Plasma Phys. **43**, 125 (2003).

[19] F. L. Waelbroeck, J. W. Connor, and H. R. Wilson, Phys. Rev. Lett. **87**, 215003 (2001).

IOP PUBLISHING PLASMA PHYSICS AND CONTROLLED FUSION

Plasma Phys. Control. Fusion **52** (2010) 124021 (17pp) doi:10.1088/0741-3335/52/12/124021

Gyrokinetic and gyrofluid investigation of magnetic islands in tokamaks

E Poli, A Bottino, W A Hornsby[1], A G Peeters[1,2], T Ribeiro, B D Scott and M Siccinio

Max-Planck-Institut für Plasmaphysik, Garching bei München, Germany
[1] Centre for Space and Astrophysics, Department of Physics, University of Warwick, UK
[2] Department of Physics, University of Bayreuth, Germany

Received 2 July 2010, in final form 31 August 2010
Published 15 November 2010
Online at stacks.iop.org/PPCF/52/124021

Abstract

The evolution of a tearing mode is a multi-scale problem, involving lengths from below the ion gyroradius up to the dimensions of the system. The effects due to finite ion Larmor radius on the island dynamics are investigated by means of numerical gyrokinetic and gyrofluid simulations in tokamak geometry. In gyrokinetic runs, the magnetic island is prescribed. The coupling induced by a static island between small and large scale fluctuations in the case of electrostatic turbulence is discussed and the role of the perturbed magnetic geometry on the electron response is highlighted. Simulations in the presence of a rotating island, excluding background turbulence, allow a clear, self-consistent determination of the electrostatic potential associated with the island rotation and of the relevant plasma profiles for arbitrary island widths. Finally, the first gyrofluid simulations showing the growth of an island in the presence of electromagnetic turbulence for parameters typical of a mid-size tokamak are presented.

(Some figures in this article are in colour only in the electronic version)

1. Introduction

The tearing instability [1, 2], appearing as magnetic islands developing on low-order rational surfaces, is often observed in tokamak experiments. A fully developed tearing mode represents a serious concern for a tokamak reactor, as it limits the achievable plasma pressure and can trigger disruption events [3]. In axisymmetric devices, the dynamics of the tearing mode is strongly affected by toroidal effects. The mode is often neoclassically driven by the drop in the bootstrap current caused by pressure flattening within the reconnected region [4–6]. Moreover, the neoclassical polarization current [7, 8] and Pfirsch–Schlüter currents [9–11] have been demonstrated to influence the island evolution. More recently, the interaction between small-scale turbulence and 'mesoscale' magnetic islands has attracted a growing attention, also because of the fact that the increasing availability of high-performance numerical resources allows the exploration of more and more realistic parameters. The importance of this mutual influence between different scales for magnetic reconnection has been long recognized in general [12] and for magnetic islands in fusion plasmas in particular [13]. As far as the influence of small on large scales is concerned, in addition to the investigation of turbulence as a source of anomalous dissipation (viscosity, resistivity) [14–18], electromagnetic turbulence has been shown to be able to provide a trigger for the growth of an island [19]. Moreover, turbulent transport contributes to determining the density and temperature profiles across the reconnected region, in turn influencing the contribution of bootstrap [20] and polarization [21] current to the island dynamics. On the other hand, the tearing mode has a major impact on the turbulence profile, as the above-mentioned pressure flattening inside the island reduces the drive for the instabilities. In addition, the turbulence is regulated by the sheared flows associated with the long-wavelength modes (this last effect being similar to that of zonal flows in axisymmetric systems). A nice overview of the properties of the mutual interaction between small and large-scale instabilities has been given by McDevitt and Diamond [17].

A magnetic island is a system exhibiting different spatial scales along and across it. In tokamaks, the poloidal wavelength of the island is of the order of the minor radius, while its width can be of the order of the ion Larmor radius or below. For this reason, kinetic studies of the tearing-mode dynamics employing the gyrokinetic theory have already been carried out in the past. Slab-geometry calculations have been performed to investigate analytically the problem of the island propagation and the role of the polarization current, the emission of drift waves and their stability in the presence of an island-perturbed equilibrium [22–25]. Numerical gyrokinetic particle-in-cell (PIC) simulations have been employed to study the reconnection problem in a collisionless plasma slab [26] and also extended to the semicollisional regime [27]. On the other hand, the gyroradius is the typical spatial scale of turbulent fluctuations in fusion plasmas. For a description of the effects of the presence of a tearing mode on microturbulence and vice versa, finite-Larmor-radius (FLR) effects must then be retained, by means of a gyrofluid or gyrokinetic approach.

It is clear that the self-consistent evolution of island and turbulence constitutes a formidable multi-scale problem. On the way to its complete solution, several routes are being explored, which reduce the size of the problem by means of appropriate simplifications. This paper is intended to present recent new results on the role of FLR effects on the dynamics of magnetic islands in toroidal plasmas. We adopt two different numerical approaches, the first based on gyrokinetic, the second on gyrofluid equations. In the former case, we rely on the separation between the typical time scales involving the development turbulence and the island growth (for a discussion see also [21, 28]). In this scheme, the magnetic island is prescribed, i.e. island rotation and width do not evolve. This excludes, of course, the feedback of short on long time scales. On the other hand, toroidicity and kinetic effects are retained. They are known to significantly change the bootstrap [29–31] and polarization current [32–34] and are, hence, potentially important for the 'closure' of the interaction loop, when neoclassical effects on the mode evolution will be considered. Two sets of gyrokinetic simulations are presented here. First, we explore the behaviour of electrostatic turbulent fluctuations in the presence of a static island, which confirm and extend, in particular through the inclusion of the perturbed magnetic geometry in the electron response [35], previous recent investigations [36]. The second part of our gyrokinetic results refers to a rotating island, for which the self-consistent electrostatic potential and the pressure profile are investigated switching off the turbulence. These simulations, which represent a first steps towards a neoclassical analysis, are found to support previous drift kinetic results [31]. The latter (gyrofluid) approach mentioned before implies a different simplification of the problem (namely, neglecting kinetic effects) but allows a simultaneous treatment of turbulence and island time scales. Here, the first results obtained for a set of plasma parameters close to those typical of the ASDEX Upgrade tokamak are presented. It is worth noting that a fluid approach has already been employed recently to resolve both turbulence and island scales in both slab geometry [37] and including curvature effects [38, 39].

In the next section, the numerical tools employed in our simulations, namely the two gyrokinetic codes ORB5 [40, 41] (PIC, global) and GKW [42, 43] (Vlasov, flux tube) and the global gyrofluid code GEMZ [44] are briefly presented, with emphasis on the different treatment of the magnetic perturbation associated with the magnetic island. Gyrokinetic results in the presence of turbulence are discussed in section 3, while the simulations of a rotating island in the absence of turbulence are presented in section 4. Section 5 is finally devoted to gyrofluid simulations. A summary and discussion of the results can be found in section 6.

2. Numerical tools

The dynamics of microinstabilities in toroidal geometry in the presence of a magnetic island is investigated in this paper employing the two complementary schemes described above, namely a gyrokinetic and a gyrofluid approach. A magnetic island developing on a given rational surface ψ_s characterized by a poloidal number m and toroidal number n can be introduced as a perturbation of the parallel vector potential (or, equivalently, of the poloidal flux $\tilde{\psi} = -R\tilde{A}_\|$, R being the major radius of the tokamak) of the form $\tilde{A}_\| = \bar{A}_\| \cos\xi$, where $\xi = m\theta - n\varphi - \omega t$ is the helical angle (θ and φ being the poloidal and toroidal angle, respectively, and ω the island rotation frequency). The corresponding perturbed magnetic field is mainly directed radially and varies in the $\nabla\xi$ direction as $\sin\xi$. A new flux label $\Omega = 2(\psi - \psi_s)^2/W_\psi^2 - \cos\xi$, where $W_\psi = \sqrt{4R\bar{A}_\| q_s/q_s'}$ is the island width in ψ units (the prime denoting differentiation with respect to ψ), can be introduced such that the total magnetic field is perpendicular to $\nabla\Omega$. With this definition, Ω varies between -1 at the island O-point (where $\psi = \psi_s$ and $\xi = 0$) and $+\infty$. The island width W is obtained in terms of W_ψ as $W = W_\psi/|\nabla\psi|$.

2.1. Gyrokinetic approach

Two gyrokinetic codes have been used in our study, based on different methods for the solution of the gyrokinetic equation.

The global PIC code ORB5 provides a numerical solution to the gyrokinetic equations in the formulation of Hahm [45]. It employs the PIC method, which is based on the introduction of an ensemble of numerical particles (markers), each one connected with a piece of the phase space associated with a given particle species. In the simulations presented here, the electrons are adiabatic and the markers represent only the main ion species i. The evolution of the markers is determined by the corresponding equations of motion, which are coupled to Maxwell's equations. The self-consistent fields are calculated projecting the charge and current associated with each marker onto a fixed spatial grid (in this paper, only simulations of electrostatic turbulence will be considered). The total distribution function is split into an analytically known time-independent part f_0 and a perturbation δf which is represented numerically. The gyrokinetic equations of motion for the markers are

$$\frac{\mathrm{d}\boldsymbol{R}}{\mathrm{d}t} = v_\parallel \boldsymbol{b} + \frac{1}{B_\parallel^*}\left[\frac{\mu B + v_\parallel^2}{\Omega_\mathrm{c}}\boldsymbol{b}\times\nabla B - \frac{v_\parallel^2}{\Omega_\mathrm{c}}\boldsymbol{b}\times(\boldsymbol{b}\times\nabla\times\boldsymbol{B}) - \nabla\langle\tilde{\phi}\rangle_g\times\boldsymbol{b}\right], \tag{1}$$

$$\begin{aligned}\frac{\mathrm{d}v_\parallel}{\mathrm{d}t} &= -\mu\left[\boldsymbol{b} - \frac{v_\parallel}{B_\parallel^*\Omega_\mathrm{c}}\boldsymbol{b}\times(\boldsymbol{b}\times\nabla\times\boldsymbol{B})\right]\cdot\nabla B \\ &\quad -\frac{Ze}{M}\left\{\boldsymbol{b} + \frac{v_\parallel}{B_\parallel^*\Omega_\mathrm{c}}\left[\boldsymbol{b}\times\nabla B - \boldsymbol{b}\times(\boldsymbol{b}\times\nabla\times\boldsymbol{B})\right]\right\}\cdot\nabla\langle\tilde{\phi}\rangle_g,\end{aligned} \tag{2}$$

$$\frac{\mathrm{d}\mu}{\mathrm{d}t} = 0, \tag{3}$$

where $\boldsymbol{R}$ is the position of the gyrocentre, $v_\parallel$ the velocity component along the magnetic field, $\boldsymbol{b}$ the unit vector along the magnetic field $\boldsymbol{B}$, μ the magnetic moment, Ω_c the cyclotron frequency, $\langle\tilde{\phi}\rangle_g$ the perturbed potential (solution of the Poisson equation) averaged over the gyroperiod, Ze and M the particle's charge and mass, respectively, and $B_\parallel^* = B + (M/Ze)v_\parallel\boldsymbol{b}\cdot\nabla\times\boldsymbol{b}$. Since along the orbits $\mathrm{d}f/\mathrm{d}t = 0$ (no collisions are considered here), δf must obey the equation

$$\frac{\mathrm{d}(\delta f)}{\mathrm{d}t} = -\frac{\mathrm{d}f_0}{\mathrm{d}t} = -\frac{\mathrm{d}\boldsymbol{R}}{\mathrm{d}t}\cdot\nabla f_0 - \frac{\mathrm{d}v_\parallel}{\mathrm{d}t}\frac{\partial f_0}{\partial v_\parallel}. \tag{4}$$

The velocity $\mathrm{d}\boldsymbol{R}/\mathrm{d}t$ includes the radial motion along the perturbed field lines. The radial component $\tilde{\boldsymbol{B}}$ of the magnetic field produced by the tearing mode accounts for the most important modification of particle orbits [46] and has been included in ORB5 by operating the substitution $\boldsymbol{b}\rightarrow\boldsymbol{b}+\tilde{\boldsymbol{b}}$ (where $\tilde{\boldsymbol{b}} = \tilde{\boldsymbol{B}}/B$) in the first term of both equations (1) and (2).

In the Vlasov flux-tube code GKW, the gyrokinetic equation is solved in the form

$$\frac{\partial g}{\partial t} + \boldsymbol{v}_\chi\cdot\nabla g + \left(v_\parallel\boldsymbol{b} + \boldsymbol{v}_\mathrm{d}\right)\cdot\nabla(\delta f) - \frac{\mu B}{M}\frac{\boldsymbol{B}\cdot\nabla B}{B^2}\frac{\partial(\delta f)}{\partial v_\parallel} = S \tag{5}$$

on a five-dimensional grid in the $(\boldsymbol{X}, \mu, v_\parallel)$ space, where $\boldsymbol{X}$ is the gyrocentre position (the index denoting the particle species is suppressed for brevity). In the previous equation, the distribution function is split into a Maxwellian background term F_M and a deviation δf, with the auxiliary function g defined as $g = \delta f + (Ze/T)v_\parallel\langle\tilde{A}_\parallel\rangle_g F_\mathrm{M}$. The velocity $\boldsymbol{v}_\chi = (\boldsymbol{b}\times\nabla\chi)/B$, with $\chi = \langle\tilde{\phi}\rangle_g + v_\parallel\langle\tilde{A}_\parallel\rangle_g$, is a combination of the $\boldsymbol{E}\times\boldsymbol{B}$ velocity and the parallel motion along the perturbed field lines, and $\boldsymbol{v}_\mathrm{d}$ is the drift velocity due to magnetic-field inhomogeneity (∇B and curvature). The electrostatic potential is the solution of the Poisson equation, while $\tilde{A}_\parallel$ is the imposed island perturbation. The source term on the right-hand side of equation (5) reads as

$$S = -\left(\boldsymbol{v}_\chi + \boldsymbol{v}_\mathrm{d}\right)\cdot\left[\frac{\nabla n}{n} + \left(\frac{v_\parallel^2}{v_\mathrm{th}^2} + \frac{\mu B}{T} - \frac{3}{2}\right)\frac{\nabla T}{T}\right]F_\mathrm{M} - \frac{Ze}{T}\left(v_\parallel\boldsymbol{b} + \boldsymbol{v}_\mathrm{d}\right)\cdot\nabla\langle\tilde{\phi}\rangle_g F_\mathrm{M}$$

(n and T are the background density and temperature, respectively, and $v_\mathrm{th} = \sqrt{2T/M}$ is the thermal velocity). In the previous equations, the contribution connected to the radial profile of the toroidal plasma rotation velocity has been omitted. With respect to the global approach described above, the physical model remains the same, but the equations are solved in a finite domain of the plasma around a given field line. Correspondingly, the so-called flux-tube ordering [47] is adopted, in which the deviation of the distribution function from its equilibrium value is assumed to be small over the region of interest, whereas its gradients can be comparable to the equilibrium gradients. For a more detailed discussion of the ordering assumptions in GKW see [43, 48] (a comparison between the global and flux-tube results is presented in section 3). GKW is written in field-aligned Hamada coordinates (ψ, ζ, s). When a magnetic equilibrium with circular concentric flux surfaces is adopted, s can be regarded as a normalized poloidal angle varying between $-1/2$ and $1/2$ ($s = \theta/2\pi$ in the large-aspect-ratio limit $\epsilon \to 0$) and $\zeta = (q\theta - \varphi)/2\pi$ is chosen such that the parallel-gradient operator $\boldsymbol{B} \cdot \nabla$ involves only $\partial/\partial s$. In these coordinates, the helical angle ξ can be expressed in the vicinity of the rational surface, which is supposed to be located at the centre of the computational box ($\bar{\psi} = \psi - \psi_s$ being the distance from this surface), expanding the safety factor appearing in the definition of ζ to the first order around $q_s = m/n$,

$$m\theta - n\varphi - \omega t = 2\pi \left(n\zeta - nsq_s'\bar{\psi}\right) - \omega t = k_\zeta \zeta - sk_\psi \bar{\psi} - \omega t.$$

Here, the island wave vector with components $k_\zeta = 2\pi n\rho_*$ and $k_\psi = q_s' k_\zeta$ has been introduced (the wave vector is expressed in units of $1/\rho_\mathrm{i}$, with the definition $\rho_* = \rho_\mathrm{i}/R$, ρ_i being the ion gyroradius). This expression shows that the periodicity constraint in the radial direction (required by the spectral approach adopted in GKW) cannot be satisfied for every value of s. Defining the radial width of the box as $\Delta\psi = [-\pi/k_\psi, \pi/k_\psi]$, the first step to impose periodicity is projecting the vector potential on the ψ-harmonics,

$$\tilde{A}_\parallel = \mathrm{e}^{\mathrm{i}(k_\zeta \zeta - \omega t)} \sum_{p=0}^{\infty} A^p(s) \mathrm{e}^{\mathrm{i}pk_\psi \bar{\psi}},$$

with

$$A^p(s) = \frac{k_\psi}{2\pi} \bar{A}_\parallel \int_{-\pi/k_\psi}^{\pi/k_\psi} \mathrm{e}^{-\mathrm{i}pk_\psi \bar{\psi}} \mathrm{e}^{-\mathrm{i}sk_\psi \bar{\psi}} \mathrm{d}\psi = \bar{A}_\parallel \frac{\sin[\pi(s+p)]}{\pi(s+p)}.$$

This simple implementation turns out to be unsatisfactory, as it leads to abrupt jumps in the vector potential at the edge of the radial computational domain, where periodicity is enforced (figure 1(*a*)). The problem, however, can be circumvented by introducing a smoothing factor at high p-harmonics (figure 1(*b*)), i.e. by operating the replacement

$$\frac{\sin[\pi(s+p)]}{\pi(s+p)} \to \exp\left[-(s+p)^2/L^2\right] \frac{\sin[\pi(s+p)]}{\pi(s+p)}$$

in the previous equation. The exact value of the scale L does not affect the results, provided it is large enough.

2.2. *Gyrofluid approach*

Following the dynamics of magnetic islands and microturbulence *simultaneously* is not presently feasible by gyrokinetic models without unphysical compromises involving the parameters of scale separation. If it is to be demonstrated that small and large scales can interact, then the results are only meaningful with the correct values of the dimensionless ratios ρ_s/a or $M_\mathrm{e}/M_\mathrm{i}$ or $\beta_\mathrm{e} = c_\mathrm{s}^2/v_\mathrm{A}^2$ or qR/L_T, where c_s is the sound speed, v_A is the Alfvén speed and ρ_s is the drift scale (also called the ion sound gyroradius). See [49, 50] for the significance these parameters, alone and in combination, have for tokamak microturbulence. A moderate sized tokamak has $a/\rho_\mathrm{s} \sim 200$, a deuterium plasma has $M_\mathrm{i}/M_\mathrm{e} = 3670$, and typical conditions have $\beta_\mathrm{e} \sim 3 \times 10^{-3}$ for the plasma core. The electromagnetic gyrofluid equations are as given in [44]. Time dependent equations for six gyrofluid moment variables (for each species, density, parallel velocity, parallel and perpendicular temperature and parallel and perpendicular heat fluxes associated with each temperature) are advanced for a singly charged, single component, purely ionized plasma. The self-consistent fields $\tilde{\phi}$ and $\tilde{A}_\parallel$ are found via the polarization and induction equations, respectively. The tilde symbol denotes

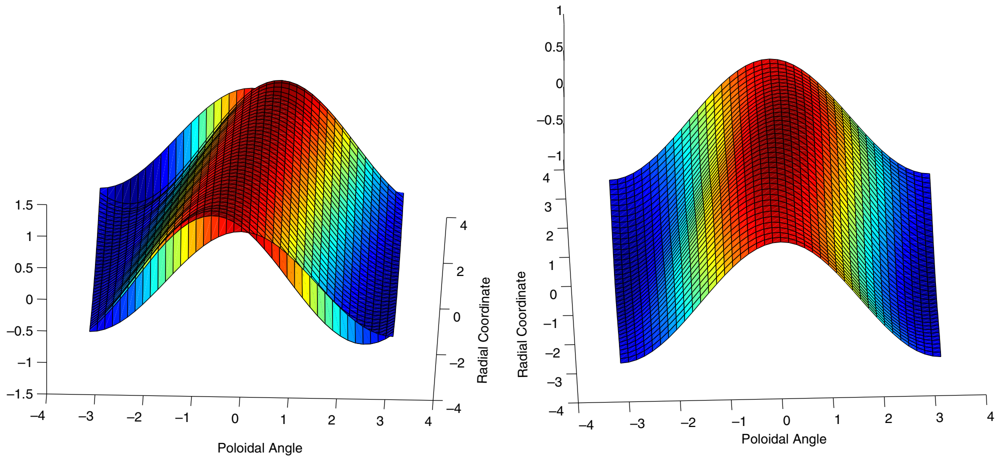

Figure 1. Implementation of a magnetic island satisfying periodicity conditions in the flux-tube code GKW: simple projection on radial Fourier harmonics, showing the deformation of the edge cells to ensure periodicity (*a*) and smoothing obtained by adding a Gaussian damping on higher harmonics (*b*).

a dependent variable. The corresponding free energy conservation law, also given there, is relevant because the energetic contact between the electromagnetic microturbulence and the much slower large-scale MHD through much faster shear-Alfvén transients involves a small amount of energy which, however, yields strong consequences. The only modification in the equations as used here is the incorporation of the current profile as a free energy source, as described in section 5. The flux surface geometry is built around the equilibrium flux surfaces. Islands are initialized or emerge naturally and are represented as part of the $\tilde{A}_\parallel$ disturbances.

For this work the geometry is updated using field-aligned conformal coordinates. Field-aligning means using a Clebsch representation $\{xys\}$, in which $x(\psi)$ is a surface label of the poloidal flux, s is a parallel coordinate set equal to either the poloidal or toroidal angles, and y is a function of both angles but through the use of the pitch parameter $q(\psi)$ satisfies $B^y \equiv \boldsymbol{B} \cdot \nabla y = 0$ exactly, everywhere. This is only possible for straight field line angle coordinates because $q = B^\varphi / B^\theta$ and to build Clebsch coordinates $\boldsymbol{B} = \chi(x)\nabla x \times \nabla y$ the condition $q = q(\psi)$ is necessary [51]. The function χ gives effective normalization. Here, φ is the geometric toroidal angle and the choice $s = \varphi$ leads to $y_k = \theta - q^{-1}(\varphi - \varphi_k)$ with the constant φ_k giving the reference position. The use of a different φ_k on each poloidal plane $\varphi = \varphi_k$ is a version of the shifted metric procedure [52] which avoids secular deformation in the metric coefficient ratio g^{xy}/g^{xx}. Here, the sign convention is for $\boldsymbol{B} = I\nabla\varphi + \nabla\varphi \times \nabla\psi$ and $\nabla R \times \nabla Z \cdot \nabla\varphi > 0$.

The linear component of the parallel derivative is calculated as $\boldsymbol{B} \cdot \nabla = B^s(\partial/\partial s)$. The conformal property is then introduced to further avoid poloidally periodic deformation in the coordinate cells, by stating $\boldsymbol{B} \cdot \nabla\theta_{\mathrm{c}} = (f_{\mathrm{c}}/R)|\nabla\psi|^2$ as the poloidal angle definition, where $f_{\mathrm{c}}(\psi)$ is the conformal flux function found by normalizing θ_{c} to a 2π-cycle for periodicity. The radial coordinate $x_{\mathrm{c}}(\psi)$ is defined as $\nabla x_{\mathrm{c}} = f_{\mathrm{c}}\nabla\psi$. The straight field line angle definition, by contrast, is defined as $\boldsymbol{B} \cdot \nabla\theta = I/qR^2$ since $B^\varphi = I/R^2$, with q found by normalizing θ to a 2π-cycle. We define $y_{\mathrm{c}} = \theta_{\mathrm{c}}$. The relationships $\theta_{\mathrm{c}}(\theta)$ and $\theta(\theta_{\mathrm{c}})$ are used to interpolate the finite difference of $\partial/\partial s$ onto a grid which is equidistant in x_{c} and y_{c} in the poloidal plane. This makes use of the fact that $y = \theta$ for $\varphi = \varphi_k$. One can then derive the coordinate

Jacobian $\nabla x_c \times \nabla y_c \cdot \nabla s = g_c^{xx}/R$ and the deformation $d = g_c^{xy}/g_c^{xx}$ using the definitions of f_c and x_c. One finds that in conventional tokamak equilibrium models $d^2 < 1$ almost everywhere, facilitating both the representation of microturbulence and iterative solvers for linear operators involving the perpendicular Laplacian $\nabla_\perp^2$, and that the conformal property $g_c^{xx} g_{cyy} = 1$ is exactly satisfied. In the cylindrical limit one can show y_c and θ both relax to η, the geometric axial angle, and x_c relaxes to $\log r$ with r the cylindrical radius. The subscript c in each of these expressions denotes the conformal coordinate system $\{x_c, y_c, \varphi\}$. For further motivation and details see [51].

3. Gyrokinetic simulations of ITG turbulence in the presence of a magnetic island

Vlasov flux tube and global PIC simulations are employed to investigate the behaviour of electrostatic ion-temperature-gradient (ITG) driven turbulence in the presence of a prescribed ($m = 3, n = 2$) magnetic island. The parameters employed in the runs of GKW are close to those of the Cyclone base case [53], $\rho_* = (2\text{–}4) \times 10^{-3}$, $R/L_T = 6.9$, $R/L_n = 2.2$, $\epsilon = 0.19$. ORB5 simulations have been run without source terms. To have a phase of slowly decaying turbulence with quasi-stationary profiles [44], a smaller value of ρ_* has been considered, typically $\rho_* = 4 \times 10^{-4}$. The gradient length for the ion temperature during the decaying-turbulence phase stays about $R/L_T \approx 7$ in the region $0.5 \lesssim \sqrt{\psi} \lesssim 0.9$ (where $\sqrt{\psi}$ is used as a normalized radial coordinate and the resonant surface is located at $\sqrt{\psi} = 0.67$). The background density was assumed to be flat, $R/L_n = 0$. A small inverse aspect ratio, $\epsilon = 0.14$, has been considered. The whole radial domain is simulated. In the PIC simulations presented here, the new electromagnetic version of ORB5 [54] has been used in the electrostatic approximation. With respect to previous PIC results [36], new code diagnostics have been implemented (e.g. on the local energy spectrum, see below), but the physical picture remains the same. In the following, it is shown that the findings of global, slowly decaying turbulence simulations agree well with local flux-tube simulations as long as the physical model remains the same, in particular with respect to the treatment of the electron dynamics. As a matter of fact, both codes assume, for the case of an adiabatic electron response, that the electrons react instantaneously to the electrostatic potential on the *unperturbed* flux surfaces. In the presence of an island, however, the axisymmetry typical of the tokamak configuration is destroyed. The only feasible way to include the *perturbed* magnetic geometry in the electron response is to treat also the electrons as a kinetic species. At the moment, however, this is not possible with ORB5 if a magnetic island is present (for an unperturbed magnetic equilibrium with nested magnetic surfaces, ORB5 simulations of electromagnetic turbulence with kinetic electrons have instead been presented recently [54]). For this reason, modes with $m = n = 0$ are excluded from ORB5 runs [36]. In this section, simulations that treat the electrons as a kinetic species are performed with the code GKW, employing the actual mass ratio of a deuterium plasma.

The first effect connected with the presence of the island seen in the simulations is the expected flattening of density and temperature profiles inside the island separatrix, after a transient phase in which they relax to the perturbed magnetic configuration. Just outside the separatrix, a steepening with respect to the unperturbed profiles is found, in particular in the region around $\xi = 0$ (i.e. at the level of the O-point), where the perturbed flux surfaces are 'compressed' by the island. However, a corresponding increase in the turbulence level is not observed. In contrast, the heat flux and the heat conductivity are reduced in this region, while they are higher across the X-point, as shown in figure 2, where the eddies can cross the rational surface. In both codes, an asymmetry in the heat conductivity at the X-point is usually seen, which can be attributed to the fact that the eddies are able to convect through

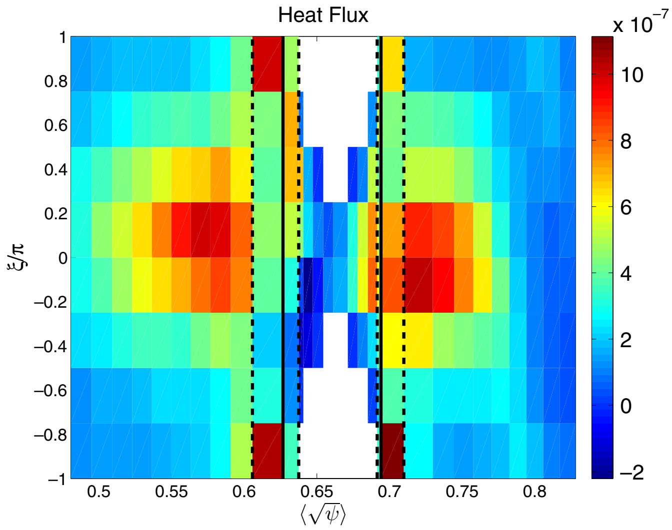

Figure 2. ORB5 simulation showing the heat flux in the island region with the associated the strong transport through the X-points ($\xi = \mp\pi$) and its reduction on the island separatrix (marked by thick vertical lines) at the O-point location ($\xi = 0$).

the island in the drift direction. This convection mechanism seems to act more effectively than diffusive turbulence spreading [55] in transporting the turbulence towards linearly stable regions inside the island. The turbulence reduction at the separatrix for $\xi = 0$ mentioned above is explained as a result of the action of the sheared flows connected with the long-wavelength components of the electrostatic potential, which 'rip apart' the eddies in analogy to what is known from zonal-flows dynamics. Figure 3 reports the time evolution of the *local* turbulence spectrum at two different radial locations in figure 2, namely $\langle\sqrt{\psi}\rangle = 0.57$ and $\langle\sqrt{\psi}\rangle = 0.63$ (angular brackets denoting the average value of the radial coordinate on the perturbed flux surface). Well outside the island, it can be seen that the $n = 2$ component of the electrostatic potential, which decays during the first phase of the ORB5 simulation (in which the profiles adjust to the perturbed equilibrium [36]), is again pumped through a nonlinear coupling with the small-scale (turbulent) modes. However, the energy of the long-scale mode is smaller than that of turbulence during most of the simulation time and the turbulent eddies efficiently transport heat across the flux surfaces. In contrast, at the island separatrix, in particular on the side towards the plasma core, the $n = 2$ mode largely dominates the other modes. The result observed in several simulations is a reduction in the heat flux at the separatrix. From the simulations performed so far [35], however, no firm conclusion can be drawn on whether nonlinearly generated sheared flows arising in the presence of small magnetic islands can contribute to the improvement of the confinement in the vicinity of rational surfaces, which has been reported in experiments [56]. Inside the island, the $\boldsymbol{E} \times \boldsymbol{B}$ transport can be dominated by long-wavelength modes. The transport due to different modes is shown in figure 4.

The picture outlined above emerges consistently from ORB5 and GKW simulations with adiabatic electrons. The inclusion of the perturbed magnetic equilibrium in the electron response through kinetic electrons in GKW, however, shows that the dynamics of the long-wavelength mode in the island region can change significantly. Figure 5 shows a snapshot of the electrostatic potential, perturbed density, total density and total density profile across the

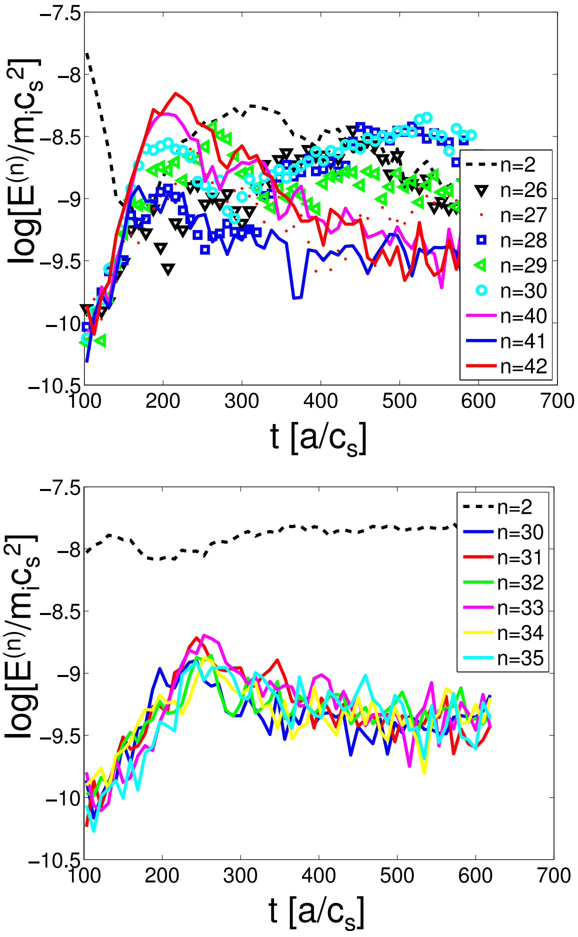

Figure 3. Time evolution of the toroidal energy spectrum (logarithm of the mode energy normalized to $M_i c_s^2$) of the potential disturbances for $\langle\sqrt{\psi}\rangle = 0.57$ (outside the island, (*a*)) and for $\langle\sqrt{\psi}\rangle = 0.63$ (island separatrix, core side, (*b*)). In the latter case, only low mode numbers (corresponding to the magnetic island) are significantly excited.

O and X-point. A large-scale electrostatic mode, which we will call 'vortex mode' following [17], develops in the centre of the magnetic island as a consequence of the nonlinear flow of energy into long wavelengths discussed above. The time evolution of this structure exhibits a complex dynamics, being non-stationary with a periodic sign reversal of the electrostatic potential. In passing, we note that a non-zero zonal-flow frequency has been observed recently in turbulence simulations including a magnetic island in slab geometry [37]. It is shown in [35] that the heat flux associated with the vortex mode at its peak intensity can largely exceed the flutter flux, i.e. the radial flux due to the parallel motion of the particles along the perturbed magnetic-field lines. On average, the flutter flux and the $\boldsymbol{E} \times \boldsymbol{B}$ flux due to the vortex mode yield a comparable contribution to the total heat transport. The strength of the mode is found to be reduced for smaller ρ_*, i.e. larger scale separation between island and turbulence. This fact could also be related, however, to the different degree of flattening of the ion temperature inside the island between both cases and the associated different behaviour of the microinstabilities. The vortex mode appears also in simulations performed for the

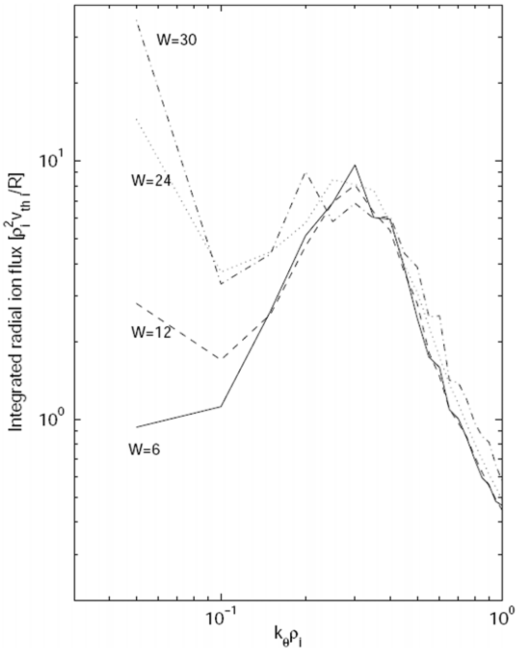

Figure 4. Radial electrostatic heat flux (integrated over the simulation box) driven by each component of the spectrum for different values of the ratio W/ρ_i (GKW simulations).

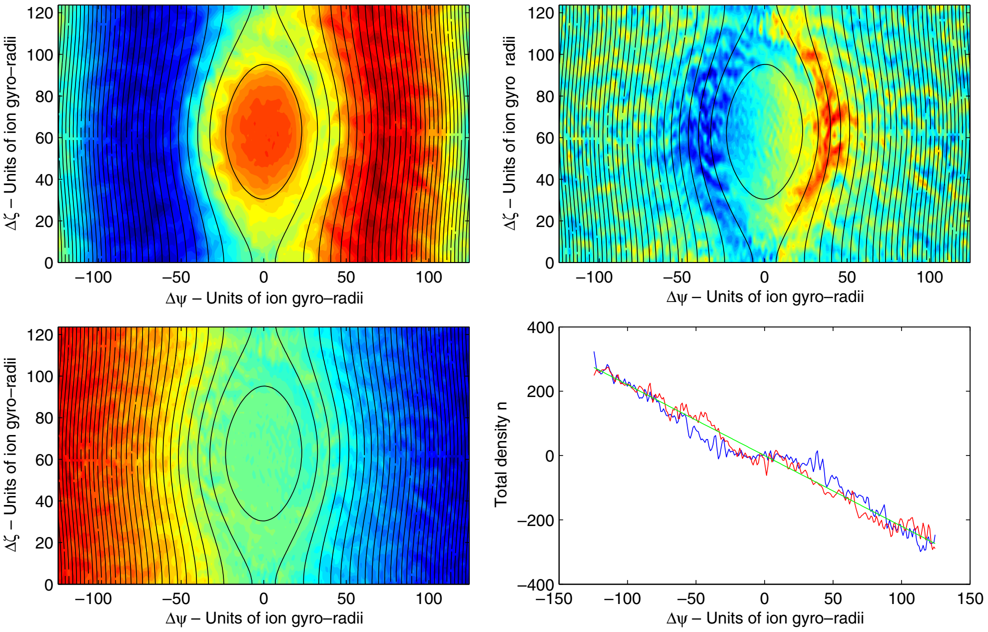

Figure 5. Snapshot of a GKW simulation showing the electrostatic potential (top left), $\delta n/n$ (top right), the total density (bottom left) and the density profiles (bottom right; the green line represents the unperturbed profile, the blue line a cut through the O-point and the red line a cut through the X-point). (Colour online.)

same plasma parameters in the case of islands rotating at the ion or electron diamagnetic frequency.

4. Turbulence-free gyrokinetic simulations of rotating islands

We now turn to simulations performed with the code GKW, in which a filter is applied on short-wavelength components of the spectrum of the electrostatic disturbances to suppress the turbulence. Moreover, the background density and temperature gradients are reduced, $R/L_n \leqslant 1$ and $R/L_T \leqslant 3$. Although neoclassical physics is still not fully tested in the code (and therefore collisions are switched off), the presence of fully kinetic electrons allows the investigation of the behaviour of the potential connected to the rotation of the island, and provides useful information on the density and the temperature in the presence of toroidal effects, which can be compared with kinetic simulations that retain neoclassical physics but not a self-consistent determination of the electrostatic potential [31]. It is worth stressing that numerical simulations can explore a parameter range which goes beyond the validity of the neoclassical analytic theory, in particular magnetic islands whose width is comparable or smaller than the ion banana width. As in the previous section, the island evolution is not computed and the (constant) island rotation frequency is treated as an input parameter.

A known result of tearing mode theory is that the potential associated with the rotation of a neoclassical magnetic island is [7, 8]

$$\tilde{\phi} = \frac{\omega q}{mc}[\psi - \psi_s - h(\Omega)], \tag{6}$$

as can be derived from the requirement $E_\parallel = -\nabla_\parallel \tilde{\phi} - (1/c)\partial \tilde{A}_\parallel/\partial t = 0$. The function $h(\Omega)$ is an integration 'constant' (deriving from the fact that $\nabla_\parallel \Omega = 0$, see section 2) which is connected with the density profile in the presence of an island [8]. Assuming no sources nor sinks in the island and a vanishing electric field away from it, $h(\Omega)$ must vanish inside the island separatrix for parity reasons (this corresponds to profile flattening), and must scale as $\psi - \psi_s$ for $\psi - \psi_s \gg W_\psi$. The $\boldsymbol{E} \times \boldsymbol{B}$ velocity connected with this electrostatic potential forces the plasma inside the island to co-rotate with it, while it vanishes at some distance from the island, where $\tilde{\phi}$ attains a constant value. When a finite island rotation is enforced in GKW simulations, and the island width is larger than the ion orbit width, a potential with the shape given by equation (6) develops, figure 6(*a*). Its peak value (at the island separatrix) exhibits the expected linear scalling with the rotation frequency ω, while it vanishes at the edge of computational domain to satisfy the periodic boundary conditions. If the rotation frequency is chosen to be in the ion diamagnetic direction, $\tilde{\phi}$ is found to be localized in the vicinity of the island, while its shape is broader if the rotation is in the electron direction. It is known that islands rotating at a frequency between 0 and the electron diamagnetic frequency lead to the emission of drift waves [23]. In this case, the maximum of the electrostatic potential outside the island is found to be localized between the O and the X-point (figure 6(*b*)), as found in analytic theory for the slab case [25].

A set of simulations has been performed at small island width (slightly smaller than the thermal ion banana width) in order to determine the density and temperature profiles in a rotating island. In recent drift-kinetic simulations [31], it was found that, when the ratio ρ_i/W is increased, the ion density perturbation exhibits more and more an adiabatic ('unmagnetized') response [22, 57]. As a consequence, due to the shape of the electrostatic potential, cf equation (6), the ion density perturbation was observed to lead to a flattening of the total density profile even in small islands rotating in the ion diamagnetic direction, and to a steepening for islands rotating in the opposite direction. Correspondingly, the bootstrap

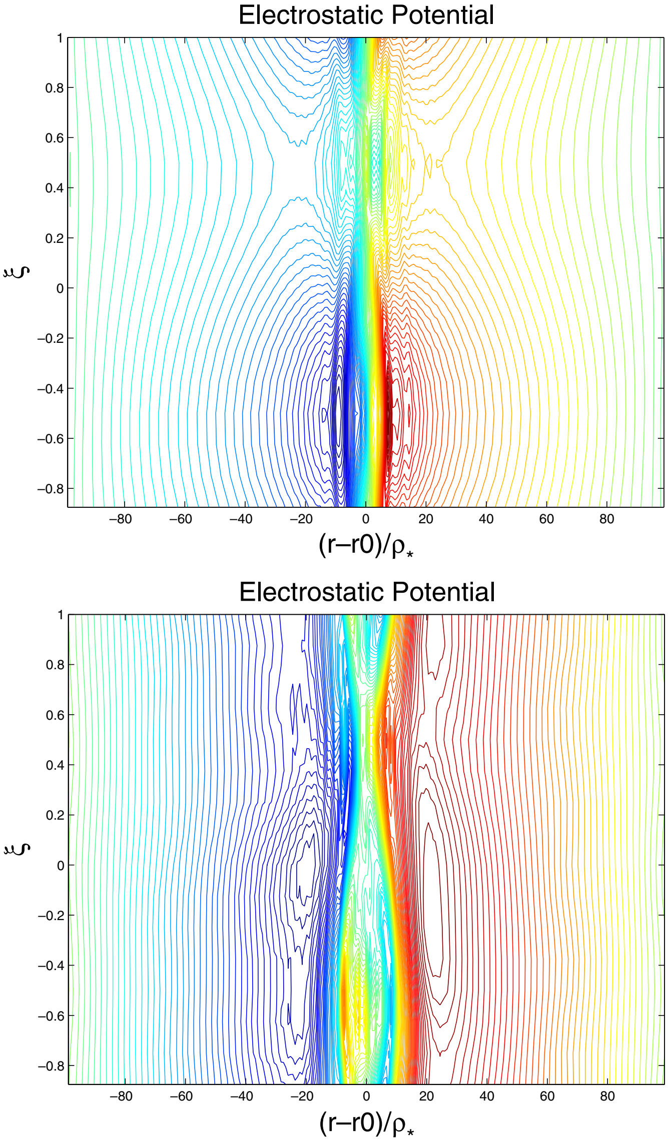

Figure 6. Electrostatic potential arising from a rotating magnetic island in the absence of turbulence for a frequency close to the electron diamagnetic frequency in the case of no equilibrium gradients (*a*) and with equilibrium gradients (*b*).

current was found to be strongly reduced in islands rotating at the ion diamagnetic frequency and largely preserved when the island frequency equals the electron diamagnetic frequency, implying an enhanced neoclassical stability in the latter case. Since, however, in the presence of an unflattened ion density quasi-neutrality was violated (the electron orbit width is always much smaller than the island width and the electron density tends therefore to be flat), in [31] the (prescribed) electrostatic potential was modified with respect to equation (6) in order to recover quasi-neutrality. In the simulations presented here, the potential is determined

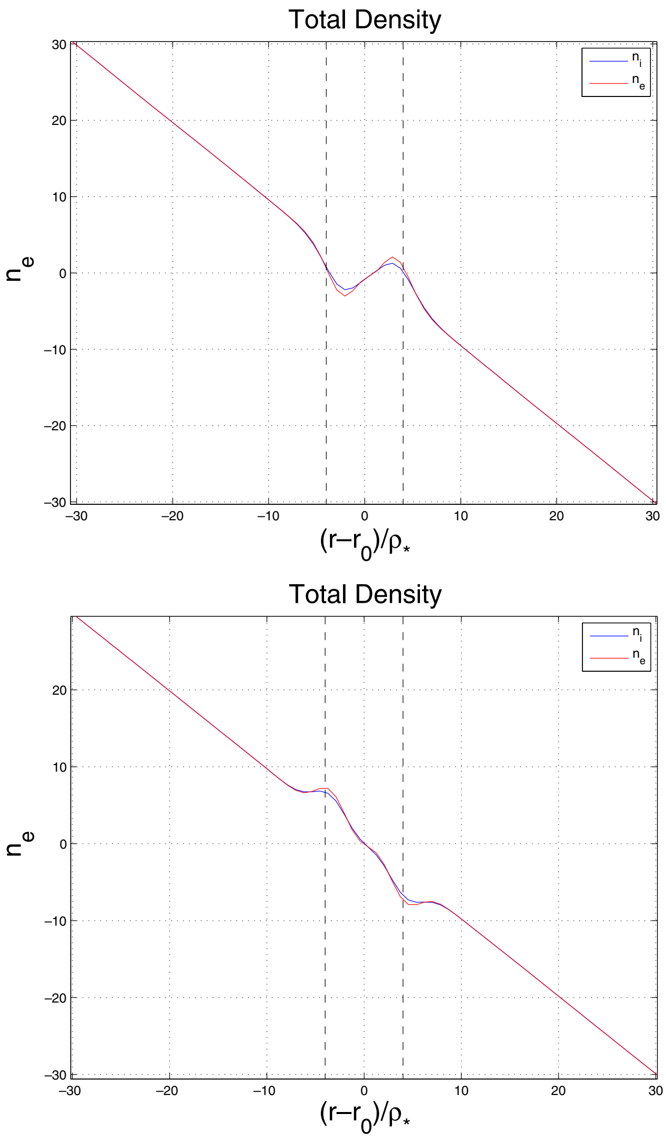

Figure 7. Density profiles for a small island rotating in the ion diamagnetic direction (*a*) and in the electron diamagnetic direction (*b*).

self-consistently from the electron response. GKW simulations show that the ion density profile exhibits the same properties as described above, the electron density profile following closely that of the ions. As can be clearly observed in figure 7, for rotation frequencies above the diamagnetic frequency, the density perturbation leads even to a positive density gradient inside the island (rotation in the ion direction) or to a gradient larger than the equilibrium one (rotation in the electron direction). In other words, these simulations support the neoclassical drift-kinetic simulations of Bergmann *et al* [31], according to which the neoclassical drive is largely suppressed in a small island rotating in the electron diamagnetic direction.

5. Self-consistent gyrofluid simulation of the island evolution in the presence of turbulence

The self-consistent interaction between magnetic islands and turbulence was studied by the GEMZ model described above. The nonlinear dynamics are followed together with local modifications in the profiles but the MHD and neoclassical flow equilibrium is removed by separating $n_z \to n_0 + \tilde{n}_z$ (e.g. for the gyrocentre density of species z) for each dependent variable. Profile functions n_0 and T_0, set equal for ions and electrons, provide gradient dynamics for the turbulence. Tearing and island dynamics are enabled by keeping $u_{e0} = -J_0/ne$ in the parallel velocity for the electrons, consistent with the chosen profile $q(x)$. The equilibrium dynamics [58] are avoided by leaving these profile functions out of the curvature terms. A small island, added consistently to $\tilde{A}_\parallel$ and $\tilde{J}_\parallel$ as a piece proportional to a simple radial profile and to $\cos \xi_0 = \cos(2\theta - \varphi)$ (here, a 2, 1 island is considered), is combined with the random-bath turbulent density fluctuations in the initial state.

The plasma parameters are typical of tokamak core conditions ($n = 3 \times 10^{19}\,\mathrm{m}^{-3}$ and $T = 2\,\mathrm{keV}$ and $B_0 = 2.5\,\mathrm{T}$) in the dimensions $R_0 = 1.65\,\mathrm{m}$ and $a = 0.5\,\mathrm{m}$. The profiles have $R/L_T = 8$ and $L_n/L_T = 3$. Various current profiles were tried. An 'exponential' case has $q = 4\exp(r_a^2 - 1)$, a parabolic case has $q = 1 + 3r_a^2$ and a tearing-unstable case $q = 3/(2 - r_a^2)$ taken from Wesson [59], where $r_a = \exp(x_c)$ is the conformal normalized minor radius. In each case $J_0 = (B_0/\mu_0 R_0)(1/r_a^2)(\partial/\partial r_a)(r_a^2/q)$ is chosen consistently. The poloidal and toroidal flux profiles ψ and ψ_t do not enter the equations but are used in the helical flux diagnostic $\Psi = R_0^{-1}[(\psi_t/2 - \psi) - \mathrm{Min}(\psi_t/2 - \psi)] + \tilde{A}_\parallel$ of the $q = 2$ rational surface (the flux label Ω introduced in section 2 can be easily derived from Ψ through a second-order expansion of ψ_t around the rational surface). Here, the sign convention is for $\boldsymbol{B} = I\nabla\varphi + \nabla\varphi \times \nabla\psi$ and $\nabla R \times \nabla Z \cdot \nabla\varphi > 0$.

The current profiles in present tokamaks are usually mildly stable to tearing for the cylindrical model and neoclassical effects are usually invoked to account for observed magnetic fluctuations consistent with magnetic islands a few centimetres wide. It is important to note that the combination of gradients and toroidal curvature is severely stabilizing for tearing modes [10], due to the action of geodesic curvature (the part acting on $\partial/\partial\psi$ of the disturbance). Hence the maintenance of the island has to be a robust effect. Turbulence has two potential effects on islands. Diffusion is more familiar, but the details of drift wave turbulence [60, 61] show that this has to act through the pressure and current fluctuations, not the $\boldsymbol{E} \times \boldsymbol{B}$ or magnetic part. The other potential effect is inverse cascade dynamics through these two components. For drift waves dynamically incompressible vorticity dynamics are active. In addition for electromagnetic cases one has the inverse helicity cascade in 2D MHD turbulence [62], which directly affects $\tilde{A}_\parallel$. Normally the nonlinear electromagnetic processes are weaker than the $\boldsymbol{E} \times \boldsymbol{B}$ ones [63]. However, in this case they have the island's component of $\tilde{A}_\parallel$ to act upon and are therefore non-negligible.

A further less-familiar component of these dynamics from the point of view of magnetic island studies is that the turbulence is dominantly ITG driven despite the presence of many other mode types and despite the mild finite-beta stabilization [50]. The tendency of the electron dynamics to equalize the pressure along field lines and within the island does not affect ion temperature fluctuations, so the effect to weaken the turbulence is negligible.

The main result of the computations so far is that the initial long-wave disturbance in $\tilde{A}_\parallel$ is not only maintained but increased during the turbulence which is well saturated. The simulations show an island activity which survives in the face of the curvature/toroidicity effects. The helical flux diagnostic Ψ forms a channel whose width depends on the magnitude of $\tilde{A}_\parallel$: the contour interval is $-1/3$ times the minimum value of Ψ, so the channel is wide for

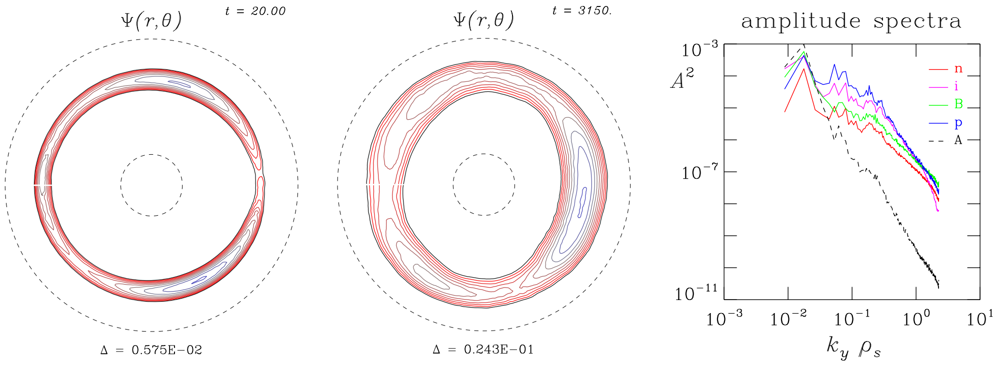

Figure 8. GEMZ simulations showing the contour plots of the helical flux Ψ at two different time slices during the simulation, $t = 20$ and $t = 3150$ (time is expressed in a/c_s units), and the disturbances spectrum (in terms of amplitude squared) for electron density (n), ion temperature (i), magnetic field (B), electrostatic potential (p) and parallel magnetic potential (A).

larger islands. The visual appearance is therefore indicative of island robustness. The form of a 2/1 island indicates island coherence and is confirmed by a corresponding peak in the disturbance spectrum, as presented in figure 8. A coupling to the $m = 3$ mode is also visible. The strength of this coupling also fluctuates as the island evolves. The tearing-unstable case shown in the figure exhibits a more clear and more coherent island but the other two cases also show strong activity albeit with less island coherence. The island activity persists despite the absence of a clear unstable-eigenmode signature in $\tilde{A}_\parallel$—one looks for a slope discontinuity in the O-point cut of $A_\parallel$ across the island, which shows neither an obvious eigenmode structure nor significant chopping by turbulence. Indeed the poloidal spectrum of $A_\parallel$ shows clear dominance by the $m = 2$ component. The control cases without turbulence but with all the toroidal and pressure gradient effects are yet to be run; these and more detailed energy transfer diagnosis will provide for more definitive findings which will be published in the future.

6. Summary and conclusions

In this paper, recent advances in numerical simulations of tearing modes in toroidal geometry, including FLR effects have been reported. The development of highly parallelized and thoroughly benchmarked gyrokinetic and gyrofluid codes, as well as the increasing availability of high-performance computer resources allow the first steps in this area, employing realistic plasma parameters. Three different approaches have been followed here. The first one relies on the fact that the tearing mode grows on a much longer time scale than the turbulence. The magnetic island can then be implemented as a static magnetic perturbation and the development of the microinstabilities retaining toroidicity and kinetic effects can be investigated. Our results for electrostatic ITG turbulence confirm previous findings [36] that outside the island the fluctuations are much larger at the X-point as compared with the O-point, where sheared flows associated with nonlinearly driven long-wavelength modes suppress the turbulence even in the presence of increased gradients. Inside the island, the turbulence is reduced because of the flattening of temperature and density profiles due to the fast parallel motion along the perturbed field lines. Eddies convected in the drift direction contribute significantly to the turbulence level inside the island in the region close to the X-point. The nonlinear coupling between small (turbulence) and large (island) scales can generate a vortex mode that can yield inside the island a transport level comparable to the parallel (flutter) transport. This mode is found only if the perturbed magnetic geometry is accounted for in the electron response. These results show that the transport in the island region has more complex behaviour than in the 'standard' paradigm [20] and confirm the importance of the coupling between small and large scale. From a computational point of view, moreover, they represent a cross-check that different approaches (local and global) to the solution of the gyrokinetic equation in the presence of an island yield a consistent physical picture if the same assumptions are made. The second method presented here again employs a toroidal gyrokinetic formalism, but excludes the turbulence. The long-term goal is in this case to study processes taking place on the collisional time scale. Although the collision operator is still not fully functional, first collisionless results for an island with an imposed rotation reveal the potentialities of this approach, which allows a determination of the electrostatic potential associated with the island rotation, of the density and current profiles. Finally, the gyrofluid simulations performed with the GEMZ code demonstrate—for the first time for realistic tokamak parameters—the role of electromagnetic turbulence for the growth of the tearing mode, whose evolution is calculated in this case self-consistently as a part of the global disturbance spectrum.

Acknowledgments

The simulations presented in this paper have been partly performed on the HPC-FF machine at the Jülich Supercomputing Centre, Germany.

References

[1] Furth H P, Killeen J and Rosenbluth M N 1963 *Phys. Fluids* **6** 459
[2] Rutherford P H 1973 *Phys. Fluids* **16** 1903
[3] Sauter O *et al* 1997 *Phys. Plasmas* **4** 1654
[4] Qu W X and Callen J D 1985 *University of Wisconsin Plasma Report* UWPR 85-5
[5] Carrera R, Hazeltine R D and Kotschenreuther M 1986 *Phys. Fluids* **29** 899
[6] Chang Z *et al* 1995 *Phys. Rev. Lett.* **74** 4663
[7] Smolyakov A I *et al* 1995 *Phys. Plasmas* **2** 1581
[8] Wilson H R *et al* 1996 *Phys. Plasmas* **3** 248
[9] Glasser A H, Greene J M and Johnson J L 1975 *Phys. Fluids* **18** 875
[10] Kotschenreuther M, Hazeltine R D and Morrison P J 1985 *Phys. Fluids* **28** 294
[11] Hegna C C 1999 *Phys. Plasmas* **6** 3980
[12] Yamada M, Kulsrud R and Ji H 2010 *Rev. Mod. Phys.* **82** 603
[13] Waelbroeck F L 2009 *Nucl. Fusion* **49** 104025
[14] Kaw P, Valeo E and Rutherford P 1979 *Phys. Rev. Lett.* **43** 1398
[15] Itoh K, Itoh S-I and Fukuyama A 1992 *Phys. Rev. Lett.* **69** 1050
[16] Diamond P H, Hazeltine R D, An Z G, Carreras B A and Hicks H R 1984 *Phys. Fluids* **27** 1449
[17] McDevitt C J and Diamond P H 2006 *Phys. Plasmas* **13** 032302
[18] Sen A, Singh R, Chandra D, Kaw P and Raju D 2009 *Nucl. Fusion* **49** 115012
[19] Itoh S-I, Itoh K and Yagi M 2004 *Plasma Phys. Control. Fusion* **46** 123
[20] Fitzpatrick R 1995 *Phys. Plasmas* **2** 825
[21] Militello F, Waelbroeck F L, Fitzpatrick R and Horton W 2008 *Phys. Plasmas* **15** 050701
[22] Connor J W and Wilson H R 1995 *Phys. Plasmas* **2** 4575
[23] Waelbroeck F L, Connor J W and Wilson H R 2001 *Phys. Rev. Lett.* **87** 215003
[24] James M and Wilson H R 2006 *Plasma Phys. Control. Fusion* **48** 1647
[25] Wilson H R and Connor J W 2009 *Plasma Phys. Control. Fusion* **51** 115007
[26] Sydora R D 2001 *Phys. Plasmas* **8** 1929
[27] Wan W, Chen Y and Parker S E 2005 *Phys. Plasmas* **12** 012311
[28] Waelbroeck F L, Militello F, Fitzpatrick R and Horton W 2009 *Plasma Phys. Control. Fusion* **51** 015015
[29] Poli E *et al* 2002 *Phys. Rev. Lett.* **88** 075001
[30] Poli E *et al* 2003 *Plasma Phys. Control. Fusion* **45** 71
[31] Bergmann A, Poli E and Peeters A G 2009 *Phys. Plasmas* **16** 092507

[32] Poli E, Bergmann A and Peeters A G 2005 *Phys. Rev. Lett.* **94** 205001
[33] Poli E, Bergmann A, Peeters A G, Appel L and Pinches S D 2005 *Nucl. Fusion* **45** 384
[34] Siccinio M and Poli E 2009 *Plasma Phys. Control. Fusion* **51** 075005
[35] Hornsby W A *et al* 2010 *Phys. Plasmas* **17** 092301
[36] Poli E, Bottino A and Peeters A G 2009 *Nucl. Fusion* **49** 075010
[37] Li J, Kishimoto Y, Kouduki Y, Wang Z X and Janvier M 2009 *Nucl. Fusion* **49** 095007
[38] Ishizawa A and Nakajima N 2007 *Nucl. Fusion* **47** 1540
[39] Muraglia M *et al* 2009 *Nucl. Fusion* **49** 055016
[40] Jolliet S *et al* 2007 *Comput. Phys. Commun.* **177** 409
[41] Bottino A *et al* 2007 *Phys. Plasmas* **14** 010701
[42] Peeters A G and Strintzi D 2004 *Phys. Plasmas* **11** 3748
[43] Peeters A G, Camenen Y, Casson F J, Hornsby W A, Snodin A P, Strintzi D and Szepesi G 2009 *Comput. Phys. Commun.* **180** 2650
[44] Scott B D 2005 *Phys. Plasmas* **12** 102307
[45] Hahm T S 1988 *Phys. Fluids* **31** 2670
[46] White R B *et al* 1983 *Phys. Fluids* **26** 2958
[47] Beer M A, Cowley S C and Hammett G W 1995 *Phys. Plasmas* **2** 2687
[48] Peeters A G *et al* 2009 *Phys. Plasmas* **16** 042310
[49] Scott B D 2003 *Plasma Phys. Control. Fusion* **45** A385
[50] Scott B D 2006 *Plasma Phys. Control. Fusion* **48** B277
[51] Ribeiro T and Scott B 2010 *IEEE Trans. Plasma Sci.* **38** 2159
[52] Scott B D 2001 *Phys. Plasmas* **8** 447
[53] Dimits A M *et al* 2000 *Phys. Plasmas* **7** 969
[54] Bottino A *et al* 2010 *IEEE Trans. Plasma Sci.* **38** 2129
[55] Hahm T S *et al* 2004 *Plasma Phys. Control. Fusion* **46** A323
[56] Joffrin E *et al* 2003 *Nucl. Fusion* **43** 1167
[57] Konovalov S V, Mikhailovskii A B, Tsypin V S and Sharapov S E 2002 *Dokl. Phys.* **47** 488
[58] Scott B D 2006 *Contrib. Plasma Phys.* **46** 714
[59] Wesson J 1997 *Tokamaks* (Oxford: Clarendon)
[60] Scott B D 1992 *Phys. Fluids* B **4** 2468
[61] Scott B D 2002 *New J. Phys.* **4** 52
[62] Biskamp D 1993 *Nonlinear Magnetohydrodynamics* (Cambridge: Cambridge University Press)
[63] Camargo S, Scott B D and Biskamp D 1996 *Phys. Plasmas* **3** 3912

Bibliography

[1] LAWSON, J. D., Proceedings of the Physical Society B **70** (1957) 6.

[2] WESSON, J., *Tokamaks*, Clarendon Press, Oxford, 1997.

[3] SHIMADA, M. et al., Nuclear Fusion **47** (2007) S1.

[4] SAUTER, O. et al., Plasma Physics and Controlled Fusion **52** (2010) 025002.

[5] LUCE, T. C. et al., Journal of Physics: Conference Series **25** (2005) 252.

[6] ESPOSITO, B. et al., Nuclear Fusion **49** (2009) 065014.

[7] MYNICK, H. E., Physics of Fluids B **5** (1993) 1471.

[8] GÜNTER, S. et al., Nuclear Fusion **47** (2007) 920.

[9] POLI, E. et al., Physics of Plasmas **6** (1999) 5.

[10] POLI, E. et al., Physical Review Letters **88** (2002) 075001.

[11] POLI, E. et al., Plasma Physics and Controlled Fusion **45** (2003) 71.

[12] BERGMANN, A. et al., Physics of Plasmas **16** (2009) 092507.

[13] POLI, E. et al., Physical Review Letters **94** (2005) 205001.

[14] POLI, E. et al., Nuclear Fusion **45** (2005) 384.

[15] SICCINIO, M. et al., Plasma Physics and Controlled Fusion **51** (2009) 075005.

[16] POLI, E. et al., Nuclear Fusion **49** (2009) 075010.

[17] POLI, E. et al., Plasma Physics and Controlled Fusion **52** (2010) 124021.

[18] POLI, E. et al., Computer Physics Communications **136** (2001) 90.

[19] RAMPONI, G. et al., Nuclear Fusion **48** (2008) 054012.

[20] FREIDBERG, J. P., *Ideal Magnetohydrodynamics*, Plenum Press, New York, 1987.

[21] BOYD, T. J. M. et al., *The Physics of Plasmas*, Cambridge University Press, Cambridge, 2003.

[22] BRAGINSKII, S. I., Reviews of Plasma Physics **1** (1965) 205.

[23] ALFVÉN, H., Arkiv för Mathematik, Astronomi och Fysik **29** (1943) 1.

[24] BISKAMP, D., *Nonlinear Magnetohydrodynamics*, Cambridge University Press, Cambridge, 1993.

[25] PRIEST, E. et al., *Magnetic Reconnection*, Cambridge University Press, Cambridge, 2000.

[26] YAMADA, M. et al., Reviews of Modern Physics **82** (2010) 603.

[27] SWEET, P., in *Electromagnetic Phenomena in Cosmical Physics* (1958) 123.

[28] PARKER, E. N., Journal of Geophysical Research **62** (1957) 509.

[29] PARKER, E. N., Astrophysical Journal Supplement Series **8** (1963) 177.

[30] PETSCHEK, H. E., in *Physics of Solar Flares*, NASA **SP-50** (1964) 425.

[31] KULSRUD, R. M., Earth Planet Space **53** (2001) 417.

[32] KADOMTSEV, B., Soviet Journal of Plasma Physics **1** (1975) 389.

[33] HASTIE, R. J., Astrophysics and Space Science **256** (1998) 177.

[34] SAUTER, O. et al., Physical Review Letters **88** (2002) 105001.

[35] CHAPMAN, I. T. et al., Nuclear Fusion **50** (2010) 102001.

[36] FURTH, H. P. et al., Physics of Fluids **6** (1963) 459.

[37] DRAKE, J. F. et al., Physics of Fluids **20** (1977) 1341.

[38] RUTHERFORD, P. H., Physics of Fluids **16** (1973) 1903.

[39] DRAKE, J. F. et al., Physical Review Letters **39** (1977) 453.

[40] HINTON, F. L. et al., Reviews of Modern Physics **48** (1976) 239.

[41] BALESCU, R., *Transport Processes in Plasmas Vol. 2: Neoclassical Transport*, North-Holland, Amsterdam, 1988.

[42] HELANDER, P. et al., *Collisional Transport in Magnetized Plasmas*, Cambridge University Press, Cambridge, 2002.

[43] BICKERTON, R. J. et al., Nature Physics **229** (1971) 110.

[44] PEETERS, A. G., Plasma Physics and Controlled Fusion **42** (2000) B231.

[45] HINTON, F. L. et al., Physics of Fluids **27** (1984) 1243.

[46] MIKHAILOVSKII, A. B., Contributions to Plasma Physics **43** (2003) 125.

[47] QU, W. X. et al., University of Wisconsin Plasma Report **UWPR 85-5** (1985).

[48] CARRERA, R. et al., Physics of Fluids **29** (1986) 899.

[49] FITZPATRICK, R., Physics of Plasmas **2** (1995) 825.

[50] CHANG, Z. et al., Physical Review Letters **74** (1995) 4663.

[51] SAUTER, O. et al., Physics of Plasmas **4** (1997) 1654.

[52] GÜNTER, S. et al., Nuclear Fusion **38** (1998) 1431.

[53] SAUTER, O. et al., Plasma Physics and Controlled Fusion **44** (2002) 1999.

[54] HORNSBY, W. A. et al., Physics of Plasmas **17** (2010) 092301.

[55] HORNSBY, W. A. et al., Plasma Physics and Controlled Fusion **53** (2011) 054008.

[56] HAZELTINE, R. D. et al., *Plasma Confinement*, Addison-Wesley, New York, 1992.

[57] LITTLEJOHN, R. G., Journal of Mathematical Physics **23** (1982) 742.

[58] PINCHES, S. D. et al., Computer Physics Communications **111** (1998) 133.

[59] BERGMANN, A. et al., Physics of Plasmas **8** (2001) 5192.

[60] GUDE, A. et al., Nuclear Fusion **39** (1999) 127.

[61] MARASCHEK, M. et al., Plasma Physics and Controlled Fusiuon **45** (2003) 1369.

[62] FITZPATRICK, R., Nuclear Fuision **33** (1993) 1049.

[63] DRAKE, J. F. et al., Physics of Fluids **26** (1983) 2509.

[64] SMOLYAKOV, A. I., Plasma Physics and Controlled Fusion **35** (1993) 657.

[65] WAELBROECK, F. L., Nuclear Fusion **49** (2009) 104025.

[66] SICCINIO, M. et al., Journal of Physics: Conference Series **260** (2010) 012019.

[67] SMOLYAKOV, A. I. et al., Physics of Plasmas **2** (1995) 1581.

[68] WILSON, H. R. et al., Physics of Plasmas **3** (1996) 248.

[69] IMADA, K. et al., Plasma Physics and Controlled Fusion **51** (2009) 105010.

[70] BERGMANN, A. et al., Physics of Plasmas **12** (2005) 072501.

[71] MIKHAILOVSKII, A. B. et al., Plasma Physics **42** (2000) 309.

[72] JAMES, M. et al., Plasma Physics and Controlled Fusion **52** (2010) 075008.

[73] HORTON, W., Reviews of Modern Physics **71** (1999) 735.

[74] GARBET, X. et al., Nuclear Fusion **50** (2010) 043002.

[75] VILLARD, L. et al., Plasma Physics and Controlled Fusion **46** (2004) B51.

[76] KAW, P. et al., Physical Review Letters **43** (1979) 1398.

[77] ITOH, K. et al., Physical Review Letters **69** (1992) 1050.

[78] DIAMOND, P. H. et al., Physics of Fluids **27** (1984) 1449.

[79] MCDEVITT, C. J. et al., Physics of Plasmas **13** (2006) 032302.

[80] SEN, A. et al., Nuclear Fusion **49** (2009) 115012.

[81] ITOH, S.-I. et al., Plasma Physics and Controlled Fusion **46** (2004) 123.

[82] MILITELLO, F. et al., Physics of Plasmas **15** (2008) 050701.

[83] HASEGAWA, A. et al., Physics of Fluids **21** (1978) 87.

[84] DIAMOND, P. H. et al., Plasma Physics and Controlled Fusion **47** (2005) R35.

[85] MATTOR, N. et al., Physics of Plasmas **1** (1994) 4002.

[86] ISHIZAWA, A. et al., Physics of Plasmas **14** (2007) 040702.

[87] NISHIMURA, S. et al., Physics of Plasmas **15** (2008) 092506.

[88] MURAGLIA, M. et al., Nuclear Fusion **49** (2009) 055016.

[89] YAGI, M. et al., Plasma and Fusion Research **2** (2007) 025.

[90] MURAGLIA, M. et al., Physical Review Letters **107** (2011) 095003.

[91] HORTON, W. et al., Physics of Fluids **24** (1981) 1077.

[92] BOTTINO, A., *Modelling of global electrostatic micro-instabilities in tokamaks*, PhD Thesis, EPFL Lausanne (2004), http://library.epfl.ch/theses/?nr=2938.

[93] FRIEMAN, E. A. et al., Physics of Fluids **25** (1982) 502.

[94] BRIZARD, A. J. et al., Reviews of Modern Physics **79** (2007) 421.

[95] BEER, M. A. et al., Physics of Plasmas **3** (1996) 4046.

[96] SCOTT, B. D., Physics of Plasmas **17** (2010) 102306.

[97] JOLLIET, S. et al., Computer Physics Communications **177** (2007) 409.

[98] PEETERS, A. G. et al., Computer Physics Communications **180** (2009) 2650.

[99] BEER, M. A. et al., Physics of Plasmas **2** (1995) 2687.

[100] DIMITS, A. M. et al., Physics of Plasmas **7** (2000) 969.

[101] HAHM, T. S. et al., Plasma Physics and Controlled Fusion **46** (2004) A323.

[102] JOFFRIN, E. et al., Nuclear Fusion **43** (2003) 1167.

[103] HORNSBY, W. A. et al., Europhysics Letters **91** (2010) 45001.

[104] HAZELTINE, R. D. et al., Physics of Plasmas **4** (1997) 2920.

[105] SCOTT, B. D., Physics of Plasmas **12** (2005) 102307.

[106] RIBEIRO, T. T. et al., IEEE Transactions on Plasma Science **38** (2010) 2159.

[107] KOTSCHENREUTHER, M. et al., Physics of Fluids **28** (1985) 294.

[108] DE LAZZARI, D. et al., Nuclear Fusion **49** (2009) 075002.

[109] DE LAZZARI, D. et al., Nuclear Fusion **50** (2010) 079801 (Erratum).

[110] TRUBNIKOV, B. A., Reviews of Plasma Physics **1** (1965) 105.

[111] STIX, T. H., *Waves in Plasmas*, AIP, New York, 1992.

[112] SWANSON, D. G., *Plasma Waves*, Academic Press, San Diego, 1989.

[113] BRAMBILLA, M., *Kinetic Theory of Plasma Waves*, Clarendon Press, Oxford, 1998.

[114] HARVEY, R. W. et al., Physical Review Letters **62** (1989) 426.

[115] KRAVTSOV, Y. A. et al., *Geometrical Optics of Inhomogeneous Media*, Springer Verlag, Berlin, 1990.

[116] BERNSTEIN, I. B., Physics of Fluids **18** (1975) 320.

[117] MAZZUCATO, E., Physics of Fluids B **1** (1989) 1855.

[118] PEETERS, A. G., Physics of Plasmas **3** (1996) 4386.

[119] PEREVERZEV, G. V., Reviews of Plasma Physics **19** (1996) 1.

[120] PEREVERZEV, G. V., Physics of Plasmas **5** (1998) 3529.

[121] POLI, E. et al., Physics of Plasmas **6** (1999) 5.

[122] POLI, E. et al., Fusion Engineering and Design **53** (2001) 9.

[123] FARINA, D., Fusion Science and Technology **52** (2007) 154.

[124] HOULBERG, W. A. et al., Nuclear Fusion **45** (2005) 1309.

[125] PRATER, R. et al., Nuclear Fusion **48** (2008) 035006.

[126] POLI, E., Fusion Science and Technology **53** (2008) 1.

[127] HEGNA, C. C. et al., Physics of Plasmas **4** (1997) 2940.

[128] ZOHM, H. et al., Plasma Physics and Controlled Fusion **49** (2007) B341.

[129] GIRUZZI, G. et al., Nuclear Fusion **39** (1999) 107.

[130] URSO, L. et al., Nuclear Fusion **50** (2010) 025010.

[131] GLASSER, A. H. et al., Physics of Fluids **18** (1975) 875.

[132] ZOHM, H. et al., Journal of Physics: Conference Series **25** (2005) 234.

[133] BERTELLI, N. et al., Nuclear Fusion **51** (2011) 103007.

[134] ZOHM, H. et al., Nuclear Fusion **41** (2001) 197.

[135] LAHAYE, R. J. et al., Physics of Plasmas **9** (2002) 2051.

[136] ISAYAMA, A. et al., Nuclear Fusion **43** (2003) 1272.

[137] HENDERSON, M. A. et al., Nuclear Fusion **48** (2008) 054013.

[138] HEIDINGER, R. et al., Fusion Engineering and Design **84** (2009) 284.

[139] RAMPONI, G. et al., Fusion Science and Technology **52** (2007) 193.

[140] MARUSHCHENKO, N. B. et al., Fusion Science and Technology **55** (2009) 180.

[141] MARUSHCHENKO, N. B. et al., Nuclear Fusion **48** (2008) 054002.

[142] POLI, E. et al., Proc. 14th Joint Workshop on ECE and ECRH (Santorini, Greece, 2006) http://www.hellasfusion.gr/images/stories/ec14/papers/61.pdf.

[143] GRASWINCKEL, M. F. et al., Nuclear Fusion **48** (2008) 054015.

[144] SAIBENE, G. et al., Proc. 21st IAEA Int. Conf. on Fusion Energy (Chengdu, China, 2006) http://www naweb.iaea.org/napc/physics/FEC/FEC2006/html/index.htm.

[145] ANGIONI, C. et al., Nuclear Fusion **43** (2003) 455.

[146] GÜNTER, S. et al., Nuclear Fusion **44** (2004) 524.

[147] CHANG, Z. et al., Nuclear Fusion **30** (1990) 219.

[148] SCOTT, B. D. et al., Physics of Fluids **28** (1985) 275.

[149] COPPI, B., Physics of Fluids **7** (1964) 1501.

[150] LANDAU, L., J. Phys (Moscow) **10** (1946) 25.

[151] FRIED, R. D. et al., *The Plasma Dispersion Function*, Academic Press, New York, 1961.